THE UNIVERSITY OF MICHIGAN

COLLEGE OF ENGINEERING
Department of Nuclear Engineering

Technical Report

NEUTRON DIFFRACTION AND INELASTIC SCATTERING BY VITREOUS BERYLLIUM FLUORIDE

Charles A. Pelizzari

DRDA Project 011111

supported by:

NATIONAL SCIENCE FOUNDATION
GRANT NO. GK-35901
WASHINGTON, D.C.

administered through:

DIVISION OF RESEARCH DEVELOPMENT AND ADMINISTRATION ANN ARBOR

February 1974

TABLE OF CONTENTS

ABSTRACT

NEUTRON DIFFRACTION AND INELASTIC SCATTERING
BY VITREOUS BERYLLIUM FLUORIDE

by

Charles Arthur Pelizzari

Chairman: John M. Carpenter

The total neutron diffraction pattern and the scattering law of vitreous BeF_2 have been measured using time-of-flight techniques.

The diffraction pattern was measured at the University of Michigan time-of-flight diffractometer for wave vector transfers in the range $0.9\text{Å}^{-1} \leq Q \leq 27\text{Å}^{-1}$. The data were corrected for container scattering, multiple scattering in the vandium reference scatterer and multiple scattering in the BeF_2 sample. Fourier transformation of the diffraction data yielded a radial density function from which termination and normalization errors were partly removed using a novel computer graphic approach.

The refined rdf was analyzed for neighbor distances, coordination numbers and root-mean-square variation in neighbor distances for Be-F, F-F and Be-Be pairs. Longer-range order was found to persist out to distances of 8-10Å. The structure parameters and long-range rdf behavior were judged to be consistent with a tetrahedral random network structure proposed by Warren. The rms peak widths were found to be smaller than those determined from X-ray diffraction by Narten, and agree closely with rms vibration amplitudes derived from a dynamical model of Bates.

The scattering law data were corrected for container scattering and multiple scattering in the vanadium reference scatterer. A generalized frequency distribution function was calculated from the measured scattering law. Systematic peaks in the generalized frequency distribution were found to correspond with previously observed Raman and infrared bands, and with maxima in the frequency distribution calculated by Bell and Dean for their tetrahedral random network model.

Comparison between the measured scattering law and a calculation including only contributions from long-wavelength acoustic modes showed the calculation to be valid only for small wave vector and energy transfer, exactly as expected.

ACKNOWLEDGEMENTS

The author is indebted to the Argonne National Laboratory Center for Educational Affairs for its support of the Thesis Parts Fellowship during which the inelastic scattering portion of this work was completed. He is also grateful to the staff of the Solid State Science Division at Argonne, and in particular to Dr. J.M. Rowe, Dr. D.L. Price, Dr. J.R.D. Copley, Dr. A. Rahman, Dr. O.C. Simpson, Mr. C.E. Ostrowski and Mr. R. Kleb for their support, guidance and assistance during his stay at Argonne.

The time-of-flight diffraction work was supported in part by the National Science Foundation under grant number GK-35901.

Finally, it is a pleasure to acknowledge the continuing support and guidance of Dr. Jack Carpenter, and the many valuable conversations with Dr. David Mildner which contributed to this work; and the sterling technical support of Ms. Janice Tracht.

LIST OF TABLES

LIST OF FIGURES

CHAPTER ONE

INTRODUCTION

1.1 Preliminary Remarks

In a time when condensed matter physicists and chemists have treated with remarkable success a large number of difficult and complex problems, even the most basic properties of the structure and dynamics of glassy solids seemingly remain beyond our theoretical grasp. Theorectical considerations of glass structure consist largely of arguments as to which of two conceptual models postulated in the early to mid 1930's less offends physical and chemical sense. Attempts to adapt conventional solid-state (i.e. crystalline) dynamical analysis to glasses typically fall flat except under severly restrictive conditions (see Chapter Six below), and little else has been tried. This rather primitive theoretical state is quite natural, for glasses lie somewhere between the two extremes which have almost exclusively been calculated: on one hand, the highly ordered periodic world of crystals where translational invariance seemingly makes all things calculable; and on the other hand the stochastic world of liquids where kinetic theories can be used to advantage. A glass is not a liquid nor is it a crystal; it may display behavior characteristic of either or both (or neither). In short, the glassy state constitutes a singularly difficult theoretical ground, one on which few are inclined to tread. We suspect that as understanding of

the liquid state catches up with that of the crystalline, the special problems of the intermediate, glassy state will begin to yield.

We begin this report of an experimental investigation of some aspects of a single glass with a brief introduction to the history of diffraction studies of glass structure and the aforementioned structural models, which have their roots in the early diffraction results.

1.2 Early History of Glass Diffraction

1.2.1. Crystallite Model. Soon after the discovery by von Laue[1] that x-rays are diffracted by crystalline solids, both Debye[2] and Ehrenfest[3] speculated that other forms of condensed matter should also exhibit characteristic diffraction patterns. It was not until 1930, however, that the first quantitative analysis of silica (SiO_2) glass diffraction was published by Randall, Rooksby and Cooper.[4] Since the dominant broad band of their diffraction pattern was centered at 1.5 $\mathring{A}^{-1}$, near the position of the (111) reflection of the crystalline silica α -cristobalite, Randall et al. suspected a simple explanation of glass structure in terms of an assemblage of microcrystallites might be appropriate. Application of the Scherrer line-width formula to their data indicated an average crystallite dimension of 15-20$\mathring{A}$. An explanation of certain anomalous refractive and thermal properties of glass in terms of what might be

called a microcrystallite model based on quartz, another crystalline silica, had earlier been offered by A.A. Lebedev[5] (about whom more later).

1.2.2. Continuous Random Network Hypothesis. Prior to 1930 diffraction studies of several crystalline polymorphs of silica had led to the conclusion that the basic unit of composition in these crystals was not the planar SiO_2 molecule, but rather a silicon atom surrounded tetrahedrally by four oxygens. These tetrahedra were apparently linked at corners so that each oxygen was bonded to silicon atoms in each of two adjoining tetrahedra. The various polymorphs of silica were found to differ only in the particular relative orientation of neighboring tetrahedra. (We quote many silica results here, because BeF_2 and SiO_2 have proven to be structurally analogous; thus isomorphs of BeF_2 are found to contain corner-linked BeF_2 tetrahedra, and one may speak of quartz-like, cristobalite-like, tridymite-like, etc., forms of BeF_2 analogous to the various SiO_2 polymorphs. This structural analogy reflects the fact that the ratios of $Be^{2+}:F^-$ and $Si^{4+}:O^{2-}$ ionic radii are nearly the same, while BeF_2 having ionic charges only half those of SiO_2 might be expected to be a somewhat "weaker" structure, which turns out to be the case.)

Zachariasen, noting these as well as similar regularities for other glass-forming oxides, postulated in 1932[6] that oxide glasses are formed by corner-linking of oxygen

polyhedra in a random manner, rather than in the regular manner of crystals. In a set of rules governing the formation of what has come to be known as a continuous random network, Zachariasen postulated that there be no sharing of edges or faces by neighboring polyhedra, and that at least three corners of each polyhedron be shared with neighbors.

Of course a continuous random network can no more easily exist in a real glass than an assemblage of tiny crystallites with sharp boundaries, separated by voids. The relative orientation of SiO_4 tetrahedra in silica glass cannot be truly random, since most of the oxygens must join two tetrahedra; the requirements of bonding impose restraints on the degree of randomness possible. If we are to avoid severly distorting a large fraction of the tetrahedra, in fact, the short-range structure of a realizable "random" network must probably look more or less like that in a crystal, with progressively less rigid ordering as one moves away from the starting point. A viable "random network" model of a glass will thus be characterized by random variation of relative polyhedron orientations only within a fairly small range about some mean.

Warren made convincing use of a realizable continuous network in the analysis of his X-ray diffraction data for SiO_2[7] and BeF_2[8] in 1934. Choosing a mean linking angle between neighboring tetrahedra (i.e. the Si-O-Si or Be-F-Be

bond angle) of 180° and using distances and coordination numbers consistent with those in crystalline modifications, Warren calculated the scattering from a random network, which he found to be in substantial agreement with experiment. Particulars of Warren's BeF_2 model are listed in table 1.

1.2.3. Modern Crystallite Model. Not everyone was as convinced as Warren that his results had proven conclusively the veracity of the random network hypothesis. In 1936 N.N. Valenkov and E.A. Porai-Koshits[9] postulated a crystallite theory of glass structure which was far more sophisticated than that of Randall et al. (It is worth noting that Randall himself had gone over to the random network hypothesis in 1934.) Noting several inadequacies of the Zachariasen-Warren random network hypothesis, Valenkov and Porai-Koshits suggested a model of glass structure based on cristobalite crystallites of 10-12Å or more on a side, which are joined through severely distorted regions to neighboring crystallites. This avoids the obvious oversimplification of the Randall model where crystallites are sharply delineated and separated by voids, but still couches the description of glass in the comfortably familiar terminology of the crystalline state (it should be apparent that the random network model is in fact a description appropriate to a liquid). It is the opinion of this worker that the modern crystallite and random network hypotheses are not in essential conflict, that in fact a realizable

TABLE 1. Warren's 1934 Random Network Model of Vitreous BeF_2

1 Be surrounded by		2 F each surrounded by	
1	Be at r=0	1	F at r=0
4	F r=1.60Å	2	Be r=1.60Å
4	Be r=3.20Å	6	F r=2.62Å
12	F r=4.00Å	6	Be r=4.00Å
12	Be r=5.20Å	9	F r=4.65+0.45Å
18	F r=5.45Å+0.45Å		
Continuous distribution beyond R_1=5.45Å		Continuous distribution beyond R_2=4.65Å	

random network will as previously stated wind up looking pretty much like the modern crystallite structure. The difference of course is only a matter of degree - whether one chooses to believe that it is the more or the less strongly ordered regions in glass which are more important. Clearly each type of region will be more or less influential in determining a particular property of glass - neither can alone provide a complete discription of all properties. (That the random network and modern crystallite hypotheses are not necessarily at odds has long ago been pointed out by A.A. Lebedev[10].)

1.2.4. Recent Developments Concerning the Crystallite Models. Both the original and the modern crystallite hypotheses were first advanced by Russians (Lebedev, Valenkov and Porai-Koshits). Accordingly we must impute quite some significance to a recently published letter[11] of Evstropyev and Porai-Koshits, in which crystallite hypotheses were in essence declared not to have been supported by the sum of experimental evidence (both diffraction and spectroscopic). The letter described discussions and a resolution made by a group of 250 Soviet scientists in December 1971 on the fiftieth anniversary of Lebedev's first crystallite hypothesis. We quote selected passages, hopefully not misrepresenting thereby the authors' intent.

> "In reports devoted to X-ray structural analysis (E.A. Porai-Koshits, V.N. Filipovich and others) and electron microscopy (F.K. Aleinikov) the speakers emphasized that... all the attempts to reveal the existence of crystallites...have failed so far. The analogous conclusion was made by V.A. Kolesova on the basis of...infrared spectroscopic investigations."

From the Resolution approved by the participants,

> "The method of infrared spectroscopy... cannot be used at present for a quantitative evaluation of the dimensions, quantity and degree of geometrical ordering of the crystallites existing in glass...Other methods... (electron microscopy, X-ray structural analysis et al.) despite their extensive development in recent years, do not permit, for some reason or other, to reveal the regions of increased ordering (crystallites) in glass... the seminar on the crystallite hypothesis considers it expedient to recommend...to pay attention to the improvement of the structural methods which can produce quantitative or even semi-quantitative information about the regions of increased ordering in glass."

One may well conclude on the basis of this letter and the Resolution it describes, that although the Soviets believe the crystallite hypothesis will ultimately be verified, they recognize that as yet there is precious little evidence to support this position.

1.3 Modern Diffraction Results on BeF_2 Glass

Several X-ray and neutron diffraction studies have

been made since the original work of Warren and Hill[9], whose results have already been discussed. We will not dwell on the details of the measurements themselves except to note when experimental conditions lead us to disbelieve certain conclusions. The neighbor distances, coordination numbers (when given) and bond angles (calculated from the distances, angles are rarely reported) are summarized in Table 2 for the X-ray measurements of Batsanova, Yur'ev and Doronina[12], Zarzycki[13] and Narten[14]. In each case the diffraction data were Fourier analyzed to give a radial density function (rdf) as first suggested by Zernike and Prins[15] and first applied to liquids by Debye and Menke[16] in the late 1920's, and first applied to glass data by Warren[17] in 1936. (A reasonably complete discussion of the rdf will be given in Chapter Two. For now we note only that from it one can calculate coordination numbers and interatomic distances.) We assign the greatest weight to the results of Narten, who took proper account of the termination effects in his Fourier transform. The Russian workers on the other hand, failed to use strictly monochromatic radiation in conjunction with a photographic recording technique; to their result we can assign but little weight. The 1.50Å Be-F distance reported by Zarzycki seems a bit too low, and indeed indicates a mean F-Be-F bond angle significantly different from the expected tetrahedral angle of 109° 28'. The 1.43Å Be-F distance found by Batsanova et al. is low

	Warren & Hill[8]	Batsanova et al.[12]	Zarzycki[13]	Narten[14]
r_{Be-F}	1.60	1.43±.015	1.50	1.554±.004
r_{F-F}	2.55	2.54	2.55	2.537±.004
r_{Be-Be}	3.20	----	3.00	3.037±.005
∠(F-Be-F)	105°	125°	116°	109.5°
∠(Be-F-Be)	180°	----	180°	155.6°
N_{Be-F}	4	4	4.4	3.8±.3
N_{F-F}	6	----	6.8	5.7±.3
N_{Be-Be}	4	----	----	3.8±.3

Table 2. Summary of X-ray diffraction results for BeF_2 glass.

beyond all belief, and in fact is the same as the Be-F distance for isolated BeF_2 molecules as determined by electron diffraction from BeF_2 gas. Narten is the only author who has calculated bond angles from his interatomic distances; we again comment that his results are of the highest quality. The scheme for taking into account termination effects used by Narten is identical in principle with that of Konnert and Karle, about which we will have much to say in Chapter Five, and which we feel is the "state of the art" technique for extracting distances, coordination numbers etc. from rdf's and incidentally for removing the unavoidable termination errors. Narten's work must certainly be considered the benchmark at this time for BeF_2 glass diffraction.

1.4 Comparison of Diffraction Methods

1.4.1. Overview. We have in the previous sections referred to both X-ray and electron diffraction measurements. In this section we will touch on some features of each method.

We will have little to say about electron diffraction as a tool for investigation of glasses. Electrons interact so strongly with condensed matter that only a very thin layer of material can be "seen" by electron diffraction; this same property makes electrons an ideal probe for investigations of gaseous substances. Since many interesting amorphous semiconductor materials are most readily prepared by vapor deposition in thin films, electron diffraction is heavily used in work on such glasses. For macroscopic chunks of stuff such as a window pane of silica glass or a lethal dose of vitreous BeF_2, however, electron diffraction can provide information only about the immediate surface regions. Since we are interested in the bulk behavior of a glass which can be had in bulk, electron diffraction is not the most appropriate experimental technique.

X-ray diffraction has been an indispensible tool in the study of condensed matter ever since von Laue discovered the phenomenon in 1912. X-ray crystallography was begun soon after Laue's discovery by W.H. Bragg and has since been refined to an incredible degree. It is fortunate that for many years X-ray diffractionists have also applied their

efforts to the study of glasses, although the analysis of glass diffraction is necessarily quite crude in comparison with what can be (and is) done with crystals. X-rays unlike electrons can probe the entire volume of an irradiated sample, and so give information characteristic of the bulk material. Their scattering by matter is comparable to that of neutrons; it is considerably simpler to increase the total amount of scattering by utilizing a more intense source of X-rays however, than to buy a similar increase in neutron intensity. X-ray sources are quite small in general, require only modest shielding and do not need licensing by the AEC. Neutron sources by contrast, are generally either nuclear reactors which have some rather obvious problems of large initial expense and frequently require an entire laboratory staff just to cope with the radiation problems they generate; or accelerator-based pulsed sources in which the accelerator and not the neutron source per se is a budget-wrecking expense. In short, an ordinary mortal, a company short of an industrial giant or even a minor university just cannot afford a neutron source useful for diffraction work, but can for a fairly modest capital expense have a respectable X-ray diffractometer. Why use neutrons at all then? The answer is that in a very real sense, neutron diffraction serves as a complement to X-ray diffraction, providing new and different information when applied to the same substances. Futhermore, there are several problems associated with X-ray

diffraction which do not arise with neutrons (and vice versa, as we shall see):

a) Since X-rays scatter from the electrons in a material, and since useful X-ray wavelengths are of the order of ionic radii, there is a diffraction effect due to scattering from different electrons in the same atom. This causes destructive interference which decreases the scattered intensity as Q increases. Neutrons on the other hand scatter from nuclei in the sample which look like point scatterers, and so there is no destructive interference to diminish scattering at large Q.

b) In addition to the elastically scattered or "unmodified" X-rays, there is also a Compton scattered or "modified" component of scattered intensity which increases with Q. The removal of this modified component to get at the unmodified (diffraction) component is difficult, especially at large Q.

c) There may be strong absorption of X-rays if the incident wavelength is near absorption edges of the sample constituents. Neutrons are also strongly absorbed by some nuclei, but on the whole X-ray absorption is a much more serious problem.

1.4.2. Complementarity of X-ray and Neutron Scattering. We have previously stated that X-ray and neutron diffraction are properly viewed as complementary techniques. One technique may be demonstrably superior in some applications, inferior in others; but on the whole both methods may be profitably applied to the same problems. The complementarity arises from the fact that X-ray and neutron scattering amplitudes differ for different atomic species. X-ray scattering factors increase with increasing atomic charge number, while neutron scattering lengths do no vary simply

with increasing Z and are in fact different for various isotopes of the same atom. Since the various species in a heteroatomic system thus have different weights for scattering of X-rays and neutrons, the same measurement done by both techniques provides two different "views" of the system. This is most important in systems composed of both light and heavy atoms (the obvious example being biological systems containing H), since the high -Z atoms would completely dominate X-ray scattering, while most nuclei have neutron scattering lengths of the same order of magnitude so no one type in general can dominate. Also possible is isotopic substitution to change the neutron scattering properties of a substance, thereby increasing even more the amount of information available from diffraction. In principle one could (using SiO_2 as an example) combine the results of one x-ray and two neutron diffraction measurements with isotopic substitution of , say, O^{18} for O^{16}, and thereby be able to experimentally separate the scattering due to Si-Si pairs, O-O pairs and Si-O pairs. This has never been successfully done, however.

Finally we look at the possibility of investigating the dynamics of condensed matter. Suppose we wish to obtain information on the energy and momentum of collective excitations in a solid or liquid, typical energies of which may be .001 - .1 ev (1-100 mev) and typical momenta (expressed in wavenumber, $k = p/\hbar$) several times 10^8/cm (several $\mathring{A}^{-1}$).

In order to directly observe the momentum and energy of such excitations, we might wish to observe radiation scattered in inelastic processes whereby momentum and energy are exchanged with the excitations; there must be a detectable change in the momentum and/or energy of the radiation quanta, in order that we may interpret the results. Thus we would ideally like both the momentum and energy of the radiation used to be comparable to those of the excitations investigated. In figure 1 we plot energy vs. wavenumbers for neutrons, electrons and photons in free space. Obviously the neutron has the desirable momentum and energy combination while both e-m radiation (X-rays) and electrons do not.

We will refrain from shouting too loudly about the ability of neutrons to scatter inelastically from collective excitations, because it is also the source of a problem when we try to do diffraction. As will be shown in Chapter Two, we would like to measure the scattering at constant Q in a diffraction measurement; our ability to do this easily is adversely affected by the occurrence of significant energy transfer in scattering. Thus X-rays are in this respect better suited for diffraction applications than are neutrons.

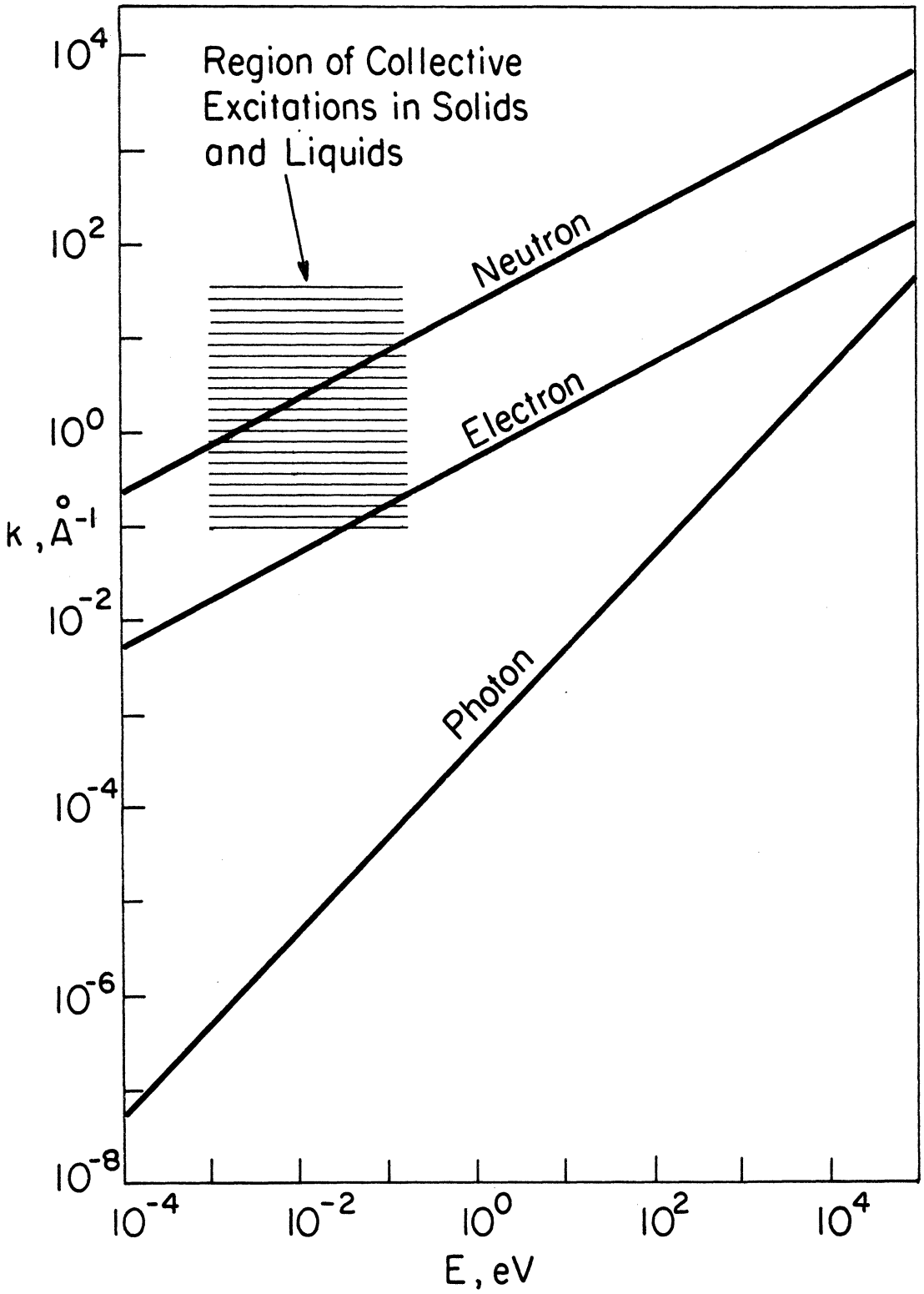

Figure 1. Energy-Wavenumber Characteristics of Various Radiations

CHAPTER TWO

THEORETICAL BACKGROUND FOR NEUTRON SCATTERING FROM DISORDERED SYSTEMS

2.1 Scattering from Static Systems

2.1.1. The Structure Factor. For a system of N rigidly bound nuclei, the neutron scattering amplitude is[18]

$$f_k(\underline{Q}) = \sum_{j=1}^{N} a_j e^{-i\underline{Q}\cdot\underline{r}_j} \tag{2.1}$$

where $\underline{r}_j$ is the position of the j-th nucleus, a_j its bound-atom scattering length and $\underline{Q} = \underline{k}' - \underline{k}$ is the change in the neutron wave vector. The differential cross section per nucleus associated with this scattering process is

$$I(\underline{Q}) = N^{-1} \left| f_k(\underline{Q}) \right|^2$$

$$= N^{-1} \sum_{i=1}^{N} \sum_{j=1}^{N} a_i a_j e^{-i\underline{Q}\cdot(\underline{r}_i - \underline{r}_j)} \tag{2.2}$$

The quantity $I(\underline{Q})/\langle a^2 \rangle$ is known as the "static structure factor", or simply the "structure factor"; it contains all the structural information available from a diffraction experiment. We will denote it by $S_s(\underline{Q})$. Thus

$$I(\underline{Q}) = \langle a^2 \rangle S_s(\underline{Q})$$

$$\langle a^2 \rangle = N^{-1} \sum_{i=1}^{N} a_i^2$$

We can simplify somewhat the present analysis by noting that Be and F are almost completely coherent scatterers, as shown in table 3[19].

isotope	σ_{coh}	$\sigma_{coh}+\sigma_{inc}$	$\sigma_{coh}/\sigma_{coh}+\sigma_{inc}$	abundance, %
Be^9	7.53	7.54	.999	100
F^{19}	3.9	4.0	.975	100

Table 3. Scattering cross sections of Be and F

Accordingly we hereafter neglect incoherent scattering entirely, and a_i will refer to the coherent bound-atom scattering length of the i th nucleus.

We can separate (2.2) into "self" and "distinct" terms,

$$\langle a^2\rangle S_s(\underline{Q}) = \langle a^2\rangle + N^{-1}\sum_{i=1}^{N}\sum_{j=1}^{N}{}' a_i a_j e^{-i\underline{Q}\cdot(\underline{r}_i-\underline{r}_j)} \qquad (2.3)$$

where the primed sum is restricted to terms with $i\neq j$.

2.1.2. Static Pair Density $\bar{g}(\underline{r})$. By noting

$$\int_V \varphi(\underline{r})\,\delta(\underline{r}-\underline{x})\,d^3r = \begin{cases}\varphi(\underline{x}), & \underline{x}\in V\\ 0, & \underline{x}\notin V\end{cases}$$

we can express (2.3) in the form

$$S_s(\underline{Q}) = 1 + N^{-1}\langle a^2\rangle^{-1}\int \sum_{i=1}^{N}\sum_{j=1}^{N}{}' a_i a_j e^{-i\underline{Q}\cdot\underline{r}}\,\delta(\underline{r}-\underline{r}_i+\underline{r}_j)\,d^3r$$

$$= 1 + \int e^{-i\underline{Q}\cdot\underline{r}}\,\bar{g}(\underline{r})\,d^3r \qquad (2.4)$$

where

$$\bar{g}(\underline{r}) \equiv N^{-1}\langle a^2\rangle^{-1}\sum_{i=1}^{N}\sum_{j=1}^{N}{}' a_i a_j\,\delta(\underline{r}-\underline{r}_i+\underline{r}_j) \qquad (2.5)$$

We call $\bar{g}(\underline{r})$ the static pair density. The determination of this function is the ultimate aim of most diffraction

measurements on glasses and liquids. Its physical meaning becomes clear on integrating (2.5) over some small region Δ :

$$\int_{\Delta} \bar{g}(\underline{r})\, d^3r$$

$$= N^{-1}\langle a^2\rangle^{-1} \sum_{i=1}^{N} \sum_{j=1}^{N'} a_i a_j \int_{\Delta} \delta(\underline{r} - \underline{r}_i + \underline{r}_j)\, d^3r \tag{2.6}$$

The integral on the right in (2.6) equals unity for each pair of indices (i,j) for which $(\underline{r}_i - \underline{r}_j) \in \Delta$. Integrating $\bar{g}(r)$ over any region Δ gives the number of pairs of nuclei in the sample whose internuclear separation lies in Δ, weighted by their scattering lengths.

It is convenient to rewrite (2.5) explicitly in terms of contributions involving nuclei of a given type in a polyisotopic system:

$$\bar{g}(\underline{r}) = N^{-1}\langle a^2\rangle^{-1} \sum_{i=1}^{N} \sum_{j=1}^{N'} a_i a_j\, \delta(\underline{r} - \underline{r}_i + \underline{r}_j)$$

$$= N^{-1}\langle a^2\rangle^{-1} \sum_{t} \sum_{n_t=1}^{N_t} \sum_{t'} \sum_{n_{t'}=1}^{N_{t'}} a_t a_{t'}\, \delta(\underline{r} - \underline{r}_{n_t} + \underline{r}_{n_{t'}})(1 - \delta_{nn'}\delta_{tt'}) \tag{2.7}$$

$$= N^{-1}\langle a^2\rangle^{-1} \sum_{t} \sum_{t'} N_t\, g_{t't}(\underline{r}) \tag{2.8}$$

where t denotes a nuclear type, n_t runs over all nuclei of type t, N_t is the total number of type t nuclei, the factor $(1-\delta_{nn'}\delta_{tt'})$ limits the double sum to distinct pairs as

before, and

$$g_{t't}(\underline{r}) = N_t^{-1} \sum_{n_t=1}^{N_t} \sum_{n'_{t'}=1}^{N_{t'}} a_t a_{t'} \delta(\underline{r} - \underline{r}_{n_t} + \underline{r}_{n'_{t'}})(1 - \delta_{nn'}\delta_{tt'}) \tag{2.9}$$

describes the distribution of nuclei of type t' about nuclei of type t. Since $\delta(\underline{r}) = \delta(-\underline{r})$ it is clear that

$$g_{t't}(\underline{r}) = \frac{N_{t'}}{N_t} g_{tt'}(-\underline{r}) \tag{2.10}$$

The functions $g_{t',t}(\underline{r})$ are in fact what one might calculate from a model of the system under consideration; the function accessible to experiment, $\bar{g}(\underline{r})$, is simply a superposition of the $g_{t',t}(\underline{r})$. In the case of a monoisotopic substance, one can experimentally determine a function even more closely connected to the structure:

$$\begin{aligned} \bar{g}(\underline{r}) &= N^{-1}\langle a^2\rangle^{-1} \sum_{i=1}^{N} \sum_{j=1}^{N}{}' a^2 \delta(\underline{r} - \underline{r}_i + \underline{r}_j) \\ &= N^{-1} \sum_{i=1}^{N} \sum_{j=1}^{N}{}' \delta(\underline{r} - \underline{r}_i + \underline{r}_j) \\ &= g(\underline{r}) \end{aligned} \tag{2.11}$$

This function can be interpreted directly in terms of the structure, while the structural information in $\bar{g}(\underline{r})$ is obscured by the scattering-length weighting of the different isotopes' contributions. One would ideally like to extract the functions $g_{t',t}(\underline{r})$ from measurements of $\bar{g}(\underline{r})$, remove the scattering-length weighting and superimpose the resulting

functions to reproduce $g(\underline{r})$. In order to do this, however, one would need n different measurements of $\bar{g}(\underline{r})$, varying in each the scattering length of at least one nuclear type, where n is the number of distinct combinations (t't) (e.g., 3 for BeF_2: Be-F, F-F and Be-Be; one x-ray and two neutron measurements with isotopic substitution would suffice).

In an isotropic medium such as a liquid, gas, powder, polycrystal or glass, $\bar{g}(\underline{r})$ cannot depend on the direction of $\underline{r}$, and we have for equation (2.4)

$$S_s(\underline{Q}) = 1 + \int_V e^{-i\underline{Q}\cdot\underline{r}} \bar{g}(\underline{r})\, d^3r$$

$$= 1 + \int e^{-i\underline{Q}\cdot\underline{r}} (\bar{g}(\underline{r}) - g_0 + g_0)\, d^3r \qquad (2.12)$$

where the integral has been extended over all space, and $g_0 \equiv \lim_{|\underline{r}|\to\infty} \bar{g}(r)$;

$$S_s(\underline{Q}) = 1 + \int_{r=0}^{\infty} 4\pi r (\bar{g}(r) - g_0) \frac{\sin Qr}{Q}\, dr + (2\pi)^3 g_0\, \delta(\underline{Q}) \qquad (2.13)$$

Ignoring the last term which represents a forward scattering contribution ($\underline{Q}$=0) which is not measured, we can write

$$Q\, i_s(Q) = \int_{r=0}^{\infty} 4\pi r (\bar{g}(r) - g_0) \sin Qr\, dr \qquad (2.14)$$

where

$$i_s(Q) \equiv S_s(Q) - 1 \qquad (2.15)$$

and $S_s(Q)$ is assumed not to contain the forward scattering contribution mentioned above.

By way of evaluating g_o, one can argue that as $\underline{r}$ becomes large, the distribution of internuclear distances will tend to look more and more uniform. Then (2.5) can be evaluated with $\delta(\underline{r}-\underline{r}_i+\underline{r}_j)$ replaced by its average value $1/V$,

$$g_o = \lim_{r\to\infty} \bar{g}(r) = N^{-1}\langle a^2\rangle^{-1} V^{-1} \left\{ \sum_{i=1}^{N}\sum_{j=1}^{N} a_i a_j - \sum_{i=1}^{N} a_i^2 \right\}$$

$$= \langle a^2\rangle^{-1} V^{-1} \left\{ N\langle a\rangle^2 - \langle a^2\rangle \right\}$$

$$\simeq \frac{N\langle a\rangle^2}{V\langle a^2\rangle}$$

$$= \rho \frac{\langle a\rangle^2}{\langle a^2\rangle} \qquad (2.16)$$

with $\langle a\rangle \equiv N^{-1}\sum_{i=1}^{N} a_i$

and $\rho = \frac{N}{V}$ is the macroscopic number density of nuclei in the sample. Note that the structure factor for an isotropic system depends only on the magnitude of Q. Equation (2.14) is of course just a Fourier sine transform; the inverse transform is

$$4\pi r(\bar{g}(r)-g_o) = \frac{2}{\pi}\int_{Q=0}^{\infty} Q i_s(Q) \sin Qr\, dQ \qquad (2.17)$$

This is the basic relationship by which $\bar{g}(r)$ is calculated from experimental $S_s(Q)$ data.

2.2 Scattering from Dynamic Systems

2.2.1. Partial differential cross section; the scattering law. Here we abandon the restriction of the previous section to systems of rigidly bound nuclei, and proceed again from first principles. As shown in standard texts,[18,19] the differential cross section per unit solid angle per unit interval of scattered neutron energy for coherent scatters is (within the framework of the first Born approximation, and using the Fermi pseudopotential)

$$\frac{\partial^2\sigma}{\partial\Omega\,\partial\epsilon} = \frac{k'}{k}\langle a^2\rangle S(\underline{Q},\omega) \tag{2.18}$$

where $\epsilon = \hbar\omega = \frac{\hbar^2}{2m}(k'^2 - k^2)$ is the energy transfer to the neutron, and

$$S(\underline{Q},\omega) = N^{-1}\langle a^2\rangle^{-1}\sum_{n_0} p_{n_0}\sum_{n}\left|\langle n|\sum_{j=1}^{N} a_j e^{-i\underline{Q}\cdot\underline{r}_j}|n_0\rangle\right|^2 \times \delta\left(\omega - \frac{E_{n_0}-E_n}{\hbar}\right) \tag{2.19}$$

is the scattering law. The sum on n_0 is a statistical average over initial states of weight p_{n_0}; the sum on n runs over all possible final states; the quantity in square brackets is a matrix element of the enclosed operator. The δ function restricts the sums to transitions with $\hbar\omega$ (energy transfer to the neutron) equal $E_{n_0}-E_n$ (energy transfer from the scattering system). By introducing suitable

time-dependent (Heisenberg) operators,[20] $\underline{r}_j(t)=e^{iHt/\hbar}\underline{r}_j e^{-iHt/\hbar}$ and the Fourier respresentation of the δ function, one can rewrite (2.19) as

$$S(\underline{Q},\omega) = (2\pi)^{-1}\int \exp(i\omega t)\, \bar{F}(\underline{Q},t)\, dt \tag{2.20}$$

where

$$\bar{F}(\underline{Q},t) \equiv N^{-1}\langle a^2\rangle^{-1} \sum_{j,\ell=1}^{N} a_j a_\ell \left\langle \exp[i\underline{Q}\cdot\underline{r}_\ell(0)] \exp[-i\underline{Q}\cdot\underline{r}_j(t)]\right\rangle_T \tag{2.21}$$

and

$$\langle A\rangle_T \equiv \sum_{n_0} \rho_{n_0}\langle n_0|A|n_0\rangle$$

In (2.21) we ignore the a_i as dynamical variables, thus restricting the treatment to systems of noninteracting spins.

2.2.2. Space and Time Dependent Correlation Function $\bar{G}(\underline{r},t)$. $\bar{F}(\underline{Q},t)$ is called the intermediate scattering function; it is intermediate in the sense of being the spatial part of a 4 dimensional space and time Fourier transform relation between the scattering law and the space and time dependent correlation function of Van Hove[21]:

$$\bar{F}(\underline{Q},t) = \int \exp(-i\underline{Q}\cdot\underline{r})\, \bar{G}(\underline{r},t)\, d^3r\ ; \tag{2.22}$$

$$S(\underline{Q},\omega) = (2\pi)^{-1}\int \exp(-i\underline{Q}\cdot\underline{r}+\omega t)\, \bar{G}(\underline{r},t)\, d^3r\, dt\ ; \tag{2.23}$$

$$\bar{G}(\underline{r},t) \equiv (2\pi)^{-3}\langle a^2\rangle^{-1} N^{-1} \sum_{j,\ell=1}^{N} a_j a_\ell \int \exp(i\underline{Q}\cdot\underline{r}) \tag{2.24}$$

$$(x)\left\langle \exp[i\underline{Q}\cdot\underline{r}_\ell(0)] \exp[-i\underline{Q}\cdot\underline{r}_j(t)]\right\rangle_T d^3Q$$

Applying the convolution rule for the Fourier transform of a product and respecting the general noncommutativity of the operators $\underline{r}_L(o)$ and $\underline{r}_j(t)$,

$$(2\pi)^{-3}\int \exp(i\underline{Q}\cdot\underline{r})\, f(\underline{r})\, g(\underline{r})\, d^3r$$

$$= \int F(\underline{Q}-\underline{Q}')\, G(\underline{Q}')\, d^3Q' \,,$$

$\bar{G}(\underline{r},t)$ can alternatively be written

$$\bar{G}(\underline{r},t) = N^{-1}\langle a^2\rangle^{-1}\left\langle \sum_{j,\ell=1}^{N} a_j a_\ell \int \delta(\underline{r}+\underline{r}_\ell(o)-r')\,\delta(r'-\underline{r}_j(t))\, d^3r' \right\rangle_T \tag{2.25}$$

2.2.3. Properties of the Correlation Function $\bar{G}(\underline{r},t)$. Although Van Hove has named $\bar{G}(\underline{r},t)$ the space and time dependent correlation function, it does not in general have the simple physical meaning that name seems to imply. For classical systems, the positions $\underline{r}_i(t)$ are simply dynamical variables (c-numbers) and (2.25) may be simplified by performing the integration on r':

$$\bar{G}^{cl}(\underline{r},t) = N^{-1}\langle a^2\rangle^{-1}\left\langle \sum_{j,\ell=1}^{N} a_j a_\ell\, \delta(\underline{r}+\underline{r}_\ell(o)-\underline{r}_j(t)) \right\rangle_T \tag{2.26}$$

$\bar{G}^{cl}(\underline{r},t)$ has a simple physical interpretation: it directly measures the probability of finding a particle at position $\underline{r}$ at time t, given that some particle was located at the orgin at time o (again, there is a weighting by neutron scattering power of pairs of nuclei just as for $\bar{g}(\underline{r})$). Such a function is called a two-time conditional pair density.

For quantum mechanical systems, the simplification

(2.26) (tantamount to replacing $\exp\left[i\underline{Q}\cdot\underline{r}_1(o)\right]\ \exp\left[-i\underline{Q}\cdot\underline{r}_j(t)\right]$ in (2.24) by $\exp\left[\ i\underline{Q}\cdot(\underline{r}_1(o)-\underline{r}_j(t)\ )\right]$) cannot be made since $\underline{r}_1(o)$ and $\underline{r}_j(t)$ are operators, in general noncommuting. Any pair of $\underline{r}_i$ taken at the same instant of time however do commute, so one can write even in the quantum mechanical case for the equal-time conditional pair density

$$\bar{G}(\underline{r},o) = N^{-1}\langle a^2\rangle^{-1}\left\langle \sum_{j,\ell=1}^{N} q_j q_\ell\, \delta(\underline{r}+\underline{r}_\ell(o)-\underline{r}_j(o))\right\rangle_T \tag{2.27a}$$

$$= N^{-1}\langle a^2\rangle^{-1}\left\langle N\langle a^2\rangle + \sum_{j,\ell=1}^{N}{}' q_j q_\ell\, \delta(\underline{r}+\underline{r}_\ell(o)-\underline{r}_j(o))\right\rangle_T \tag{2.27b}$$

$$= \delta(\underline{r}) + \bar{g}(\underline{r}) \tag{2.27c}$$

If the identification

$$\bar{g}(\underline{r}) = N^{-1}\langle a^2\rangle^{-1}\left\langle \sum_{j,\ell=1}^{N}{}' q_j q_\ell\, \delta(\underline{r}+\underline{r}_\ell(o)-\underline{r}_j(t))\right\rangle_T \tag{2.28}$$

is made. Clearly the form of (2.28) is the same as that of (2.5) where $\bar{g}(\underline{r})$ was defined for the static system. More than this, its physical content is the same. Aside from the statistical average in (2.28), which could as well be applied to (2.5) given that several configurations of the N-particle static system are possible, (2.28) is the exact analog of (2.5) for a static system whose N particles are at the positions $\underline{r}_1=\underline{r}_1(o)$, $\underline{r}_2=\underline{r}_2(o)$, etc. Equation (2.28) may be thought of as the evaluation of (2.5) for a system frozen in position at t=0. $\bar{G}(\underline{r},o)$ thus has the character

of a "snapshot" of the dynamic N-particle system taken at the instant t=0.

By examining the inverse transform of (2.23),

$$\bar{G}(\underline{r},t) = (2\pi)^{-3} \int \exp[i(\underline{Q}\cdot\underline{r} - \omega t)]\, S(\underline{Q},\omega)\, d^3Q\, d\omega \tag{2.29}$$

one finds a means of experimentally determining $\bar{G}(\underline{r},o)$:

$$\bar{G}(\underline{r},o) = (2\pi)^{-3} \int \exp[i\underline{Q}\cdot\underline{r}]\, S(\underline{Q},\omega)\, d^3Q\, d\omega$$

$$= (2\pi)^{-3} \int \exp[i\underline{Q}\cdot\underline{r}]\, S(\underline{Q})\, d^3Q \tag{2.30}$$

with the identification

$$S(\underline{Q}) = \int_{-\infty}^{\infty} S(\underline{Q},\omega)\, d\omega \tag{2.31}$$

Thus combining (2.28) and (2.30),

$$\delta(\underline{r}) + \bar{g}(\underline{r}) = (2\pi)^{-3} \int \exp[i\underline{Q}\cdot\underline{r}]\, S(\underline{Q})\, d^3Q \tag{2.32}$$

or by analogy with (2.4),

$$S(\underline{Q}) = 1 + \int \exp[-i\underline{Q}\cdot\underline{r}]\, \bar{g}(\underline{r})\, d^3r \tag{2.33}$$

We will call $S(\underline{Q})$, the integral at constant $\underline{Q}$ of $S(\underline{Q},\omega)$, the "structure factor". It is the analog of the static structure factor introduced previously, containing the same type of information but arrived at via a more realistic analysis.

We have already discussed the information content of $\bar{g}(\underline{r})$ and its Fourier transform $S_s(\underline{Q})$ in terms of the static system model. We have now found that by arranging to measure

$S(\underline{Q})$ as defined in (2.31) we can collect the same sort of information for the more realistic dynamic model. If instead of $S(\underline{Q})$ we measure only the "elastic diffraction"[22] $S(\underline{Q},o)$, we obtain different information as can be seen from equation (2.23):

$$S(\underline{Q},o) = (2\pi)^{-1}\int \exp[-i\underline{Q}\cdot\underline{r}]\,\bar{G}(\underline{r},t)\,d^3r\,dt$$

$$= (2\pi)^{-1}\int \exp[-i\underline{Q}\cdot\underline{r}]\,\Gamma(\underline{r})\,d^3r, \qquad (2.34)$$

$$\Gamma(\underline{r}) \equiv \int_{-\infty}^{\infty}\bar{G}(\underline{r},t)\,dt$$

Thus by Fourier transformation of $S(\underline{Q},o)$, one obtains $\Gamma(\underline{r})$ which is somewhat difficult to interpret, and not $\bar{g}(\underline{r})$ as when $S(\underline{Q})$ is transformed. It is clear then that to gain access to $\bar{g}(\underline{r})$ using neutron scattering, one must measure the total coherent scattering at each value of $\underline{Q}$, ie, measure the structure factor $S(\underline{Q})$. We postpone until later consideration of the feasability of arranging a neutron scattering experiment which will actually measure $S(\underline{Q})$, a difficult question indeed.

Finally, we note that for isotropic systems, $\bar{g}(\underline{r}) = \bar{g}(r)$ only and (2.33) can be orientation averaged to yield

$$S(Q) = 1 + \int_{r=0}^{\infty} 4\pi r(\bar{g}(r)-g_o)\,\frac{\sin Qr}{Q}\,dr + (2\pi)^3 g_o\,\delta(\underline{Q}) \qquad (2.35)$$

or

$$4\pi r(\bar{g}(r)-g_o) = \frac{2}{\pi}\int_0^{\infty} Q\,i(Q)\,\sin Qr\,dQ \qquad (2.36)$$

with i(Q)=S(Q)-1 and the forward scattering term proportional to $\delta(\underline{Q})$ has again been ignored. The analysis of glass diffraction data is based on equation (2.36).

2,2,4. Scattering from Systems of Harmonically Bound Nuclei. Here we derive expressions for the elastic and one-quantum inelastic scattering cross sections for a large system of harmonically vibrating particles. We utilize the very general and elegant formalism of Zemach and Glauber[23] for scattering from molecules; we treat the entire glass sample as a single "molecule" in the sense of their work. The starting point here is equation (3.20) of the paper by Zemach and Glauber for the partial differential cross section of the harmonically vibrating system:

$$\frac{\partial^2\sigma}{\partial\Omega\,\partial\epsilon} = (2\pi\hbar)^{-1}\frac{k'}{k}\sum_{\nu,\nu'}^{\rightarrow} a_\nu a_{\nu'}\int \exp\left[-i\omega t + i\underline{Q}\cdot(\underline{b}_\nu - \underline{b}_{\nu'})\right]\prod_{\lambda=1}^{3N}\left\langle X^\lambda_{\nu\nu'}\right\rangle_T dt \qquad (2.37)$$

where b_ν is the position of the ν^{th} nucleus,

$$\omega = \epsilon/\hbar$$

and

$$\left\langle X^\lambda_{\nu\nu'}\right\rangle_T \equiv \exp\left\{-\frac{\hbar}{M_{\nu\nu'}}\left[(\underline{Q}\cdot\underline{\zeta}^\lambda_\nu)^2 + (\underline{Q}\cdot\underline{\zeta}^\lambda_{\nu'})^2\right](4\omega_\lambda)^{-1}\coth(\beta\omega/2)\right\}$$

$$(x)\sum_{n_\lambda=-\infty}^{\infty}\exp(in_\lambda\omega_\lambda t)\exp(-\beta n_\lambda\omega_\lambda/2)$$

$$(x)\, I_{n_\lambda}\left[\frac{\hbar(\underline{Q}\cdot\underline{\zeta}^\lambda_\nu)(\underline{Q}\cdot\underline{\zeta}^\lambda_{\nu'})}{2M_{\nu\nu'}\omega_\lambda\sinh(\beta\omega_\lambda/2)}\right] \qquad (2.38)$$

with

$\underline{C}_\nu^\lambda$ = the polarization vector of the ν^{th} particle in the λ^{th} normal mode, defined by $\underline{u}_\nu(t) = m_\nu^{-1/2} \sum_\lambda \underline{C}_\nu^\lambda q_\lambda(t)$ where $\underline{U}_\nu(t)$ is the displacement of particle ν from equilibrium and $q_\lambda(t)$ is the λ^{th} normal coordinate.

ω_λ = the frequency of the λ^{th} normal mode

$M_{\nu\nu'} = (m_\nu m_{\nu'})^{\frac{1}{2}}$

$I_n(x)$ = the modified Bessel function of the first kind of order n

$\beta = \hbar$/Boltzmann's constant / absolute temperature

The continued product $\prod_\lambda$ can be factored as

$$\prod_{\lambda=1}^{3N} \langle \chi_{\nu\nu'}^\lambda \rangle_T = \prod_{\lambda=1}^{3N} \exp\left\{-\frac{\hbar}{M_{\nu\nu'}}\left[(\underline{Q}\cdot\underline{C}_\nu^\lambda)^2 + (\underline{Q}\cdot\underline{C}_{\nu'}^\lambda)^2\right](4\omega_\lambda)^{-1} \coth(\beta\omega_\lambda/2)\right\}$$

$$(x) \quad \prod_{\lambda=1}^{3N} \sum_{n_\lambda=-\infty}^{\infty} \exp(i n_\lambda \omega_\lambda t) \exp(-\beta\omega_\lambda n_\lambda/2)$$

$$(x) \quad I_{n_\lambda}\left[\frac{\hbar(\underline{Q}\cdot\underline{C}_\nu^\lambda)(\underline{Q}\cdot\underline{C}_{\nu'}^\lambda)}{2M_{\nu\nu'}\omega_\lambda \sinh(\beta\omega_\lambda/2)}\right] \qquad (2.39)$$

The first continued product of exponentials can be rewritten as the exponential of a sum,

$$e^{-2W_{\nu\nu'}} = \exp\left\{-\sum_{\lambda=1}^{3N} \frac{\hbar}{M_{\nu\nu'}}\left[(\underline{Q}\cdot\underline{C}_\nu^\lambda)^2 + (\underline{Q}\cdot\underline{C}_{\nu'}^\lambda)^2\right] \coth(\beta\omega_\lambda/2)/4\omega_\lambda\right\} \qquad (2.40)$$

which is the Debye-Waller factor expressing the diminution of scattered intensity arising from delocalization of particles in thermal vibration.

Focusing attention now only on the continued product of infinite sums,

$$\sum = \prod_{\lambda=1}^{3N} \sum_{n_\lambda=-\infty}^{\infty} \exp(i n_\lambda \omega_\lambda t) \exp(-\beta \hbar n_\lambda \omega_\lambda / 2)$$

$$(x)\ I_{n_\lambda}\left[\frac{\hbar(\underline{Q}\cdot\underline{\zeta}_\nu^\lambda)(\underline{Q}\cdot\underline{\zeta}_{\nu'}^\lambda)}{2M_{\nu\nu'}\omega_\lambda \sinh(\beta\hbar\omega_\lambda/2)}\right] \tag{2.41}$$

which can also be written

$$\sum = \sum_{\{n_\lambda\}}' \prod_{\lambda=1}^{3N} \exp(i n_\lambda \omega_\lambda t) \exp(-\beta n_\lambda \omega_\lambda t)$$

$$(x)\ I_{n_\lambda}\left[\frac{\hbar(\underline{Q}\cdot\underline{\zeta}_\nu^\lambda)(\underline{Q}\cdot\underline{\zeta}_{\nu'}^\lambda)}{2M_{\nu\nu'}\omega_\lambda \sinh(\beta\hbar\omega_\lambda/2)}\right] \tag{2.42}$$

where $\{n_\lambda\}$ represents a (3N)-tuple of numbers $(n_1, n_2 \ldots n_{3N})$ and the sum on $\{n_\lambda\}$ extends over all possible (3N)-tuples as $n_1, n_2, \ldots n_{3N}$ all vary from $-\infty$ to ∞. Combining (2.37), (2.38), (2.40) and (2.42),

$$\frac{\partial^2 \Gamma}{\partial\Omega\partial\epsilon} = (2\pi\hbar)^{-1} \frac{k'}{k} \sum_{\nu,\nu'}' q_\nu q_{\nu'} \int \exp[-i\omega t + i\underline{Q}\cdot(\underline{b}_\nu - \underline{b}_{\nu'})]\ e^{-2W_{\nu\nu'}}$$

$$(x) \sum_{\{n_\lambda\}}' \prod_{\lambda=1}^{3N} \exp(i n_\lambda \omega_\lambda t) \exp(-\beta n_\lambda \omega_\lambda/2)$$

$$(x)\ I_{n_\lambda}\left[\frac{\hbar(\underline{Q}\cdot\underline{\zeta}_\nu^\lambda)(\underline{Q}\cdot\underline{\zeta}_{\nu'}^\lambda)}{2M_{\nu\nu'}\omega_\lambda \sinh(\beta\omega_\lambda/2)}\right] \tag{2.43}$$

$$= \frac{k'}{\hbar k} \sum_{\nu,\nu'}' q_\nu q_{\nu'} \exp[i\underline{Q}\cdot(\underline{b}_\nu - \underline{b}_{\nu'})]\ e^{-2W_{\nu\nu'}}$$

$$(x) \sum_{\{n_\lambda\}}' \delta(\omega - \sum_\lambda n_\lambda \omega_\lambda) \exp(-\beta \sum_\lambda n_\lambda \omega_\lambda/2)$$

$$(x) \prod_{\lambda=1}^{3N} I_{n_\lambda}\left[\frac{\hbar(\underline{Q}\cdot\underline{\zeta}_\nu^\lambda)(\underline{Q}\cdot\underline{\zeta}_{\nu'}^\lambda)}{2M_{\nu\nu'}\omega_\lambda \sinh(\beta\hbar\omega_\lambda/2)}\right] \tag{2.44}$$

The sum on $\{n_\lambda\}$ has been integrated term by term over all t to produce the energy-conserving δ functions; this step is of course only justified if the sum is uniformly convergent throughout the range of integration. We ignore this question entirely (being a dilettante in theory saves considerable work at times such as this).

There is one set $\{n_\lambda\}$ with all elements zero; this corresponds to an event wherein no quanta are exchanged with any normal modes, i.e., elastic scattering. The contribution from this single elastic event is

$$\frac{\partial^2\sigma_{el}}{\partial\Omega\partial\epsilon} = \frac{k'}{\hbar k}\sum_{\nu,\nu'} q_\nu q_{\nu'} \exp\left[i\underline{Q}\cdot(\underline{b}_\nu - \underline{b}_{\nu'})\right] e^{-2W_{\nu\nu'}}$$

$$(x)\prod_{\lambda=1}^{3N} I_0\left[\frac{\hbar(\underline{Q}\cdot\underline{\epsilon}_\nu^\lambda)(\underline{Q}\cdot\underline{\epsilon}_{\nu'}^\lambda)}{2M_{\nu\nu'}\omega_\lambda \sinh(\beta\omega_\lambda/2)}\right]\delta(\omega) \qquad (2.45)$$

In order to approximate the I_0 contributions, we simply assume that their arguments are small,

$$\frac{\hbar(\underline{Q}\cdot\underline{\epsilon}_\nu^\lambda)(\underline{Q}\cdot\underline{\epsilon}_{\nu'}^\lambda)}{2M_{\nu\nu'}\omega_\lambda \sinh(\beta\omega_\lambda/2)} \ll 1 ,$$

so that the modified Bessel functions can be approximated to lowest order:

$$I_n(x) \simeq (x/2)^{|n|}/(|n|)!$$

or specifically

$$I_0(x) \simeq 1$$

$$I_1(x) \simeq x/2 . \qquad (2.46)$$

Then (2.45) becomes

$$\frac{\partial^2\sigma_{el}}{\partial\Omega\partial\epsilon} \simeq \frac{k'}{\hbar k}\sum_{\nu,\nu'} a_\nu a_{\nu'} \exp\left[i\underline{Q}\cdot(\underline{b}_\nu-\underline{b}_{\nu'})\right] e^{-2W_{\nu\nu'}}\delta(\omega) \tag{2.47}$$

For "one-quantum" events, i.e. those for which the set $\{n_\lambda\}$ contains (3N-1) zeroes and a single one (2.44) is

$$\frac{\partial^2\sigma^{(1)}}{\partial\Omega\partial\epsilon} = \frac{k'}{\hbar k}\sum_{\nu,\nu'} a_\nu a_{\nu'} \exp\left[i\underline{Q}\cdot(\underline{b}_\nu-\underline{b}_{\nu'})\right] e^{-2W_{\nu\nu'}}$$

$$(x)\sum_{\lambda=1}^{3N}\delta(\omega-\omega_\lambda)\exp(-\beta\omega_\lambda/2)$$

$$(x)\, I_1\left[\frac{\hbar(\underline{Q}\cdot\underline{\zeta}_\nu^\lambda)(\underline{Q}\cdot\underline{\zeta}_{\nu'}^\lambda)}{2M_{\nu\nu'}\omega_\lambda\sinh(\beta\omega_\lambda/2)}\right]\prod_{\mu\neq\lambda} I_0\left[\frac{\hbar(\underline{Q}\cdot\underline{\zeta}_\nu^\mu)(\underline{Q}\cdot\underline{\zeta}_{\nu'}^\mu)}{2M_{\nu\nu'}\omega_\mu\sinh(\beta\omega_\mu/2)}\right]$$

$$= \frac{k'}{\hbar k}\sum_{\nu,\nu'} a_\nu a_{\nu'} \exp\left[i\underline{Q}\cdot(\underline{b}_\nu-\underline{b}_{\nu'})\right] e^{-2W_{\nu\nu'}}$$

$$(x)\sum_{\lambda=1}^{3N}\delta(\omega-\omega_\lambda)\exp(-\beta\omega_\lambda/2)\,\frac{\hbar(\underline{Q}\cdot\underline{\zeta}_\nu^\lambda)(\underline{Q}\cdot\underline{\zeta}_{\nu'}^\lambda)}{4M_{\nu\nu'}\omega_\lambda\sinh(\beta\omega_\lambda/2)} \tag{2.48}$$

2.3 Scattering from Acoustic Modes in Disordered Systems of Harmonic Oscillators

Here we attempt to calculate approximately the scattering law for an oversimple model of a glass, one which requires no more knowledge than we have of the real properties of a glass. To completely specify even the one-quantum scattering as expressed in equation (2.48), we must diagonalize a 3Nx3N matrix to obtain the normal modes

of the system — where N is of order 10^{23}. In a crystal, symmetry considerations make it possible to consider a much smaller matrix as a function of the phonon wave vector $\underline{q}$. However the size of this matrix is only 3n x 3n, where n is the number of atoms in a unit cell of the crystal.

In a glass we have no corresponding symmetry, and must either investigate what other means can be used to reduce the size of the problem, or else set out to consider only a small part of the problem in the first place.

What do we know about glasses that may be useful in calculating the scattering law? For one thing, glasses like all solids transmit sound waves. The wavelength of these waves however, must be sufficiently long that the glass appears to be a continuous medium. If the wavelength is too short, we will no longer have wavevector as a good characterization for the modes. We certainly know something about the glass structure; we have measured the neutron diffraction pattern and from it computed the neutron rdf. Although it is an integral property of the structure, still this information may prove useful.

Suppose all we know about glass is its structure factor and that it transmits sound waves. Let us try to calculate the one-phonon scattering from sound waves. It is convenient to rearrange equation (2.48) somewhat

$$\frac{\partial^2 \sigma^{(1)}}{\partial \Omega \, \partial E} = \frac{k'}{\hbar k} N \langle a^2 \rangle \exp(-\beta\omega/2) \, \tilde{S}(\underline{Q}, \omega) \qquad (2.49)$$

where

$$\tilde{S}(\underline{Q},\omega) = [2\omega \sinh(\beta\omega/2)]^{-1} N^{-1} \langle a^2 \rangle^{-1} \sum_{\lambda=1}^{3N} \sum_{\nu,\nu'} \bar{a}_\nu a_{\nu'} e^{-2W_{\nu\nu'}}$$

$$(x)\ \frac{\hbar}{2M_{\nu\nu'}} (\underline{Q}\cdot\underline{\epsilon}_\nu^\lambda)(\underline{Q}\cdot\underline{\epsilon}_{\nu'}^\lambda) \exp\left[i\underline{Q}\cdot(\underline{b}_\nu - \underline{b}_{\nu'})\right] \delta(\omega-\omega_\lambda)$$

$$= [2\omega \sinh(\beta\omega_\lambda/2)]^{-1} \sum_{\lambda=1}^{3N} F_\lambda(\underline{Q})\, \delta(\omega-\omega_\lambda) \qquad (2.50)$$

Note that ω_λ has been replaced by ω and brought out of the λ sum wherever it appeared in (2.48). The $\delta(\omega-\omega_\lambda)$ factor allows us to do this. We call $F_\lambda(\underline{Q})$ the "inelastic structure factor" and $\check{S}(\underline{Q},\omega)$ the "symmetrized scattering law" since it has the property $\check{S}(-\underline{Q},-\omega)=\tilde{S}(\underline{Q},\omega)$ while the unsymmetrized scattering law apparently satisfies $S(-\underline{Q},-\omega) = \exp(\beta\omega/2)\, S(-\underline{Q},-\omega) = \exp(\beta\omega)\, S(Q,\omega)$ which is called the detailed balance condition. The factoring of $\tilde{S}$ as a function of ω times the inelastic structure factor sum is made for convenience since $F_\lambda(\underline{Q})$ contains all the effect of the λ mode, while the factor depending on ω is the same for all modes with frequency ω.

Now to incorporate the assumption of acoustic wave modes- we will treat modes for which nuclear displacements have the form

$$u_\nu(t) = \sum_\lambda Q_\lambda(\underline{q}) \exp(i\underline{q}\cdot\underline{b}_\nu + i\omega_\lambda t) \qquad (2.51)$$

and will assume that $\omega_\lambda = v_\lambda q$ as is true for sound waves in a continuous medium. Furthermore, we will assume there

are only two values of ν_λ, one for the longitudinal and one for the transverse modes; a mode is longitudinal or transverse if the polarization vector $\underline{a}_\lambda(\underline{q})$ is parallel or perpendicular to the propagation vector $\underline{q}$. We expect one longitudinally and two (orthogonal) transversely polarized modes. Now let us explicitly write down the acoustic-mode portion of the scattering law, which we call $\tilde{S}^A$:

$$\tilde{S}^A(Q,\omega) = [2\omega \sinh(\beta\omega/2)]^{-1} \sum_{\underline{q},j} F_{\underline{q}j}(\underline{Q})\, \delta(\omega-\omega_j(\underline{q}))$$

$$= [2\omega \sinh(\beta\omega/2)]^{-1} N^{-1}\langle a^2\rangle^{-1} \sum_{\underline{q},j} \frac{\hbar}{2}[\underline{Q}\cdot\underline{e}_j(\underline{q})]^2 \sum_{\nu,\nu'} a_\nu a_{\nu'} e^{-2W_{\nu\nu'}}$$

$$(\times)\, \exp[i(\underline{Q}+\underline{q})\cdot(\underline{b}_\nu-\underline{b}_{\nu'})]\, \delta(\omega-\omega_j(\underline{q})) \qquad (2.52)$$

We recognize the sum over atoms in (2.52) as the elastic structure factor,

$$S_e(\underline{Q}+\underline{q}) = N^{-1}\langle a^2\rangle^{-1} \sum_{\nu,\nu'} a_\nu a_{\nu'} e^{-2W_{\nu\nu'}} \exp[i(\underline{Q}+\underline{q})\cdot(\underline{b}_\nu-\underline{b}_{\nu'})] \qquad (2.53)$$

so

$$F_{\underline{q}j}(\underline{Q}) = \frac{\hbar}{2}[\underline{Q}\cdot\underline{e}_j(\underline{q})]^2 [1+S_e(\underline{Q}+\underline{q})] \qquad (2.54)$$

We transform the sum over $\underline{q}$ in (2.52) to an integral in the usual manner,

$$\sum_{\underline{q}} \rightarrow \frac{V}{(2\pi)^3}\int d^3q$$

where V is the sample volume.

Thus

$$\tilde{S}^A(\underline{Q},\omega) = [2\omega\sinh(\beta\omega/2)]^{-1} \sum_j \frac{V}{(2\pi)^3} \int F_{\underline{q}j}(\underline{Q})\, \delta(\omega - \underline{v}_j\cdot\underline{q})\, d^3q \tag{2.55}$$

$$= [2\omega\sinh(\beta\omega/2)]^{-1} \sum_j \frac{V}{(2\pi)^3} \int \frac{\hbar}{2} [\underline{Q}\cdot\underline{a}_j(\underline{q})]^2 \times [1 + S_e(\underline{Q}+\underline{q})]\, \delta(\omega - \underline{v}_j\cdot\underline{q})\, d^3q \tag{2.56}$$

Now to evaluate the $\underline{q}$ integral, we need expressions for the $\underline{a}_j(\underline{q})$. Since we have only longitudinal and transverse modes this is simple: for the L modes,

$$a_L(\underline{q}) = a_L(\hat{q}) = a_L\hat{q} \tag{2.57}$$

for the T modes,

$$a_{T_1}(\underline{q}) = a_{T_1}(\hat{q}) = \underline{b}_1 \times \hat{q}$$
$$a_{T_2}(\underline{q}) = \underline{b}_2 \times \hat{q} \tag{2.58}$$

and $\underline{b}_1\cdot\underline{b}_2=0$ to insure orthogonality of the T_1 and T_2 modes. We can evaluate the numerical value of a_L and the a_T using the normalization condition for the $\underline{c}_\nu^\lambda$, expressed in terms of the $\underline{a}$'s:

$$\delta_{\lambda\lambda'} = \sum_{\nu=1}^{N} \underline{c}_\nu^\lambda \cdot \underline{c}_\nu^{\lambda'} = \sum_{\nu=1}^{N} m_\nu\, \underline{a}_L(\hat{q})\cdot\underline{a}_L(\underline{q}) \tag{2.59}$$

for L modes and

$$\delta_{\lambda\lambda'} = \sum_{\nu=1}^{N} \underline{c}_\nu^\lambda \cdot \underline{c}_\nu^{\lambda'} = \sum_{\nu=1}^{N} m_\nu \, \underline{a}_{T_1}(\hat{q}) \cdot \underline{a}_{T_1}(\hat{q})$$

$$= \sum_{\nu=1}^{N} m_\nu \, \underline{a}_{T_2}(\hat{q}) \cdot \underline{a}_{T_2}(\hat{q}) \tag{2.60}$$

for T modes. Using (2.57) and (2.59) we find

$$\sum_{\nu=1}^{N} \underline{a}_L(\hat{q}) \cdot \underline{a}_L(q) m_\nu$$

$$= \sum_{\nu=1}^{N} a_L^2 m_\nu = a_L^2 M \, .$$

M is apparently the total mass of the system. Using (2.58) and (2.60),

$$\sum_{\nu=1}^{N} \underline{a}_{T_1}(\hat{q}) \cdot \underline{a}_{T_1}(\hat{q}) m_\nu = a_{T_1}^2 M$$

and analogously for $\underline{a}_{T_2}(q)$. In toto then, the normalizations are

$$a_L^2 = a_{T_1}^2 = a_{T_2}^2 = M^{-1} \tag{2.61}$$

Now to evaluate the integral in (2.56). We first note that for systems of interest here, S_e is a function only of the magnitude of its argument. Also noting $\delta(ax) = a^{-1}\delta(x)$, we write for the q- integral

$$J_L(Q) = \int [Q \cdot \underline{a}_L(\hat{q})]^2 [1 + S_e(|Q+q|)] \, \delta(\omega - v_L q) \, d^3q$$

$$= v_L^{-1} \int Q^2 q^2 \mu^2 [1 + S_e(\sqrt{Q^2+q^2+2qQ\mu})] \, \delta(q - \tfrac{\omega}{v_L}) \, d^3q \tag{2.62}$$

with $\mu = (\underline{Q}\cdot\hat{\underline{q}})\, Q^{-1}$. To evaluate (2.62) we use a spherical polar coordinate system with polar axis along $\underline{Q}$,

$$J_L(\underline{Q}) = 2\pi\omega_L^{-1}\int_{-1}^{1} Q^2 a_L^2 \mu^2 \left[1 + S_e\left(\sqrt{Q^2+q^2+2Qq\mu}\right)\right] \delta(q-\omega/v_L)\, q^2\, dq\, d\mu$$

$$= 2\pi Q^2 a_L^2 \omega^2 v_L^{-3} \int_{-1}^{1} \mu^2 \left[1 + S_e\left(\sqrt{Q^2+\omega^2 v_L^{-2}+2Qv_L^{-1}\omega\mu}\right)\right] d\mu$$

$$= 2\pi Q^2 M^{-1} \omega^2 v_L^{-3} \left\{\frac{2}{3} + \int_{-1}^{1} \mu^2 S_e\left(\sqrt{Q^2+\omega^2 v_L^{-2}+2Qv_L^{-1}\omega\mu}\right) d\mu\right\}$$

(2.63)

Similarly we find

$$J_T(\underline{Q}) = J_{T_1}(\underline{Q}) + J_{T_2}(\underline{Q})$$

$$= \int \left\{\left[\underline{Q}\cdot\underline{a}_{T_1}(\hat{q})\right]^2 + \left[\underline{Q}\cdot\underline{a}_{T_2}(\hat{q})\right]^2\right\}\left[1 + S_e(|\underline{Q}+\underline{q}|)\right] \delta(\omega - v_T q)\, d^3q$$

$$= 2\pi Q^2 \omega^2 v_L^{-3} a_{T_1}^2 \int_{-1}^{1} (1-\mu^2)\left[1 + S_e\left(\sqrt{Q^2+\omega^2 v_T^{-2}+2\omega v_T^{-1} Q\mu}\right)\right] d\mu$$

noting that $(\underline{Q}\cdot\underline{a}_{T_1})^2 + (\underline{Q}\cdot\underline{a}_{T_2})^2$ is just the squared projection of $\underline{Q}$ on a plane normal to $\underline{q}$, and using the fact that $a^2_{T_1} = a^2_{T_2}$. Thus

$$J_T(\underline{Q}) = 2\pi Q^2 \omega^2 v_L^{-3} M^{-1} \left\{\frac{4}{3} + \int_{-1}^{1} (1-\mu^2)\, S_e\left(\sqrt{Q^2+\omega^2 v_T^{-2}+2Q\omega v_T^{-1}\mu}\right) d\mu\right.$$

(2.64)

Substituting J_L and J_T into equation (2.56) for the acoustic-mode scattering law we have finally

$$\tilde{S}^{A}(\underline{Q},\omega) = [2\omega \sinh(\beta\omega/2)]^{-1} \frac{V}{(2\pi)^3} \frac{\hbar}{2} [J_L(\underline{Q}) + J_T(\underline{Q})]$$

$$= [2\omega \sinh(\beta\omega/2)]^{-1} \frac{V}{N_u} (2\pi)^{-2} \frac{\hbar Q^2}{2M_u} \omega^2$$

$$(\times) \left\{ v_L^{-3} \left[\frac{2}{3} + \langle \mu^2 \rangle (Q, \omega, v_L) \right] \right.$$

$$\left. + v_T^{-3} \left[\frac{4}{3} + \langle 1-\mu^2 \rangle (Q, \omega, v_T) \right] \right\} \qquad (2.65)$$

We have separated the total system mass M into the product of a "unit of composition" mass M_u, and the number N_u of such units. A unit of composition can be whatever is convenient; in our case one Be and 2 F's is an obvious choice. The ratio V/N_u is just the reciprocal density of such units, ρ_u^{-1}. The quantity $\hbar Q^2/2M_u$ may be thought of as a recoil energy (it is actually an angular frequency) associated with the transfer of momentum $\hbar Q$ to a single unit of composition. For convenience we have also introduced the moments

$$\langle f(\mu) \rangle (Q, \omega, v) \equiv \int_{-1}^{1} f(\mu) S_e \left(\sqrt{Q^2 + \omega^2 v^{-2} + 2Q\omega v^{-1}\mu} \right) d\mu \qquad (2.66)$$

2.4 Generalized Frequency Distribution Function, $G(\underline{Q}, \omega)$

As an aid in interpretation of the inelastic scattering data, we will reduce them to a functional form in which the underlying information about the system's normal mode frequencies will be made more clearly visible. We define

$$G(\underline{Q},\omega) = \tilde{S}(\underline{Q},\omega)\, 2\omega \sinh(\beta\omega/2)\left[\frac{\hbar Q^2}{2M_{uc}}\right]^{-1} \tag{2.67}$$

with $\tilde{S}(Q,\omega)$ as in equation (2.50). This function is easily calculable from $\tilde{S}(Q,\omega)$, which we get out of the inelastic scattering data reduction procedure (note that equation (2.50) represents only one-quantum scattering; we must assume multi-quantum contributions are small for the present analysis to be valid.) Now consider the frequency dependence of $G(Q,\omega)$, which we first write explicitly:

$$G(\underline{Q},\omega) = \left[\frac{\hbar Q^2}{2M_u}\langle a^2\rangle\right]^{-1} \frac{1}{N} \sum_{\lambda=1}^{3N} \left\{ \sum_{\nu} \frac{\hbar a_\nu^2}{2m_\nu} e^{-2W_{\nu\nu}} (\underline{Q}\cdot\underline{\epsilon}_\nu^\lambda)^2 + \sum_{\nu,\nu'}{}' \frac{\hbar a_\nu a_{\nu'}}{2M_{\nu\nu'}} e^{-2W_{\nu\nu'}} (\underline{Q}\cdot\underline{\epsilon}_\nu^\lambda)(\underline{Q}\cdot\underline{\epsilon}_{\nu'}^\lambda) \exp\left[i\underline{Q}\cdot(\underline{b}_\nu - \underline{b}_{\nu'})\right] \right\} \otimes \delta(\omega-\omega_\lambda) \tag{2.68}$$

We will not attempt to evaluate the interference terms, but will focus attention on the self terms which we separate and call G_s. In the simplest case of a monatomic system

$$a_\nu^2/m_\nu = \langle a^2\rangle/M_u \quad \text{and}$$

$$G_s(\underline{Q},\omega) = \frac{e^{-2W}}{N} \sum_{\lambda=1}^{3N} \sum_{\nu} (\hat{\underline{Q}}\cdot\underline{\epsilon}_\nu^\lambda)^2 \delta(\omega-\omega_\lambda) \tag{2.69}$$

$$= \frac{e^{-2W}}{N} \sum_{\nu} \hat{\underline{Q}}\cdot\underline{\underline{G}}_\nu(\omega)\cdot\hat{\underline{Q}} \tag{2.70}$$

where we have defined the "polarization weighted directional

frequency distribution" according to

$$G_{\nu\alpha\beta}(\omega) = \frac{1}{N}\sum_{\lambda=1}^{3N} C_{\nu\alpha}^{\lambda} C_{\nu\beta}^{\lambda}\, \delta(\omega-\omega_\lambda) \tag{2.71}$$

and $C_{\nu\alpha}^{\lambda}$ is the α^{th} component of $\underline{C}_\nu^\lambda$. The determination of the functions $\underline{\underline{G}}_\nu(\omega)$ is as close as we can come using neutron scattering to a measurement of the actual normal mode frequency distribution of the system,

$$g(\omega) = \frac{1}{N}\sum_{\lambda=1}^{3N} \delta(\omega-\omega_\lambda) \tag{2.72}$$

Note that the normalization of the $\underline{C}_\nu^\lambda$ implies

$$\sum_\nu \text{trace}\, \underline{\underline{G}}_\nu(\omega) = \sum_\nu \sum_\alpha G_{\nu\alpha\alpha}(\omega)$$
$$= \sum_\nu \frac{1}{N}\sum_{\lambda=1}^{3N} (\underline{C}_\nu^\lambda \cdot \underline{C}_\nu^\lambda)\, \delta(\omega-\omega_\lambda) = g(\omega)$$

Unfortunately, in the present case we have a polyisotopic system, and in reality one cannot ignore the interference terms in (2.68). We can however, still evaluate $G(\underline{Q},\omega)$ using (2.67) and we expect that (treated as a function of ω) it will at the very least exhibit the same singularities as $g(\omega)$. Just for the record, we write down a polyatomic analogue of (2.70) including interference terms:

$$G(\underline{Q},\omega) = \left[\frac{\hbar Q^2}{2M_u}\langle a^2\rangle\right]^{-1} \sum_{\nu,\nu'} \frac{\hbar a_\nu a_{\nu'}}{2M_{\nu\nu'}} e^{-2W_{\nu\nu'}}\, \underline{Q}\cdot\underline{\underline{G}}_\nu^{\nu'}(\underline{Q},\omega)\cdot\underline{Q}$$

where

$$G_{\nu\alpha\beta}^{\nu'}(\underline{Q},\omega) = \frac{1}{N}\sum_{\lambda=1}^{3N} C_{\nu\alpha}^{\lambda} C_{\nu'\beta}^{\lambda}\, \delta(\omega-\omega_\lambda)\, \exp\left[i\underline{Q}\cdot(\underline{b}_\nu - \underline{b}_{\nu'})\right]$$

by analogy with $\underline{\underline{G}}_{\nu}(\omega)$.

There is little need to point out that the dynamical information contained in $G(\underline{Q},\omega)$ for a polyatomic system is considerably obscured by the various weighting factors (scattering length, scatterer mass, Debye-Waller factor, polarization and interference factors) appearing in (2.68), as well as by the additional spherical averaging over $\underline{Q}$ which occurs in a glass. As we shall see later, however, the $G(Q,\omega)$ function computed from glass scattering law data can still provide some insight on the nature of $g(\omega)$ for the glass.

CHAPTER THREE

EXPERIMENTS

3.1 Time of Flight Diffraction

3.1.1. Method. We begin by writing down a very general expression for the result of a neutron scattering measurement in which the scattered beam is not explicitly energy analyzed. For the counting rate per unit solid angle per unit time at angle ϑ and time t, we may write

$$C(t,\vartheta) = \int_{E'=0}^{\infty} \eta(E') \int_{E=0}^{\infty} p(E,E',\vartheta) \int_{\tau=0}^{\infty} I(t-\tau,E) \quad F(E,E',\vartheta)$$

$$(x)\ \delta\left(\tau - \frac{L}{v} - \frac{L'}{v'}\right)\, d\tau\, dE\, dE' \tag{3.1}$$

with

$E' = mv'^2/2$ = the energy of a scattered neutron

$E = mv^2/2$ = the energy of an incident neutron

$\eta(E')$ = the detector efficiency at neutron energy E'

$p(E,E',\vartheta)$ = the probability of single scattering through angle ϑ with energy change from E to E' for an infinitesimally thin target

$I(t-\tau,E)$ = the intensity of the neutron source at time $t-\tau$ and energy E.

$F(E,E',\vartheta)$ = a correction for nonideal scattering in the sample (this includes both "attenuation" and "multiple scattering" effects, based on the assumption that the neutron interacts instantaneously with the sample)

L, L' = flight path lengths between source and sample, and between sample and detector

In general, if N scattering units are illuminated by the beam,

$$\rho(E, E', \vartheta) = N \frac{\partial^2 \sigma}{\partial \Omega \partial E} (E'-E, \vartheta)$$

We will consider cases of the above general relation, which we classify according to the nature of the source term in equation (3.1):

a) conventional diffraction

$$I(t-\tau, E) \simeq \phi(E_o)\ \delta(E-E_o), \text{ independent of } t-\tau$$

where E_o is the fixed incident energy and $\phi(E_o)$ is the monochromatic flux at E_o.

b) time-of-flight diffraction

$$I(t-\tau, E) \simeq S(E)\ \delta(t-\tau)$$

where S(E) is the energy-dependent intensity, in neutrons/unit area, of a source pulse. In the conventional diffraction case, (3.1) becomes

$$C_x(\vartheta) = \phi(E_o) \int_{E'=0}^{\infty} \eta(E')\ N \frac{\partial^2 \sigma}{\partial \Omega \partial E} (E'-E_o, \vartheta)\ F(E_o, E', \vartheta)\ dE' \tag{3.2}$$

In the time-of-flight diffraction case,

$$C_T(t, \vartheta) = \int_{E'=0}^{\infty} \eta(E') \int_{E=0}^{\infty} N \frac{\partial^2 \sigma}{\partial \Omega \partial E} (E'-E, \vartheta)\ F(E, E', \vartheta)\ S(E)$$

$$(\times)\ \delta\left(t - \frac{L}{v} - \frac{L'}{v'}\right)\ dE\, dE' \tag{3.3}$$

Each type of diffractometer may be thought of as measuring the integral of the partial differential cross section along some path in (Q,ϵ) space. In order to understand exactly what function one measures in a given experiment, it is necessary to examine the integration paths of the various types of diffractometers.

For the conventional diffractometer at a scattering angle ϑ, the instrumental integration path is determined by conditions

$$\epsilon = E' - E_o$$

$$Q^2 = |\underline{k}' - \underline{k}_o|^2 = \frac{2m}{\hbar^2}\left(E' + E_o - 2\sqrt{E'E_o}\cos\vartheta\right) \tag{3.4}$$

and is shown in figure 2 for a variety of E_o and ϑ. For the time-of-flight diffractometer, the integration path is determined by

$$\frac{L}{v} + \frac{L'}{v'} = t \tag{3.5}$$

or

$$E' = \frac{m}{2}\left(\frac{L'}{t - L/\sqrt{2E/m}}\right)^2 \tag{2.6}$$

which depends on the flight path lengths L and L'. Examination of (2.5) shows that for $L \gg L'$, t is determined mainly by the incident energy $mv^2/2$, while for $L \ll L'$, t is determined mainly by the scattered energy $mv'^2/2$. Loci of constant time of arrival in the (Q,ϵ) plane are shown in

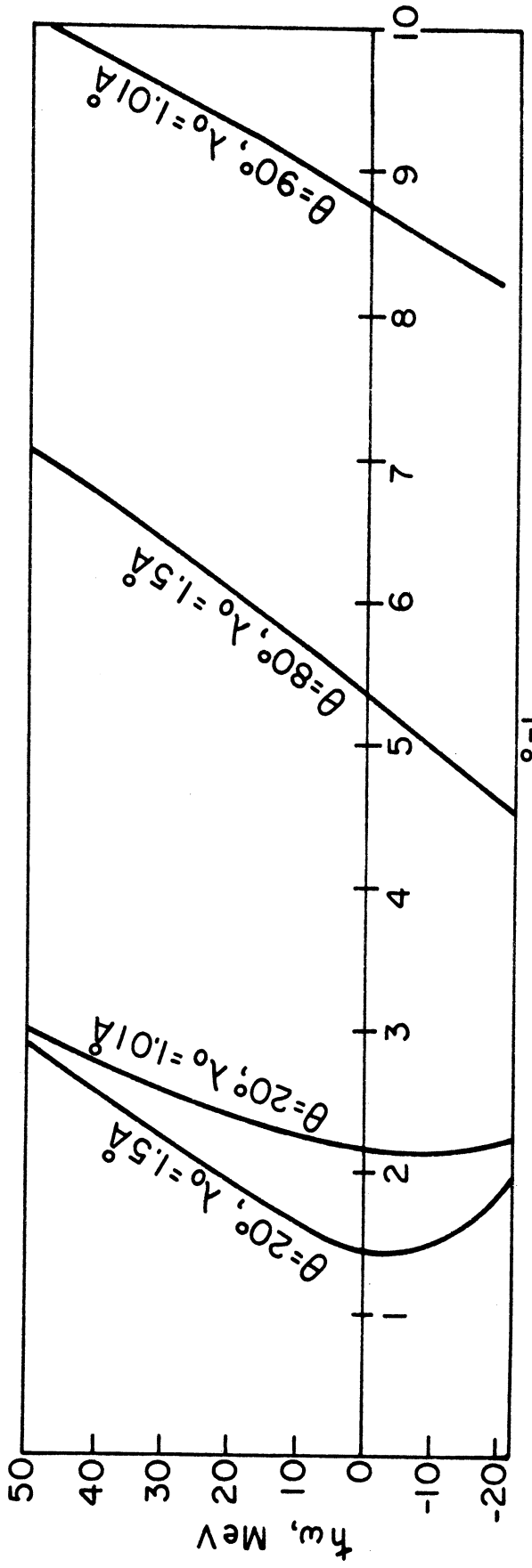

Figure 2. Loci of constant angle for monochromatic neutrons.

figure 3 for 90° scattering and for various choices of L and L', all with the total path length L+L'=5 meters.

When one measures an experimental point at $Q_e = 2k \sin \vartheta/2$ using either diffraction method, what one gets is thus not $S(Q_e)$ but the integral of $\frac{\partial^2\sigma}{\partial\Omega\partial\epsilon}(Q,\epsilon)$ (weighted by detector efficiency, and in the time of flight case by the incident intensity) along a path such as those shown in figures 2 and 3.

Recalling that one wishes to measure

$$S(Q_e) = \int S(Q_e,\omega)\, d\omega$$

$$= \langle a^2 \rangle^{-1} \int \frac{\partial^2\sigma}{\partial\Omega\partial\epsilon}\, d\epsilon$$

it appears that the most favorable arrangement is that whose integration path is most nearly vertical, and figures 2 and 3 show that this condition is best fulfilled by the time of flight diffractometer with L=L'. Furthermore, for the case L=L' the integration path is more nearly vertical for smaller times of arrival, i.e., for higher energy at a given scattering angle.

Carpenter and Sutton[24] have examined the effects of the detector efficiency and incident spectrum in "weighting" the integration performed by diffractometers: their conclusion is that the equal flight path (L=L') time of flight configuration provides a good approximation to the structure factor. Powles,[25] Sinclair and Wright[26] and others however prefer to apply what are called Placzek[27] corrections to

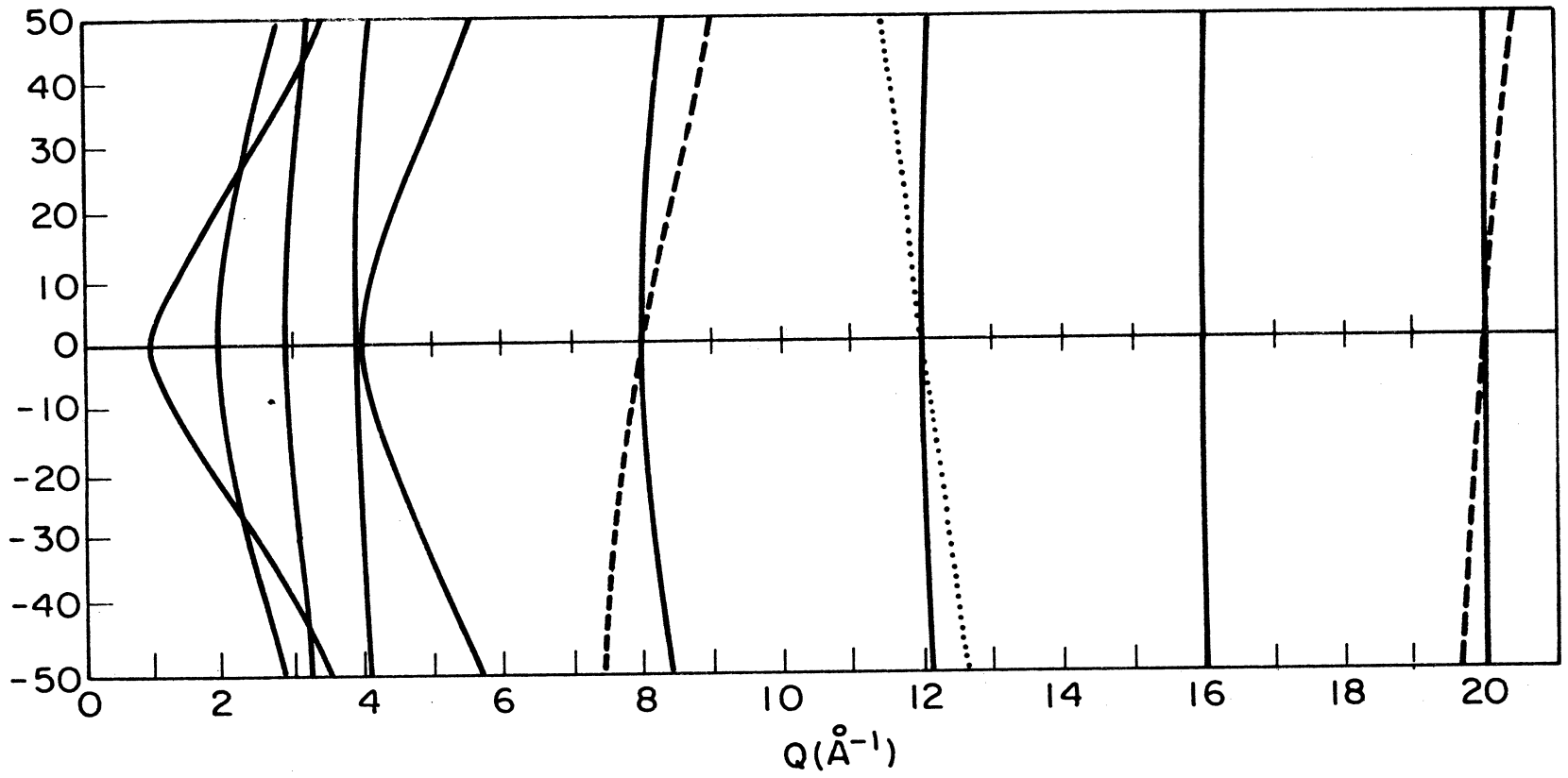

Figure 2. Loci of Constant Time of Arrival for Neutron Scattering at 20° and 90°. Solid lines, L=L′; dotted lines, L=0.25 L′; dashed lines, L=4L′. The leftmost four curves are calculated for 20° scattering, the remainder for 90°.

extract S(Q) from the diffraction data. A series of corrections was calculated by Placzek and by Wick[28] in terms of the energy moments of the scattering law; these corrections of course can only be calculated insofar as the energy moments are known.

We consider the subject of whether or not Placzek corrections are preferable to an equal flight path arrangement as unsatisfactorily resolved at the present time; we show here some experimental results supporting the equal flight path method. Figure 4 compares measured structure factor data for glassy BeF_2 from the Michigan equal-flight-path diffractometer, with integrated scattering law data from the Argonne time-of-flight spectrometer. We have made the comparison at an equivalent level of data reduction in both cases; multiple scattering and resolution effects are not corrected for. It is emphasized that these are totally independent measurements and that no normalization of one to the other has been made. With the exception of the immediate vicinity of the first two peaks in S(Q), where differences in multiple scattering and resolution effects are expected to be greatest (as will be explained later, the configuration of the target was different for the two experiments; multiple scattering and resolution effects are expected to be more severe for the time-of flight diffractometer, consistent with the trend of figure 4) the agreement is within several percent throughout the region

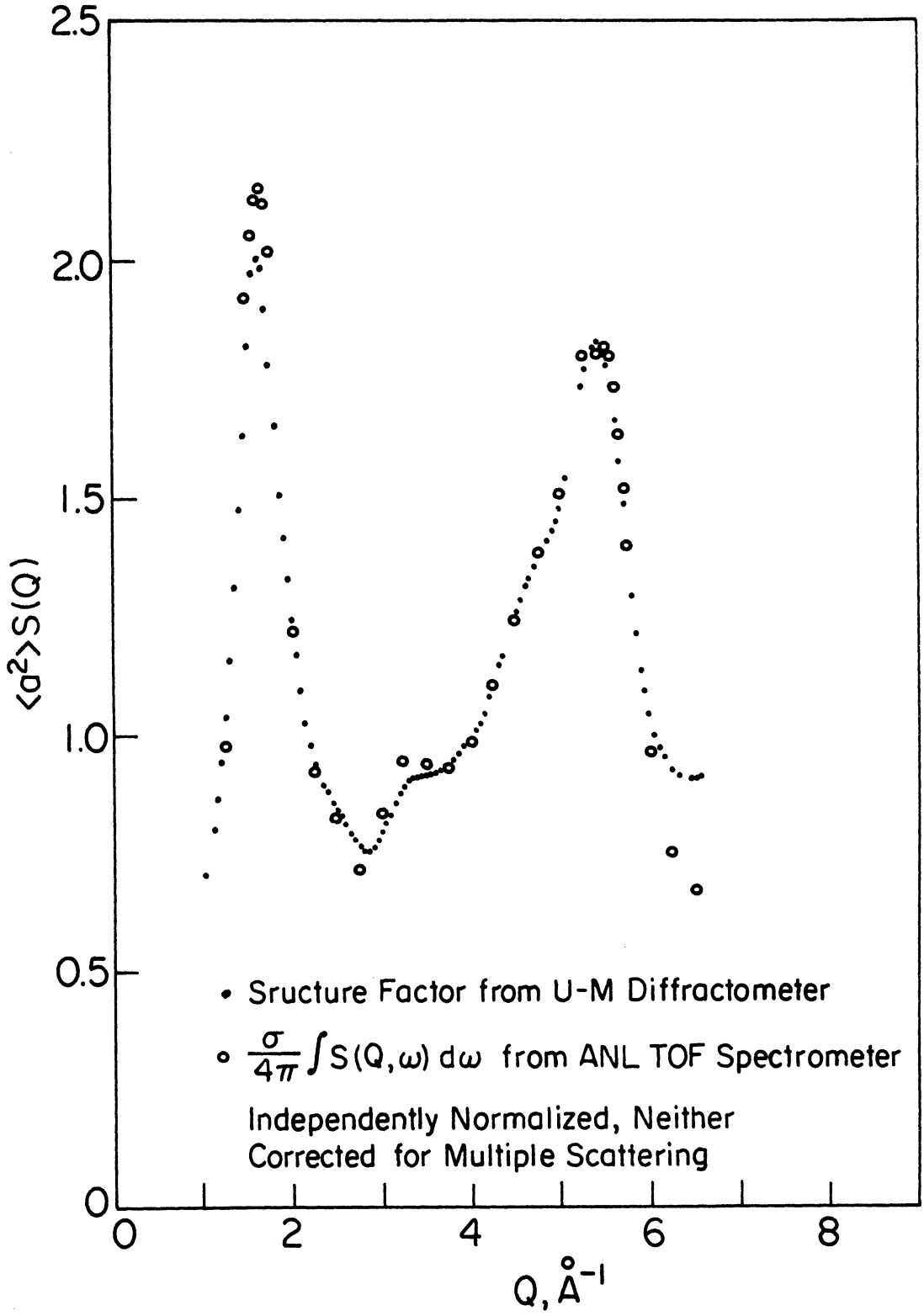

Figure 4. Comparison of Measured Structure Factor of Vitreous BeF_2 with Integration of Measured Scattering Law

$1.0 < Q < 6\text{Å}^{-1}$ where the scattering law integration is reliable. This is well within the combined statistical error of the two measurements; we thus assert that the equal-flight-path arrangement provides a reasonably good measurement of S(Q) even for a sample such as BeF_2 composed of light nuclei where Placzek corrections might be expected to be severe. This may be due at least in part to a fortuitous cancellation of errors due to omitted Placzek corrections in the sample and reference; but this seems improbable at best.

3.1.2. Time of Flight Diffractometer. The equal-path time-of-flight diffractometer at the University of Michigan has been described in detail elsewhere[29]. We repeat only pertinent details here.

The diffractometer operates at beam port J of the Ford Nuclear Reactor, viewing the D_2O source tank[30]. (The general layout is shown in figure 5.) The beam is coarsely defined and shielded by a 103" long plug in the beam port, with an exit beam size of 1.97" x .54" (height x width). Between the rotor and sample is a 95" long, 1" x 3/8" collimator which together with the chopping rotor collimates the beam to .0092 x .0079 radian (vertical x horizontal). Beam size at the target is 1.5" x .5". A rotating collimator (10" diameter fiberglass resin rotor, denoted "rotor 1" in figure 5) in the beam upstream from the chopping rotor cuts down the unwanted fast component of the beam, thereby reducing

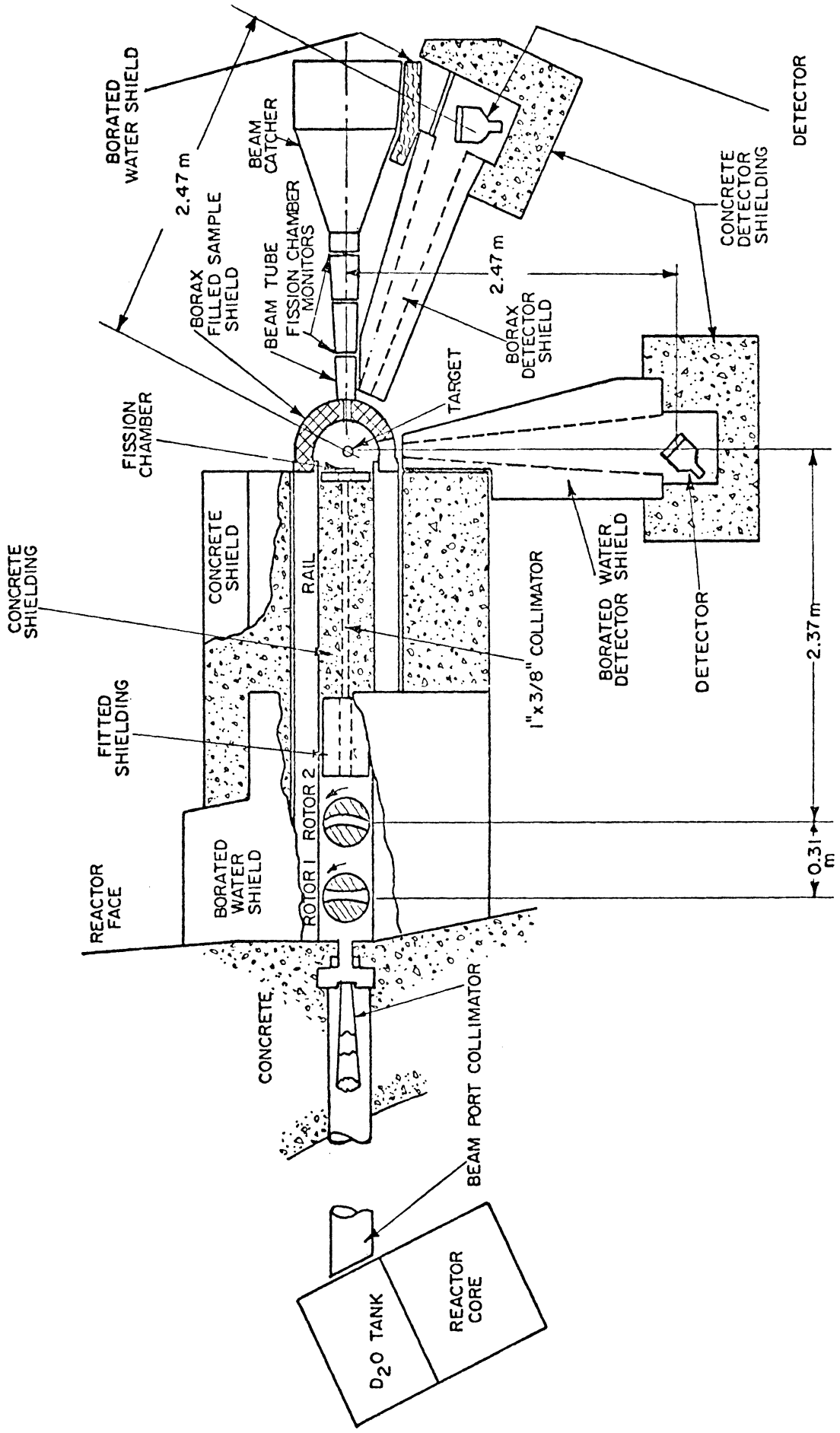

Figure 5. Schematic Drawing of the Two Rotor Time-of-Flight Diffractometer

background counting rates. Distance from rotor 2 to the sample position is nominally 2.37 meters.

Banks of 5" x 5" scintillator type neutron detectors are placed at nominally 2.47 meters from the sample, at scattering angles of 20° and 90°. The detector faces are situated tangent to time-focusing loci[31] at the respective angles. Borax, borated water, B_4C, concrete and cadmium in various amounts shield the detectors from room returned neutrons.

The TMC 1024-channel time-of-flight analyzer is normally used to analyze four scattered intensities in 256-channel segments: sample scattering at 90° and 20°, and reference scattering (see below) at 90° and 20°. A homemade instrument, the "Quadapter"[32], routes detector signals into the appropriate memory segment after pulse shape discrimination against gamma-ray induced pulses.[33] A variable delay of from 1 to 2047 microseconds precedes the start of analysis after each rotor opening.

3.1.3. Vanadium Reference Method. Writing for the partial differential cross section

$$\frac{\partial^2\sigma}{\partial\Omega\partial\epsilon}(Q,\epsilon) \simeq \langle a^2\rangle S(Q_e)\,\delta(\epsilon) \qquad (3.7)$$

which we will call the "static approximation", Equation (3.3) becomes

$$C_T(t,\vartheta) = \eta(E)\, N \langle a^2 \rangle S(Q_e)\, F(E,\vartheta)\, S(E)\, \delta\left(t - \frac{L+L'}{v}\right)$$

(3.8)

For a similar measurement on an incoherent elastic reference scatterer, for which

$$\frac{\partial^2 \sigma^R}{\partial \Omega \partial \epsilon} \simeq \frac{\sigma_R}{4\pi} \delta(\epsilon)$$

we have

$$C^R(t,\vartheta) = \eta(E)\, N\, \frac{\sigma_R}{4\pi}\, F^R(E,\vartheta)\, S(E)\, \delta\left(t - \frac{L+L'}{v}\right)$$

(3.9)

Dividing (3.8) by (3.9),

$$\frac{C_T(t,\vartheta)}{C_T^R(t,\vartheta)} = \frac{N \langle a^2 \rangle S(Q_e)\, F(E,\vartheta)}{N_R\, \sigma_R/4\pi\, F^R(E,\vartheta)} \qquad (3.10)$$

Now if the properties of the reference scatterer are known and F^R can be calculated, $S(Q_e)F(E,\vartheta)$ can be extracted from (3.10), without knowledge of either the detector efficiency or the source intensity. Furthermore, if the measurements are made more or less simultaneously by alternating the sample and reference scatterers in the target position, any fluctuations in $\eta(E)$ or $S(E)$ on a time scale long compared to the target cycling time will average out in forming the ratio (3.10)

A useful reference scatterer is vanadium, whose coherent and incoherent cross sections are .03 and 5.13 barns[34] respectively, constant in energy to excellent approximation[35], and predominantly elastic.

The reference scatterer used in the present measurement was a V plate of dimensions 2"x4"x.125", with density N_R=.0720 atoms/b-cm. The sample and reference scatterers were alternated in the target position each 5 minutes; the total counting time at each of two rotor speeds was about two weeks.

3.2 Time of Flight Inelastic Scattering Spectroscopy

Returning to equation (3.1) we treat the case of a pulsed monochromatic neutron source: $I(t-\tau, E) = \phi(E_0)\,\delta(E-E_0)\,\delta(t-\tau)$

$$C_I(t,\vartheta) = \int_{E'=0}^{\infty} \eta(E')\, p(E_0, E', \vartheta)\, \phi(E_0)\, F(E_0, E', \vartheta) \cdot \delta\left(t - \frac{L}{v_0} - \frac{L'}{v'}\right) dE' \qquad (3.11)$$

If we displace the time origin by L/v_0 so that time is measured from the instant at which the burst reaches the target,

$$C_I(t,\vartheta) = \eta(E_1)\, p(E_0, E_1, \vartheta)\, \phi(E_0)\, F(E_0, E_1, \vartheta)\, m L'^2 t^{-3} \qquad (3.12)$$

with $E_1 = \frac{m}{2}\left(\frac{L'}{t-L/v_0}\right)^2$. Thus each time of arrival t is uniquely associated with a particular final energy. Furthermore, since

$$\epsilon = E_1 - E_0 = \frac{m}{2}\left(\frac{L'}{t-L/v_0}\right)^2 - E_0$$

and

$$Q^2 = \frac{2m}{\hbar^2}\left(E_0 + E_1 - 2\sqrt{E_0 E_1}\cos\vartheta\right)$$

each different combination of ϑ and t corresponds to a unique point in the (Q,ω) plane. The optimum way to perform such a measurement then, is to time analyze simultaneously the output of several detectors at different scattering angles; thereby measuring $S(Q,\omega)$ at a set of points (one for each time channel) along a locus such as that shown in figure 2. Loci for the present measurement are shown in figure 6. It is then a simple matter of interpolation between angles to arrive at $S(Q,\omega)$ at constant Q, probably the most generally useful presentation of scattering law data.

We pause to remark that the TOF spectrometer is most useful for cases in which $S(Q,\omega)$ information is desired at all Q and ω, since all this information is simultaneously gathered by the TOF instrument. This is in contrast to the constant -Q scans possible with triple-axis spectrometers, where the scan is limited to a small range of Q and ω of interest. For this reason the triple axis systems are more useful for phonon measurements in crystals where the positions of peaks are more important than the overall shape of $S(Q,\omega)$; conversely the TOF spectrometer is most useful in measurements on isotropic systems such as liquids and glasses.

3.2.1. Thermal Neutron Time of Flight Spectrometer (TNTOFS). The time-of-flight spectrometer (TNTOFS) at the Argonne National Laboratory CP-5 reactor has been fully

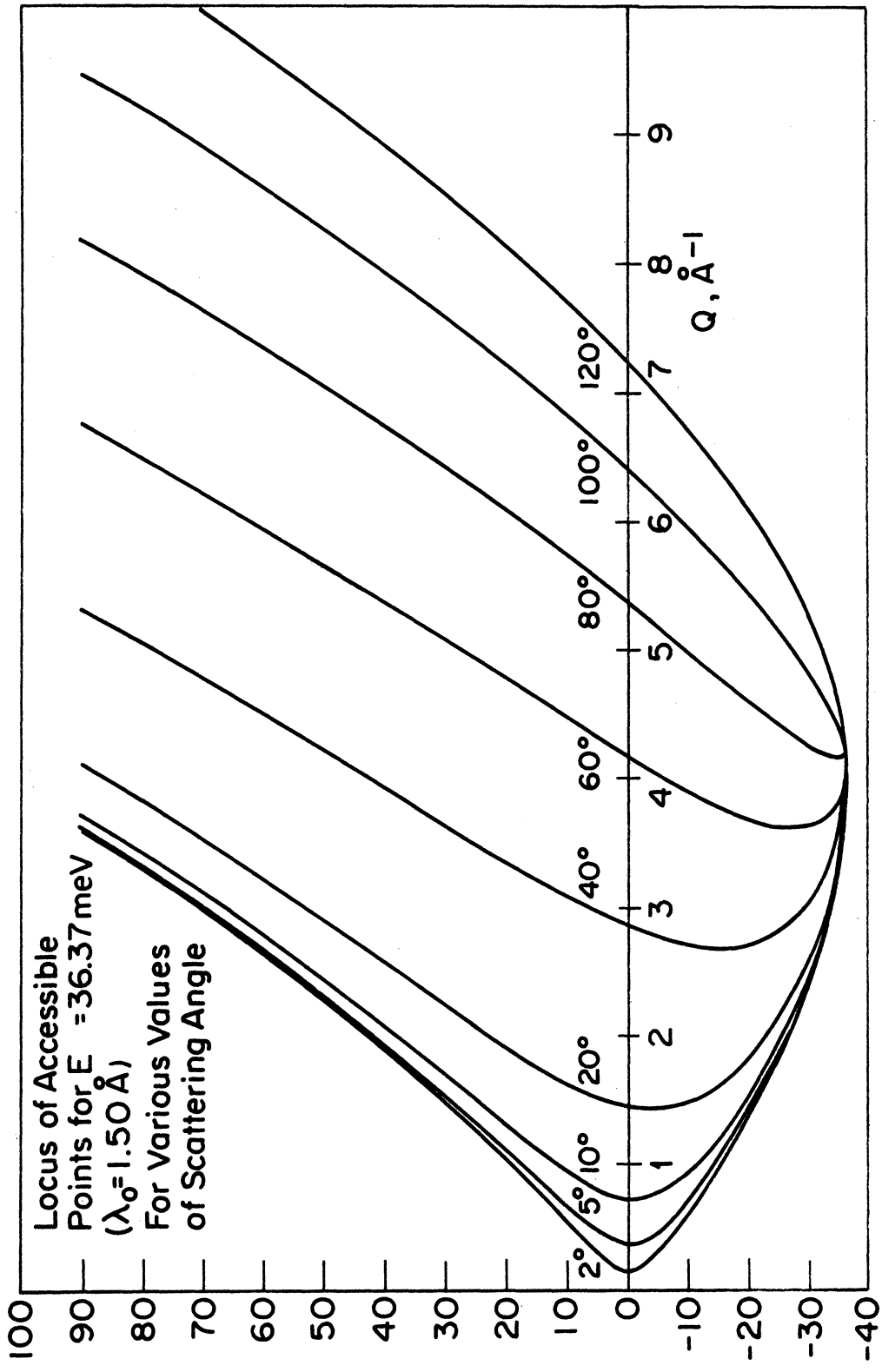

Figure 6. Integration Paths for the TNTOFS Experiment

described elsewhere.[36] We present only the briefest description here. A plan view of the TNTOFS is shown in figure 7.

A monochromatic component of the reactor neutron beam is selected by the double-crystal monochromator. Use of the double monochromator effectively eliminates gamma-ray and fast neutron contamination in the monochromated beam with their associated shielding and background problems, as well as allowing a more compact layout of the spectrometer with constant monochromator take-off angle. In the present experiment, copper crystals cut for (220) reflection were used to produce a monochromatic beam of nominal 1.5Å wavelength. The 1.5Å beam was filtered through 6" of MgO single crystals held at 77 K, to remove any short wavelength contamination. A 3" diameter Fermi chopper was used to pulse the beam at 18,320 pulses/minute.

Ninety-five 1" diameter He^3 proportional counters situated with axes vertical on an arc 2.5 meters from the target position were used to monitor the scattered intensity. These were divided into 31 subgroups each consisting of two, three or four adjacent detectors; the signal responses of all detectors in a given subgroup were analyzed as a unit. The grouping of detectors entails a relaxing of Q resolution due to increased angular spread vis à vis a single detector, with a concomitant increase in counting rate. Most of the detectors used had an active length of 18", with a few 9"

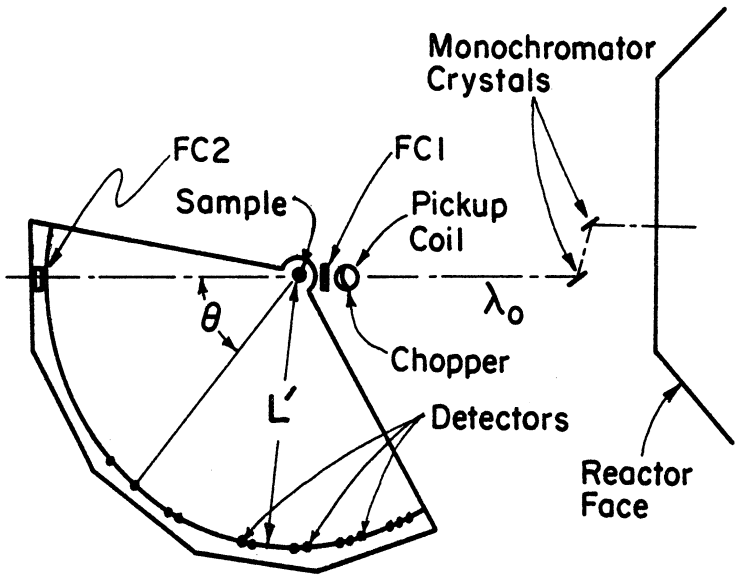

Figure 7. Plan View of the INTOFS

or 4½" long detectors at the smaller scattering angles to preserve Q resolution. The range of scattering angles monitored in the present experiment was $13.2° \leq \vartheta \leq 120°$.

The entire 4096 channel memory of the Nuclear Data 50/50 time of flight analyzer was utilized in a configuration of 32 subgroups of 128 channels each (the 32nd subgroup was used to analyze the signal of the two beam monitors.)

Vanadium was used as a reference scatterer in the TNTOFS measurement, but the details of the method used are quite different from that described above for the time of flight diffractometer. At TNTOFS a separate run was made with a thin V sample as target, and the calculated detector efficiency was adjusted for each subgroup to reproduce the theoretical value of the V elastic scattering in the data analysis. The adjusted detector efficiencies were then used in the analysis of the sample data. Such a procedure depends quite heavily on the detector efficiencies remaining constant throughout the V, sample and empty container runs; this may not be a particularly bad assumption in the case of the He^3 detectors, but the fission chamber beam monitors used to measure the integrated incident intensity for each run tended to vary quite a bit during these measurements. This is overcome to some extent by use of a supplementary monitor, a He^3 detector which measures scattering of the incident beam by the chopper. It is this peripheral monitor

and not the beam monitors per se which was taken in the present experiment to provide a measure of integrated beam intensity at the target position.

3.3. BeF_2 Sample

The vitreous BeF_2 was prepared by C. Bamberger of ORNL. It is in granular form, granule dimensions being typically 1-2 mm. Immediately on preparation the BeF_2 was placed into .25" O.D. aluminum tubes which were sealed at both ends with O-ringed plugs, crimped and filled with epoxy cement (see figure 8). Each of the 14 tubes contains 1 gram of BeF_2, filled with approximately 62% void fraction. The effective BeF_2 mass density averaged over the sample volume is 0.75 g/cm^3.

For use at the time of flight diffractometer, six tubes were arranged with axes vertical as shown in figure 9. The choice of 45° inclination between the beam and the target face is made on the basis of time focusing considerations for the 90° detector bank. The effective thickness of BeF_2 along the beam (averaged across the target) for this arrangement is 1.085 cm yielding an effective area density in the beam of .0104 BeF_2/b. It is worth pointing out that the choice of 45° rotation of the target with respect to the incident beam, which optimizes time focusing for 90° scattering in reflection geometry, results in suboptimal focusing at 20° and in fact causes the 20° scattering

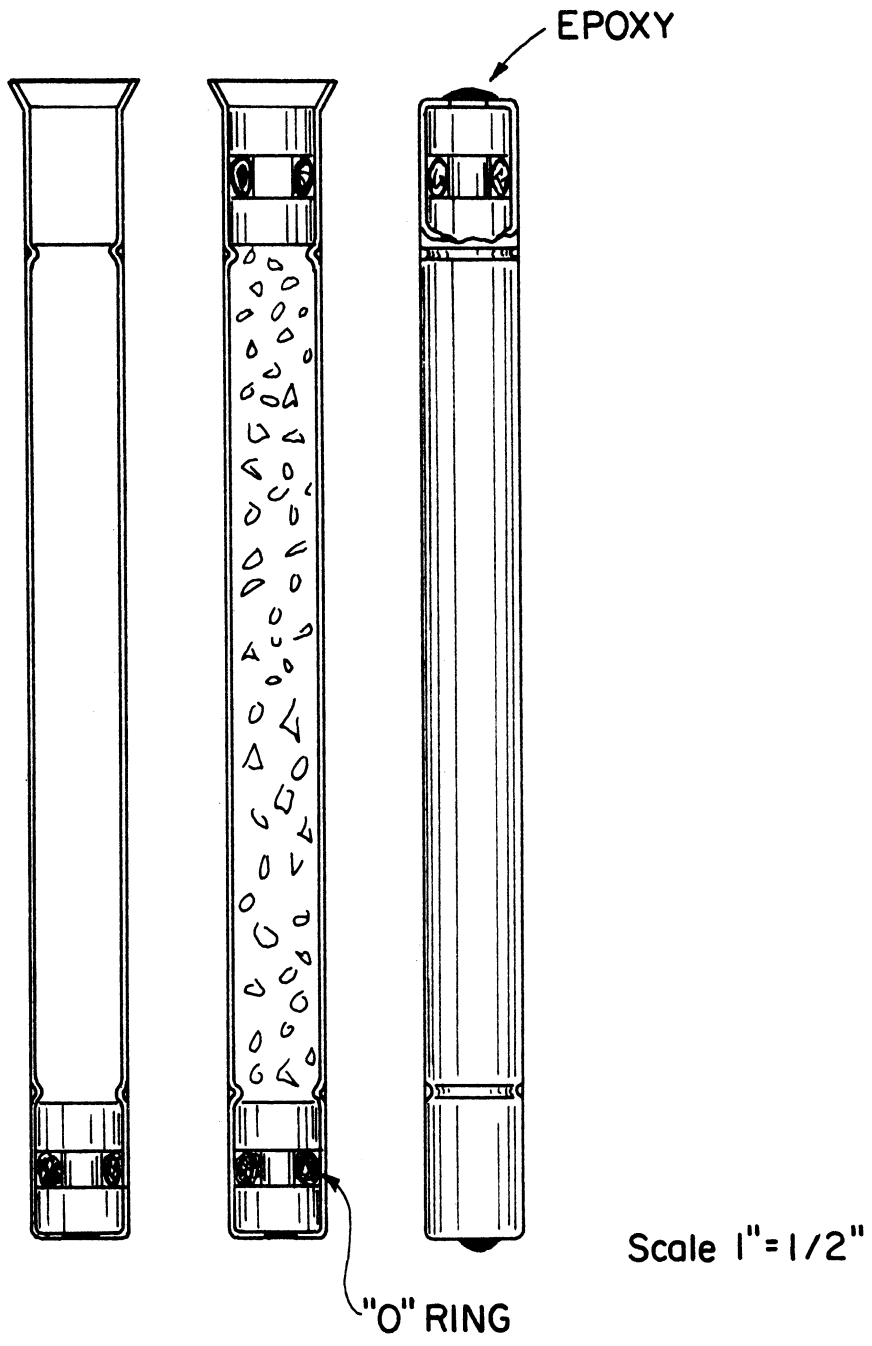

Figure 8. Encapsulation of the BeF_2 Granules.

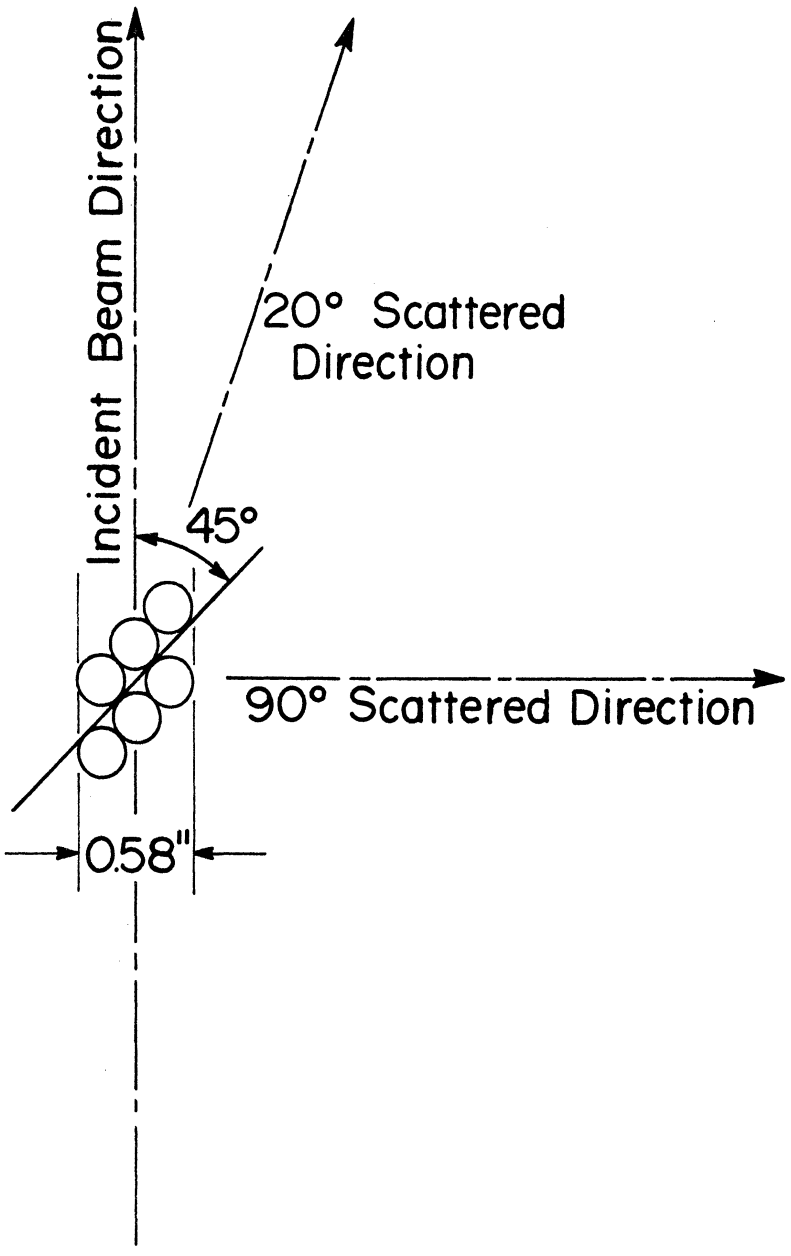

Figure 9. Target Arrangement for the Time-of-Flight Diffractometer

to be in transmission geometry. This introduces some complications into the calculation of the various geometric correction factors, but is deemed worthwhile solely on the basis of improvement in resolution at 90° . Making separate measurements at 90° and 20°, each with the target in the respective optimum focused geometry, was not considered a viable alternative; since the 20° bank measures at low Q where the resolution is adequate even in nonfocused geometry, the superior efficiency of making both measurements simultaneously was opted for.

For the TNTOFS measurement, all 14 sample tubes were assembled into a single layer with axes horizontal (figure 10).

Cadmium leaves .020" thick were placed between adjacent tubes to prevent intertube multiple scattering. This decoupling of the tubes not only reduces the severity of multiple scattering contributions, but also amkes the calculation of a multiple scattering correction somewhat simpler (see next chapter).

The single layer of tubes was placed in the TNTOFS beam with the sample face rotated 45° clockwise from the beam direction. As shown in figure 11, this resulted in transmission geometry at all scattering angles examined in this experiment. A cadmium mask with a 3.76" x .88" rectangular aperture placed normal to the beam direction, upstream from the target, was used to accurately define the beam

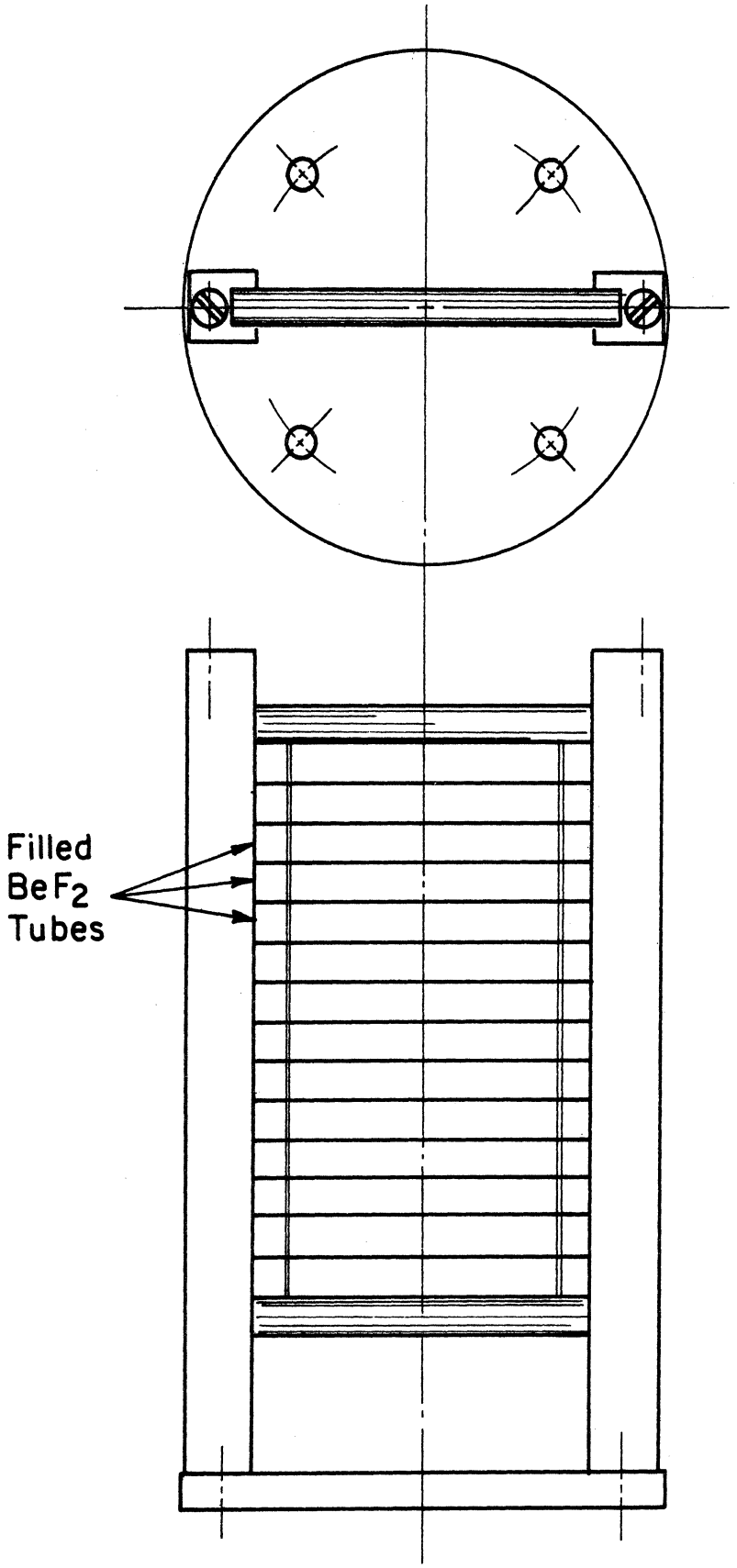

Figure 10. Target Arrangement for the TNTOFS

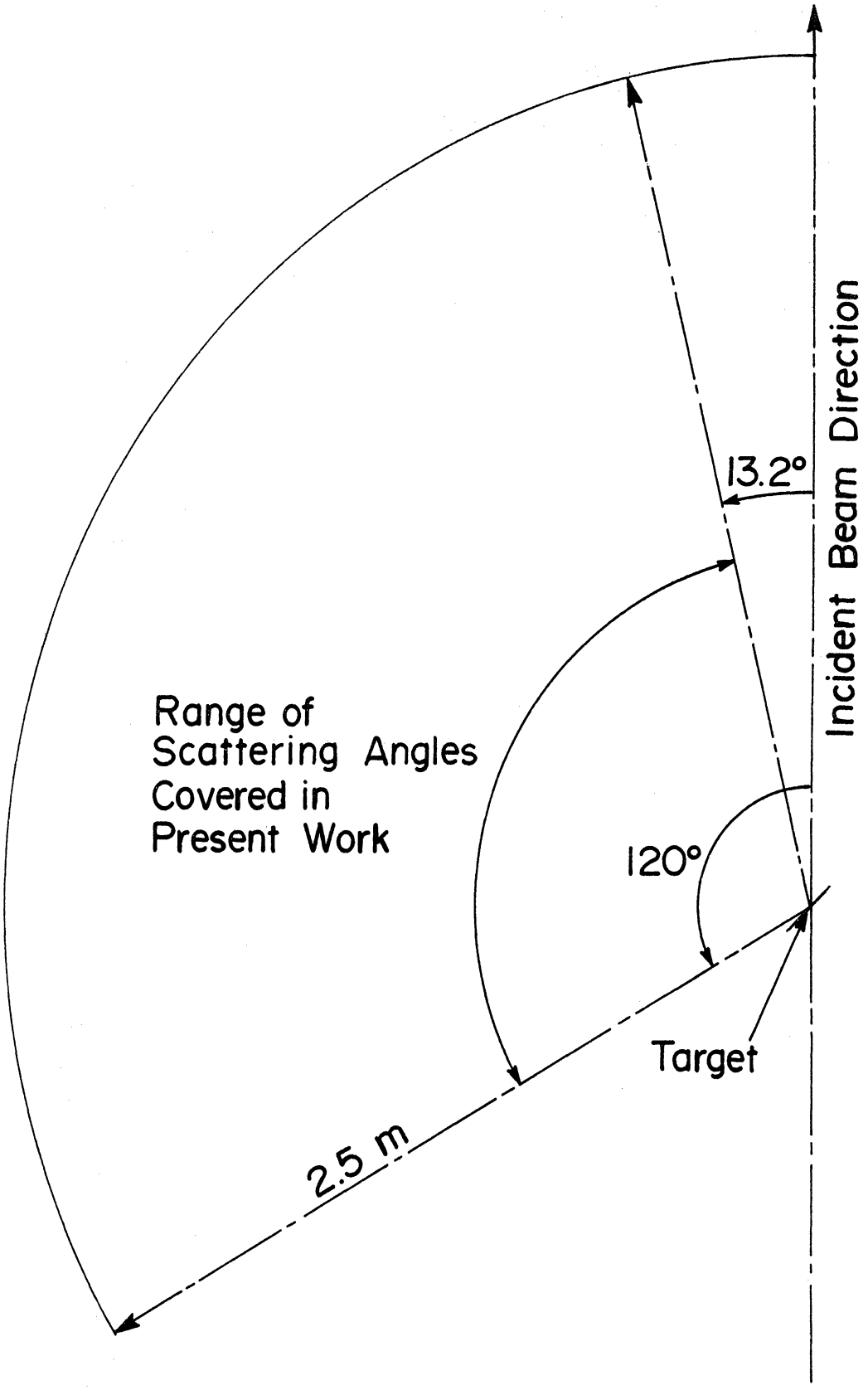

Figure 11. Geometry of the TNTOFS Experiment

area. The same mask was used in the V reference scatterer normalization run. Effective thickness of the filled region of the target for this configuration is $\pi r/2\sin\beta$; r the inside radius of a tube and β the rotation angle away from the beam direction. For the present case, this is .634 cm. The sample area density in the beam for this configuration is .6077 BeF_2/b.

CHAPTER FOUR

CALCULATION OF THE STRUCTURE FACTOR FROM DIFFRACTION DATA

4.1 Introduction

In the discussion of the V reference method in Chapter Three, we asserted that by forming the ratio of sample to reference scattering we could get at the sample structure factor:

$$\frac{C^S(t,\theta)}{C^R(t,\theta)} = \frac{N\langle a^2\rangle S(Q_e)\, F(E,\theta)}{N_R\, \sigma_R/4\pi\, F^R(E,\theta)} \tag{4.1}$$

In this chapter we will deal with two problems: first, to move from raw data to the sample and reference scattering intensities C^S and C^R; and second, to calculate the factors $F(E,\theta)$ and $F^R(E,\theta)$, and thereby become able to extract $S(Q_e)$ from (4.1).

Before beginning a detailed description of the data reduction manipulations, we briefly outline the entire procedure. It is summarized in the following steps:

(1) Remove the background contribution from both sample and vanadium raw data.

(2) Form the ratio of sample to vanadium counting rates.

(3) Make a preliminary removal of the container contribution from the sample scattering.

(4) Estimate the sample scattering cross section, and utilize it in effecting a final removal of container scattering.

(5) Compute the factor F^R to correct the intensity ratio.

(6) Compute an improved scattering cross section estimate and differential cross section.

(7) Compute the factor F and correct the differential cross section estimate for multiple scattering.

(8) Iterate if necessary, steps (6) and (7).

The factors $F(E,\vartheta)$ and $F^R(E,\vartheta)$ will be called "multiple scattering corrections." We take this term to mean the following - suppose we have an infinitesimally thin slab sample, such that the incident beam has no chance of being attenuated before scattering, and the scattered neutrons have no chance of interacting after scattering. Then we will see scattering proportional to $\rho t \langle a^2 \rangle S(Q)$, which we call P_I, the probability of scattering for an "ideally behaved" sample (ρ is the number density and t the thickness of the sample). In this ideal case we detect only once-scattered neutrons. If the target is somewhat thicker, the sample is not uniformly illuminated due to the attenuation of the incident beam by scattering; the front of the target "shadows" the back. Furthermore, once-scattered neutrons heading for a detector may interact (i.e. be scattered or absorbed) with the sample and be removed from the scattered beam. These two effects taken together reduce the once-scattered intensity seen at the detector, and are simply termed "attenuation." We may define an "attenuation correction" $F_A(E,\vartheta)=P_1(E,\vartheta)/P_I(E,\vartheta)$ where $P_1(E,\vartheta)$ is the probability of observing once-scat-

tered neutrons for the thick target. It is obvious, however, that we cannot have attenuation effects going on without also having some probability of a twice-scattered, thrice-scattered, etc., neutron happening along into the detector (except possibly for strongly absorbing sample materials). We can define a hierarchy of probabilities of single scattering, double scattering, etc. resulting in our detection of a scattered neutron:

$$P_T = P_1 + P_2 + \cdots = P_1 + P_M$$
$$= P_I F_A (1 + P_1^{-1} P_M)$$
$$= P_I F$$

One may choose to call $F_A = P_I^{-1} P_1$ an "attenuation correction" and $1 + P_1^{-1} P_M$ a "multiple scattering correction", which is applied to make up for the inadequacy of the "attenuation correction." This is no more than an exercise in algebra and reflects the fact that one must really know $F = P_I^{-1} P_T$ to get at the interpretable quantity P_I from the observed quantity P_T. In point of fact F_A is generally quite simple to calculate while $1 + P_1^{-1} P_M$ is generally quite difficult. We will utilize a Monte Carlo approach to compute P_I, P_1, P_M and hence F; and we will refer to F as a multiple scattering correction.

4.2 Calibration of the Diffractometer

Before proceeding with the data analysis, it is useful

to establish a calibration of the instrument in terms of Q vs. observed time of arrival. This must be done for each different rotor speed used to accumulate data. We define an overall timing error, t_{err}, by the following relation between observed time of arrival and actual time of flight from rotor to detector for channel n:

$$t = (n - 1.5)\Delta t + t_{del} + t_{err} = t_{obs} + t_{err} \qquad (4.3)$$

with t the true time of flight, n the observed channel number, Δt the channel width, t_{del} the preset delay between rotor opening and analyzer start signal and t_{err} the overall timing error. The fixed contribution of $-1.5\ \Delta t$ is due to the fact that the time analyzer requires some time to store a count presented at its signal input; thus a count stored in channel n actually arrived in the interval $(n-1.5)\ \Delta t \pm \frac{1}{2}\Delta t$. We allow t_{err} to absorb all the possible sources of timing errors, principally misalignment of the "rotor open" signal device and delays introduced by the detector electronics.

In order to establish a calibration, we take advantage of the fact that the diffraction pattern of a powder or polycrystal consists of sharp Bragg peaks at well-defined values of Q. Using the Bragg law $n\lambda = 2d \sin \vartheta/2$ for lattice planes with spacing d, and the flight time for neutrons of wavelength λ over a path of length L+L',

$$t(\lambda) = (L+L')/v(\lambda) = \frac{m}{h}(L+L')\lambda$$

$$t_{hkl} = \frac{m}{h}(L+L')\,2d_{hkl}\sin\vartheta/2 = \frac{m}{h}(L+L')\lambda_{hkl} \qquad (4.4)$$

for Bragg scattering from planes (hkl). If a polycrystalline sample produces Bragg peaks in channels n_i which can be identified as due to Bragg planes (hkl), one has then combining (4.4) with (4.3),

$$\frac{m}{h}(L+L')\lambda_{hkl} = (n_i - 1.5)\Delta t + t_{del} + t_{err} = t_{hkl} + t_{err} \qquad (4.5)$$

The adjustable parameters in this relation are $(L+L')\sin\vartheta/2$ and t_{err}. If the indexing of Bragg peaks has been done correctly, all the points (t_{hkl}, λ_{hkl}) should lie on a straight line whose slope and intercept at $\lambda = 0$ fix the adjustable parameters $(L+L')\sin\vartheta/2$ and t_{err}, respectively. In practice we assume a value for ϑ, which fixes the λ associated with each plane. Only the path length L+L' is treated as unknown. For example, the Bragg peaks from the aluminum container seen superimposed on the 90° BeF_2 data of figure 12 can be indexed as shown*, and the resulting λ vs. t plot (figure 13) yields $t_{err} = -t(\lambda=0) = 44\ \mu$sec and $L+L' = \frac{h\Delta t}{m\Delta\lambda} = 4.90$ meters. The accuracy of our estimate for ϑ is irrelevant in determining Q(t) since $Q = 2\pi/d$ and the calibration of d vs. t is independent of our chosen ϑ.

*Information on aluminum Bragg scattering is presented in table 4.

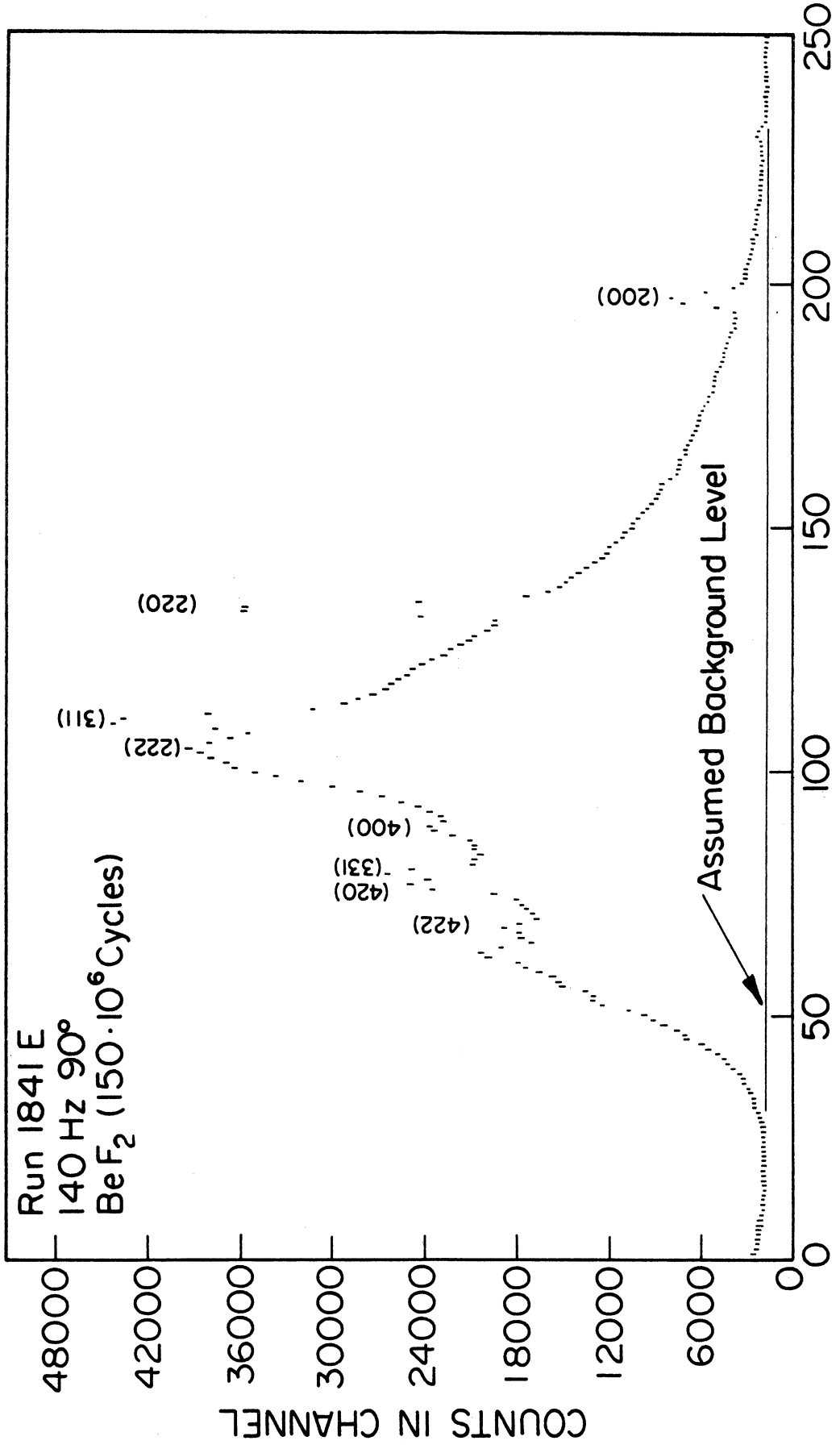

Figure 12. Vitreous BeF_2 Diffraction Data

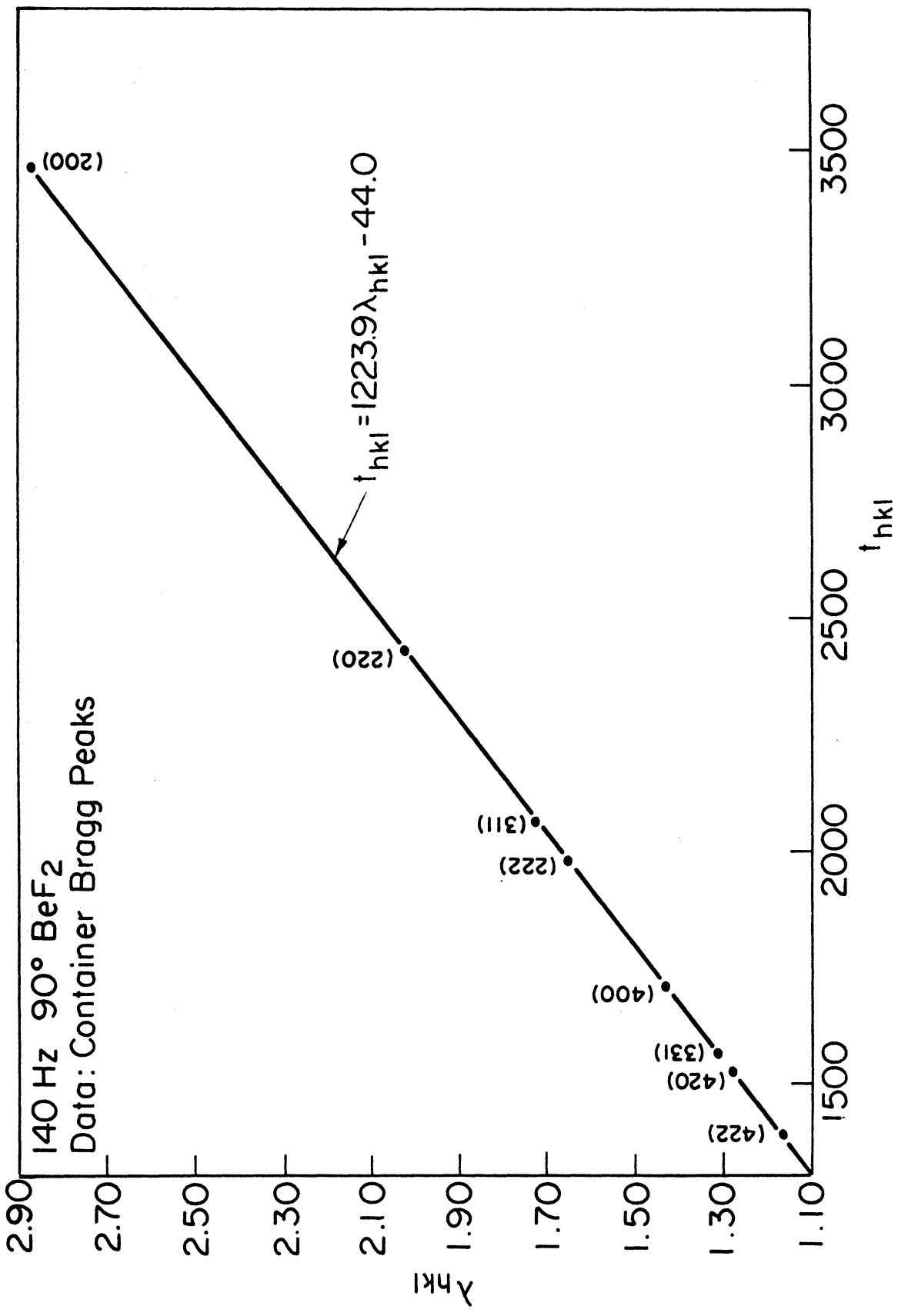

Figure 13. Calibration of the diffractometer

TABLE 4. Bragg Scattering by Aluminum

Plane	Multiplicity	d(Å)	Q(Å^{-1})
111	4	2.33803	2.68738
200	3	2.02479	3.10313
220	6	1.43174	4.38849
311	12	1.22099	5.14597
222	4	1.16901	5.37479
400	3	1.01240	6.20622
331	12	0.92904	6.76299
420	12	0.90551	6.93883
422	12	0.82662	7.60105
333	4	0.77934	8.06218
511	12		
440	6	0.71587	8.77698
531	24	0.68450	9.17923
442	12	0.67493	9.30938
600	3		
620	12	0.64029	9.81302
533	12	0.61756	10.17420
622	12	0.61050	10.29186
444	4	0.58471	10.74581
551	12	0.56705	11.08047
711	12		
640	12	0.56158	11.18840
642	24	0.54115	11.61079
553	12	0.52721	11.91779
731	24		
800	3	0.50620	12.41245
733	12	0.49473	12.70022

Each scattering angle of course gives its own value for $(L+L')\sin\vartheta/2$, but t_{err} should be the same for both angles since only minor electronic delays differ between the two.

4.3 Background Removal and Reduction to Intensity Referred to Vanadium

4.3.1. Procedure. One has two options regarding the determination background: measure it separately (i.e. with no sample in the beam) or obtain it from the data. We have chosen the latter alternative. In a typical set of raw data such as that shown in figure 12, one sees a broad central peak due to sample scattering, superimposed on a background intensity which can be approximately represented by a straight line in the region where sample scattering is appreciable. If one arranges the analyzer channel width and scattering delay to ensure that a region of no sample scattering is observed both earlier and later than the central peak, a line can be fitted to those regions and subtracted as background. This is shown in figure 12. The same method of background subtraction may be applied to the V data.

A program, DATRED, written to perform the first data reduction steps, does the following:

a. Read in various parameters including analysis timing information, calibration parameters, duration of runs, etc.

b. Read in sample, V and (optionally) background data

c. If specified, fit and subtract a linear background contribution from sample and V data

d. Perform a 5-point weighted smoothing of the V data

e. Compute point-by-point the ratio of sample to V scattering, and the associated statistical error.

4.3.2. Coherent Scattering from Vanadium. At this point in the analysis a totally unexpected problem was detected. Several distinctly unphysical features in the intensity ratios (see e.g. figure 14) prompted a reexamination of the raw data and were traced to the apparently unphysical features shown in figure 15. These sharp peaks in the V scattering were, however, identified as Bragg reflections from that almost totally incoherent scatterer. Recall that V has a coherent cross section of .03 barns compared to 5.13 barns incoherent; the small coherent contribution is manifested in figure 15. Peaks were observed to values of Q corresponding to the (110),(200), (222) and (211) reflections in V.* Since they are rather small and narrow, it was a simple matter to interpolate the incoherent scattering under them.

4.4. Matching and Interpolation of Individual Data Sets

*Information on vanadium Bragg scattering is summarized in table 5.

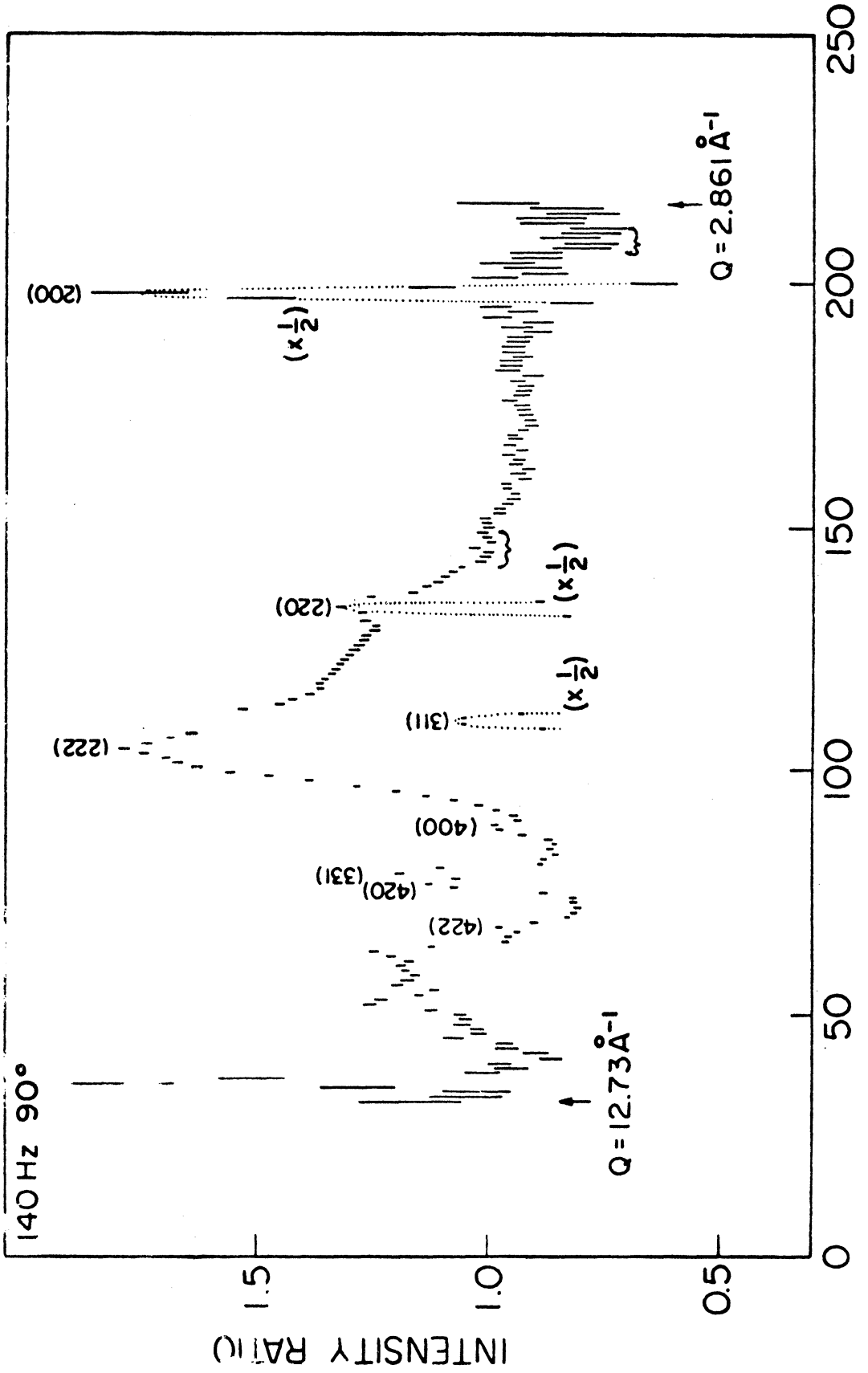

Figure 14. Intensity Ratio Showing Errors from V Bragg Peaks

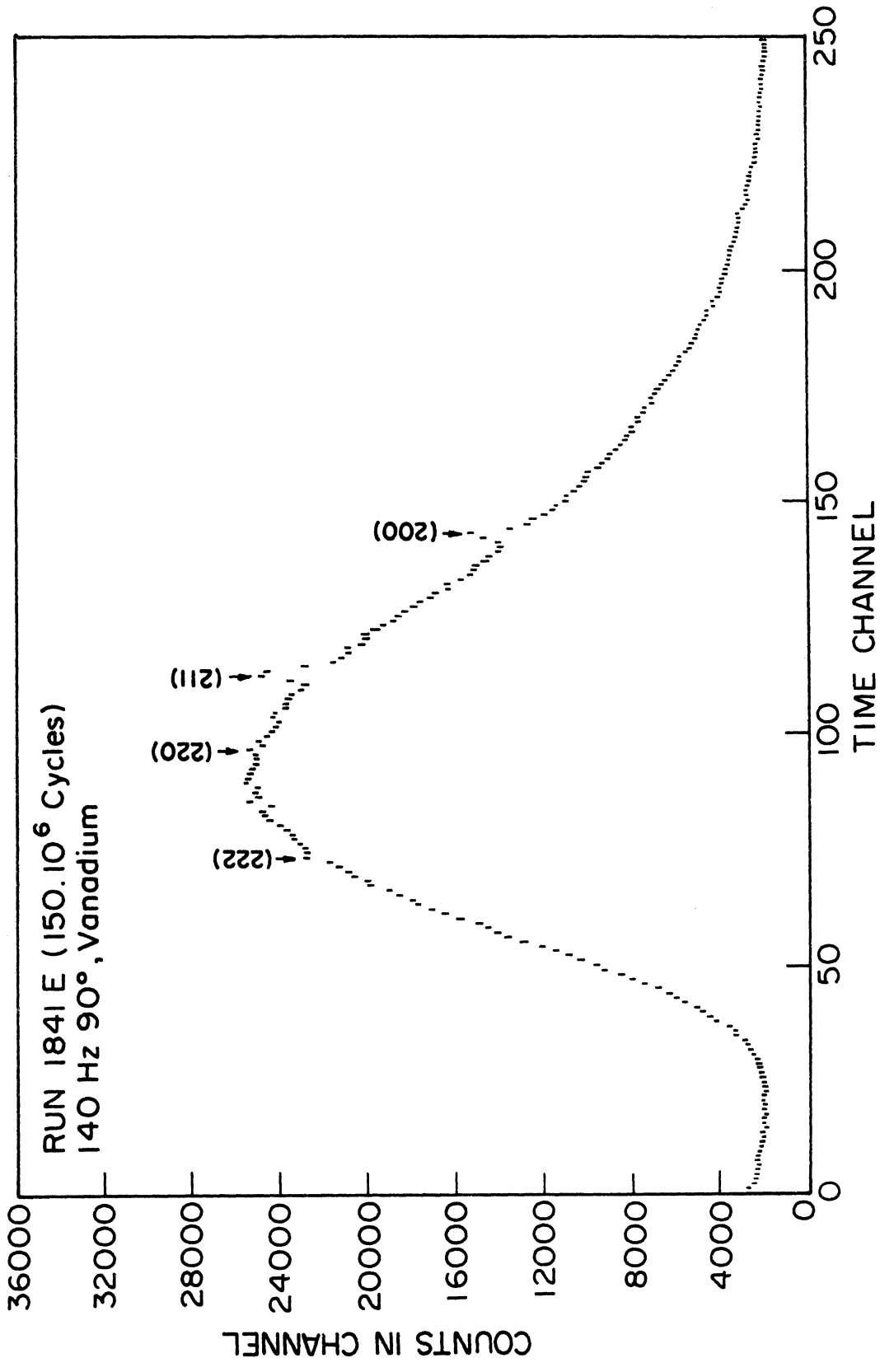

Figure 15. Vanadium Diffraction Data with Bragg Peaks

TABLE 5. Bragg Scattering by Vanadium

Plane	Multiplicity	d(Å)	Q(Å^{-1})
110	12	2.138	2.938
200	6	1.512	4.156
211	24	1.235	5.089
220	12	1.069	5.877
310	24	.956	6.570
222	8	.873	7.198
321	48	.839	7.492
400	6	.756	8.311
330	12	.713	8.815
420	24	.676	9.292
332	24	.645	9.746
422	24	.617	10.179
431	48	.593	10.595
501	24		
521	48	.552	11.380
440	12	.535	11.753
530	24	.519	12.115
433	24		
422	24	.504	12.467
600	6		

There are several purposes for which the entire experimental structure factor is needed. The actual data are in the form of four sets, each measured with a different combination of rotor speed and scattering angle, and each extending only over a limited Q range. Furthermore the data are tabulated on an equally spaced time-of-arrival mesh, which transforms to an unequally spaced Q mesh. It is then necessary to patch the several data sets together and sometimes to interpolate onto an equally spaced Q mesh; calculated corrections are applied to the individual data sets since most corrections are scattering angle dependent.

The range over which each data set proves useful is determined by statistical accuracy. We have chosen the criterion in establishing ranges for use of each data set, that fractional statistical error (as calculated by DATRED, and which is unchanged by VANCOR but affected by container scattering removal and also by the multiple scattering correction) be everywhere minimized. As seen from plots of raw data or intensity ratios (figures 16-19) the statistical error is smallest in the middle portion of a data set and smoothly worsens toward either end. This makes application of the above criterion quite simple. The ranges of Q covered by the present four runs are established by the minimum error criterion to be: 140 Hz at 20°, $0.9\text{Å}^{-1} \leq Q \leq 2.42\text{Å}^{-1}$; 480 Hz at 20°, $2.45\text{Å}^{-1} \leq Q \leq 2.95\text{Å}^{-1}$; 140 Hz at 90°, $2.98\text{Å}^{-1} \leq Q \leq 9.0\text{Å}^{-1}$; 480 Hz at 90°, $9.05\text{Å}^{-1} \leq Q \leq 27.\text{Å}^{-1}$. The overall

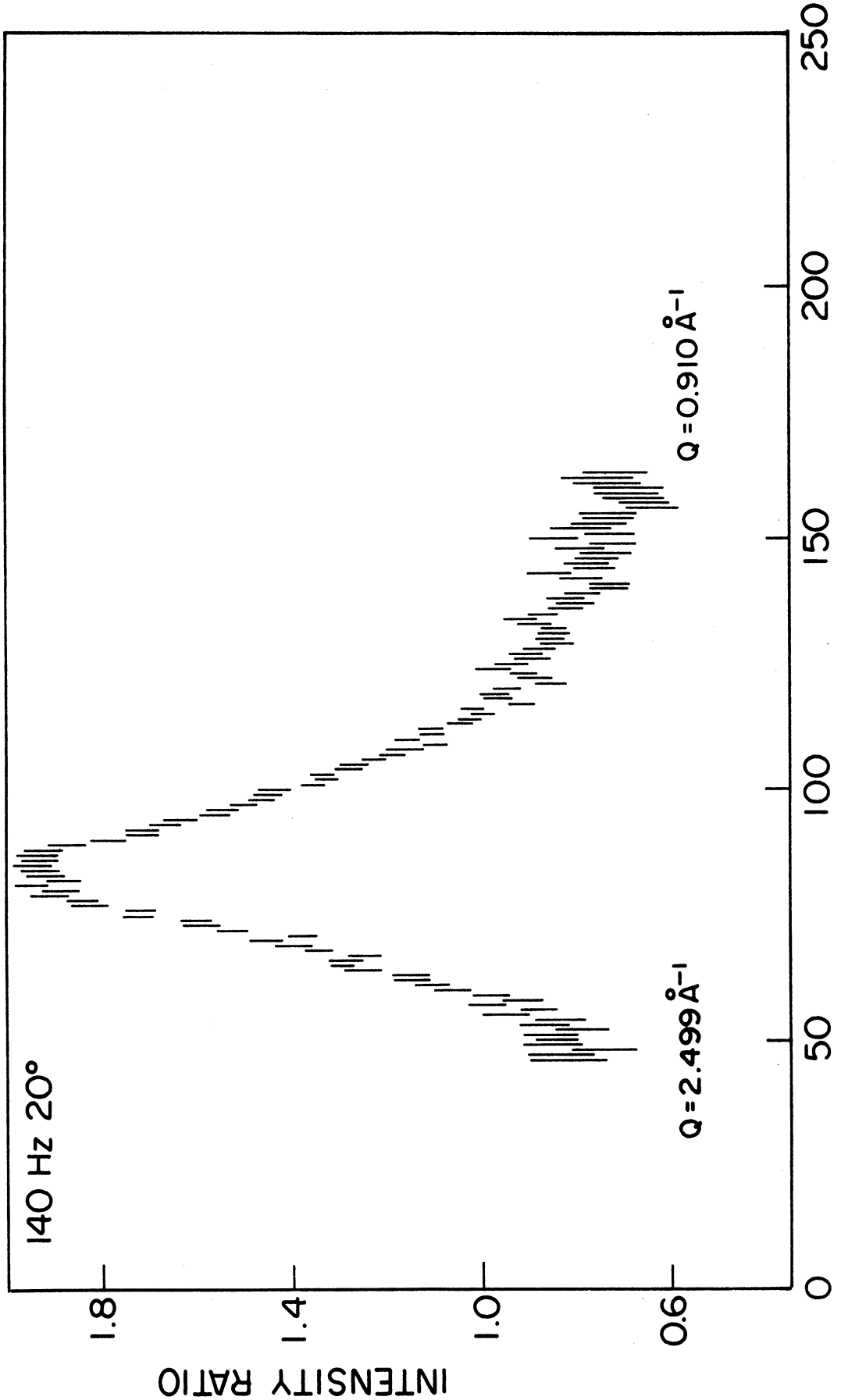

Figure 16. Intensity Ratio from 140 Hz 20° Data

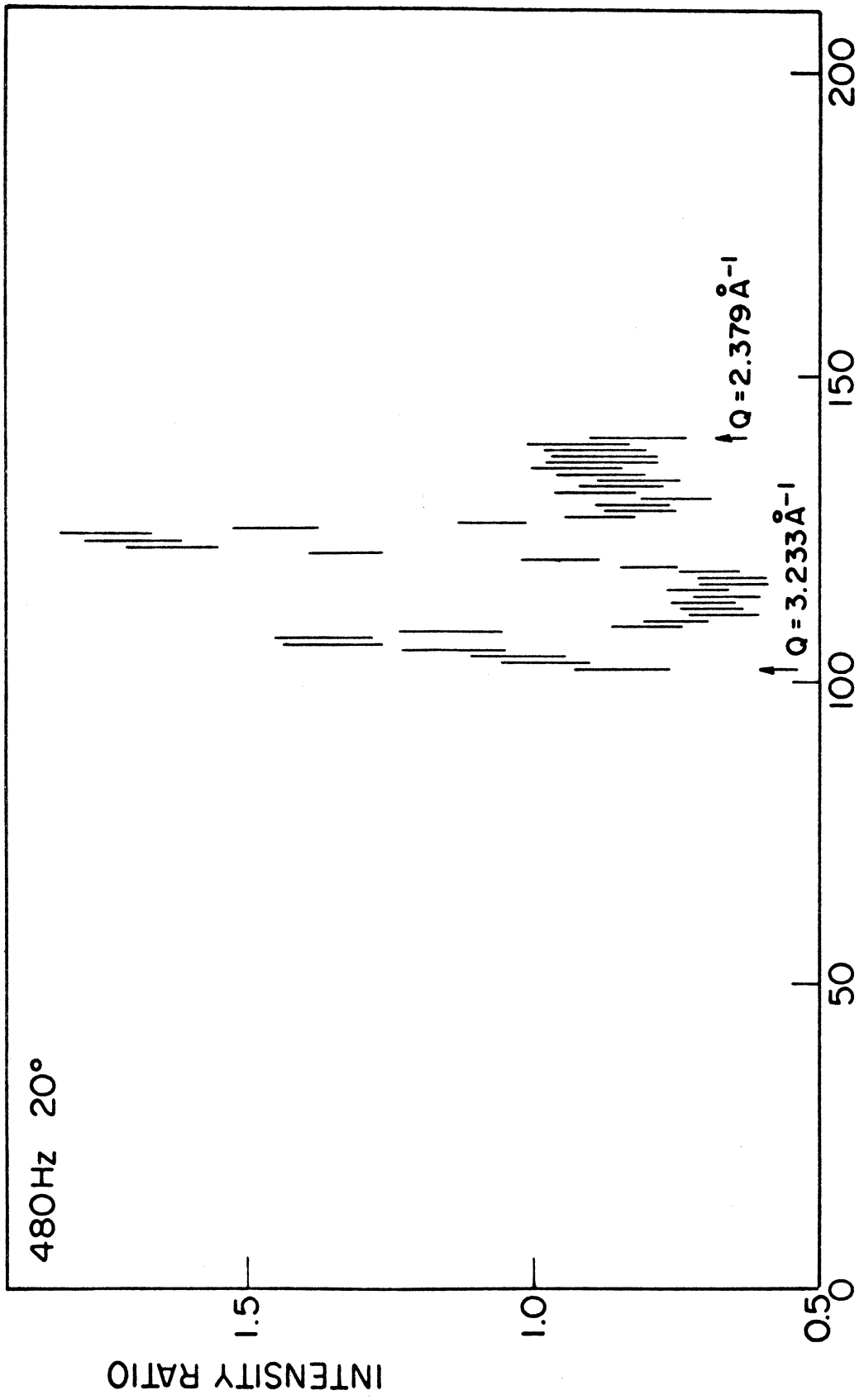

Figure 17. Intensity Ratio from 480 Hz 20° Data

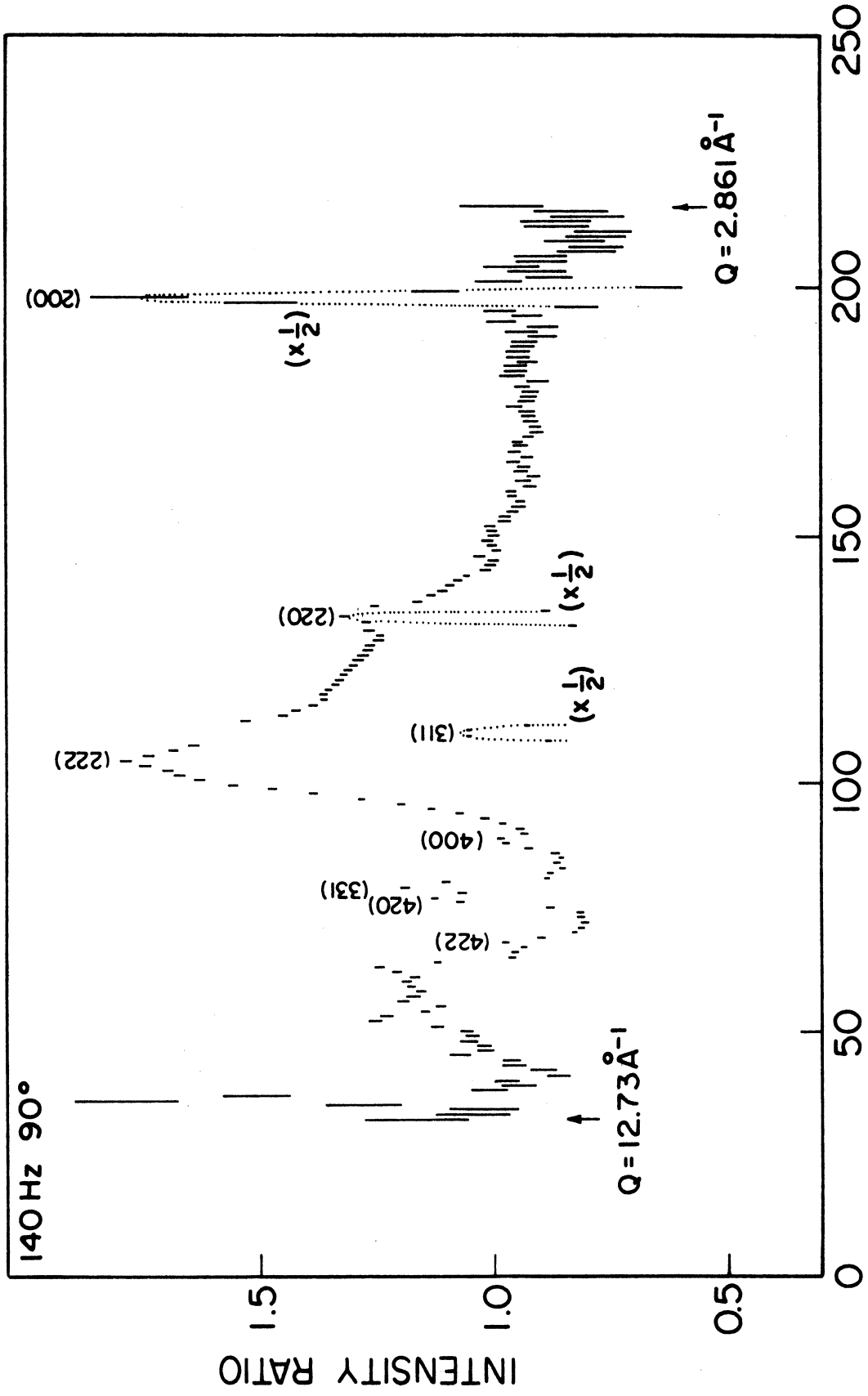

Figure 18. Intensity Ratio from 140 Hz 90° Data

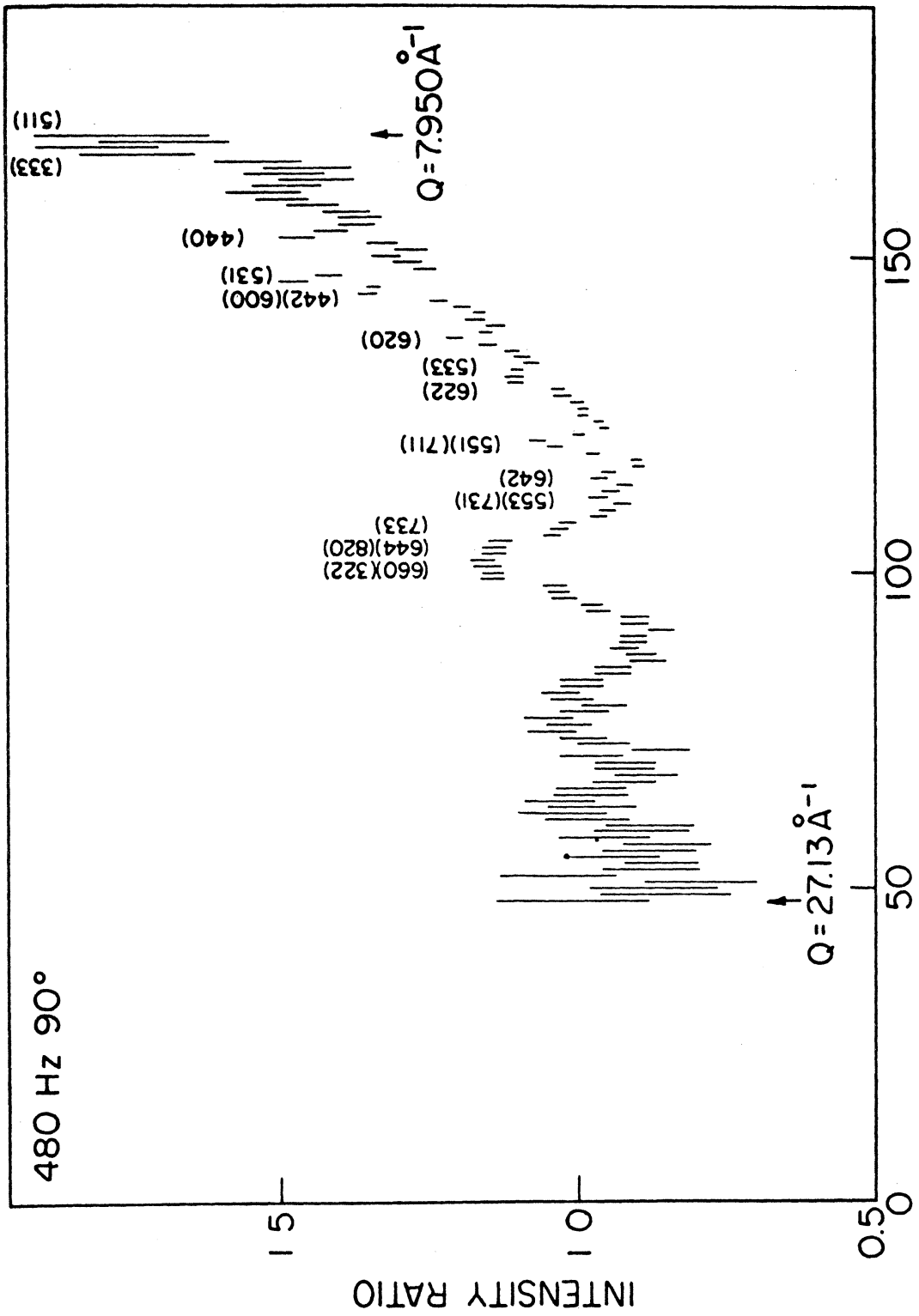

Figure 19. Intensity Ratio from 470 90° Data

upper and lower limits of 0.9Å^{-1} and 27Å^{-1} are chosen so that no data are used with fractional statistical error of more than 10% in the count from an individual time channel.

Having chosen the range for each data set there may or may not be a mismatch between any two data sets at a joining point. For intermediate steps in the data reduction process, we eliminate mismatches by scaling the individual data sets with respect to each other; the fully corrected data will be expected to match acceptably well without scaling. To interpolate onto an equally spaced Q mesh, we use a cubic spline smoothing polynomial computed by a program obtained from Argonne's Applied Mathematics Division.[37] This polynomial can optionally smooth the data, taking into account their statistical uncertainty; we smooth to a limited extent in some instances, not at all in others. A typical smoothing spline through part of the 140 Hz 20° data is shown in figure 20; note particularly its inability to adequately fit the peak region. This failure is most bothersome in the small Q region where peaks are relatively sharp; we overcome it by hand interpolation in the peak regions.

4.5 Normalization of Diffraction Data

The problem of normalizing the diffraction data may be treated in several ways. In doing the measurement by a V reference method we expect that the data will be correctly normalized with respect to the V incoherent scattering cross

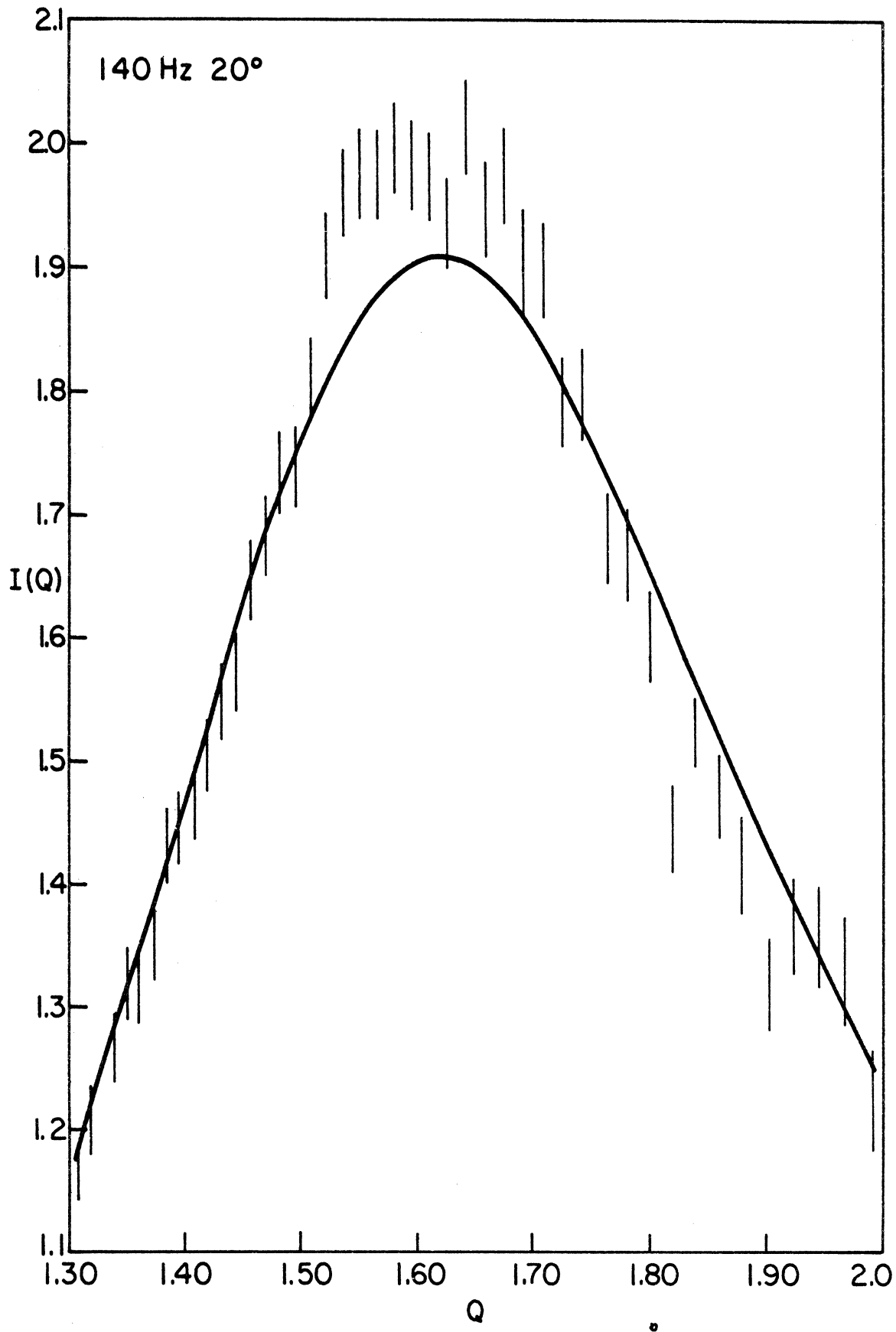

Figure 20. Smoothing spline fit to 140 Hz 20° data.

section. However, various sources of error may cause the data to be improperly normalized. We can check on the shape of the measured structure factor (but not its magnitude) by applying one of several integral normalization conditions derived from the relation between structure factor and radial density function:

$$4\pi r(\bar{g}(r)-g_0) = \frac{2}{\pi}\int_0^\infty Q\,i(Q)\sin Qr\,dQ \tag{4.6}$$

First, note that for small r the function $\bar{g}(r)$ must be zero since no two nuclei can approach each other closer than a fixed distance of order several Angstroms due to interatomic repulsion. For very small r, we also approximate sin Qr by Qr and so

$$-4\pi r g_0 = \frac{2}{\pi}\int_0^\infty Q\,i(Q)\,Qr\,dQ \tag{4.7}$$

or

$$-2\pi^2 g_0 = \int_0^\infty Q^2 i(Q)\,dQ \tag{4.8}$$

This relation was noted by Krogh-Moe.[38] Since i(Q)=S(Q)-1 which is calculated from the observed intensity I(Q) by

$$i(Q) \simeq [I(Q) - I(\infty)]/I(\infty) \tag{4.9}$$

this normalization procedure can only help us to choose an appropriate $I(\infty)$, and not to scale the entire structure factor. Hence the statement above, that such normalizations

are sensitive only to the shape of the structure factor. We have made use of the Krogh-Moe normalization by adjusting the upper Q limit of data used so that equation (4.8) reproduces the known value of g_o, which is

$$g_o = \rho_u \left[\sum_{uc} a_i\right]^2 \Big/ \sum_{uc} a_i^2 \tag{4.10}$$

with ρ_u the unit cell number density. For BeF_2 at 1.96 g/cm^3 mass density, g_o=.0736/Å^3. An upper limit of 26.8Å^{-1} for the data of figure 26 reproduces this value via equation (4.8) and yields a value of $I(\infty) = I(26.8Å^{-1})$=1.085 b/ster/$BeF_2$. This does not compare well with the expected value of $\langle a^2 \rangle$ =1.238 b/ster/BeF_2, about which more later.

Another normalization condition due to Rahman[39] is obtained from (4.6) by a further sine transform over a small region:

$$\int_0^R 4\pi r(\bar{g}(r)-g_o)\sin\mu r\,dr = \int_0^R \left\{\frac{2}{\pi}\int_0^\infty Qi(Q)\sin Qr\,dQ\right\}\sin\mu r\,dr \tag{4.11}$$

if R is less than the first neighbor distance,

$$-\int_0^R 4\pi r g_o \sin\mu r\,dr = \int_0^R \left\{\frac{2}{\pi}\int_0^\infty Qi(Q)\sin Qr\,dQ\right\}\sin\mu r\,dr \tag{4.12}$$

$$-4\pi g_o \mu^{-2}[\sin\mu R - \mu R\cos\mu R] = \frac{2}{\pi}\int_0^\infty Qi(Q)\int_0^R \sin Qr\sin\mu r\,dr\,dQ \tag{4.13}$$

$$4\pi^2 R g_o\, j_1(\mu R) = \int_0^\infty Qi(Q)\left\{j_0[(Q-\mu)R] - j_0[(Q+\mu)R]\right\}dQ \tag{4.14}$$

where $j_1(\mu R)=(\mu R)^{-2}(\mu R \cos \mu R-\sin \mu R)$ is the first-order spherical Bessel function.

For any value of R less than the first neighbor distance, we must have the right side of equation (4.14) which depends on the diffraction pattern of the substance under consideration, equal (as a function of μ) to the left side which is simply a multiple of the fixed function $j_1(\mu R)$. The transform of Qi(Q) defined by equation (4.14) must have the same j_1 shape for every isotropic substance provided only that R is smaller than any internuclear distance. It is interesting to note that one can derive any number of normalization conditions similar to (4.14) by multiplying both sides of (4.6) by some function of r and integrating over a range $0 \leq r \leq R$. The simplest of all is obtained by integrating (4.6) as it stands:

$$-\int_0^R 4\pi r g_0 \, dr = \frac{2}{\pi}\int_0^R \int_0^\infty Q i(Q) \sin Qr \, dQ \, dr \tag{4.15}$$

$$(\pi R)^2 g_0 = \int_0^\infty i(Q)\left[1-\cos QR\right] dQ \tag{4.16}$$

Furthermore, all these integral normalizations reduce to the Krogh-Moe condition for very small R: witness the Rahman condition:

$$\lim_{R\to 0}\left\{-\int_0^R 4\pi r g_0 \sin \mu r \, dr\right\} = \lim_{R\to 0}\left\{\int_0^R \frac{2}{\pi}\int_0^\infty Q i(Q) \sin Qr \sin \mu r \, dQ \, dr\right\}$$

$$\lim_{R\to 0}\left\{-\int_0^R 4\pi r g_0 \mu r\, dr\right\} = \lim_{R\to 0}\left\{\int_0^R \frac{2}{\pi}\int_0^\infty Q i(Q) Q r \mu r\, dQ\, dr\right\}$$

$$\lim_{R\to 0}\left\{-4\pi g_0 \int_0^R \mu r^2 dr\right\} = \lim_{R\to 0}\left\{\frac{2}{\pi}\int_0^\infty Q^2 i(Q)\, dQ \int_0^R \mu r^2 dr\right\}$$

$$-2\pi^2 g_0 = \int_0^\infty Q^2 i(Q)\, dQ$$

or the simple condition (4.16),

$$\lim_{R\to 0}(\pi R)^2 g_0 = \lim_{R\to 0}\int_0^\infty i(Q)[1-\cos QR]\, dQ$$

$$\lim_{R\to 0}\pi^2 g_0 R^2 = \lim_{R\to 0}\int_0^\infty i(Q)\left[\frac{-(QR)^2}{2!}\right] dQ$$

$$-2\pi^2 g_0 = \int_0^\infty Q^2 i(Q)\, dQ$$

Obviously, there is much information in the various normalization conditions. The interpretation of a plot of both sides of (4.14), for instance, for some value of R as a function of μ (see figure 21) is not clear, which diminishes somewhat the practical utility of such conditions. They are quite useful in comparing data from different measurements on the same substance (as in the original paper of Rahman), but one is hard pressed to decide what data changes would improve the none-too-satisfying agreement of figure 21. Indeed, since the left side of (4.14) has the same shape for every substance, one can obviously modify i(Q) to a form which bears no relation to the structure factor of the substance under study, but which satisfies (4.14) as well as, or better than, one's experimental i(Q). We have thus not

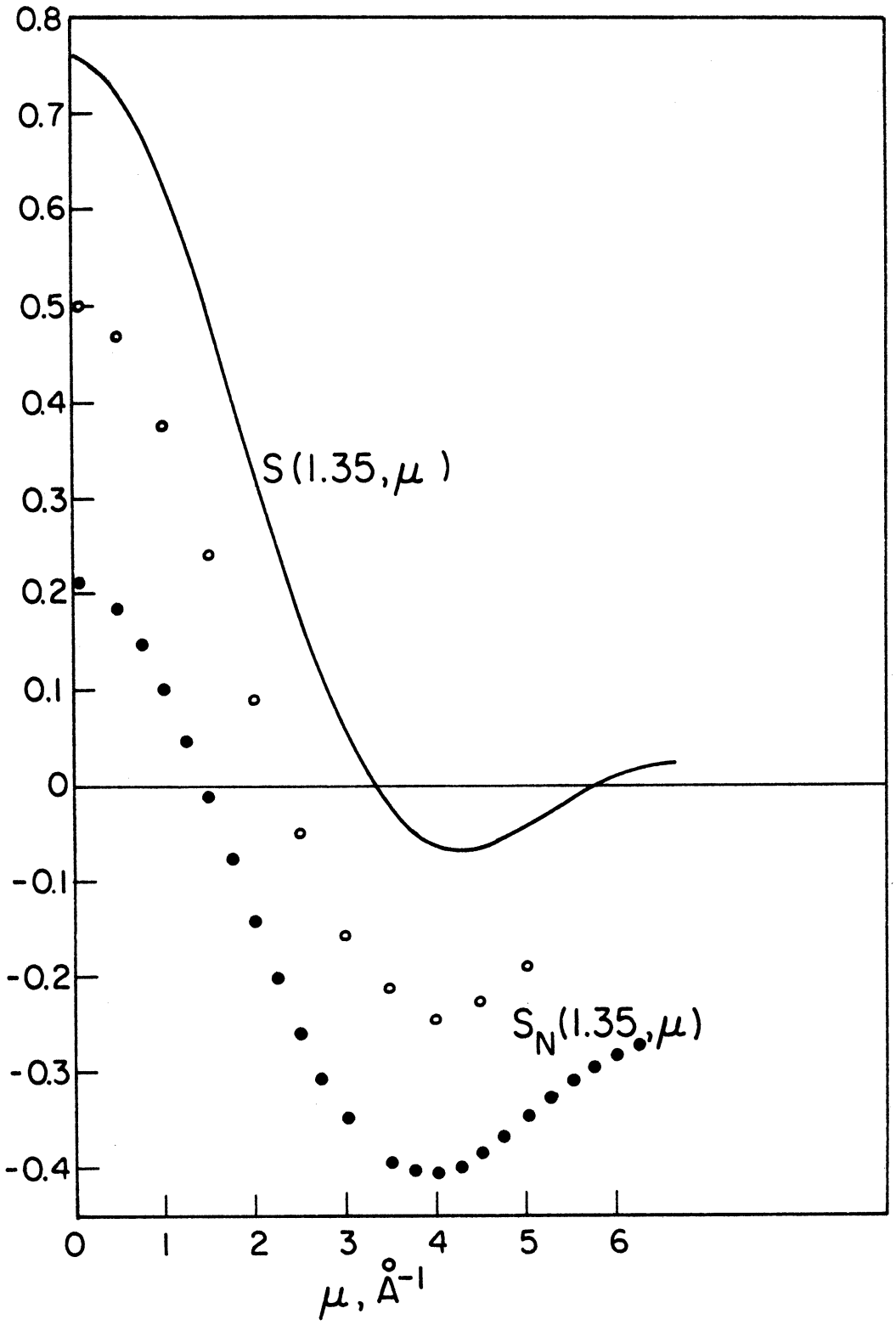

Figure 21. Rahman Normalization Integral for Partially Corrected Data. Solid curve, theoretical value; open circles, data with multiple scattering correction; dots data without multiple scattering correction.

attempted to make corrections to the data based on the Rahman normalization, but we note with pleasure that the multiple scattering corrected data satisfy (4.14) better than the uncorrected data (see figure 21).

4.6 Removal of Container Scattering

At this point the intensity ratio contributions from both the BeF_2 and the aluminum container and can be expressed

$$\left[C^S(t,\vartheta)\,F^S(E,\vartheta) + C^{AL}(t,\vartheta)\,F^{AL}(E,\vartheta)\right] / C^R(t,\vartheta)$$

from which we wish to obtain $C^S(t,\vartheta)/C^R(t,\vartheta)$ before proceeding to multiple scattering corrections. The factor F^S expresses the effect of the container on the observed sample scattering intensity, and F^{Al} the effect of the sample on the observed container scattering intensity.

We dispose of F^S as follows: the fraction of the beam unattenuated by the tube walls is of order $e^{-\Sigma_T^{AL} t_w}$ where t_w is the wall thickness, .0254 cm, and $\Sigma_T^{Al} \simeq .098\ cm^{-1}$. Thus accounting for attenuation of both incident and scattered beams, one expects to see an attenuation effect of about $1-e^{-\Sigma_T^{AL}(2t_w)} \simeq .005$. Multiple scattering contributions will be even less; we thus set $F^S=1$ and proceed.

F^{AL} expresses the effect of the contents of the container tubes on the observed tube scattering. It is simply the ratio of the observed scattering of full to empty tubes. We illustrate (Appendix) by calculating F^{AL} for a simple

tube - the extension to multiple-tube geometry is obvious. The integration involved is by necessity done numerically, and the results for the six-tube array used in the diffraction measurement is shown in figure 22 as a function of the sample cross section Σ_T^S. In order to apply these corrections to extract $C^S(t,\ell)$ from the data, we must have an approximate sample cross section, since F^{AL} varies with Σ_T^S. We are at least nearly in a position to compute Σ_T^S from the data; for in the static approximation,

$$\frac{d\sigma}{d\Omega}(\vartheta) \simeq \langle a^2 \rangle S(Q)$$

and by definition the microscopic total scattering cross section is the integral of the differential cross section, i.e. for $\sigma_s^S(E) = \rho^{-1} \Sigma_s^S(E)$ we can write

$$\sigma_S(E_o) = \int_{4\pi} \frac{d\sigma}{d\Omega}(E_o, \hat{\Omega})\, d\hat{\Omega} \qquad (4.17)$$

$$\simeq \langle a^2 \rangle \int_{4\pi} S(Q)\, d\hat{\Omega} \qquad (4.18)$$

in the static approximation. Recalling $Q = 2k_o \sin \vartheta/2$ or

$$Q^2 = 4k_o^2 \sin^2 \vartheta/2$$

$$= 4k_o^2 \left(\frac{1-\mu}{2}\right) \; ; \; \mu \equiv \cos\vartheta$$

so at fixed k_o, $2QdQ = -2k_o^2 d\mu$

or $d\mu = -QdQ/k_o^2$

so

$$\sigma_S(E_o) \simeq \langle a^2 \rangle \int_{\varphi=0}^{2\pi} \int_{\mu=-1}^{1} S(Q)\, dQ\, d\mu = \langle a^2 \rangle \frac{2\pi}{k_o^2} \int_{Q=0}^{2k_o} Q\, S(Q)\, dQ \qquad (4.19)$$

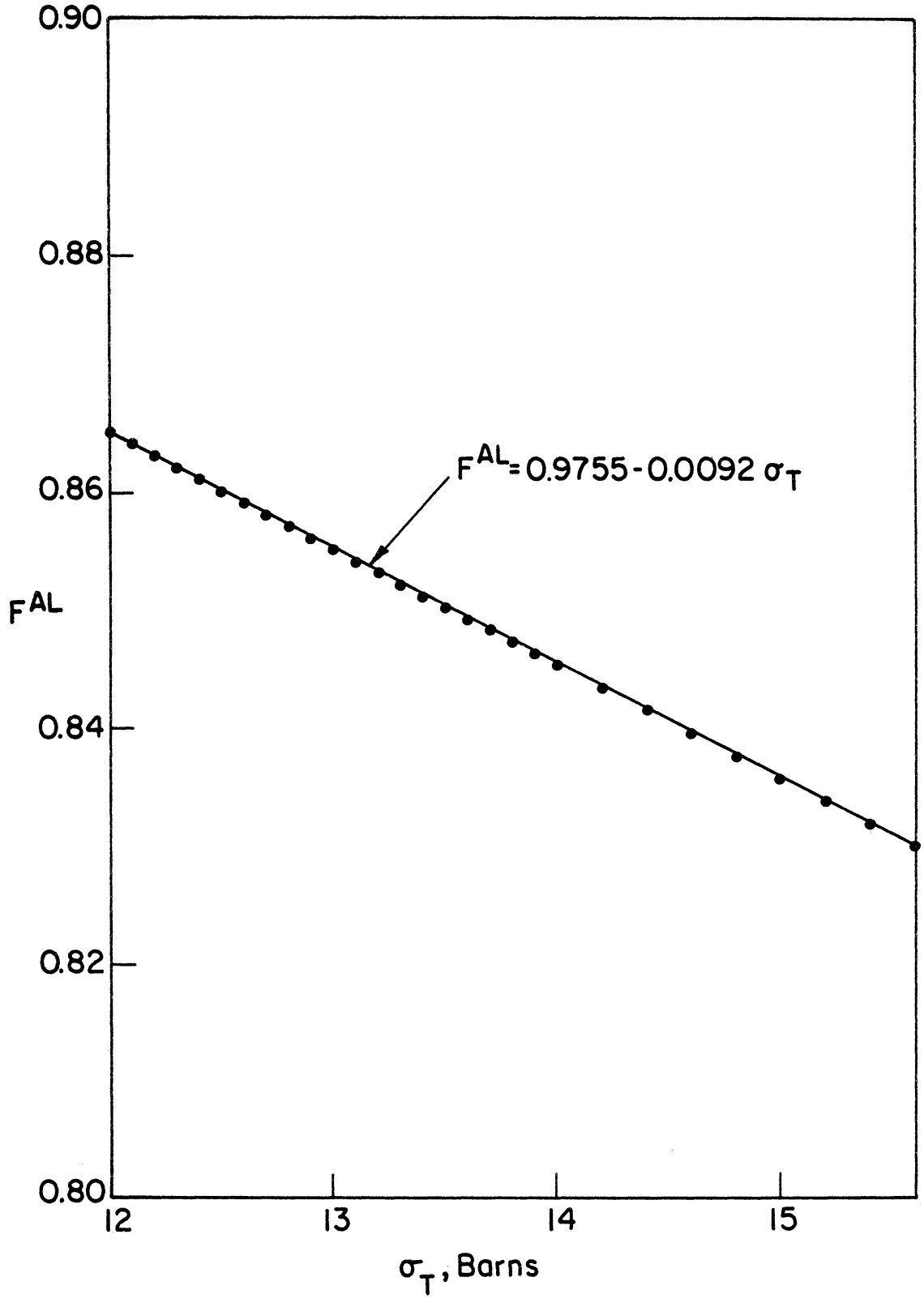

Figure 22. Container Self-Shielding Factor

By effecting a rough removal of the container scattering, we can arrive at a crude estimate for $\langle a^2 \rangle S(Q)$; which yields an approximate cross section via (4.19) for use in a more careful removal of the container scattering. Since the cross section at this point can only be considered approximate, a technique allowing some variation in the cross section used for removal of container scattering was adopted. By using a constant value for $\Sigma_T^{Al}(E)$, the factor $F^{AL}(E,\vartheta)$ becomes a function only of $\Sigma_T^S(E)$ and the scattering angle ϑ, as in figure 22; since F^{Al} is nearly linear as a function of Σ_T^S, it can be interpolated rather than calculated for each value of Σ_T^S. For the sample cross section Σ_T^S we use $(1+\alpha)$ times the approximate cross section shown in figure 23 which was obtained by interpolating a smooth curve under the container Bragg peaks in the intensity ratio data. We allow the normalization parameter α to vary within the range $-.1 \leq \alpha \leq .1$ and choose α so that the function

$$R^S(t,\vartheta) - R^E(t,\vartheta)\, F^{AL}(E,\vartheta)$$

is made most smooth (R^S, R^E are the intensity ratios for the sample and empty runs). It happens that this particular bit of parameter fiddling was done using a graphic computer terminal to display the data with peaks substracted, and to adjust α (and hence F^{AL}) so $R^S - F^{Al} R^E$ is acceptably smooth.

4.7 Correction for Multiple Scattering in the Vanadium Reference Scatterer

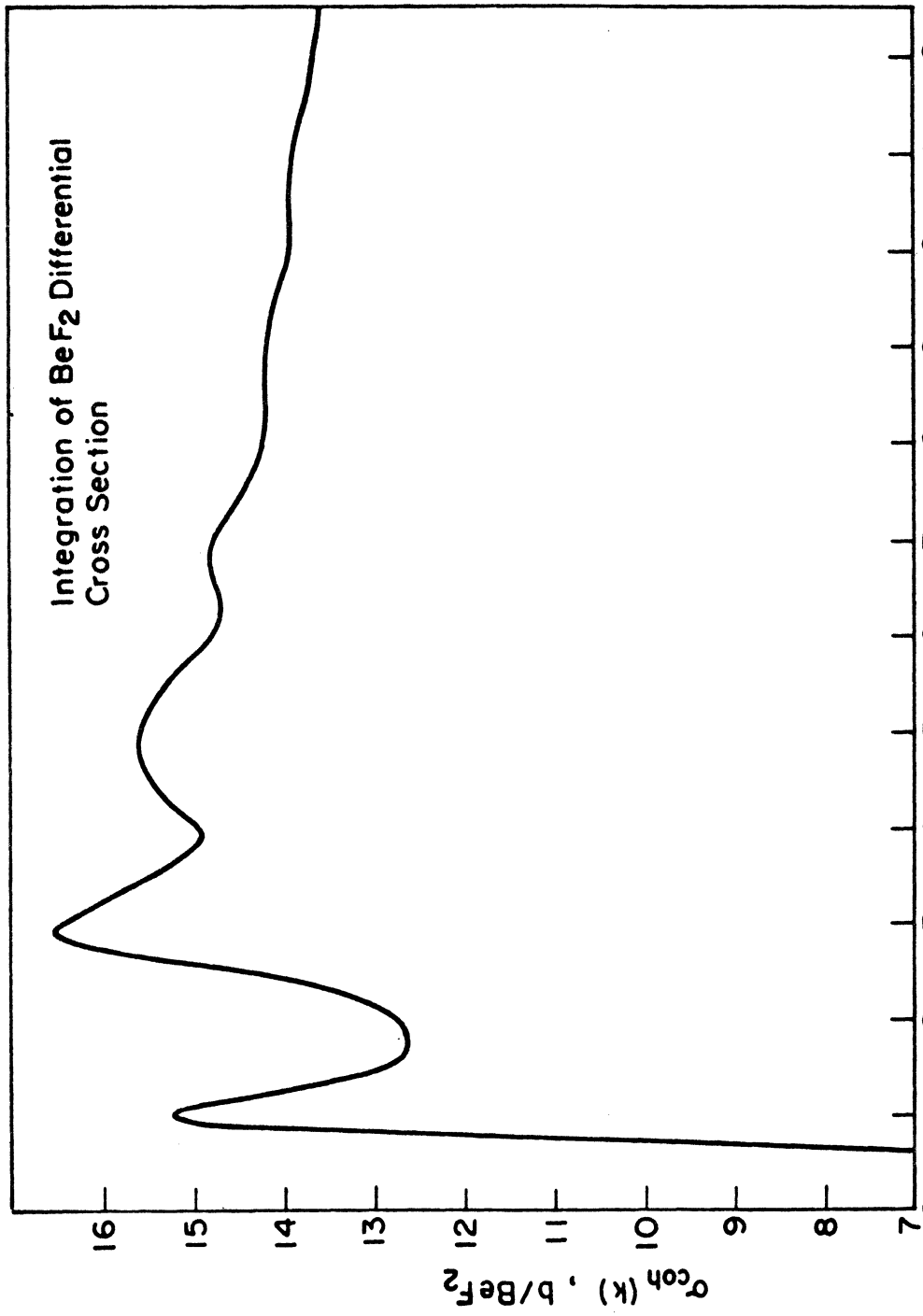

Figure 23. BeF_2 Scattering Cross Section from Partially Corrected Diffraction Data.

Calculation of the multiple scattering correction factor $F^R(E,\Omega)$ for the reference scatterer is considerably simplified by the fact that scattering from V is nearly isotropic, and predominantly elastic. Again invoking the static approximation, we write the total scattered intensity from V as[40]

$$V(Q) = V_1(Q)+V_2(Q)+V_3(Q)+\ldots$$

where $V_1(Q)$ contains contributions only from once-scattered neutrons, $V_2(Q)$ from twice-scattered, etc. As shown by Vineyard[41] for an isotropic scatterer $V_{n+1}(Q)/V_n(Q)$ changes little with n if $n > 2$, and so

$$V(Q) = V_1(Q) + V_2(Q)\left\{1 + \sum_{n=3}^{\infty} \frac{V_n(Q)}{V_2(Q)}\right\}$$

$$\simeq V_1(Q) + V_2(Q) \sum_{n=2}^{\infty} \left[\frac{V_2(Q)}{V_1(Q)}\right]^n$$

$$= V_1(Q) + V_2(Q)\left[1 - \frac{V_2(Q)}{V_1(Q)}\right]^{-1}$$

For an infinitely large but thin plate the first and second orders of scattering can readily be calculated (Appendix) and so also $F^R(E,\Omega) = V(Q)\left(\frac{N_R\sigma_R}{4\pi}\right)^{-1}$. We have written a program, VANCOR, which reads as input the intensity ratios computed by DATRED (or in the present case, intensity ratios with container scattering removed) and computes an appropriate $F^R(E,\Omega)$ for each data point. Microscopic scattering and absorption cross sections of V are taken to be 5.13 barns and $5.06(.0253/E)^{\frac{1}{2}}$ barns, respectively (E in eV). The angular integrations (Appendix) are performed numerically

on a mesh of $\frac{2\pi}{20}$ (azimuthal) by 2/10 (polar, expressed in $\mu = \cos\vartheta$). The computed correction factor is shown in figure 24.

4.8 Multiple Scattering Correction

4.8.1. Preliminaries. The multiple scattering correction $F(E,\vartheta)$ was computed using a Monte Carlo simulation technique. This approach to the problem of multiple scattering corrections was developed by Bischoff [42,43] for use in the time-of-flight inelastic scattering program at RPI[44]. Adaptation to slow-neutron measurements, and in particular to the Argonne time of flight spectrometer, was made by Copley[45] who introduced many innovations into the method. We use a condensed version[46] of the Copley code, treating the scattering as though entirely elastic; i.e., no inelastic data are used in the correction of the diffraction data. The Argonne inelastic scattering code is called MSCAT; our version is titled MSCATD.

Ideally, one might like to include the effects of the sample container in a Monte Carlo simulation such as this, and thereby eliminate the need for a separate step of container scattering removal. Unfortunately this is quite complicated, and we have not yet built it into MSCATD.

4.8.2. Method. We present briefly here the details of the Monte Carlo simulation, beginning with the general

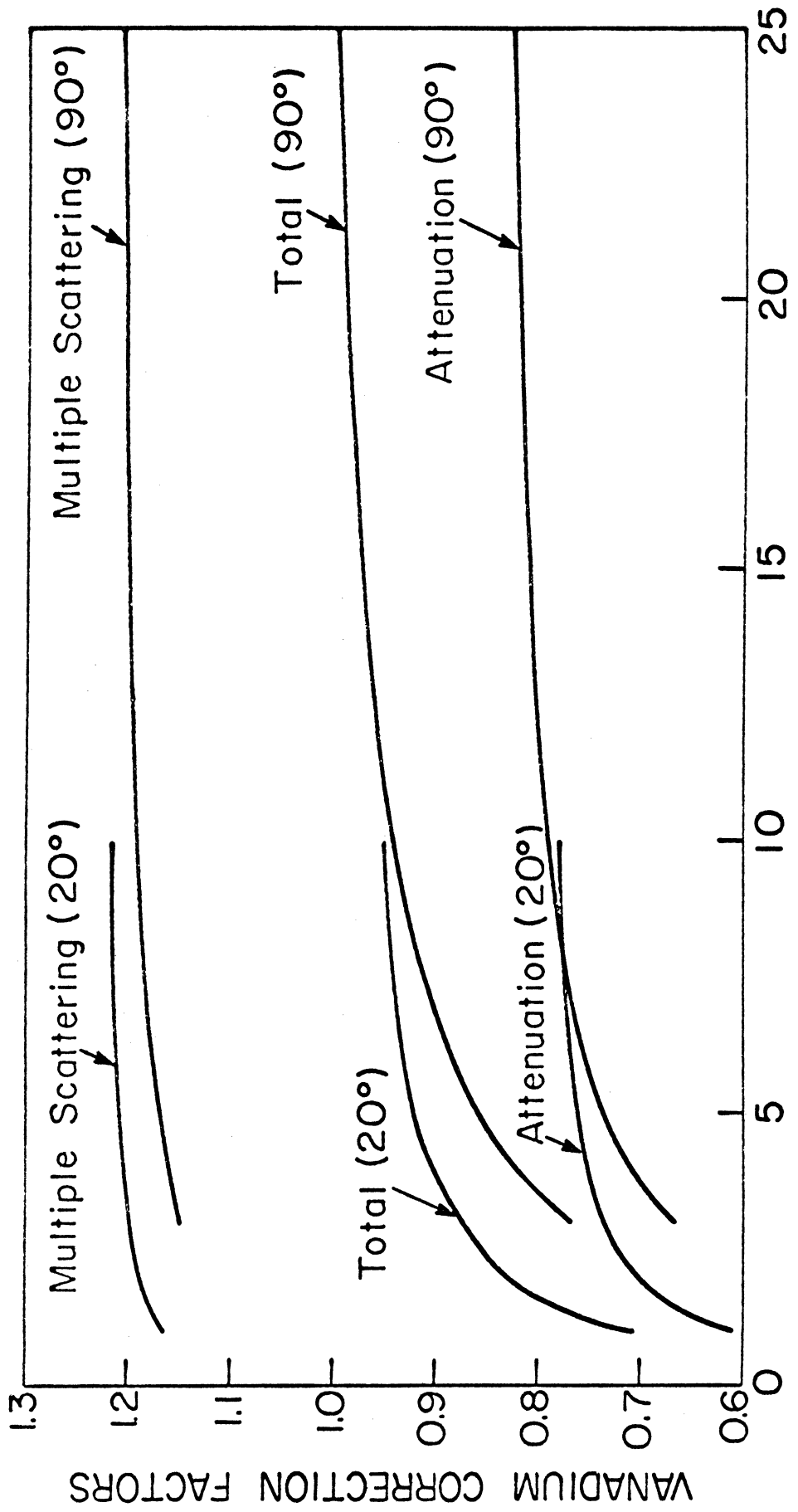

Figure 24. Vanadium Correction Factors as a function of Momentum Transfer for the two Detector Banks

approach. For a uniform monoenergetic neutron beam incident on a sample of known geometry, we can compute an average contribution to the response of a bank of detectors at scattering angle ϑ by simulating histories of many neutrons in the beam, which enter the sample at various points. This response can be separated into first order, second order, third order, etc. so we can compute $P_I/(P_1+P_2+P_3+...)$, P_1/P_I, $P_1/(P_2+P_3+...)$ and whatever other ratios we may wish to examine.

The sample material must be characterized in terms of macroscopic scattering and total cross section Σ_s and Σ_T; and differential cross section used in the simulation should be a reasonable model of that of the actual sample, in order that the corrections calculated be a good approximation to those for the real sample.

In practice, we have no better differential cross section model for use in the simulation than the experimental data themselves. We may wish to initially estimate multiple scattering corrections on some other basis and use a provisionally corrected experimental differential cross section as the model. There is but one way to test the acceptability of a model differential cross section: to calculate multiple scattering corrections, apply them to the uncorrected experimental data, and see if the model is reproduced acceptably well. If the match is good, we can say with confidence that the model differential cross section is a good approximation to $\langle a^2 \rangle S(Q)$ in equation (4.1). In principle

one could adopt an iterative approach, whereby if the model is not acceptably reproduced by the corrected experimental data one recalculates corrections using the corrected data as model. It is not entirely clear if such an approach would eventually converge (and if so, to what). We have not followed this iterative approach and have computed corrections only once, based on an initial model. Before displaying the model differential cross section and the resulting correction factors, we briefly describe the simulation process.

4.8.3. Simulation. The calculation begins with a single neutron with energy E_o traveling along the incident beam direction $\hat{\Omega}_o$. We choose at random a point on the entrance face of the sample, $\underline{r}_o=(x_o,y_o,z_o)$ (constrained to lie within the beam area, of course) and say that the neutron enters the sample there. Associated with any point on the entrance surface (or any point in the sample for that matter) and with any direction is a unique distance along that particular direction to the point where the neutron would leave the sample if it continued unmolested on its way. We call this distance $t(\underline{r}, \hat{\Omega})$ the "effective thickness." The probability of an interaction occuring along the incident neutron's path is then

$$p(t_o \leq t(\underline{r}_o, \hat{\Omega}_o)) = 1 - e^{-\Sigma_T(E_o)\, t_o}$$

We choose a random number ξ from a uniform distribution between 0 and 1, and then solve for l_o such that $p(l_o)/p(t_o)= \xi$.

This fixes the next interaction point via the relation $\underline{r}=\underline{r}_0+l_0\hat{\Omega}_0$. We require the interaction to occur at $\underline{r}_1$. Notice that there is no chance for $l_0 \geqslant t_0$, i.e. no chance for the neutron to escape the target. This is efficient since we keep the neutron in use, but unphysical; we take the effect of this device into account by lowering the "statistical weight" of the neutron from its initial value of 1 down to $p(t_0)$. This correctly accounts for the fact that we have forced an interaction to occur which in reality would only occur with probability $p(t_0)$. At the point $\underline{r}$ we require a scattering event to occur; the probability of this is Σ_S/Σ_T, given that some event occurs. We therefore multiply the statistical weight by Σ_S/Σ_T. To establish a new direction of travel, we choose a value of Q for the scattering event at $\underline{r}_1$ as follows: again pick a random ξ number $0 \leq \xi \leq 1$, and choose Q_1 such that

$$\int_0^{Q_1} Q \frac{d\sigma}{d\Omega}(Q)\,dQ \Big/ \int_0^{2k_0} Q \frac{d\sigma}{d\Omega}(Q)\,dQ = \xi$$

This fixes the scattering angle ϑ by $Q = 2k_0 \sin\vartheta/2$. Together with a random azimuthal angle (eg, $2\pi\xi$) this establishes a new direction of travel $\hat{\Omega}_1$.

Before proceeding to the next interaction however, we stop to do some scoring. To each detector in the bank at scattering angle ϑ, can be assigned a probability of detection for a neutron scattered at $\underline{r}_1$ simply on the basis of the effective sample thickness t_{D_i} between $\underline{r}_1$ and the

detector i. The "score" for this event for the i^{th} detector is just $e^{-\Sigma_T t_{D_i}}$ times the current statistical weight of the neutron times the relative cross section for scattering into the detector:

$$S_i^1 = e^{-\Sigma_T t_{D_i}} p(t_0) \frac{\Sigma_s}{\Sigma_T} \frac{\Delta\Omega_D}{\sigma_s} \frac{d\sigma}{d\Omega}(\hat{\Omega}_0 \rightarrow \hat{\Omega}_D)$$

We have included the subscript 1 to indicate that this score is for a once scattered neutron; later collisions will contribute to higher orders of scattering.

Having seen the neutron through its first scatter, the rest is repetition. At each collision point $\underline{r}_n=(x_n, y_n, z_n)$ with the neutron moving in direction $\hat{\Omega}_{n-1}$ we score each detector for n^{th} order scattering. We then choose a new direction $\hat{\Omega}_n$, compute $t_n(\underline{r}_n, \hat{\Omega}_n)$, change the neutron's statistical weight to

$$W_n = W_{n-1} \frac{\Sigma_s}{\Sigma_T} p(t_n)$$

and choose the next interaction point just as the first was chosen. The score for n^{th} order scattering into the i^{th} detector is

$$S_i^n = e^{-\Sigma_T t_{D_i}} W_n \frac{\Delta\hat{\Omega}_D}{\sigma_s} \frac{d\sigma}{d\Omega}(\hat{\Omega}_{n-1} \rightarrow \hat{\Omega}_D)$$

and the score for n^{th} order scattering into the ϑ detector bank is

$$S^n(\vartheta) = W_n \sum_i u_i e^{-\Sigma_T t_{D_i}} \frac{\Delta\Omega_D}{\sigma_s} \frac{d\sigma}{d\Omega}(\hat{\Omega}_{n-1} \rightarrow \hat{\Omega}_D)$$

The sum runs over all the detectors in the ϑ bank, each with weight u_i. We allow this neutron to collide along its merry way until its statistical weight drops below a cutoff value

w_c; at which point we either (a) double its weight, or (b) terminate its history, with equal probability. This "Russian Roulette" tends to concentrate the calculation of low-weight events in fewer neutrons without biasing the simulation. Since the simulated neutrons cannot "leak out" or be "absorbed" under the rules we have set forth, it is necessary to provide such a means for ending their histories.

After simulating the histories of a reasonably large number of neutrons, we compute the quantities of interest, the correction factors, by comparing the total scores (normalized to a "per incident neutron" basis) for various orders of scattering with each other and with the normalized score which would result from single scattering in an "ideally behaved" sample,

$$S^I(Q) = \sum_D u_D \frac{N}{A} \frac{d\sigma}{d\Omega}(\hat{\Omega}_o \rightarrow \hat{\Omega}_D) \Delta\Omega_D$$

with N the total number of nuclei illuminated by the beam, and A the beam area. The normalized scores are in fact probabilities, and the quantities P_1/P_I, P_M/P_1 etc. can be computed by using appropriate scores for the probabilities.

We repeat the simulation for each scattering angle, and for incident energies such that $Q_e = 2\sqrt{\frac{2mE}{\hbar^2}} \sin \vartheta/2$ covers the desired range. In practice, every collision can be scored for all the different scattering angles of interest, so the consideration of numerous scattering angles does not require much additional work over that for one angle.

The results of simulations for various values of Q_e

are shown in figure 25. These were interpolated and smoothed to some extent using a cubic spline smoothing polynomial. The error flags indicate a standard deviation in the calculated correction factors, due to the statistical nature of the simulation process. The number of histories traced in any simulation is of course determined by the required level of statistical accuracy in the correction factors. We have compiled 200 histories at each incident neutron energy represented in figure 25. The model differential cross section used in these simulations was simply the four sets of experimental data, patched together by scaling each set and renormalized to make the Krogh-Moe integral normalization reproduce the bulk density of BeF_2 glass, 1.96 g/cm^3. (Note that this is for us a microscopic density only, since in our sample there are voids on a macroscopic scale.) These model data are shown in figure 26 along with the scaling factor by which each set was multiplied. The experimental data with smoothed correction factors applied are shown in figure 27.

4.9 Inelastic Scattering Data Reduction

Data from the time of flight spectrometer were reduced to scattering law form as described by Copley[40]. We will not elaborate here on the data reduction procedures.

As previously mentioned, a vanadium reference scatterer was used to calibrate the He^3 neutron detectors. Correction was made for the following effects:

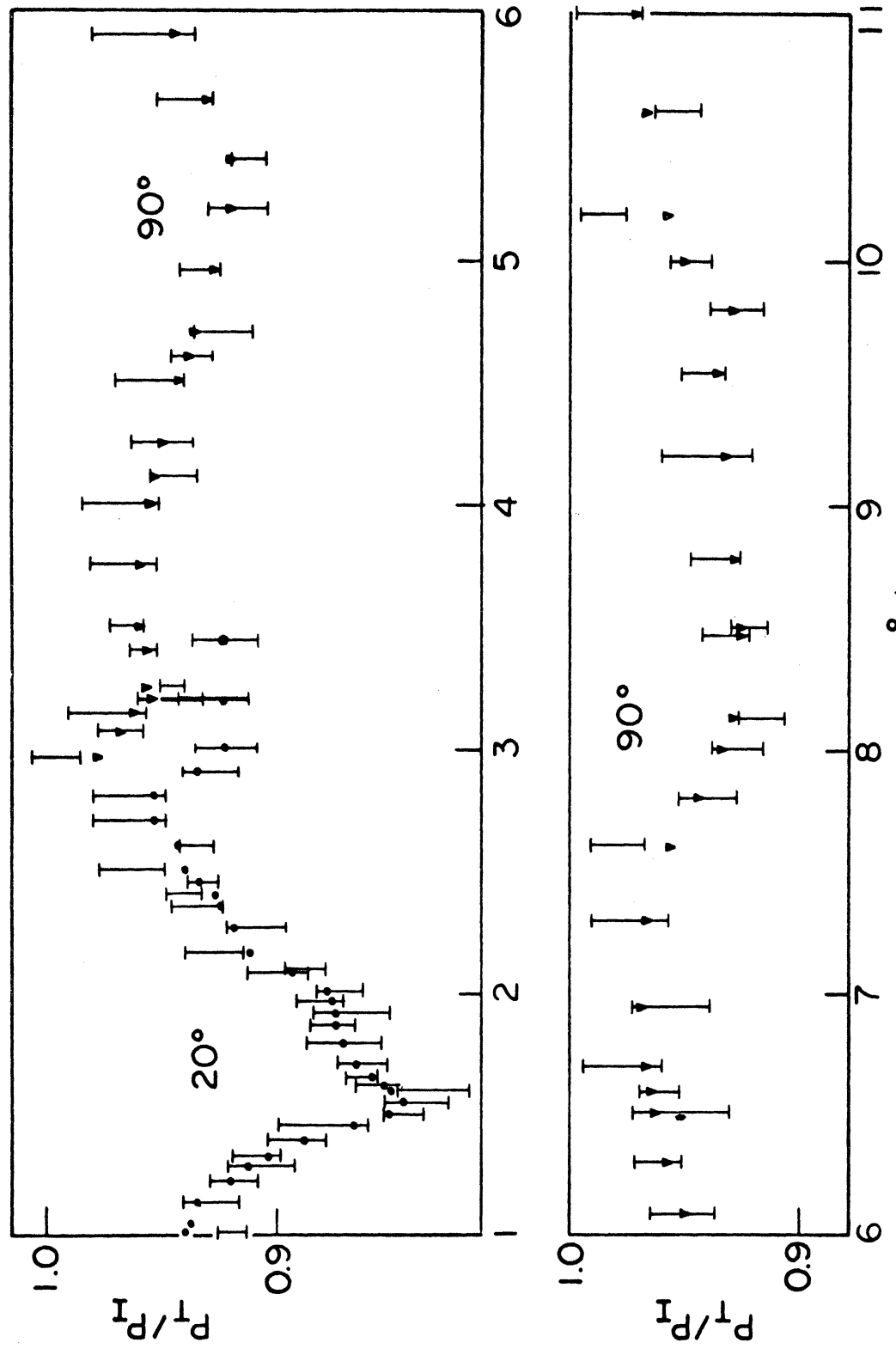

Figure 25(a). Multiple Scattering Correction Factors

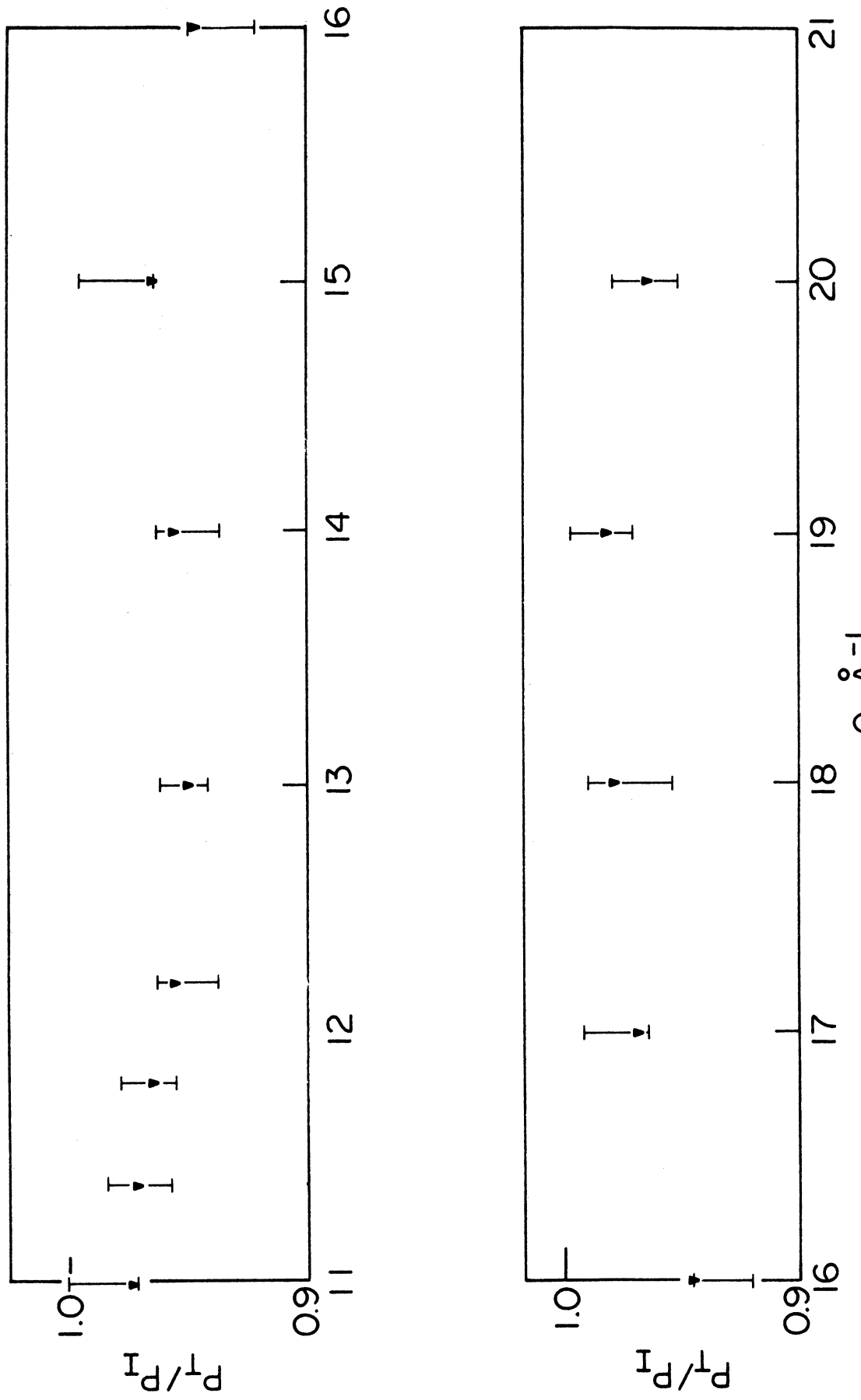

Figure 25(b). Multiple Scattering Correction Factors

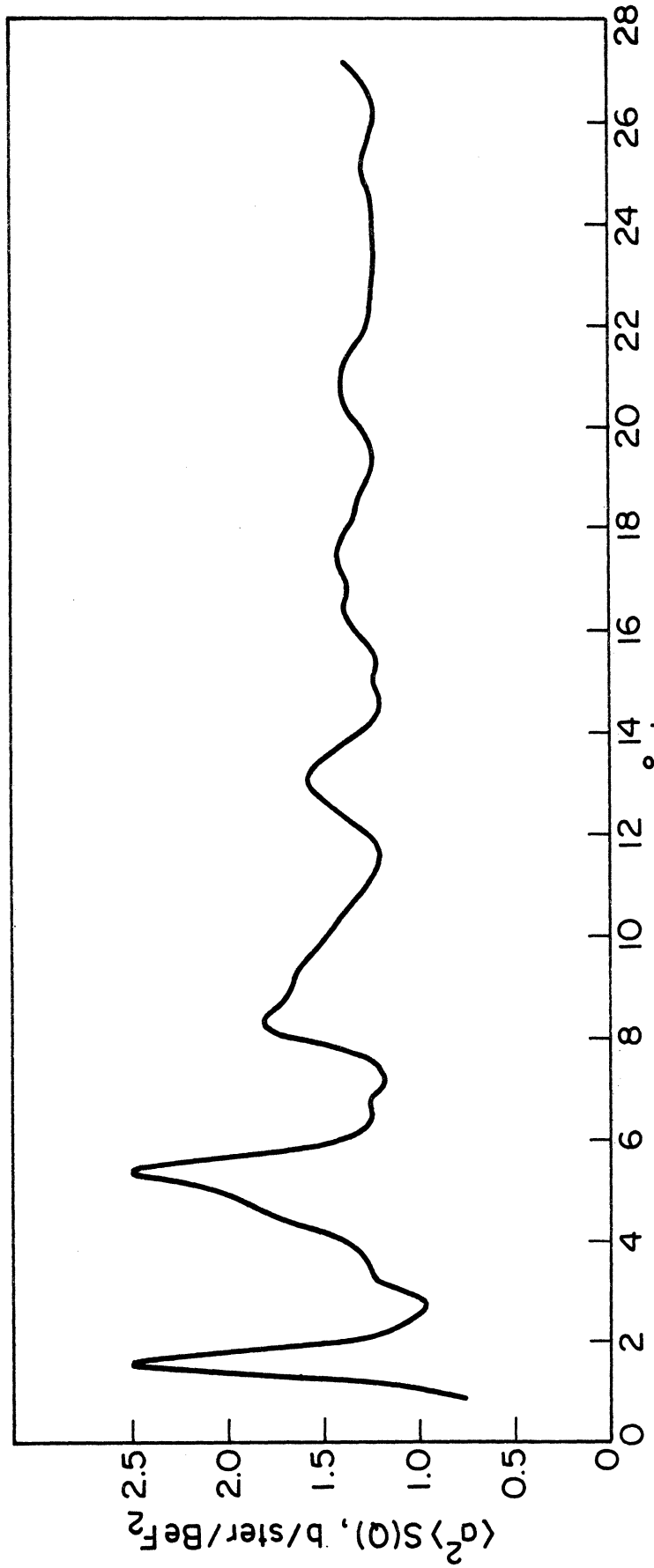

Figure 26. Model BeF_2 Structure Factor for Multiple Scattering Simulation

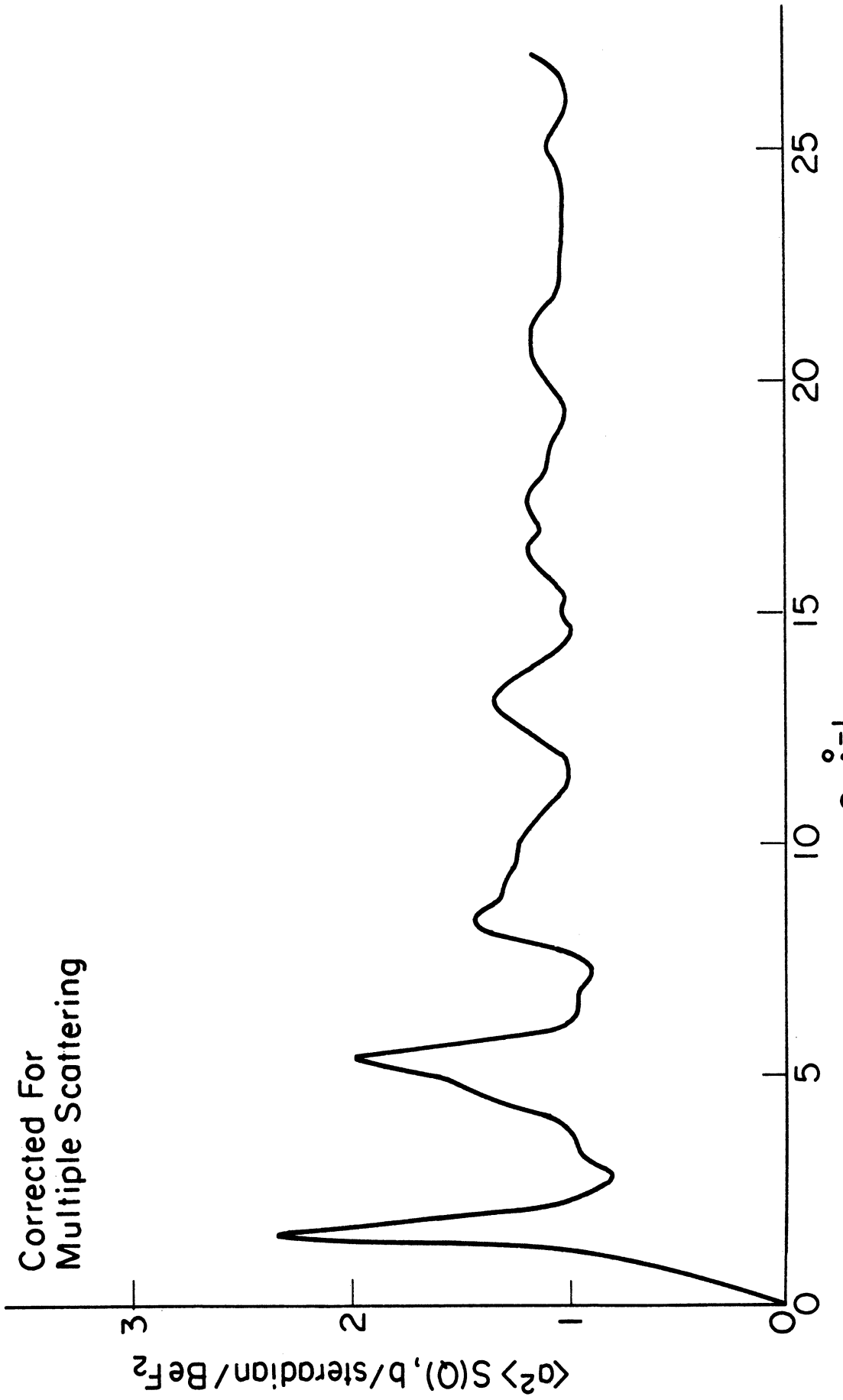

Figure 27. Fully Corrected BeF2 Structure Factor

a) background counting rates in sample and empty runs

b) container contribution to the sample scattering

c) multiple scattering in the reference scatterer, calculated as described for the diffraction measurement.

We made no attempt at a multiple scattering correction; the main problem was a lack of a suitable model to extend the data to large Q. Since we are not particularly interested in the shape of the elastic peak and require knowledge only of the location of other features in $S(Q,\omega)$, we have also omitted a resolution correction.

Using the reduced $S(Q,\omega)$ data we have also computed the generalized frequency distribution function $G(Q,\omega)$ introduced in section 2.4, namely

CHAPTER FIVE

COMPUTATION AND REFINEMENT OF THE RADIAL DENSITY FUNCTION

5.1 Introduction

In this chapter we touch briefly on some of the computational and analytic problems which must be dealt with in doing Fourier transforms in real life. We say "in real life" because in principle there need be no hitches whatever in the evaluation of eq.(2.36), which we repeat here for convenience:

$$4\pi r(\bar{g}(r)-g_0) = \frac{2}{\pi}\int_0^\infty Q\, i(Q) \sin Qr\, dQ \qquad (5.1)$$

with

$$i(Q) \equiv S(Q) - 1 \qquad (5.1a)$$

In practice there are several problems we must face which bear on the evaluation of (5.1). These we will discuss here are:

a) the representation of the integral in (5.1) by a sum

b) the effect of our lack of i(Q) data in the regions $Q_{max} < Q$ and $0 \leq Q < Q_{min}$

c) the effect of our imprecise knowledge of i(Q) in the region of $Q_{min} \leq Q \leq Q_{max}$ due to statistical imprecision and to possible normalization errors.

5.2 Discretization of the Fourier Transform

5.2.1. Available Methods. Here we may make any of several choices, opting for more or less computationally efficient and sophisticated techniques. The most efficient techniques are the so-called "fast Fourier Transforms" (FFT) of which the algorithm of Cooley and Tukey[47] is the prototype. These techniques take advantage of a priori knowledge of phase

relationships between various components in a Fourier series to reduce the amount of computation required. They represent the known function and its transform as vectors of length n, and constitute optimized algorithms for evaluating the nxn matrix equation

$$\underline{T} = \underline{\underline{M}}\,\underline{F}$$

with $\underline{T}$ the vector of transform values, $\underline{F}$ the vector of known function values, and $(\underline{\underline{M}})_{kj} = e^{i2kj/n}$. Such techniques work best for highly composite n, and in particular for $n = 2^p$ they are spectacularly efficient, resulting in reduction of computing labor by a factor roughly p/n.

We have chosen a less efficient but simpler alternative, that of approximating the integral in (5.1) by a sum. In this approximation:

$$4\pi r(\bar{g}(r) - g_0) \simeq \frac{2}{\pi} \sum_{j=1}^{n}{}' Q_j i(Q_j) \sin Q_j r \, \Delta Q \qquad (5.2)$$

with

$$Q_j = (j - \tfrac{1}{2})\Delta Q \quad ; \quad \Delta Q = Q_{max}/n$$

This is computationally a terribly crude and inefficient process, but has the advantage for our purposes of eliminating the relationship implicit in FFT between the Q mesh and the r mesh, $\Delta r = 2\pi/(n\Delta Q)$. We can also save at least some computation by tabulating the sine function and interpolating, rather than computing every sine needed. Most important for our purposes, we can calculate as few or as many transform values as needed at whatever values of r we wish; the FFT techniques requiring the computation of exactly n transform values on a mesh of $2\pi/Q_{max}$, given n values of Qi(Q) on a

mesh of Q_{max}/n. One can artificially extend the data to a larger value of Q, say $Q'_{max} \leq Q_{max}$, by setting

$$S(Q) = S(Q_{max}); \; Q_{max} < Q \leq Q'_{max}$$

and thus become able to calculate the rdf on a denser mesh of spacing $2\pi/Q'_{max}$. The extension to Q'_{max}, however, obviously entails increasing the number of data points, and in the square matrix FFT techniques, the number of transform points which must be calculated. There is still no possibility of computing only a small number of points in the region of peaks in the rdf on a very fine mesh, and the rest on a relatively coarse mesh.

5.2.2. Computation. A program DATINV has been written which does the following:

a) reads in I(Q) values on an equally spaced mesh

b) forms the function Qi(Q) using as $I(\infty)$ either the last value of I(Q), or another value specified by the user

c) optionally weights Qi(Q) by $e^{-\alpha Q^2}$ with α controlled by the user (the use of such modification functions will be discussed later)

d) evaluates the transform (5.2) on an equally spaced r mesh specified by the user

e) evaluates the Krogh-Moe normalization integral

f) optionally computes the first, second and third r moments of $\bar{g}(r)-g_o$ for use in finding coordination numbers, neighbor distances, etc.

g) optionally prints and/or stores all the computed functions.

Typically, one evaluates $4\pi r(\bar{g}(r)-g_o)$ on a relatively coarse mesh over a wide range of r (eg. $0.0\text{Å} < r < 10.0\text{Å}$ by .05Å) and

then on a relatively fine mesh (eg. .01Å) in the region of peaks. The transforms of the fully corrected S(Q) of figure 27 is shown in figure 28.

5.3 Errors in the Transform[48]

5.3.1. Termination Errors. The limits of integration in Q space in equation (5.1) are 0 to ∞. We of course cannot hope to measure S(Q) for all Q, $0 \leqslant Q < \infty$; we must live with $Q_{min} \lesssim Q \lesssim Q_{max}$. We will not be concerned with the region $0 \lesssim Q < Q_{min}$, since in the transform (5.1) there is a weighting of i(Q) by Q; the small Q region is thus relatively unimportant in its contribution to (5.1). We extrapolate S(Q) smoothly to zero below Q_{min} (Q_{min}=.9Å^{-1} in the present case). There is a small error due to the extrapolation to S(0)=0; the correct value of S(0) is related to the isothermal compressibility of the sample, but does not differ significantly enough from zero to give trouble (especially when weighted by Q near Q=0).

The lack of data in the region beyond Q_{max} is a far more serious problem with which we must come to grips, since we will have no way around it.

It will be useful first to derive the mathematical form of the spurious oscillations in $4\pi r(\bar{g}(r)-g_o)$, which we will call "termination errors." We begin by substituting the inverse transform of (5.1),

$$Q\,i(Q) = \int_0^\infty 4\pi r(\bar{g}(r)-g_o)\sin Qr\,dr \qquad (5.3)$$

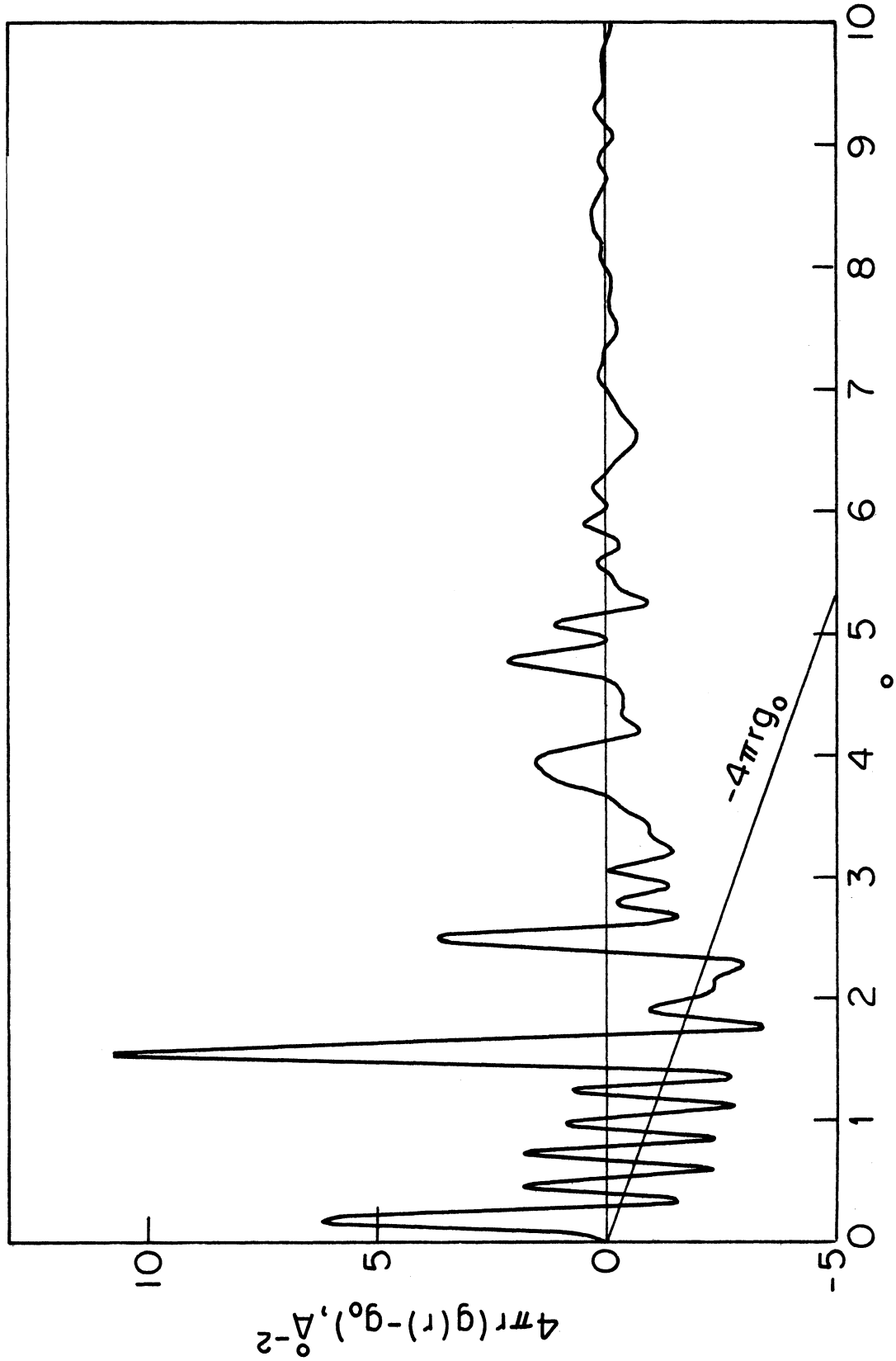

Figure 22. Experimental SeF_2 Radial Density Function

into (5.1) which then becomes

$$4\pi r(\bar{g}(r)-g_0) = \frac{2}{\pi}\int_0^\infty\int_0^\infty 4\pi r'(\bar{g}(r')-g_0)\sin Qr'\sin Qr\,dr'dQ \quad (5.4)$$

which is just a statement of the Fourier integral theorem, appropriate to this problem. Now we define an "experimental" $\bar{g}_e(r)$ by the truncated transform

$$4\pi r(\bar{g}_e(r)-g_0) = \frac{2}{\pi}\int_0^{Q_{max}} Q\,i(Q)\sin Qr\,dQ \quad (5.5)$$

This is the function we arrive at by transforming the experimental Qi(Q). Substituting (5.3) into (5.5), we obtain an expression which is analogous to (5.4):

$$4\pi r(\bar{g}_e(r)-g_0) = \frac{2}{\pi}\int_0^{Q_{max}}\int_0^\infty 4\pi r'(\bar{g}(r')-g_0)\sin Qr'\sin Qr\,dr'dQ \quad (5.6)$$

This relates the experimentally observed $\bar{g}_e(r)$ to the true $\bar{g}(r)$ of the sample. We may perform the Q integral in (5.6),

$$\int_0^{Q_{max}}\sin Qr'\sin Qr\,dQ = \frac{1}{2}\int_0^{Q_{max}}[\cos Q(r-r') - \cos Q(r+r')]\,dQ$$

$$= \frac{Q_{max}}{2}\left[j_0(Q_{max}(r-r')) - j_0(Q_{max}(r+r'))\right]$$

so (5.6) is finally

$$4\pi r(\bar{g}_e(r)-g_0) = \frac{Q_{max}}{\pi}\int_0^\infty 4\pi r'(\bar{g}(r')-g_0)\left[j_0(Q_{max}(r-r')) - j_0(Q_{max}(r+r'))\right]dr' \quad (5.7)$$

The experimental rdf of figure 28 is thus a convolution of the true rdf with an oscillatory function. We have only (!) to solve the singular integral equation (5.7) to unfold the desired true rdf from the experimental rdf. Being practical, we will seek only an approximate solution; but first we will mention another possible source of error in $\bar{g}_e(r)$.

5.3.2. Normalization Error. If we have incorrectly normalized the structure factor data, the function transformed in (5.5) will be not

$$Qi(Q) = Q\,[I(Q)/I(\infty) - 1]$$

but

$$Qi'(Q) = Q\,[I(Q)/(1+f)I(\infty) - 1]$$

where f is the fractional error in our determination of $I(\infty)$. Then

$$\begin{aligned} Qi'(Q) &= Qi(Q) - Q\,I(Q)/I(\infty) + Q\,I(Q)/(1+f)I(\infty) \\ &= Qi(Q) + Q\,I(Q)/I(\infty)\,[1/(1+f) - 1] \\ &= Qi(Q) - [Qi(Q) + Q]\,\frac{f}{1+f} \\ &= \frac{1}{1+f}\,Qi(Q) - \frac{f}{1+f}\,Q \end{aligned} \tag{5.8}$$

Denoting by $\bar{g}_e'(r)$ the erroneous experimental rdf obtained by transforming $Qi'(Q)$, which we get by substituting (5.8) into (5.5),

$$\begin{aligned} 4\pi r(g_e'(r) - g_o) &= \frac{1}{1+f}\,4\pi r(\bar{g}_e(r) - g_o) - \frac{f}{1+f}\,\frac{2}{\pi}\int_0^{Q_{max}} Q \sin Qr\,dQ \\ &= \frac{1}{1+f}\,4\pi r(\bar{g}_e(r) - g_o) - \frac{f}{1+f}\,\frac{2Q_{max}^2}{\pi}\,j_1(Q_{max}r) \end{aligned} \tag{5.9}$$

What we have plotted in figure 28 is in fact $4\pi r(\bar{g}_e'(r) - g_o)$ and not $4\pi r(\bar{g}_e(r) - g_o)$ since we have not yet made sure that no normalization error is present. If we know f, it is a simple matter to get $4\pi r(\bar{g}_e(r) - g_o)$ by

$$4\pi r(\bar{g}_e(r) - g_o) = (1+f)\,4\pi r(\bar{g}_e'(r) - g_o) + \frac{2Q_{max}^2}{\pi}\,j_1(Q_{max}r) \tag{5.10}$$

and then proceed to treat equation (5.7). In practice we do not know f; if we did, we would have done the normalization correctly in the first place rather than leave it until this point. We therefore have to get at $\bar{g}(r)$ through an equation

incorporating the effects expressed in both (5.7) and (5.9):

$$4\pi r(\bar{g}'_e(r)-g_o) = \frac{Q_{max}}{\pi(1+f)}\int_o^\infty 4\pi r'(\bar{g}(r')-g_o)\left[j_o(Q_{max}(r-r'))\right.$$

$$\left.-j_o(Q_{max}(r+r'))\right]dr' \quad -\frac{f}{1+f}\frac{2Q_{max}^2}{\pi}j_1(Q_{max}r) \qquad (5.11)$$

Equation (5.11) relates the rdf derived from an improperly normalized experimental structure factor to the true rdf, and reduces to (5.7) in the case of proper normalization (f=0).

5.3.3. Resolution in the Experimental rdf. The broadening of peaks in the experimental rdf, implicit in equation (5.7), bears on our ability to resolve contributions arising from closely spaced peaks in the true rdf. An infinitely sharp peak at $r=r_o$ in the true rdf would appear in the experimental rdf as

$$\frac{Q_{max}}{\pi}\left[j_o(Q_{max}(r-r_o))-j_o(Q_{max}(r+r_o))\right]$$

which (ignoring the second term, which is negligible compared to the first for $r\sim r_o$) has height Q_{max}/π and FWHM $3.79/Q_{max}$. We may thus expect to be unable to resolve contributions from peaks in the true rdf separated by less that about $4/Q_{max}$, which is $r_{min}=.16\text{Å}$ for the present case with $Q_{max}=25\text{Å}^{-1}$. We do not expect (or see) any peak separations in the vitreous BeF_2 rdf as small as this, so the broadening effect does not present a resolution problem for us. In any case, the broadening can be removed to some extent by applying a competent termination error correction (section 5.4 below).

5.4 Suppression or Removal of Transform Errors

5.4.1. Modification Functions. Having at least some quantitative grasp of the termination effects, we must proceed to deal with them. The crudest and least effective method available, but the one which has been most used for many years, is to try to minimize the problem through weighting of the diffraction data. If we multiply the Qi(Q) function by a modification function--let us use a Gaussian, for example--before transforming, the termination satellites will be altered somewhat, and hopefully made less serious. The analysis of Waser and Schomaker[48] however shows that every common choice of modification function not only fails to significantly reduce the termination errors, but also tends to broaden the peaks in the rdf. In the context of the analytic methods presented later, the use of any modification function is entirely redundant and in fact quite equivalent to the use of no modification function at all. As a device for suppressing termination errors, we must conclude that data modification is none too effective. (In fairness we must point out that the use of a Gaussian modification function--or "artificial temperature factor" or "convergence factor"--does have the salutory effect of decreasing the weight given to the large Q region where statistics tend to be worst in X-ray and neutron diffraction measurements.) We will require that a useful procedure remove nearly all the termination effects (and ideally also remove the effects of the unknown normalization error.)

5.4.2. Method of Kaplow, Strong and Averbach[49]. The method used by Kaplow, Strong, and Averbach to suppress termination errors in their study of liquid lead and mercury has been applied by several workers[49] with considerable success. This method does not require knowledge of the analytical form of the termination errors as expressed by equations (5.7) and (5.11). We will use the notation of Kaplow et **al.** in which

$$F(Q) \equiv Qi(Q)$$

and

$$G(r) \equiv 4\pi r(\bar{g}(r)-g_o).$$

The first step is to transorm the experimental data F^e using several different termination points. Those features in the resulting G^e which change position with termination point are deemed to be spurious. The spurious features thus identified are removed from G^e as are all the features below the first coordination peak (where $\bar{g}(r)$ must be zero). The rdf thus corrected, G^c, is then transformed to yield a function F^c which is calculated for $0 \lesssim Q \lesssim Q_{max}$ and also beyond Q_{max}. At this point one begins to iterate the following steps:

a) truncate F^c at Q_{max} and transform

b) compare the resulting rdf with G^c from which F^c was calculated, to identify spurious features

c) correct G^e using the identified spurious features, and alter G^c based on a comparison with G^e

d) compute a new F^c from the corrected G^c, and compare with F^e.

Steps (a)-(d) are repeated until F^c matches F^e in the region $0 \lesssim Q \lesssim Q_{max}$, and G^c changes little from one iteration to the next. At this point F^c is used to extend F^e beyond Q_{max}, and the transform of the resulting extended F^e is the final G(r) with termination errors removed.

We have chosen not to use this procedure, not because it fails to adequately remove the termination effects--it can in fact do quite well--but because the steps taken in the correction procedure are largely arbitrary. Even the initial identification of spurious features is not foolproof--real features may change shape and thus appear to move, and the movement of spurious features is not so great as to preclude the possibility of a small though real feature lying underneath a spurious one being wiped out in the very first step. Furthermore, it does not admit inclusion of the effects of a normalization error. In spite of our reservations concerning this procedure we do not denigrate its effectiveness when properly used; Yarnell et al.[50] effected an almost total removal of termination effects from their liquid argon rdf in a single iteration using a method very similar to this one, which they attribute to Verlet.

5.4.3. Method of Narten and of Konnert and Karle. Konnert and Karle of the Naval Research Laboratory have developed a very powerful method[51] for removal of termination effects and normalization error (and, indeed, several other sources of error we have not worried about, such as errors in measured background or imprecise knowledge of X-ray scat-

tering factors). The technique can be extended to include nearly any source of error one can postulate; it operates via a least-squares refinement procedure.

The basic assumption made by Konnert et al. is that the unmeasured diffraction pattern beyond Q_{max} would, if it could be measured, affect only the shape of the first few peaks in the rdf. In addition, it is assumed that the dominant contribution in i(Q) to an rdf peak at r_{ij} (one of the first few peaks) is

$$C_{ij}(Q) = N_{ij} \frac{a_i a_j}{\langle a^2 \rangle} \exp(-l_{ij}^2 Q^2/2) j_0(Q r_{ij}) \tag{5.12}$$

The shape thus forced on the (ij) coordination peak in the rdf is

$$P_{ij}(r) = \frac{2}{\pi} \int_0^\infty Q C_{ij}(Q) \sin Qr \, dQ$$

$$= \sqrt{\frac{\pi}{2}} \frac{N_{ij} a_i a_j}{\pi r_{ij} \langle a^2 \rangle} \left\{ \exp\left[-(r_{ij}-r)^2/2l_{ij}^2\right] - \exp\left[-(r_{ij}+r)^2/2l_{ij}^2\right] \right\} \tag{5.13}$$

The second exponential term is negligible compared to the first except near r=0, so the overall shape of the coordination peak is approximately Gaussian; this is certainly not a particularly bad assumption on its face.

Characterizing a small number of short-range peaks (three in the case of vitreous SiO_2, the subject of their work: Si-O, O-O, and Si-Si) by expressions such as (5.12) and (5.13), a "short-range diffraction pattern" and a "short-range rdf" are parametrized. When the short-range diffraction pattern and the unmeasured portion beyond Q_{max} are subtracted from the

infinite-range diffraction pattern, the remainder is a subset of the experimental data in the range $0 \leq Q \leq Q_{max}$. This "residual diffraction pattern" $i'(Q)$ is the transform of a "residual rdf" $D'(r)$ (in the notation of Konnert and Karle, $D(r) \equiv 4\pi r(\bar{g}(r)-g_o)$) completely determined by diffraction data below Q_{max}; and furthermore $D'(r)$ should be completely free of termination errors, since Q_{max} is as good as ∞ for an upper limit on the transform of $i'(Q)$, which hopefully dies away below Q_{max}.

The way is clear now to proceed with refinement of the rdf. All one need do is adjust the parameters N_{ij}, r_{ij} and l_{ij} to make the transform of

$$Qi'(Q) = Qi(Q) - Q \sum_{sd} N_{ij} \frac{z_i z_j}{\langle z^2 \rangle} \exp(-2\sigma_{ij}^2 Q^2/2) j_0(Q r_{ij}) \tag{5.14}$$

free of any feature in the short-distance region (note the sum over "sd" in equation (5.14) runs over the short distances being removed from the rdf). This should be possible if we have correctly assumed that only the region beyond Q_{max} and the postulated contributions (5.12) give rise to short-range structure in the rdf.

The adjustment of parameters is accomplished using a standard nonlinear least-squares refinement technique such as the Gauss-Newton iteration or the method of steepest descent.

We feel there is much to recommend the procedure of Konnert and Karle. One attractive feature is the ease with which one can account for the other sources of error--in our

case, it would be desirable to include the effects of a narmalization error, as previously stated. This would simply add another parameter (the fractional normalization error f) to the least-squares fitting problem. Perhaps more significant on physical grounds is the fact that one does not try to artificially extend the diffraction data, as in the procedure of Kaplow et al. In this method, one makes up one's mind to do without the data beyond Q_{max}, and see what refinement can be done on the basis of what one actually knows. The fundamental approximation of a damped j_o shape for peaks in the short-range diffraction pattern with resulting Gaussian peaks in the short-range rdf, is really the only thing one must buy; after that the method proceeds free of approximation. As to the acceptability of the Gaussian shape for short-range rdf peaks, it is probably safe to say that any deviation from the Gaussian peak shape at short distances in the true rdf is reflected in the diffraction pattern only in the region beyond Q_{max}, and thus cannot be calculated from our diffraction data in any case. It seems a reasonable statement then, that the Konnert and Karle procedure when properly executed yields a refined rdf which is as close to the true rdf of the sample substance as we can possibly come on the basis of a limited range diffraction measurement.

We would be remiss not to give credit in this discussion to A.H. Narten, whose X-ray diffraction study of glassy BeF_2 was mentioned in Chapter One. As early as 1969 (three years before published application of the Konnert and Karle refine-

ment procedure) Narten and Levy[52] utilized a procedure identical in principle in their X-ray diffraction study of water. This procedure was alluded to in Chapter One, having also been applied by Narten to his BeF_2 glass data[13]. Narten utilizes a least-squares variation of a model $i_M(Q)$ which is a sum of short-distance terms such as (5.12), plus a term accounting for continuous pair density at large r, against the experimental i(Q). Refinement at the level of i(Q) rather than the level of $\bar{g}(r)$ offers the advantage of reducing the amount of computation required, but introduces the additional assumption that there be no contributions to the diffraction pattern other than those from short-distance and continuous terms. The Konnert and Karle procedure admits the possibility of structure in $\bar{g}(r)$ not confined to short distances but not in the continuum region either. On this basis we would be hard pressed to declare the slightly more general but considerably more costly procedure of Konnert and Karle superior to that of Narten.

Having so highly praised this method for suppression of termination and normalization errors, it becomes imperative to explain why we have not utilized it in the present work. The answer, simply stated, is time and money. Time: as we became adequately informed of this method in late 1973 when there was not sufficient time to seriously develop a program applying it. Money: as even though we began work on the aforementioned program, charges for computation became prohibitive. To illustrate the large amount of computation

implicit in the method, consider that any competent nonlinear least-squares fitting algorithm requires knowledge at each iteration of not only the total squared deviation, but also its partial derivative with respect to each parameter in the fitting function. The fitting function in the present case is the Fourier transform of equation (5.14); each of its partial derivatives requires as much work in the evaluation as the function itself, and there are 3n of these (n the number of short-range peaks modeled). This adds up to a considerable amount of computing labor per iteration, and numerous iterations are in general necessary to converge on a satisfactory solution. All of this boils down to the fact that in order to apply this method at a reasonable cost, one must have access to a computer of the number-crunching variety--and we do not.

5.4.4. Graphic Removal of Termination Errors. The method described in this section was developed with the intent to take advantage of the particular computing environment of The University of Michigan; that environment being one of a medium power computer, certainly not a number-cruncher but with features (e.g. a large virtual memory) which make it ideally suited to a time-sharing system. In addition a large variety of terminal devices are available, and the Computing Center Staff provide the user with much software support for his use of these devices. We have found invaluable in our treatment of the termination error problem the Tektronix 4010 storage tube (graphic) terminals available at no charge to the user in the Computing Center, and the Integrated Graphics software

package (developed by Mr. James Blinn of the Computing Center) which has proven the sine qua non for our profitable use of the graphic terminal in an interactive mode.

We will proceed to describe our graphic trial-and-error solution of equation (5.11). We will include the normalization error f in the equations, since it has proven useful to have the effects of f included in the graphic procedure. First we note that if the experimental rdf $4\pi r(\bar{g}_e'(r)-g_0)$ and a model rdf $4\pi r(\bar{g}_M(r)-g_0)$ are both tabulated on the same mesh, and if the mesh is sufficiently fine that we can approximate the tabulated function

$$4\pi r(\bar{g}_M(r)-g_0) \simeq \sum_{i=1}^{N} G_i\,\delta(r-r_i)\;;\quad r_i=(i-\tfrac{1}{2})\Delta r \tag{5.15}$$

then equation (5.11) has a very simple form when (5.15) is substituted:

$$\begin{aligned}4\pi r_n(\bar{g}_e'(r_n)-g_0) &= \frac{Q_{max}}{\pi(1+f)}\int_0^{\infty}\sum_{i=1}^{N} G_i\,\delta(r'-r_i)\left[j_0(Q_{max}(r_n-r'))\right.\\ &\left.-j_0(Q_{max}(r_n+r'))\right]dr' - \frac{f}{1+f}\,\frac{2Q_{max}^2}{\pi}\,j_1(Q_{max}r_n)\\ &= \frac{Q_{max}}{\pi(1+f)}\sum_{i=1}^{N} G_i\left[j_0(Q_{max}(r_n-r_i))-j_0(Q_{max}(r_n+r_i))\right]-\frac{f}{1+f}\,\frac{2Q_{max}^2}{\pi}\,j_1(Q_{max}r)\end{aligned} \tag{5.16}$$

Equation (5.16) predicts the experimental rdf we would obtain by inverting diffraction data, out to Q_{max}, from a substance whose true rdf is $4\pi r(\bar{g}_M(r)-g_0)$. This prediction is of course based on the assumption that the only errors possible in the transform are the termination and normalization effects

as expressed in equation (5.11). The simple principle of our graphic method is to adjust the G_i (and f) so that (5.15) reproduces as closely as possible the experimentally determined rdf. There is of course no guarantee that the model arrived at by this procedure is the only solution to equation (5.11); but it is certainly a solution, and we assert that any significantly different solution would have some physically unacceptable features by which we could rule it out.

In practice, the graphic error removal program (titled GRAFIK) proceeds as follows:

a) reads the experimental rdf

b) prompts the user for g_o and Q_{max}

c) displays the experimental rdf on the screen as a solid curve

d) allows the user to set $\bar{g}_M(r)=0$ in any region he chooses

e) initializes the model by making $\bar{g}_M(r)=\bar{g}'_e(r)$ in regions not required to be zero

f) displays the model as a histogram superimposed on the experimental rdf

g) folds the model into equation (5.16) with f=0 initially

h) displays the folding as a series of crosses

i) prompts the user to make adjustments to the model or to exercise one of several other options, then returns to step (f) if iteration is to continue

j) iterate steps (f-i) until the crosses lie upon the solid curve acceptably well.

The "other options" at step (i) include giving a nonzero value to the normalization error f, integrating peaks in the model, changing the scale of the display or blowing up a specified

region of the picture, and terminating the fitting procedure with optional disk and/or print and/or plotter output.

A typical refinement of an experimental rdf given at 200 mesh points takes 15 to 20 minutes at the terminal; most of this time is spent pondering one's next move, so the computing time is far less than the elapsed time. This is ideal since one is charged relatively little in the Michigan Terminal System for "idling" as opposed to actual computing. Results of a refinement of the rdf in figure 28 are shown in figure 29. Our failure to accurately reproduce the oscillations near r=0 can be traced in part to the resolution correction we failed to apply. The results of Sutton's[53] work on vitreous SiO_2 show that the effect of the resolution correction is to bring the low-r oscillations in the experimental rdf closer to their predicted form; i.e., to improve the match at low r in figure 29. Sutton's results show that the real features in the rdf are essentially unaffected by the resolution correction. Since we are interested in the rdf and not the structure factor per se, we can thus get away without the resolution correction. In the case of diffraction from liquids, the structure factor is itself of considerable interest, and in particular, the details of its shape at low Q. A resolution correction must clearly be applied in such cases.[50]

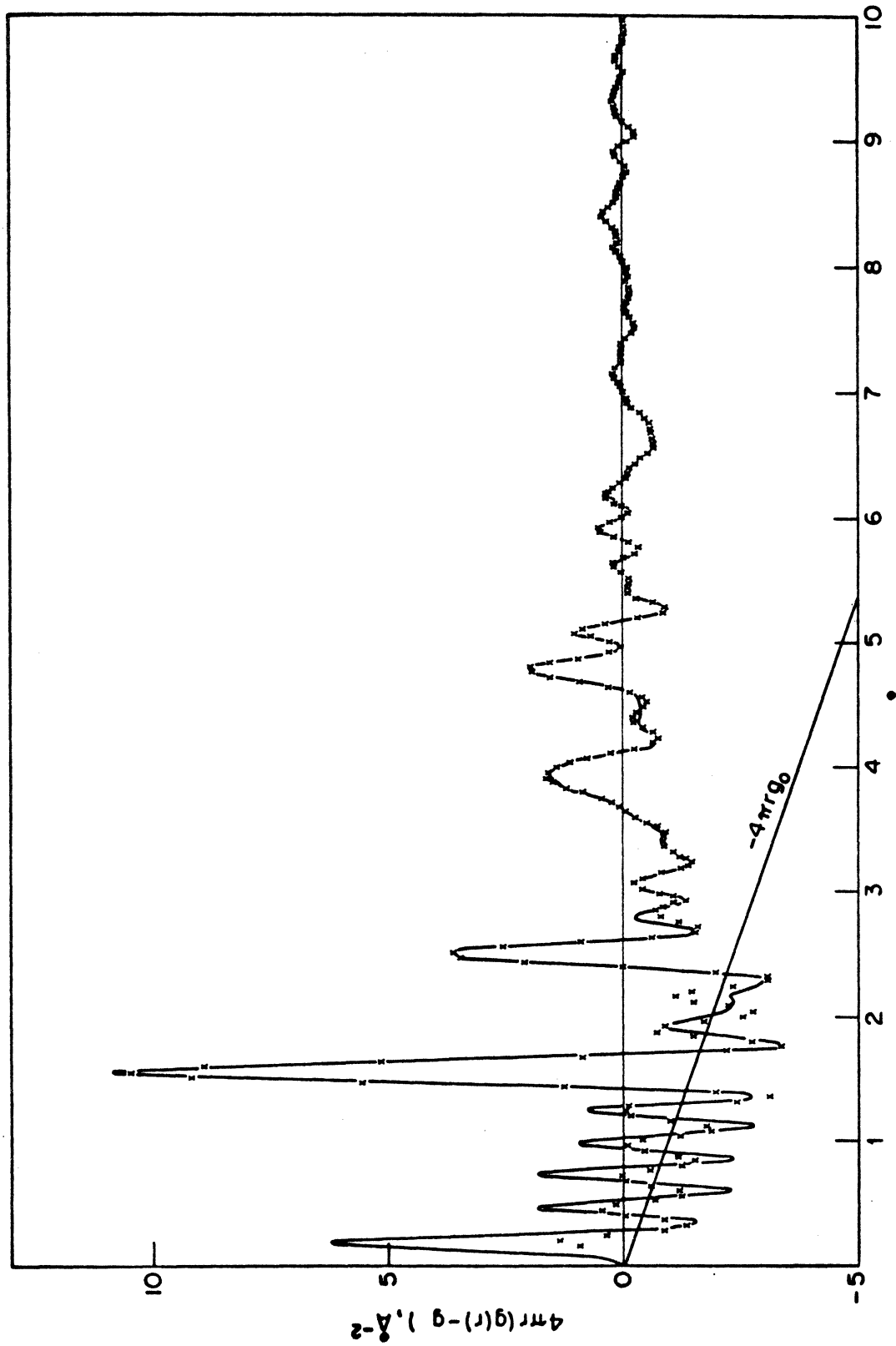

Figure 29. Refinement of the Experimental RDF. Curve-experimental rdf; crosses - model with errors folded in.

5.5 Implications of the Termination Errors for Large-Q Diffraction

We close this chapter on a note of reflection concerning the termination errors. Since the problem arises from our inability to measure the structure factor beyond a fairly small value of Q_{max}, one might expect at first that by going to a larger and larger Q_{max}, we could eventually overcome the termination errors. This unfortunately turns out not to be the case. That the problem of termination (and, incidentally, normalization) errors is in fact exacerbated by increasing Q_{max} can be seen from equation (5.11). Immediately obvious is the fact that the amplitude of the termination ripples is proportional to Q_{max}, and of the normalization ripples to the square of Q_{max}. Furthermore the frequency of the ripples is proportional to Q_{max}, so they become more numerous as well as larger with increasing Q_{max}. In fact, reflection on the form of equation (5.11) indicates that only for Q_{max} so large that $2\pi Q_{max}^{-1}$ is small compared to the width of the narrowest feature in $\bar{g}(r)$ will we begin to get away from the termination error problem. This may correspond to Q_{max} in the range of 50 to 100Å^{-1} or more, depending on the exact nature of the material under investigation.

The implications of the foregoing considerations for work of the sort described here are clear. If we expect to gain anything by extending the Q range of our measurements, we had better be prepared to deal effectively with the increasingly severe termination effects. Only if we can push Q_{max} far

beyond presently attainable limits will we be able to avoid entirely the termination error problem.

CHAPTER SIX

ANALYSIS OF EXPERIMENTAL RESULTS

6.1 Analysis of the RDF

6.1.1. Information in the rdf. We have previously noted that the rdf contains information on the relative arrangement of nuclei in the sample. In particular, the function $4\pi r^2 \bar{g}(r) \Delta r$ represents the normalized number of nuclear pairs with spacing in Δr at r, weighted by their scattering lengths. From such a function, which may correctly be called a pair distribution ($\bar{g}(r)$ itself is not a pair distribution in the literal sense), we may deduce certain average properties of the sample structure, such as coordination numbers, neighbor distances and near-square thermal displacements for the various pairs of nuclear species.

6.1.2. Preliminary comments on the fully corrected experimental rdf. The rdf with graphic termination effect removal applied (figure 30) is our best estimate of the true rdf of vitreous BeF_2. That we have not been completely successful in removing the nonphysical features has already been mentioned. In particular, the feature centered about 2.8Å is almost certainly spurious, as is the small feature at about 3.3Å. We may note further that the first coordination peak at 1.56Å rises and falls too sharply; we would expect a more gradual variation in pair density both above

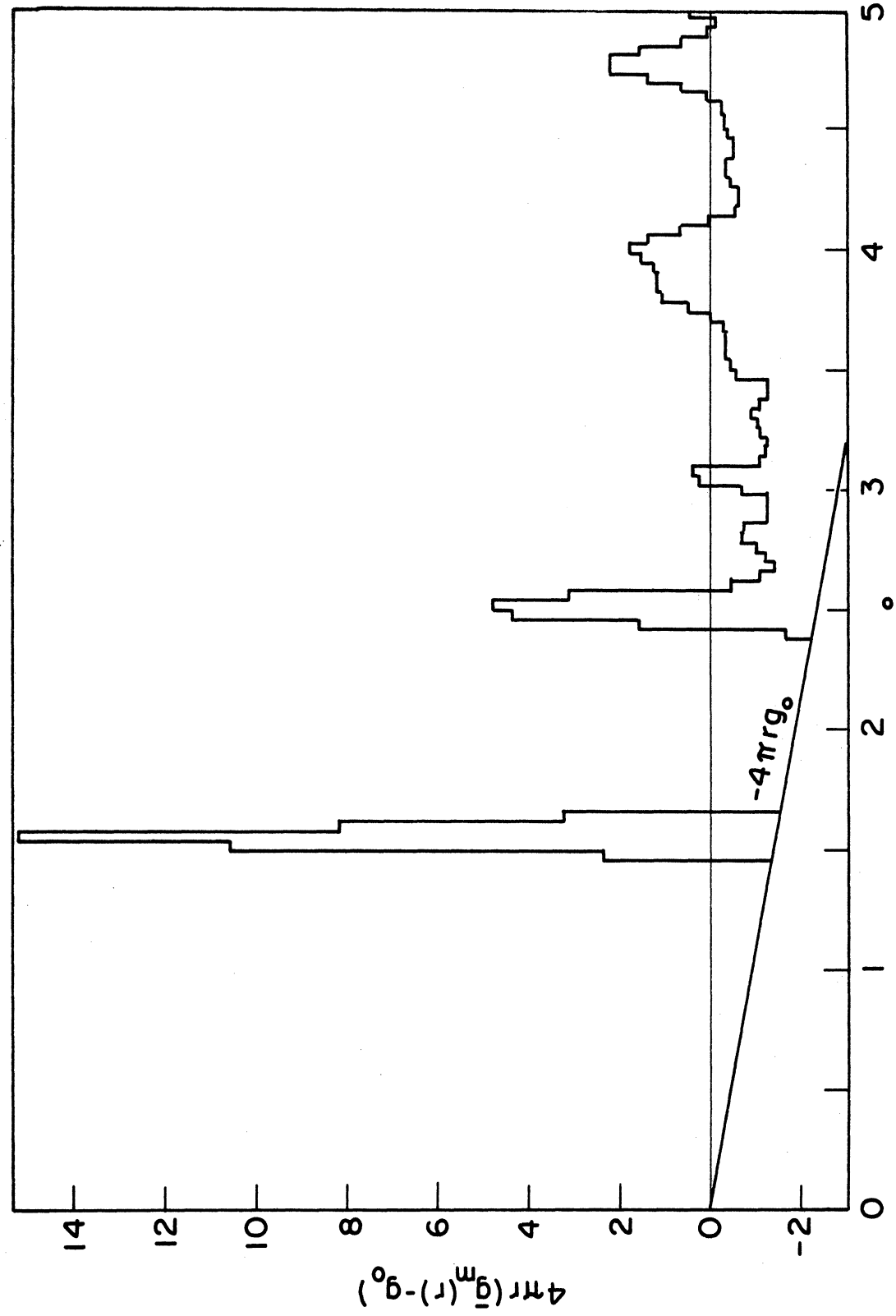

Figure 30 (a). Refined BeF^2 Radial Density Function.

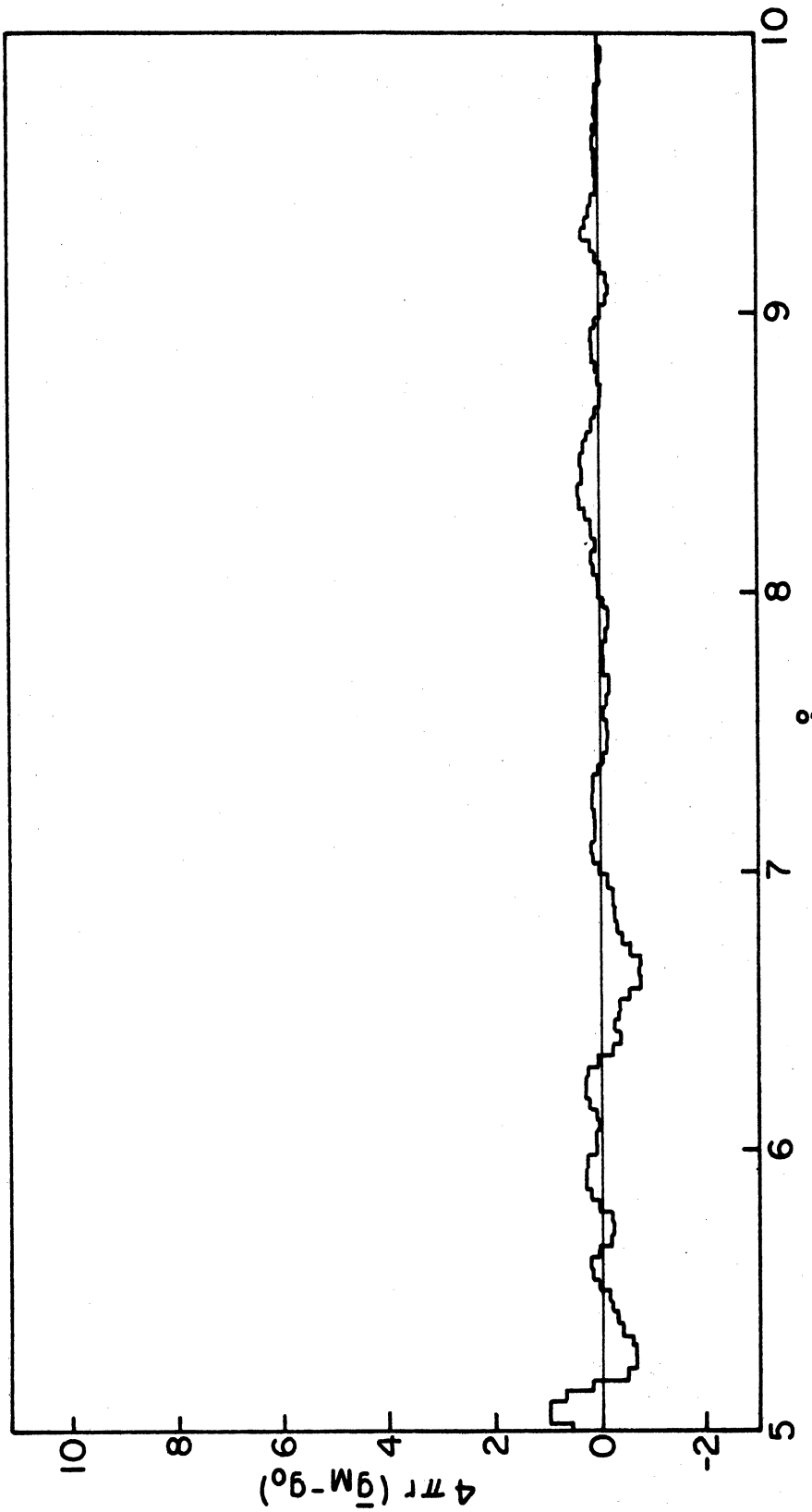

Figure 30 (b). Refined BeF_2 Radial Density Function

and below the peak. Without trying to explain away these and other shortcomings of this final rdf model, we feel it necessary to point out the very simple nature of the modeling procedure used, and to stress that there may well be sources of spurious structure in the rdf which we did not take into account (for example, the possibility of spurious structure in I(Q) contributing to the rdf was not considered).

6.1.3. Identification of features in the rdf. With reference to previous work on vitreous BeF_2, we can immediately determine which atom pairs contrubute to the first few rdf peaks. Warren's 1934 model (table 1), for example, predicts peaks due to Be-F pairs (with coordination number $\bar{n}$=4) at 1.60Å, due to F-F pairs ($\bar{n}$=6) at 2.62Å, due to Be-Be pairs ($\bar{n}$=4) at 3.20Å, due to second-neighbor Be-F pairs ($\bar{n}$=12) at 4.00Å, due to second neighbor F-F pairs ($\bar{n}$=9) at 4.65±0.45Å, and due to second-neighbor Be-Be pairs ($\bar{n}$=12) at 5.20Å. We can thus with some confidence (subject to further verification) label the peak at 1.56Å in figure 30 as due to first-neighbor Be-F coordination; at 2.52Å, first-neighbor F-F; at 3.06Å, first-neighbor Be-Be; at roughly 4.0Å, second-neighbor Be-F (which we abbreviate Be-(2)F); at 4.80Å, second-neighbor F-F (F-(2)F); and at 5.06Å, second-neighbor Be-Be (Be-(2)Be). It is ridiculous to expect that any features beyond the first can be explained completely in terms of only one pair type; it is apparent from figure 30 that the features beyond the F-F peak are not resolved, and we must

expect significant overlap of the peaks at larger r. The assignment of atom pair types to the peaks beyond Be-Be, although qualitatively reasonable on the basis of the various structural models, cannot be pushed too hard in a quantitative sense; we will not even attempt to analyze the peaks beyond Be-Be.

6.1.4. Analysis of the Be-F peak. We expect the Be-F peak to reflect a coordination number of 4, i.e. to show four fluorines bonded to each beryllium. We must take into account the scattering length weighting; we can see from equation (2.8),

$$\bar{g}(r) = N^{-1}\langle a^2\rangle^{-1} \sum_{t} \sum_{t'} N_t g_{t't}(r)$$

that in the vicinity of the Be-F peak

$$\bar{g}(r) = N^{-1}\langle a^2\rangle^{-1} \left\{ N_{Be}\, g_{FBe}(r) + N_F\, g_{BeF}(r) \right\} \tag{6.1}$$

where (repeating equation (2.9))

$$g_{t't}(\underline{r}) = N_t^{-1} \sum_{n_t=1}^{N_t} \sum_{n'_{t'}=1}^{N_{t'}} a_t a_{t'} \delta(\underline{r} - \underline{r}_{n_t} + \underline{r}_{n'_{t'}})(1 - \delta_{nn'}\delta_{tt'})$$

describes the distribution of type t' nuclei about an average type t nucleus. Furthermore we know from equation (2.10) that in the isotropic case,

$$g_{t't}(r) = N_{t'}/N_t \; g_{tt'}(r)$$

Since we also know that $N_F = 2N_{Be}$ and that $N = N_F + N_{Be}$, we can write for the first peak in $\bar{g}(r)$

$$\bar{g}(r) = \langle a^2 \rangle^{-1} \left\{ \frac{1}{3} g_{FBe}(r) + \frac{2}{3} g_{BeF}(r) \right\} \tag{6.2}$$

and using equation (2.10),

$$g_{BeF}(r) = \frac{1}{2} g_{FBe}(r) \tag{6.3}$$

so that

$$\bar{g}(r) = \langle a^2 \rangle^{-1} \left\{ \frac{2}{3} g_{FBe}(r) \right\} \tag{6.4}$$

If we redefine a^2 on the basis of a unit of composition,

$$\langle a^2 \rangle_u = a_{Be}^2 + 2a_F^2$$

$$= 3N^{-1} \sum_{i=1}^{N} a_i^2 = 3\langle a^2 \rangle$$

which is just three times the value used in Chapter Two, then

$$\bar{g}(r) = 2\langle a^2 \rangle_u^{-1} g_{FBe}(r) \tag{6.5}$$

We know that $g_{FBe}(r)$ describes the coordination of fluorines around berylliums, so we expect its integral over the first peak (properly weighted) to yield the coordination number:

$$\int_{\substack{\text{Be-F} \\ \text{peak}}} 4\pi r^2 g_{FBe}(r)\,dr = a_F a_{Be} \bar{n}_{FBe}$$

$$= (.565)(.774)\,\bar{n}_{FBe}$$

$$= .437\,\bar{n}_{FBe} \tag{6.6}$$

and

$$\int_{\substack{Be\text{-}F\\ peak}} 4\pi r^2 \bar{g}(r)\,dr = .706\,\bar{n}_{FBe}$$

If $\bar{n}_{FBe}$ is 4.0 as we expect, then the integral of $\bar{g}(r)$ over the first peak should be 2.84. If we sum up the area of the first peak in $4\pi r^2\bar{g}_M(r)$, figure 31, we find

$$\sum_{r=1.48}^{1.64} 4\pi r^2 \bar{g}_M(r)\,\Delta r = 2.929$$

which implies $\bar{n}_{FBe}$=4.14. We are thus comfortably close to the expected coordination number of 4.0 (3.5% high). On the basis of our finding $\bar{n}_{FBe}$=4.14, we have no reason to conjecture that any coordination other than fourfold is present.

Since $4\pi r^2\bar{g}(r)$ represents a distribution of pairs, we can also extract the mean pair separation,

$$\bar{r}_{BeF} = \int_{\substack{Be\text{-}F\\ peak}} 4\pi r^3 \bar{g}(r)\,dr \Big/ \int_{\substack{Be\text{-}F\\ peak}} 4\pi r^2 \bar{g}(r)\,dr$$

Again from the model rdf, we find

$$\sum_{r=1.48}^{1.64} 4\pi r^3 \bar{g}_M(r)\,\Delta r = 4.573$$

so that

$$\bar{r}_{BeF} = 4.573/2.929 = 1.561\ \text{Å}$$

Knowing the centroid of the peak we can compute its variance,

$$\langle \Delta r^2 \rangle_{BeF} = \int_{\substack{BeF\\ peak}} 4\pi r^2 \bar{g}(r)(r-\bar{r})^2\,dr \Big/ \int_{\substack{BeF\\ peak}} 4\pi r^2 \bar{g}(r)\,dr$$

We find from the model rdf that

$$\sum_{r=1.48}^{1.64} 4\pi r^2 g_M(r)(r-\bar{r})^2\,\Delta r = .00558$$

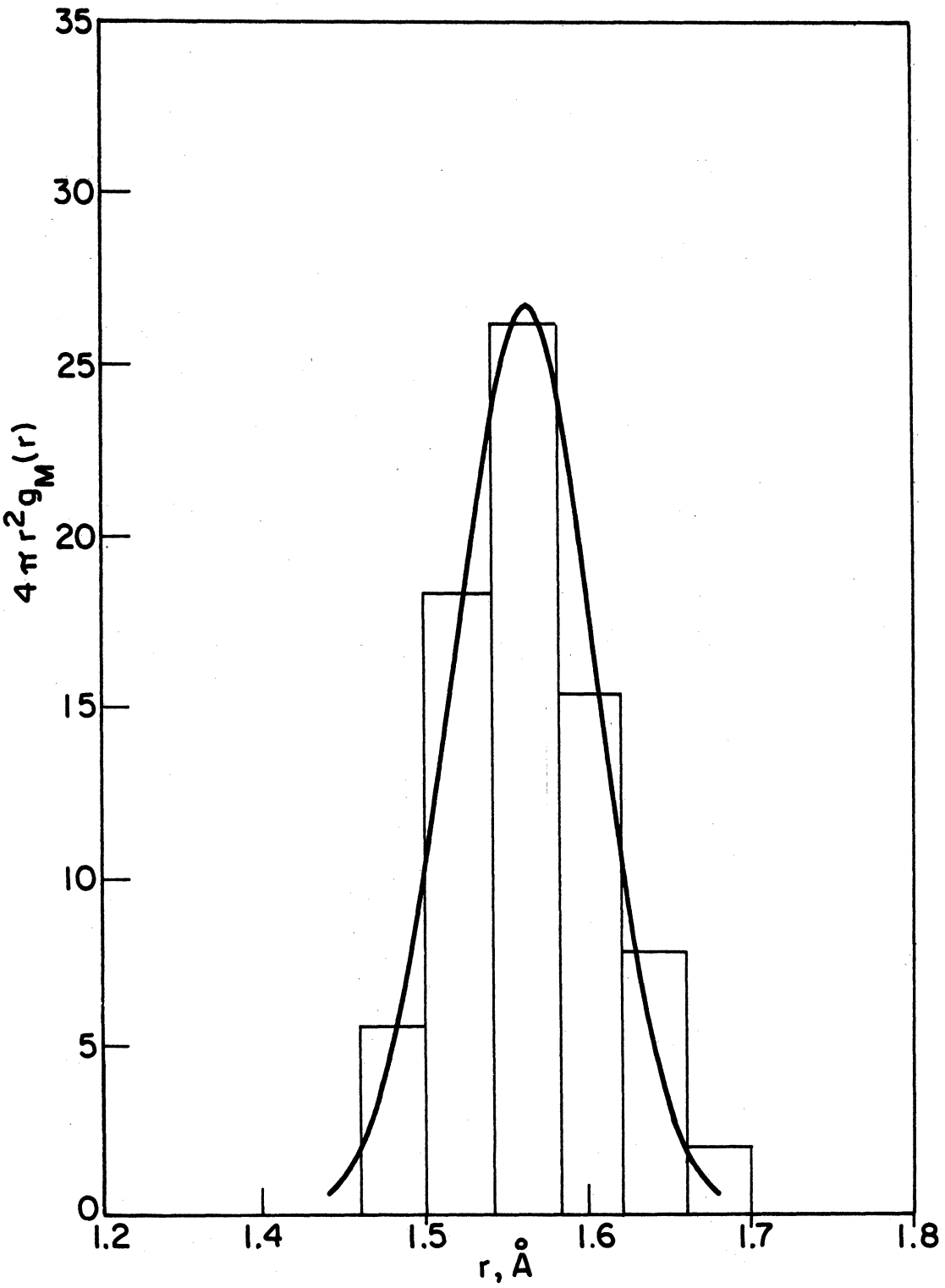

Figure 31. Be-F Peak in the Refined RDF

so the variance is

$$\langle \Delta r^2 \rangle_{BeF} = .00558/2.929 = .00190 \text{ Å}^2$$

and the rms width is

$$\langle \Delta r^2 \rangle_{BeF}^{1/2} = .0436 \text{ Å}$$

We may interpret this rms width of $4\pi r^2 \bar{g}_M(r)$ directly as an estimate of the rms deviation of the Be-F pair spacing from its mean value in vitreous BeF_2.

For comparison, we have superimposed on the peak in figure 31 a Gaussian with centroid, variance and area equal to those of the model peak. This Gaussian is a reasonable fit to the model histogram; we mentioned in connection with the Konnert and Karle termination error procedure that an assumption of the correctness of such Gaussian peaks is basic to that procedure.

6.1.5. Analysis of the F-F peak. If the F-F peak were isolated, we could evaluate the indicated coordination number:

$$\int_{\substack{FF \\ peak}} 4\pi r^2 \bar{g}(r) dr = \int_{\substack{FF \\ peak}} 4\pi r^2 \langle a^2 \rangle_u^{-1} \{2 g_{FF}(r)\} dr$$

$$= 2\langle a^2 \rangle_u^{-1} a_F^2 \bar{n}_{FF} = .516 \bar{n}_{FF}$$

The F-F peak in $4\pi r^2 \bar{g}_M(r)$, figure 32, is not isolated, however; contributions fron the Be-Be peak and from the apparently spurious peak between the F-F and Be-Be peaks overlap with the F-F peak on the high-r side. We have chosen to integrate only as far as the minimum of $4\pi r^2 \bar{g}_M(r)$, and to accept whatever inaccuracies that may introduce. On this

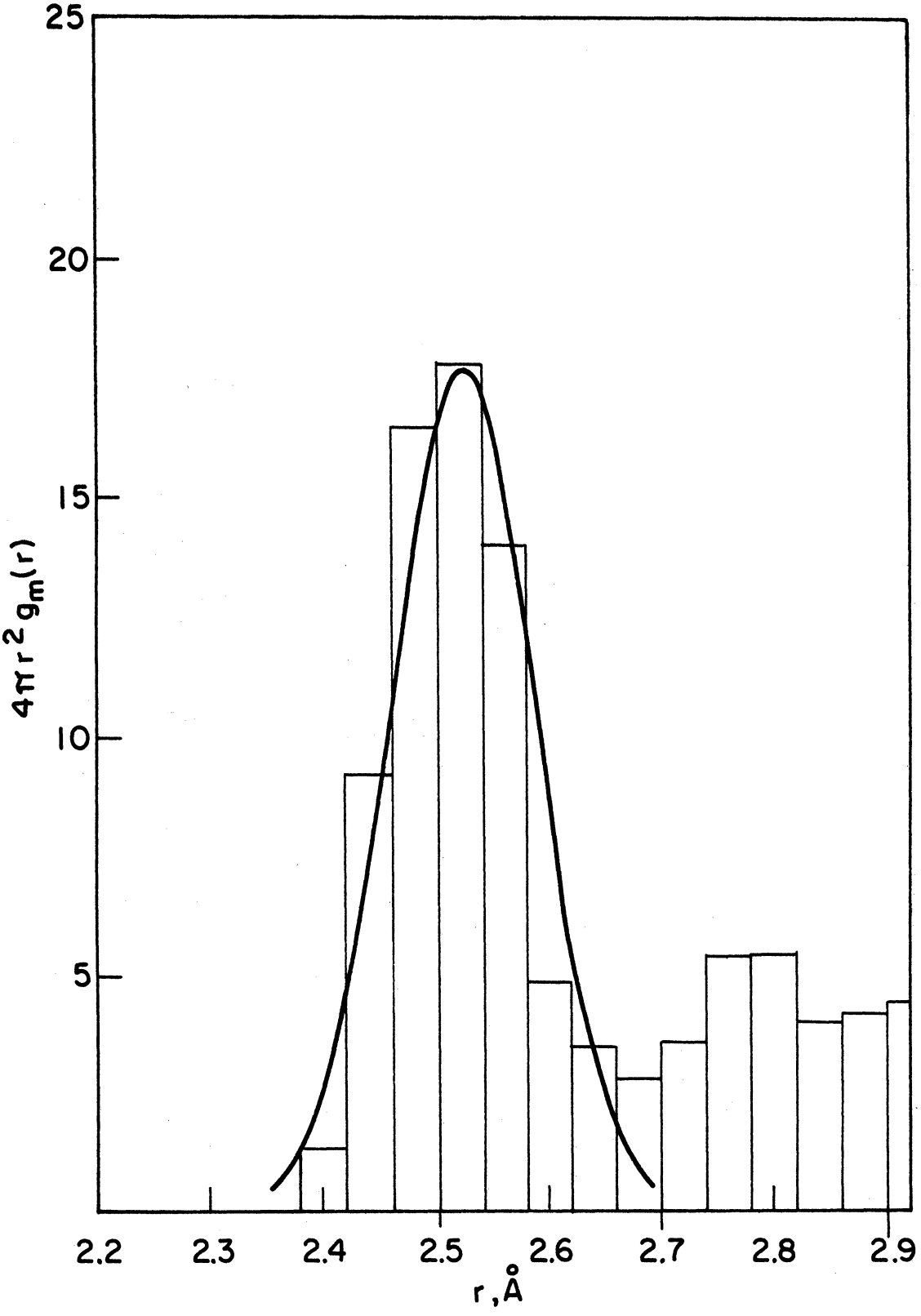

Figure 32. F-F Peak in the Refined RDF

basis, we find

$$\sum_{r=2.40}^{2.68} 4\pi r^2 \bar{g}_M(r)\,\Delta r = 2.804$$

$$\sum_{r=2.40}^{2.68} 4\pi r^3 \bar{g}_M(r)\,\Delta r = 7.077$$

so $\bar{n}_{FF}=5.43$, $\bar{r}_{FF}=2.524\text{Å}$. Using this value for $\bar{r}$, we also find

$$\sum_{r=2.40}^{2.68} 4\pi r^2 \bar{g}_M(r)\,(r-\bar{r})^2\,\Delta r = .01124$$

so the variance is

$$\langle \Delta r^2 \rangle_{FF} = .00401\ \text{Å}^2$$

and the rms width is

$$\langle \Delta r^2 \rangle_{FF}^{1/2} = .0633\ \text{Å}$$

Again we have shown a Gaussian with the experimental area, centroid and variance superimposed on the model histogram; the fit is not as good as for the Be-F peak, as the F-F model peak is markedly asymmetric.

6.1.6. Analysis of the Be-Be peak. The Be-Be peak in $4\pi r^2\bar{g}_M(r)$, figure 33, is even less well defined than the F-F peak. Again we have chosen to integrate between the minima of $4\pi r^2\bar{g}_M(r)$ on each side of the peak. Were the peak isolated, we would obtain

$$\int_{\substack{BeBe\\peak}} 4\pi r^2 \bar{g}(r)\,dr = \int_{\substack{BeBe\\peak}} 4\pi r^2 \langle a^2\rangle_u^{-1} g_{BeBe}(r)\,dr$$

$$= \langle a^2\rangle_u^{-1} a_{Be}^2\, \bar{n}_{BeBe}$$

$$= .484\ \bar{n}_{BeBe}\,.$$

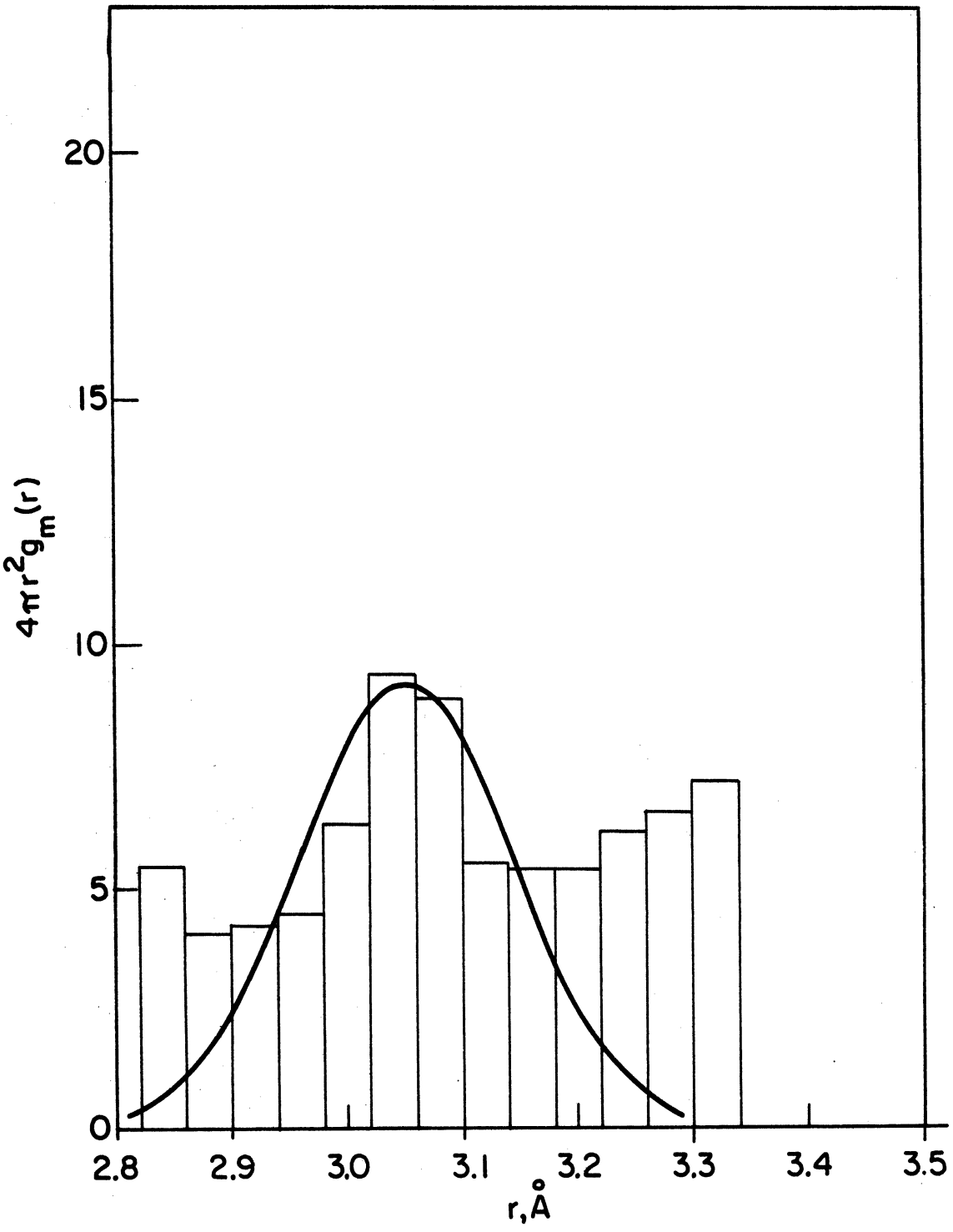

Figure 33. Be-Be Peak in the Refined RDF

Evaluating the area of the model rdf and moments between the minima of $4\pi r^2 \bar{g}_M(r)$, we find

$$\sum_{r=2.88}^{3.20} 4\pi r^2 \bar{g}_M(r)\,\Delta r = 2.148$$

$$\sum_{r=2.88}^{3.20} 4\pi r^3 \bar{g}(r)\,\Delta r = 6.552$$

from which we have $\bar{n}_{BeBe}$=4.44, $\bar{r}_{BeBe}$=3.050. Recognizing that the estimate for $\bar{n}_{BeBe}$ is not very good, we may still have confidence in the centroid value. If we leave off one histogram bar on each end of the sum, we have a smaller estimate of the coordination number:

$$\sum_{r=2.92}^{3.16} 4\pi r^2 \bar{g}_M(r)\,\Delta r = 1.768$$

$$\sum_{r=2.92}^{3.16} 4\pi r^3 \bar{g}_M(r)\,\Delta r = 5.403$$

from which $\bar{n}_{BeBe}$=3.65 and $\bar{r}_{BeBe}$=3.056. This coordination number estimate is just as far from what we expect as the original one; the true value undoubtedly lies somewhere between. From examining $4\pi r^2 \bar{g}_M(r)$, we see that there is considerable overlap from nearby features, so we cannot really expect to get a clean estimate of the Be-Be coordination number. Likewise we will have some difficulty establishing the Be-Be peak variance. Adopting the first set of values above for the centroid and coordination number (i.e., $\bar{r}_{BeBe}$=3.050A, $\bar{n}_{BeBe}$=4.44) we find

$$\sum_{r=2.88}^{3.20} 4\pi r^2 \bar{g}_M(r)\,(r-\bar{r})^2\,\Delta r = .0186$$

so

$$\langle \Delta r^2 \rangle_{BeBe} = .0186/2.148 = .00865 \text{ Å}^2$$

$$\langle \Delta r^2 \rangle_{BeBe}^{1/2} = .093 \text{ Å} .$$

Again we have plotted a Gaussian with the experimental Be-Be centroid, area and variance on figure 33. The fit to the model histogram is not particularly striking; but this comes as no surprise since the model peak itself is not very well defined.

6.1.7. Evaluation of mean bond angles. The mean F-Be-F and Be-F-Be bond angles can be evaluated in a straight forward manner from the peak centroid positions. To do this we simply consider a triangle (figure 34) with (taking the F-Be-F angle first) fluorines at two vertices and a beryllium at the third. Two sides then have length equal to the Be-F distance we have determined, and the third side is equal to the F-F distance. The F-Be-F bond angle is then

$$\measuredangle(F\text{-}Be\text{-}F) = 2\sin^{-1}\left[\frac{\bar{r}_{FF}}{2\bar{r}_{BeF}}\right] = 107.9^\circ$$

Similarly we find

$$\measuredangle(Be\text{-}F\text{-}Be) = 2\sin^{-1}\left[\frac{\bar{r}_{BeBe}}{2\bar{r}_{BeF}}\right] = 155.6^\circ$$

We summarize our analysis of the first three coordination peaks in our model rdf in table 6, and also repeat the results presented in table 2.

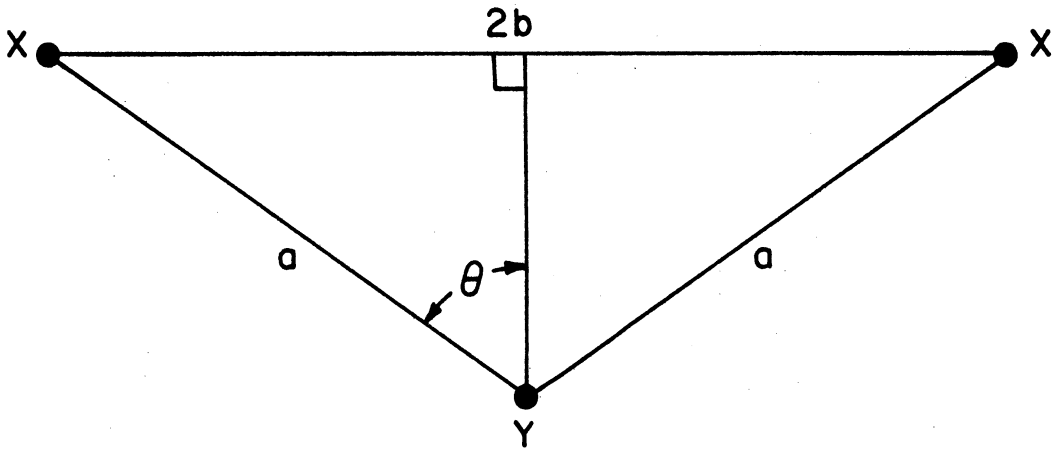

$$\measuredangle (X-Y-X) = 2\theta = 2\,\mathrm{Sin}^{-1}(b/a)$$

$$= 2\,\mathrm{Sin}^{-1}(\bar{r}_{XX}/2\bar{r}_{XY})$$

Figure 34. Geometry for calculation of bond angles. X,Y= Be or F.

TABLE 6. Comparison of Present Diffraction Results with Previously Published Work on Vitreous BeF_2

	This work*	Warren & Hill[8]	Batsanova et al.[12]	Zarzycki[13]	Narten[14]	Bates[54]
$\bar{r}_{BeF}$ (Å)	1.561±.020	1.60	1.43±.015	1.50	1.554±.004	.....
$\bar{r}_{FF}$ (Å)	2.524±.043	2.55	2.54	2.55	2.537±.004	.....
$\bar{r}_{BeBe}$ (Å)	3.050±.092	3.20	.....	3.00	3.037±.005	.....
$\measuredangle$(F-Be-F)	107.9°±3.6	105	125	116	109.5	.....
$\measuredangle$(Be-F-Be)	155.4°±9.0	180	.....	180	155.6	.....
$\bar{n}_{BeF}$	4.14±.04	4	4	4.4	3.8±.3	.....
$\bar{n}_{FF}$	5.43±.07	6	.....	6.8	5.7±.3	.....
$\bar{n}_{BeBe}$	4.44±.10	4	.....	.....	3.8±.3	.....
$\langle\Delta r^2\rangle^{1/2}_{BeF}$ (Å)	.044±.009	.....	.....	.....	.083	.064
$\langle\Delta r^2\rangle^{1/2}_{FF}$ (Å)	.063±.015	.....	.....	.....	.103	.073
$\langle\Delta r^2\rangle^{1/2}_{BeBe}$ (Å)	.093±.023	.....	.....	.....	.132	.074

*See Appendix Four for calculation of estimated uncertainties.

6.2 Comparison of RDF Results with Previous Work

6.2.1. Comparison with diffraction results. The comparison of individual peak positions, etc., among the various works does not require much comment; we are pleased to note that our results agree best with those we indicated in Chapter One as being the most reliable.

We will take time here to compare our results with those of Narten, which we feel are the highest quality of all the published diffraction results on vitreous BeF_2. Our peak positions agree reasonably well with Narten's with the possible exception of the F-F distance. Our experimental coordination numbers for F-F and Be-Be are somewhat far off, but still respectably close. (On reflection, it seems that all the problems just noted could have been overcome had we used a somewhat finer r-mesh in the computation of $\bar{g}_M(r)$).

Most encouraging is the fact that our experimental values for the rms peak widths in $4\pi r^2\bar{g}(r)$, while considerably lower than those reported by Narten, are in quite good agreement with the rms vibration amplitudes calculated by Bates[54] for his dynamical model of vitreous BeF_2 based on the β-quartz structure. Except for the Be-F peak, where Bates' amplitude value lies midway between our rms peak width and that of Narten, our values are considerably closer to those of Bates than are Narten's. The discrepancy between his values for the rms amplitudes and those of Narten was noted by Bates, who conjectured that low-frequency acoustic modes

not included in his dynamical model might be responsible for broadening the X-ray rdf peaks. This seems unlikely, since the wavelengths of low-frequency acoustic modes in vitreous BeF_2 are quite large compared to the first few neighbor distances (we will have more to say about this in our discussion of the inelastic scattering results below) so there should not be appreciable broadening of the coordination peaks from this source. In any case, our results certainly support Narten's assertion that the breadths of the vitreous BeF_2 rdf peaks are sufficiently small to be due entirely to thermal vibration.

6.2.2. Comparison with structural models. There are several structural models with which we may compare our refined experimental rdf. The previously mentioned work of Narten consisted in part of comparison of his X-ray rdf with a model based on the β -quartz structure with a number of random vacancies introduced. We have already noted our agreement or disagreement with several features of Narten's model (since the model fits his X-ray rdf quite acceptably, our comparison with the diffraction results constitutes a comparison with the model). We will make comparisons with two other models of a disordered BeF_2 structure--one a traditional random-network model (a "ball and stick" model), and one, the by-product of a molecular dynamics calculation (computer simulation) of BeF_2 liquid.

6.2.3. Bell and Dean vitreous SiO_2/BeF_2 "Model V." R.J. Bell of the National Physical Laboratory (U.K.) has generously provided us with a full set of coordinates of the atom sites in the largest of a series of models constructed by Dr. Bell and P. Dean. The model represents 188 Be and 426 F atoms, and was constructed according to a set of rules consistent with the Zachariasen random network hypothesis (there have been a number of such models built, by Bell and Dean and others[56]). From the model coordinates we have computed $\bar{g}(r)$ according to equation (2.7), utilizing scattering lengths appropriate to BeF_2 (the model can also be considered to represent SiO_2 or GeO_2). The function $4\pi r^2\bar{g}(r)$ for the Bell and Dean model is shown in figure 35. We have computed peak areas, centroids and variances from the model rdf; these are displayed in table 7.

TABLE 7. Peak Analysis of Neutron RDF from Bell and Dean Model V

Peak	$\bar{n}$	$\bar{r}$	$\langle \Delta r^2 \rangle^{1/2}$
Be-F	4.00	1.561Å	.054Å
F-F	6.18	2.546Å	.112Å
Be-Be	4.45	3.051Å	.086Å
	∠(F-Be-F) = 109.3°		
	∠(Be-F-Be) = 155.5°		

Unfortunately the statistics in the model rdf are rather bad at larger values of r. It is apparent that one cannot hope to build such a model which represents more than a small

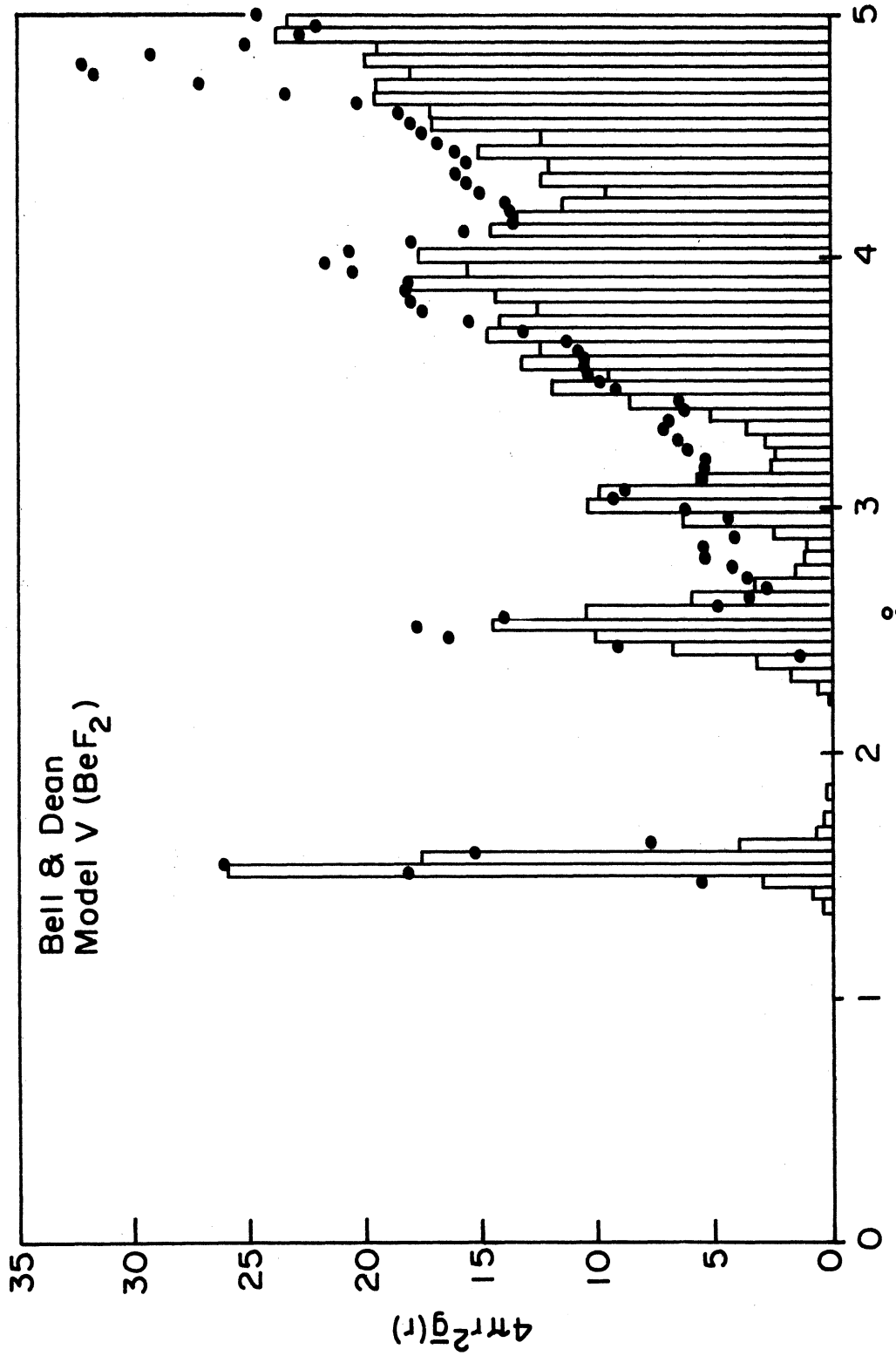

Figure 35. RDF for Bell and Dean Model V. Histogram, model rdf; dots, refined experimental rdf.

region in an actual material; even the (physically) very large Model V represents only a region of radius roughly 13Å (we arrived at this "equivalent radius" by computing the average distance between atom sites on the surface of the model, noting that for a sphere the average chord length is 4/3 times the radius). We note that the variations in Be-F and Be-Be first neighbor distances for the Bell and Dean model are quite close to our observed values; the F-F width on the other hand, is even larger than that observed by Narten, which we feel to be an overestimate of the true value. We also note that the Be-Be coordination number is overestimated from the neutron rdf even though the coordiantion number calculated from the individual pair distribution $4\pi r^2 g_{BeBe}(r)$ is 3.98, ½% below the expected value of 4. This explains to some extent our own overestimate of $\bar{n}_{BeBe}$; the effect is simply due to overlap of the Be-Be and F-F pair distributions above and below the Be-Be peak, and additionally, to overlap of the Be-F and Be-Be distributions above the Be-Be peak. This is of course no different than what we expected when we first noted that the F-F and Be-Be peaks were not sufficiently isolated to provide clean estimates of $\bar{n}_{FF}$ and $\bar{n}_{BeBe}$. The Bell and Dean model neutron rdf overestimates $\bar{n}_{FF}$, however, and our experimental value was a considerable underestimate (again, the coordination number calculated from $g_{FF}(r)$ is less than 1% different from the expected value of 6).

In the larger-r region, experimental rdf in general agrees reasonable well with the model rdf. The presence of

some residual spurious detail in the experimental rdf, and the statistical variations in the model rdf together make a detailed comparison in the region beyond the Be-Be peak of dubious value. We can certainly conclude, however, that the Bell and Dean Model V is not in substantial disagreement with our experimental rdf.

6.2.4. Rahman "frozen liquid" BeF_2 model. Molecular dynamics calculations have had widespread application in the study of liquid structure and dynamics. Aneesur Rahman of Argonne has kindly provided us[57] with a set of pair correlation functions derived from his molecular dynamics work on BeF_2. Simply stated, a molecular dynamics calculation is a computer simulation of the motion of a reasonably large number of particles interacting via some postulated force law. Knowing the positions of all the particles, the force on each can be calculated. One can then allow the particles to move under the influence of the calculated forces for a short time; after which new forces can be calculated and the simulation continued. The suitability of this technique for the simulation of liquid motion is readily apparent; to our knowledge, there has been no previous attempt to identify a "frozen" (or perhaps more properly, a "supercooled") molecular dynamics liquid structure with a glass.

In the present case, Be^+ and F^- ions were simulated; the resulting liquid (figure 36) shows that the ions arranged themselves into the familiar tetrahedral BeF_2 structure.

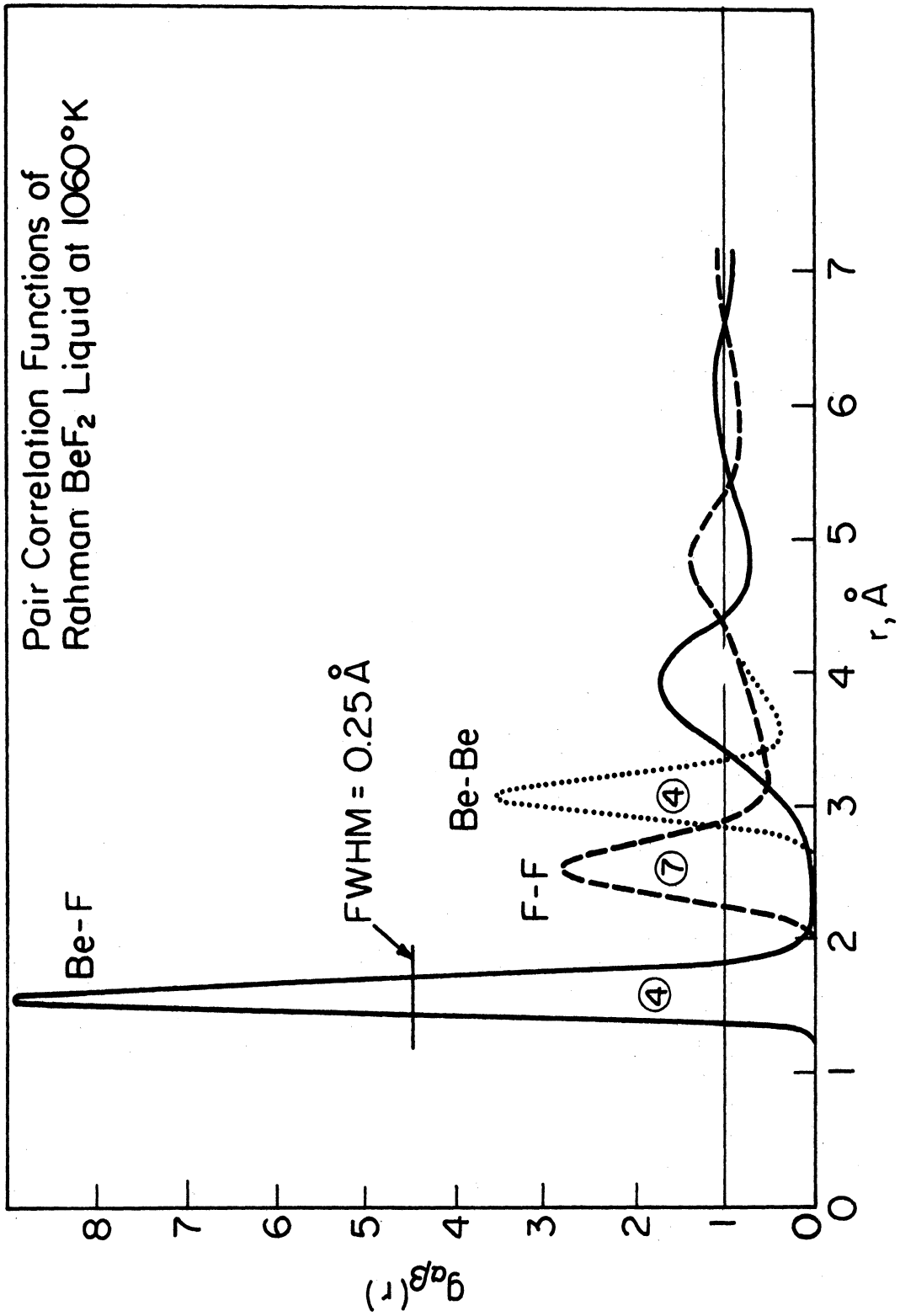

Figure 36. Pair Correlation Functions of Rahman BeF_2 Liquid Model

The BeF_2 liquid was "cooled" by reducing the total system energy, until the mean particle energy was brought to a level corresponding to a temperature of 480°K, at which point the structure became static. Pair correlation functions for the 480K BeF_2 system are shown in figure 37. Comparison with the liquid pair functions of figure 36 shows that the coordination peaks are considerably sharper and higher, with the areas of course unchanged. The fact that the peaks are only marginally narrower in the 480K case indicates that crystallization has been avoided; the structure at 480K is remarkably similar to that of the liquid.

We have also computed the neutron rdf, $\bar{g}(r)$, for the supercooled liquid model. This is shown in figure 38. Extracting the usual parameters from the coordination peaks in $4\pi r^2\bar{g}(r)$, we find the values given in table 8.

TABLE 8. Peak Parameters in Rahman "Supercooled" Liquid Model $4\pi r^2\bar{g}(r)$

Peak	$\bar{n}$	$\bar{r}$	$\langle \Delta r^2 \rangle^{1/2}$
Be-F	4.01	1.575Å	.081Å
F-F	5.94	2.577Å	.193Å
Be-Be	5.61	3.061Å	.118Å
	$\measuredangle$ (F-Be-F) = 109.8°		
	$\measuredangle$ (Be-F-Be) = 152.7°		

The overlap of the coordination-peaks is so severe in this case that we cannot get a good estimate of $\bar{n}_{BeBe}$ from the neutron rdf (but note that the integration of $4\pi r^2 g_{BeBe}(r)$

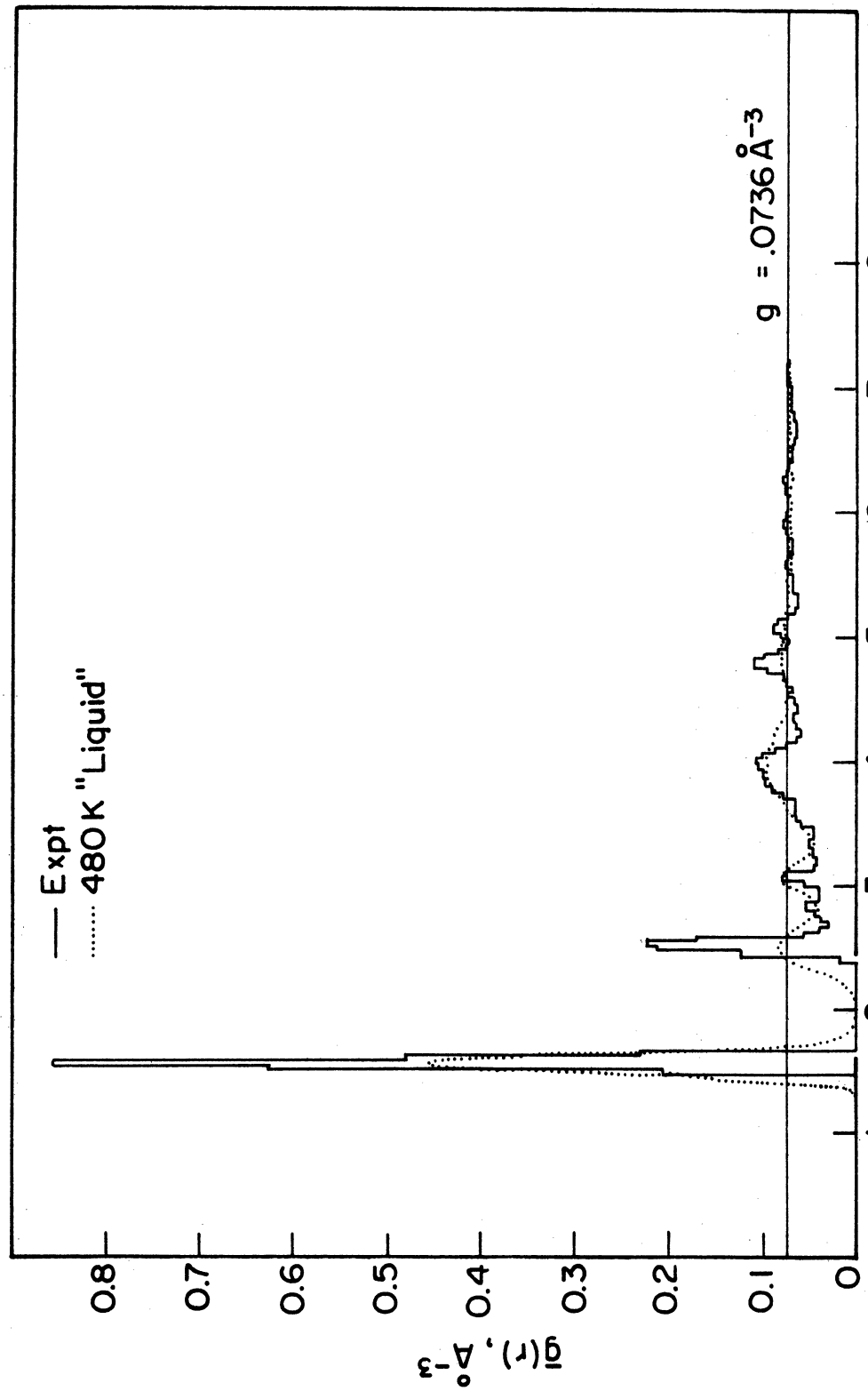

Figure 37. Neutron RDF of Rahman Supercooled BeF_2 Liquid Model. Curve, model rdf; histogram, refined experimental rdf.

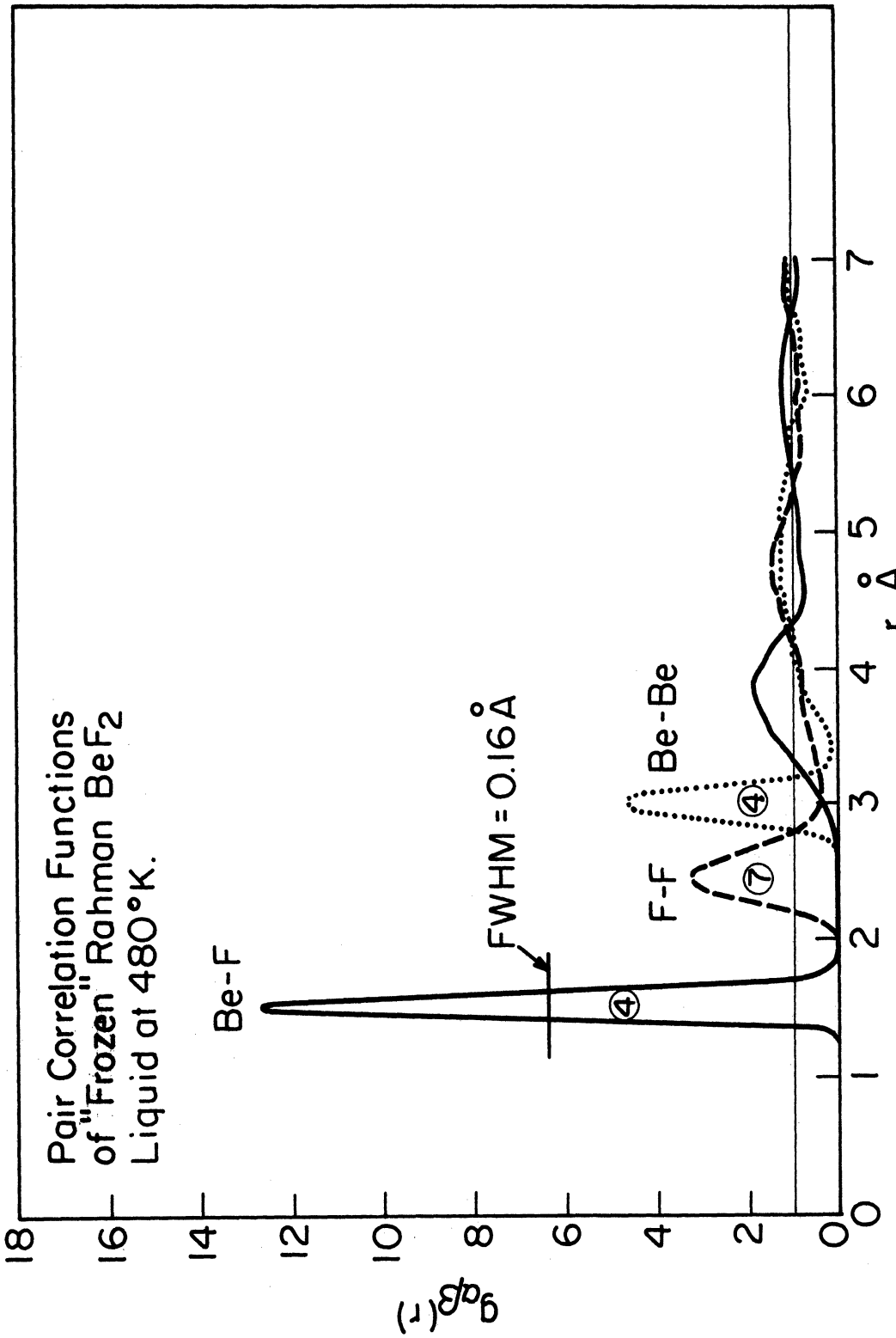

Figure 38. Pair Correlation Functions of Rahman Supercooled BeF_2 Liquid Model

yields the expected value of 4 as indicated on figure 37). With the exception of the Be-Be peak, all the coordination peaks for this model are significantly broader than in our observed rdf. In addition, the peak centroid positions differ appreciably from those we (and other workers) have determined. We conclude that the supercooled molecular dynamics liquid does not represent a model of the BeF_2 glass structure.

6.3 Interpretation of Inelastic Scattering Results

6.3.1. Overview. There is a wealth of information concerning the dynamics of vitreous BeF_2 contained in the scattering law we have measured. As we indicated in Chapter Two, however, this information is obscured to a large extent due in part to the polyatomic nature of BeF_2, and in part due to interference effects which can complicate the frequency dependence of the scattering law. We must rely heavily on various assumptions, which may or may not be valid in various regions of momentum and energy transfer space in order to extract from the measured scattering law any information directly interpretable in terms of the dynamics of vitreous BeF_2.

We will attempt only the simplest analysis of the measured scattering law; first comparing features in the "generalized frequency distribution function" $G(Q,\omega)$, (section 2.4) derived from the experiment with bands observed in infrared absorption and Raman scattering measure-

ments on vitreous BeF_2, and then comparing our calculation of the "acoustic mode scattering law" (section 2.3) with the measured scattering law.

6.3.2. Spectroscopic results on vitreous BeF_2. We will analyze the experimental $G(Q,\omega)$ in terms of three spectroscopic studies of vitreous BeF_2: the infrared absorption work of Zarzycki and Naudin[58], the Raman spectroscopy of Batsanova et al.[11], and the infrared and Raman studies of Bates[54]. We summarize the findings of these authors in table 9.

TABLE 9. Infrared and Raman Bands of Vitreous BeF_2

Author	Zarzycki & Naudin[58]	Batsanova et al.[11]	Bates[54,59]
observed frequencies in cm^{-1}*	800	900-910	805
	715	760	410
	435	392	280
		246	

*1 cm^{-1} optical wave number is equivalent to an energy transfer of .124 meV, or an angular frequency of .189 ps^{-1}.

6.3.3 Other information on the vitreous BeF_2 frequency distribution. Unfortunately most of the spectroscopic data is at higher frequencies than we can reach using thermal neutron inelastic scattering. We are fortunate to have some other frequency distribution information.

Bell, Bird and Dean[60] have calculated the vibrational spectrum of several of the Bell and Dean random network

models. We quote the results for their Model II (503 atoms) considered as BeF_2: Bell et al. have also calculated spectra for the model taken as SiO_2 and GeO_2. The calculated spectrum for the BeF_2 model contains four main peaks, at 195, 335, 630 and 715 cm^{-1}. The lower two of these four frequencies are accessible to us via thermal neutron scattering. Bell et al. suggest that the 195 cm^{-1} peak is probably due to bond-bending and bond-rocking vibrations of F atoms, and the 335 cm^{-1} peak to bond-stretching F vibrations.

The only published inelastic neutron scattering results on vitreous BeF_2 are those of Leadbetter and Wright.[61] By utilizing very coarse time-of-flight resolution in their cold neutron experiment (4.24 meV incident energy), Leadbetter and Wright were able to collect statistically meaningful data over a very wide range of energy transfer, out to 500 cm^{-1} and beyond. They were of course unable to resolve much fine detail in the scattering law, but the glass scattering law is not expected to show particularly sharp structure so this inability may be of small importance. Utilizing a function analogous to our $G(Q,\omega)$, Leadbetter and Wright concluded that there are peaks in the glass frequency spectrum $g(\omega)$ at frequencies of 38 ± 4 cm^{-1}, 60 ± 5 cm^{-1}, 80 ± 5 cm^{-1}, and 105 ± 5 cm^{-1}. They also reached the important conclusion that at least for low Q and ω, the positions of peaks in the scattering law can be plotted as "average dispersion curves" as for polycrystals.[62] This is not particularly surprising if we truly believe in the importance of

long-wavelength acoustic modes in determining one-quantum scattering at low Q and ω, but it is certainly interesting that wave-vector conservation conditions appear to operate much as for polycrystals, near the first peak of the glass structure factor (the region in Q space near the first peak in the structure factor is analogous to the second Brillouin zone in a crystal). This is a clear manifestation of the importance at low Q and ω of the interference terms we were so anxious to ignore in equation (2.68).

6.3.4. Interpretation of the generalized frequency distribution $G(Q,\omega)$. As stated in section 4.9, we have transformed the measured scattering law to the function $G(Q,\omega)$ defined by equation (2.67). We have included plots of $G(Q,\omega)$ for each detector subgroup in the TNTOFS experiment as an appendix. Each subgroup, it will be recalled, represents the scattering at fixed scattering angle with approximately 1.8° angular resolution. We have only displayed the upscattering (neutron energy gain) portion of the data in the Appendix. The downscattering (energy loss) data are much more densely spaced due to the time-of-flight mesh, but typically extend only over a limited range of energy transfer ($\omega < 30$ ps^{-1}). The upscattering data seem quite adequate for the present purposes.

The curve drawn through the data points are cubic spline smoothing functions (see section 4.4) with the smoothing

parameter chosen for each subgroup to make the fit pleasing to the author (we would assert that the spline function fits shown are if anything conservatively drawn). The splines used here are considerably less stiff than those used for the structure factor data.

In light of the discussion of Chapter Two and of the results of Leadbetter and Wright, we have chosen to divide the data further into what we will call "low-Q" and "high-Q" regions. The low-Q region encompasses data subgroups 2 through 8, the high-Q region subgroups 9 through 32 (this corresponds to $2.90 \lesssim Q_e \lesssim 6.90$ in the high-Q region, where Q_e is the value of Q at $\omega=0$ for each subgroup). Recall that we expect the self terms in equation (2.68) to become relatively more important as Q increases; thus we may expect the one-quantum scattering in the high-Q region to be influenced to a lesser extent by interference terms than that in the low-Q region. On the other hand, if we wish to map out "average dispersion curves" by plotting the positions of maxima in $G(Q,\omega)$, the data in the low-Q region will probably be more useful.*

There is a caveat concerning the interpretation of $G(Q,\omega)$ in the high-Q region, however. The G function has a simple interpretation only for one-quantum scattering; it was derived on the assumption that one-quantum scattering is dominant. This assumption unfortunately becomes worse

*The high-Q region as we have defined it corresponds roughly to the third and higher Brillouin zones in a crystal; the low-Q region to the second zone.

as Q increases, so that as interference effects die out, multiquantum scattering processes come increasingly into the picture and do their own job of obscuring the desired information in $G(Q,\omega)$. Since we have no easy handle on the magnitude of the multiquantum terms in the scattering law, we will continue to ignore their presence and turn to the problem of extracting the information on $g(\omega)$ contained in $G(Q,\omega)$.

DeWette and Rahman[63] have shown that for a polycrystal $G(Q,\omega)$ may have much more structure than $g(\omega)$. It seems a fair statement on the basis of their detailed calculations for noble gas polycrystals, that $G(Q,\omega)$ show peaks for all values of ω at which the derivative of $g(\omega)$ is discontinuous. This includes Van Hove singularities ("corners") as well as peaks in $g(\omega)$, so it is misleading to say simply that peaks in $G(Q,\omega)$ correspond to peaks in $g(\omega)$. $G(Q,\omega)$ may also have peaks at values of ω not corresponding to pronounced features in $g(\omega)$. This is because of the influence of the polarization factors $\underline{Q}\cdot\underline{e}_\nu^\lambda$ in equation (2.68), which may cause $G(Q,\omega)$ to vary sharply in regions where the character of the atomic motions changes.

We have utilized the following simple procedure to identify the values of ω for which $G(Q,\omega)$ has systematic maxima (ie, those appearing in a number of detector subgroups) in the high-Q region: first, associate with each peak in $G(Q,\omega)$ at a given angle, the value of ω correspond-

ing to the local maximum in $G(Q,\omega)$. Next, plot as a function of ω the total number of peaks (in all subgroups of the high-Q region) appearing in $\Delta\omega$ about ω. We illustrate such a plot for $\Delta\omega = 2.5$ ps^{-1} (=13.3 cm^{-1}) in figure 39. The positions of peaks in figure 39 are listed in table 10.

TABLE 10. Systematic Maxima of $G(Q,\omega)$

57 ± 8 cm^{-1}	194 ± 5 cm^{-1}
88 ± 10 cm^{-1}	263 ± 15 cm^{-1}
126 ± 10 cm^{-1}	354 ± 15 cm^{-1}
164 ± 10 cm^{-1}	

Our peaks at 57 ± 8 and 88 ± 10 cm^{-1} undoubtedly correspond to those observed by Leadbetter at 60 ± 5 and 80 ± 5 cm^{-1}. We do not see a peak corresponding to that observed at 105 ± 5 cm^{-1} by Leadbetter, though our peak at 126 ± 10 cm^{-1} may be the same. Our peak at 194 ± 5 cm^{-1} probably corresponds to the 195 cm^{-1} peak calculated by Bell et al., and the peak at 354 ± 15 cm^{-1} to that calculated at 335 cm^{-1}. Our peak at 263 ± 15 cm^{-1} lies between the IR band of Batsanova et al. at 246 cm^{-1}, and the strong Raman band of Bates et al. at 280 cm^{-1}; there is considerable structure in the plot of figure 39 in this region, and we are hard pressed to make an unequivocal statement concerning this peak. There remains our observed peak at 164 ± 10 cm^{-1}; it corresponds to no other reported band, yet there is no question of its presence in our $G(Q,\omega)$.

We recognize the very simple nature of our algorithm

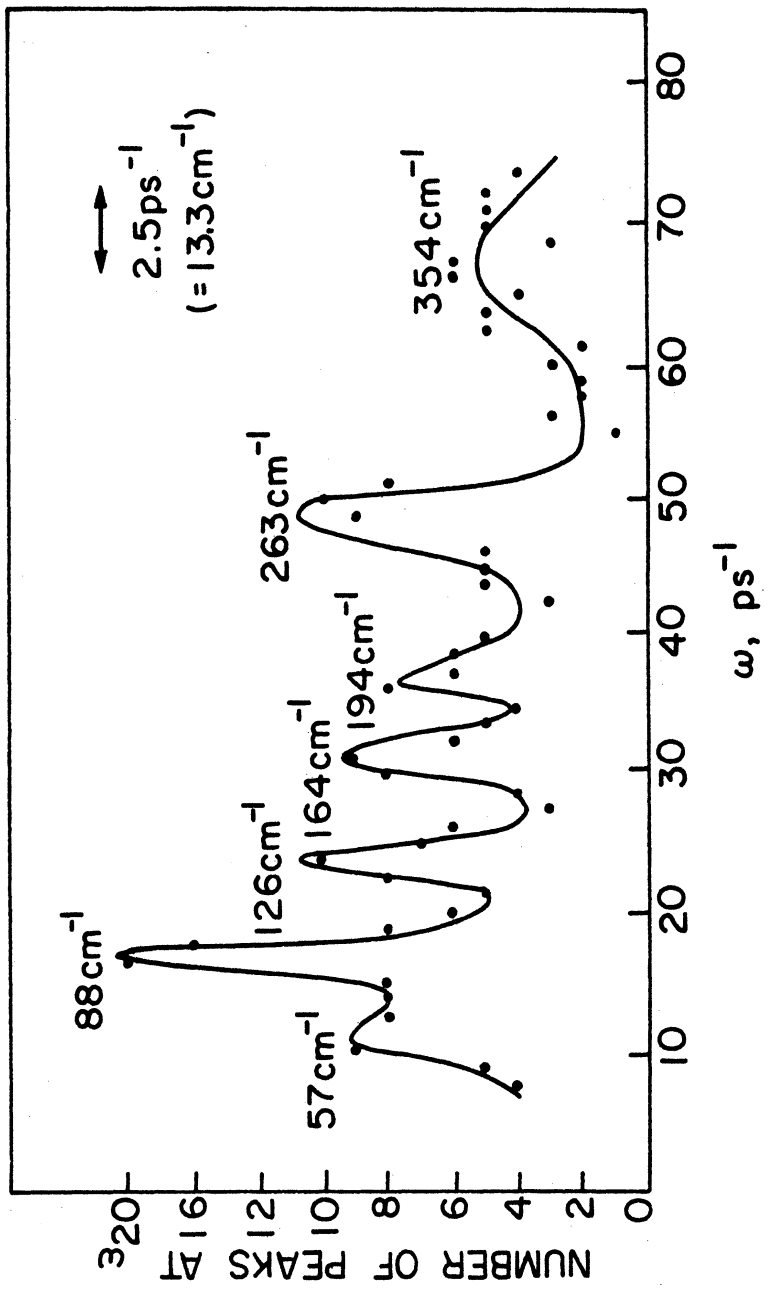

Figure 39. Determination of systematic maxima in G(Q,ω).

for identifying systematic peaks in $G(Q,\omega)$. Certainly there is a great deal of subjective judgment involved, at every step of the process beginning with the selection of smoothing spline parameters, and finally with picking peaks off a plot such as figure 39. We do not intend to apologize for using such a simple procedure; we feel that despite its simplicity it has worked admirably well.

6.3.5. Comparision with the calculated acoustic-mode scattering law. We have calculated the acoustic-mode scattering law derived in section 2.3 for comparison with the experimental results. We have used the bulk density of vitreous BeF_2, 1.96 g/cm^3, and the sound velocities quoted by Leadbetter and Wycherley[64] which were measured by Kurkjian, $v_l = 4.231$ km/sec and $v_T = 2.814$ km/sec.

The structure factor which appears in the expressions for the acoustic-mode scattering law is not the total, but the elastic structure factor. In principle our measured scattering law for vitreous BeF_2 can be integrated to give the elastic structure factor. We have chosen instead to use an approximate elastic structure factor which is just out measured total structure factor weighted by an approximate Debye-Waller factor. We have proceeded thus because it is the total structure factor we have in detail; to get the elastic structure factor on a sufficiently fine Q-mesh would require considerable interpolation rendering the result

approximate anyway. To get the approximate Debye-Waller exponent, we have plotted the ratio of elastic to total scattering as determined by integration of the measured scattering law, vs. Q^2 as shown in figure 40. This plot shows that the ratio can be roughly approximated by $e^{-.02Q^2}$, which is the approximate Debye-Waller factor we have used in evaluation of the acoustic-mode scattering law.

The results of evaluation of the acoustic-mode scattering law for several angles is shown in figures 41-44. We have chosen to plot $G(Q,\omega)$ instead of $S(Q,\omega)$. We see from the figures that the acoustic $G(Q,\omega)$ underestimates the measured G at the smallest angle, fits pretty well in subgroup 4, and overestimates the measured G at the larger angles, if we confine attention to the region $-8ps^{-1} < \omega < 8ps^{-1}$. The failure to fit at larger ω is no surprise, since the picture of purely longitudinal and purely transverse modes with linear dispersion curves cannot be trusted at large

It is very interesting that the agreement is best for the angles (e.g. subgroup 4 at 21.6°) which correspond to an elastic Q near the first diffraction peak at 1.60Å^{-1}. A possible explanation is that in this region (where Leadbetter has shown an average dispersion curve exists) our assumption of simple longitudinal and transverse acoustic modes with no dispersion is at its best; and in particular the no-dispersion assumption (i.e. $\omega = q$) is best quite close to the first diffraction peak where the

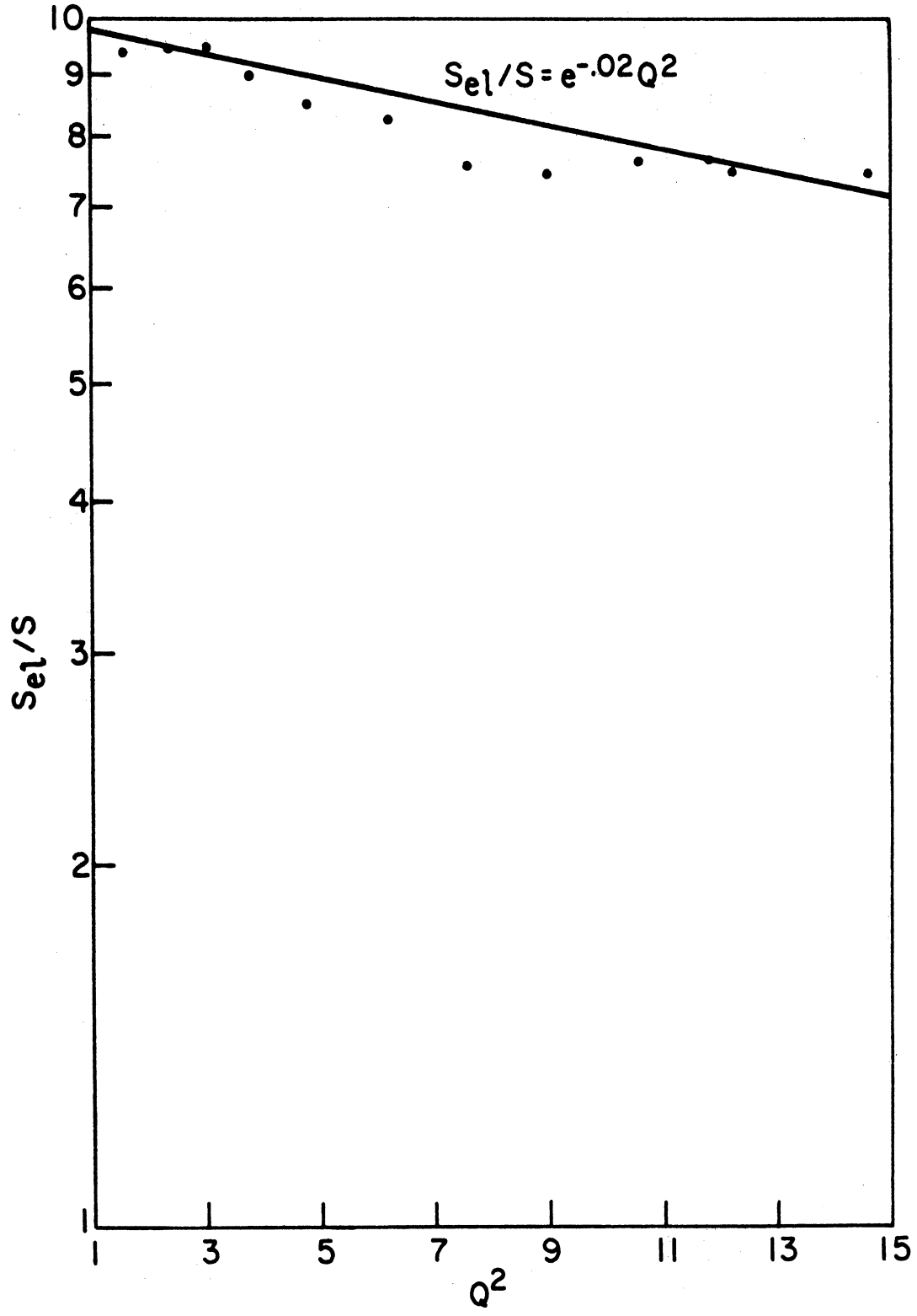

Figure 40. Determination of Approximate Debye-Waller Exponent

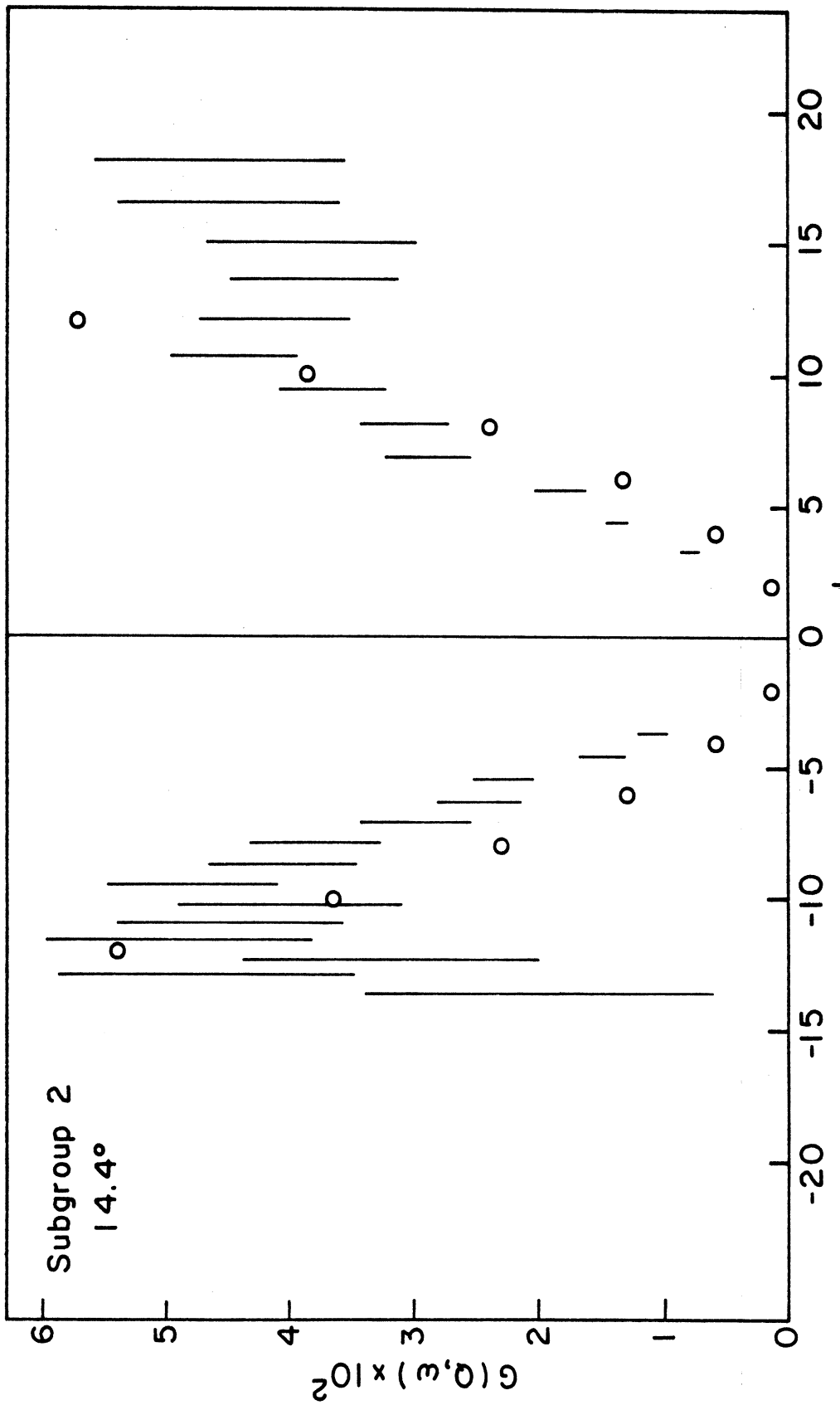

Figure 41. Comparison of Acoustic-mode $G(Q,\omega)$ with measured $G(Q,\omega)$

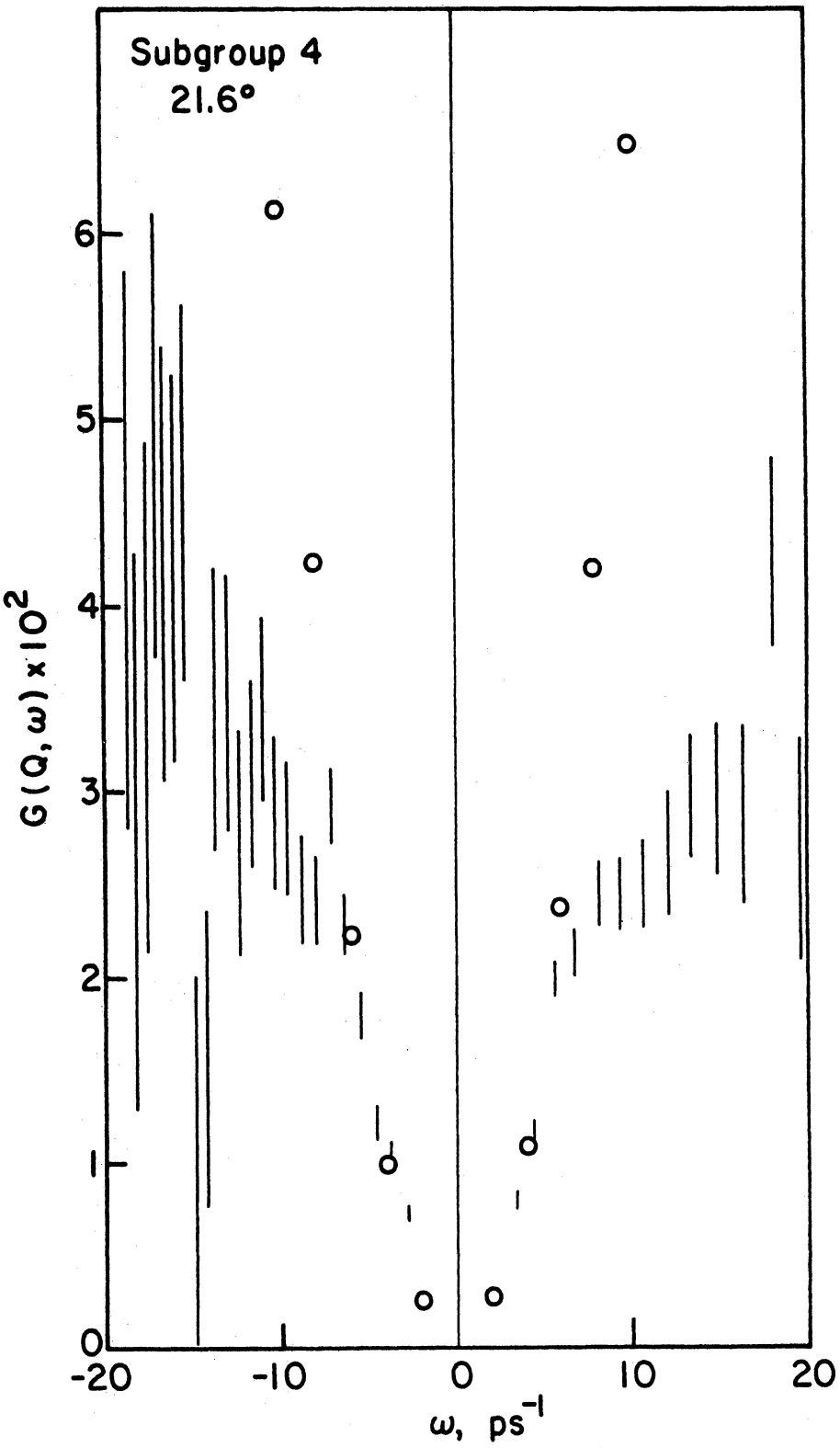

Figure 42. Comparison of Acoustic-mode G(Q, ω) with measured G(Q, ω)

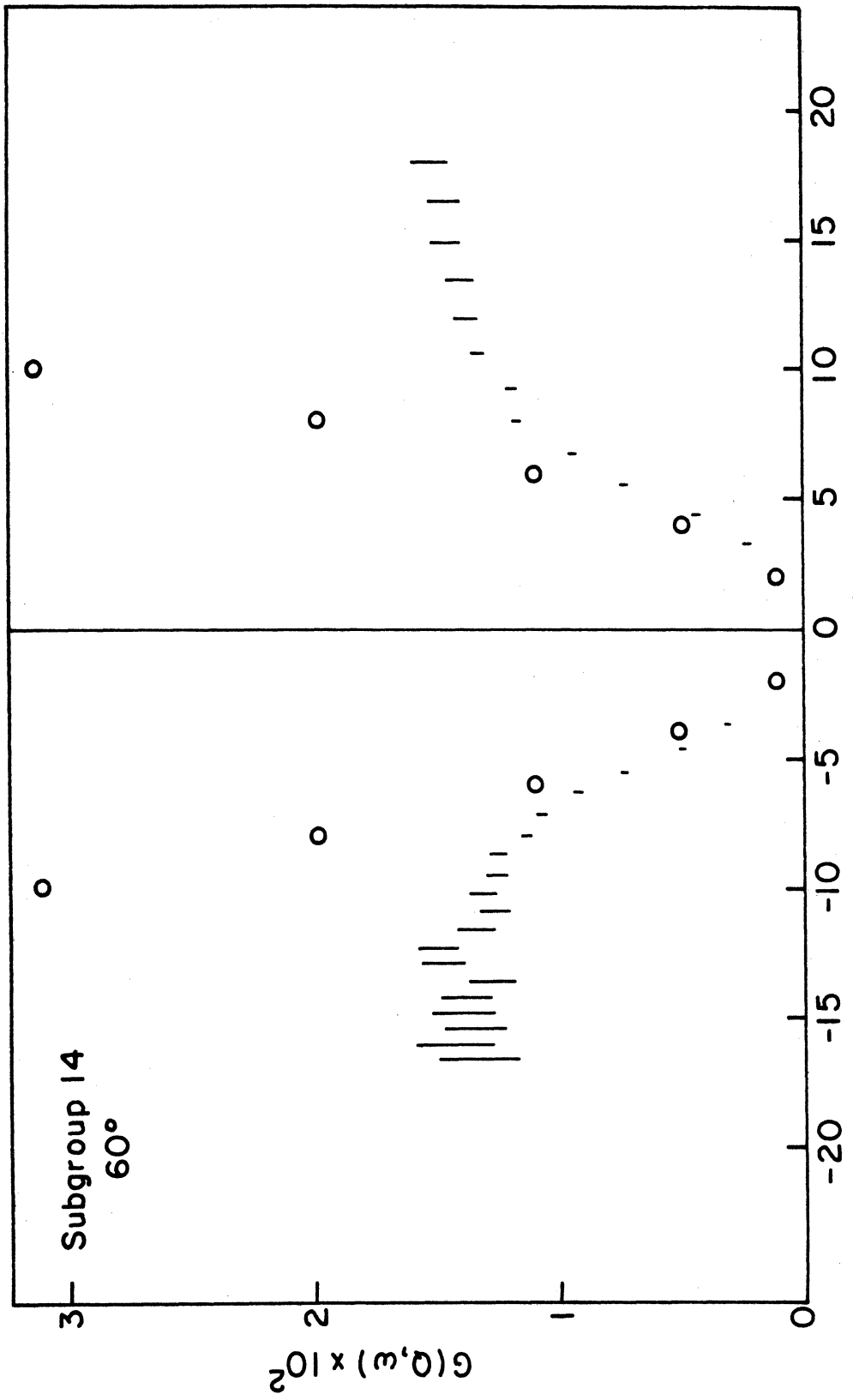

Figure 43. Comparison of Acoustic-mode $G(Q,\omega)$ with measured $G(Q,\omega)$

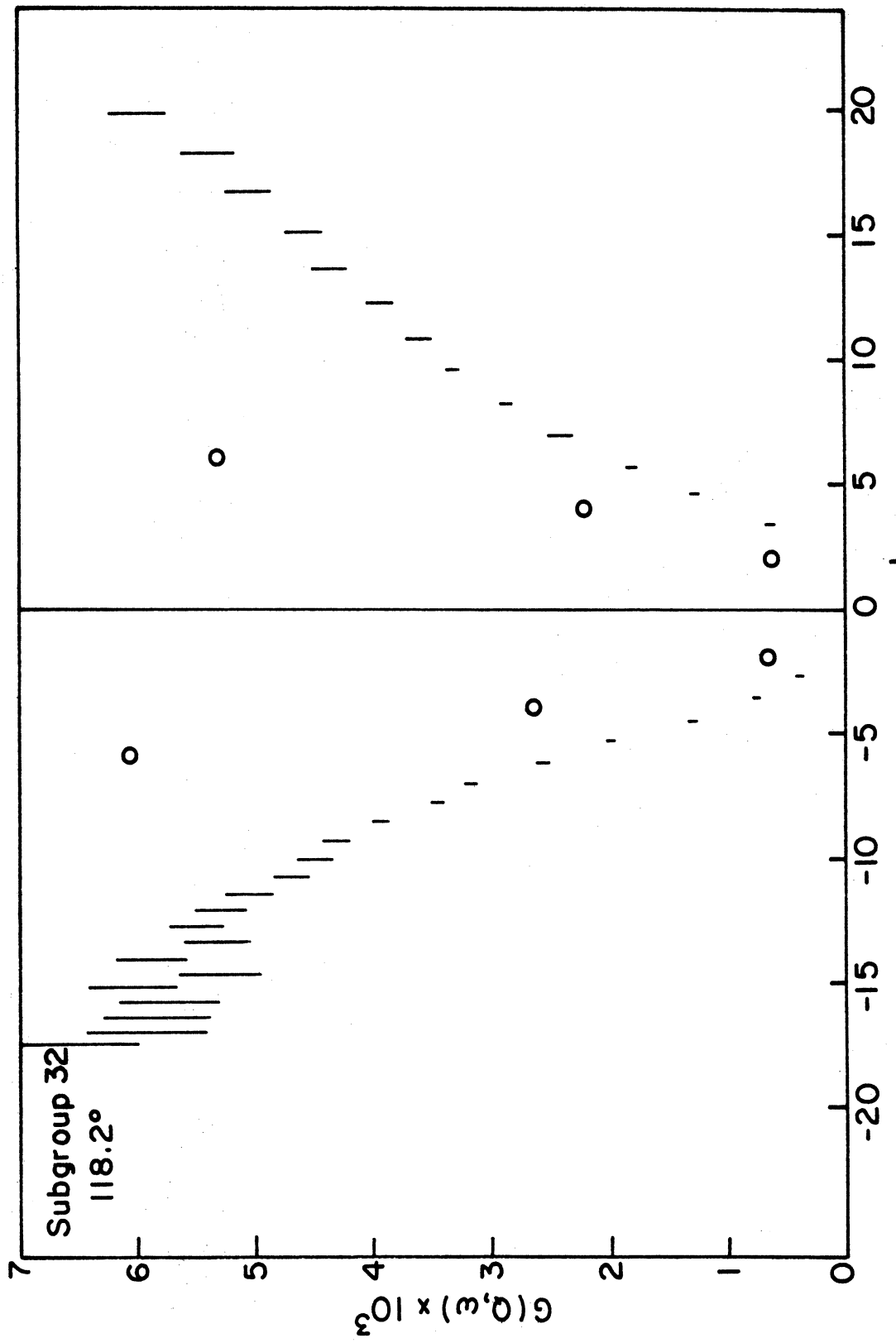

Figure 44. Comparison of Acoustic-mode $S(Q,\omega)$ with measured $G(Q,\omega)$

average dispersion curve has not yet broken over from its initial linear rise.

We may estimate the wavelength of our "long-wavelength" acoustic modes from the frequency at which the calculation begins to fail. Taking this value as $\omega_m = 8\ ps^{-1}$, we find for L modes

$$\omega_m = v_L q_m^L$$

$$8 \cdot 10^{12}\ sec^{-1} = (4.23 \cdot 10^5\ cm/sec)\, q_m^L$$

$$q_m^L = 1.9 \cdot 10^7\ cm^{-1}$$

or

$$\lambda_L = 2\pi / q_m^L = 3.3 \cdot 10^{-7}\ cm = 33\ \text{Å}$$

and for T modes,

$$q_m^T = 2.8 \cdot 10^7\ cm^{-1}$$

$$\lambda_T = 22\ \text{Å}$$

These would appear to indicate the minimum wavelength at which the simple modes we have assumed can provide a decent picture of the glass dynamics, at least as reflected in the scattering law.

APPENDIX ONE

THE FUNCTION $G(Q,\omega)$ FOR VITREOUS BeF_2

We present plots of the measured scattering law interpolated at several values of Q, and of the function $G(Q,\omega)$ at constant angle (for positive energy transfers) from the 31 detector subgroups.

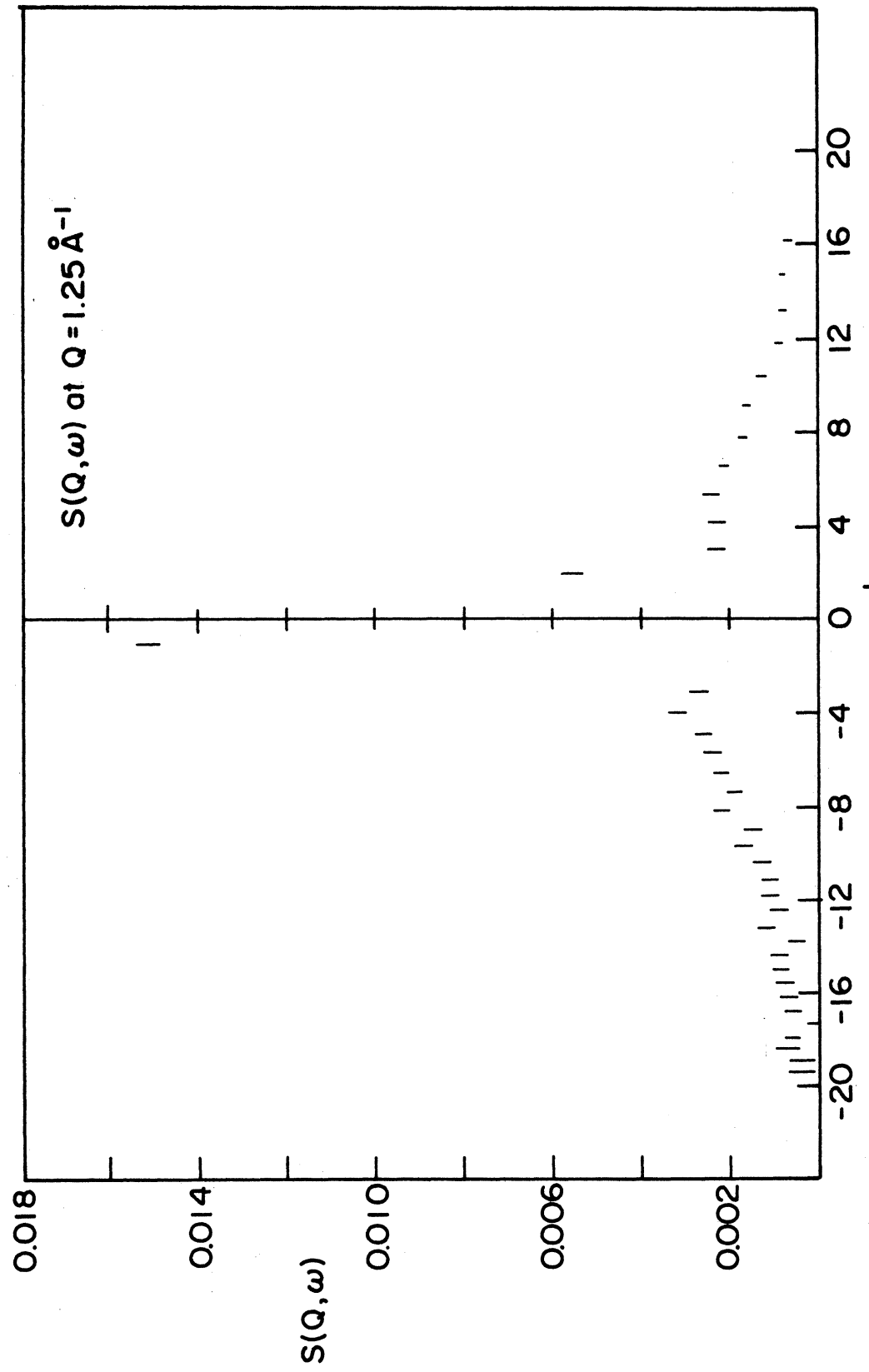

Figure A1. $S(Q,\omega)$ interpolated at $Q = 1.25\text{Å}^{-1}$

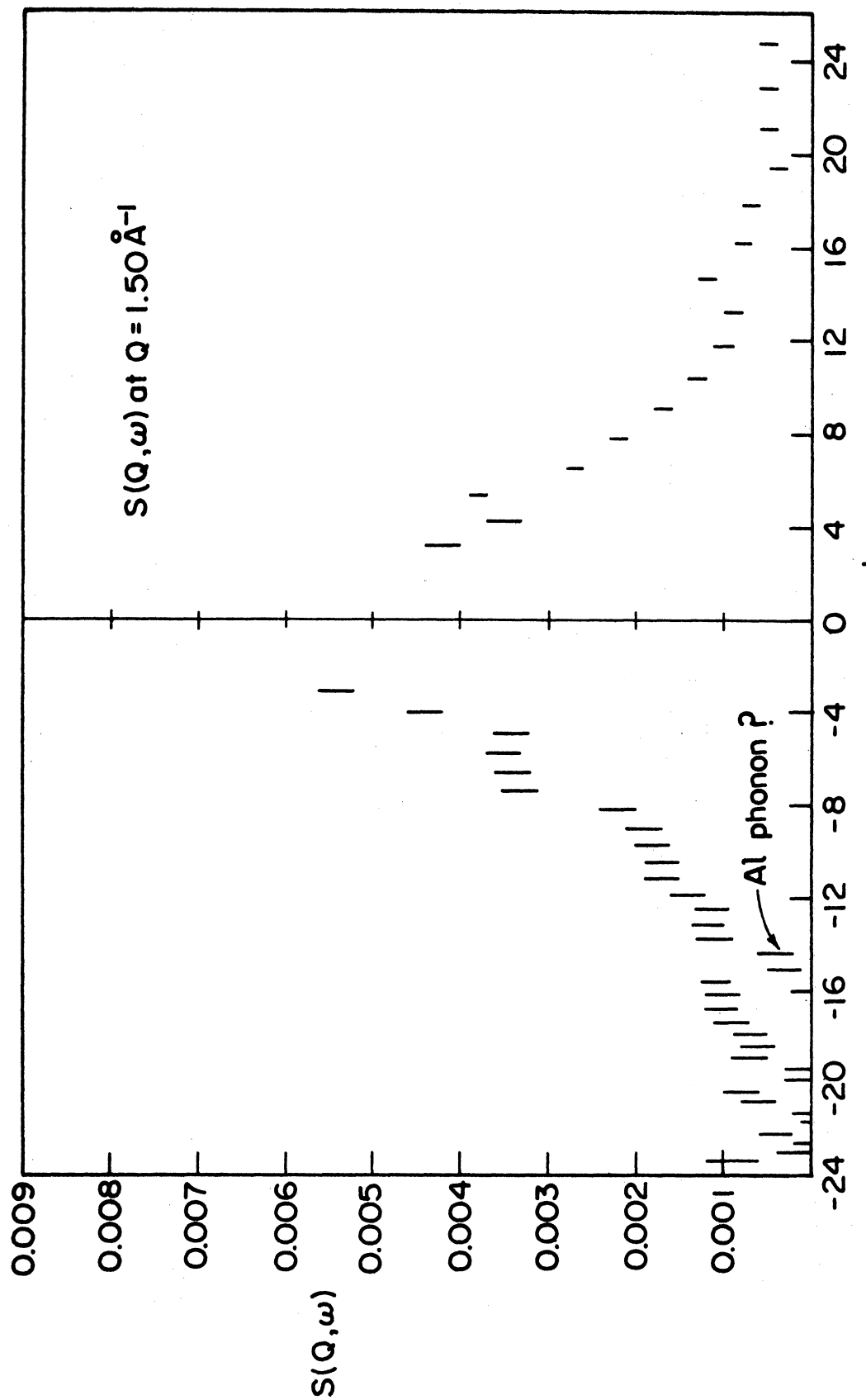

Figure A2. S(Q, ω) interpolated at Q= 1.50Å^{-1}

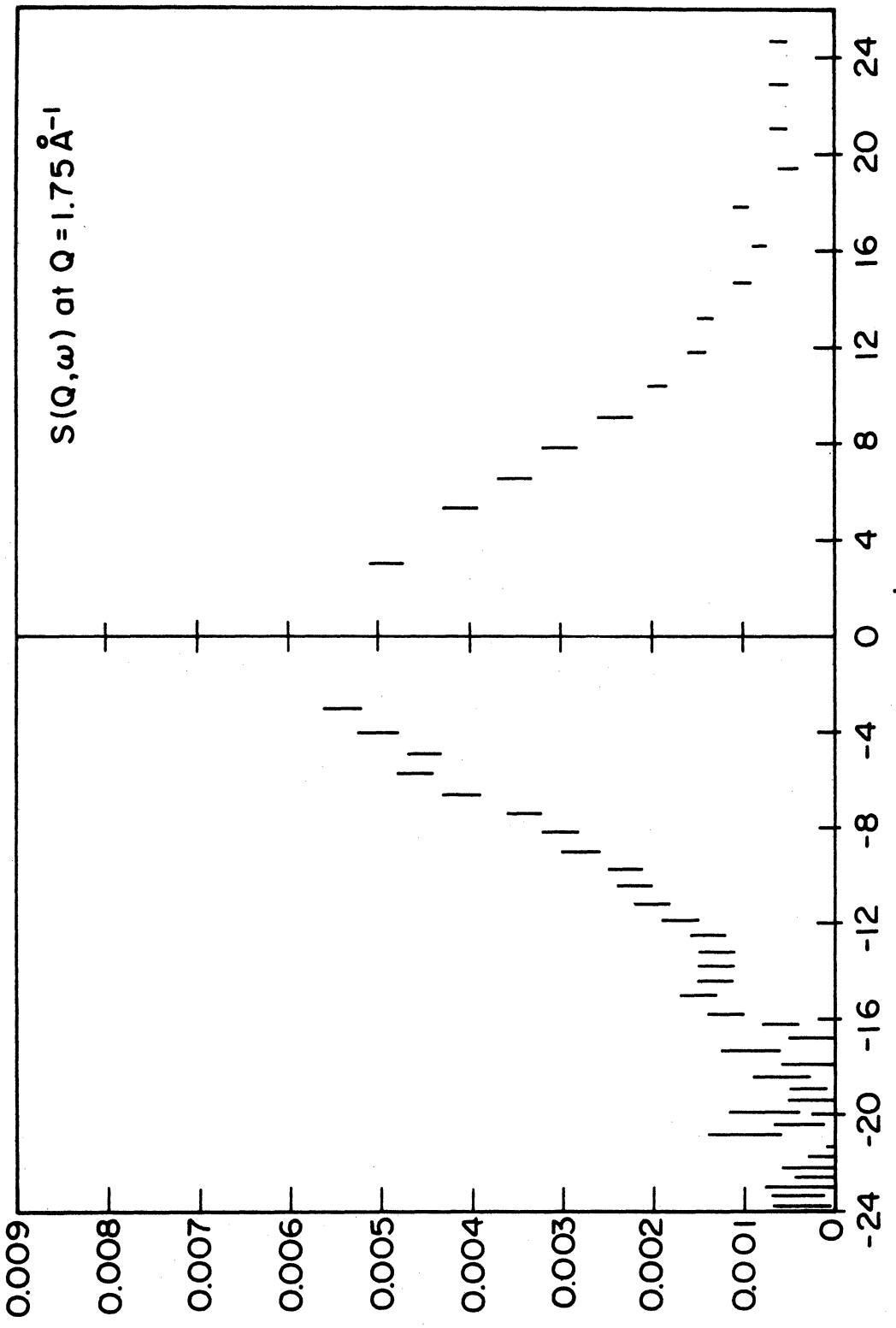

Figure A3. $S(Q,\omega)$ interpolated at $Q=1.75\text{Å}^{-1}$

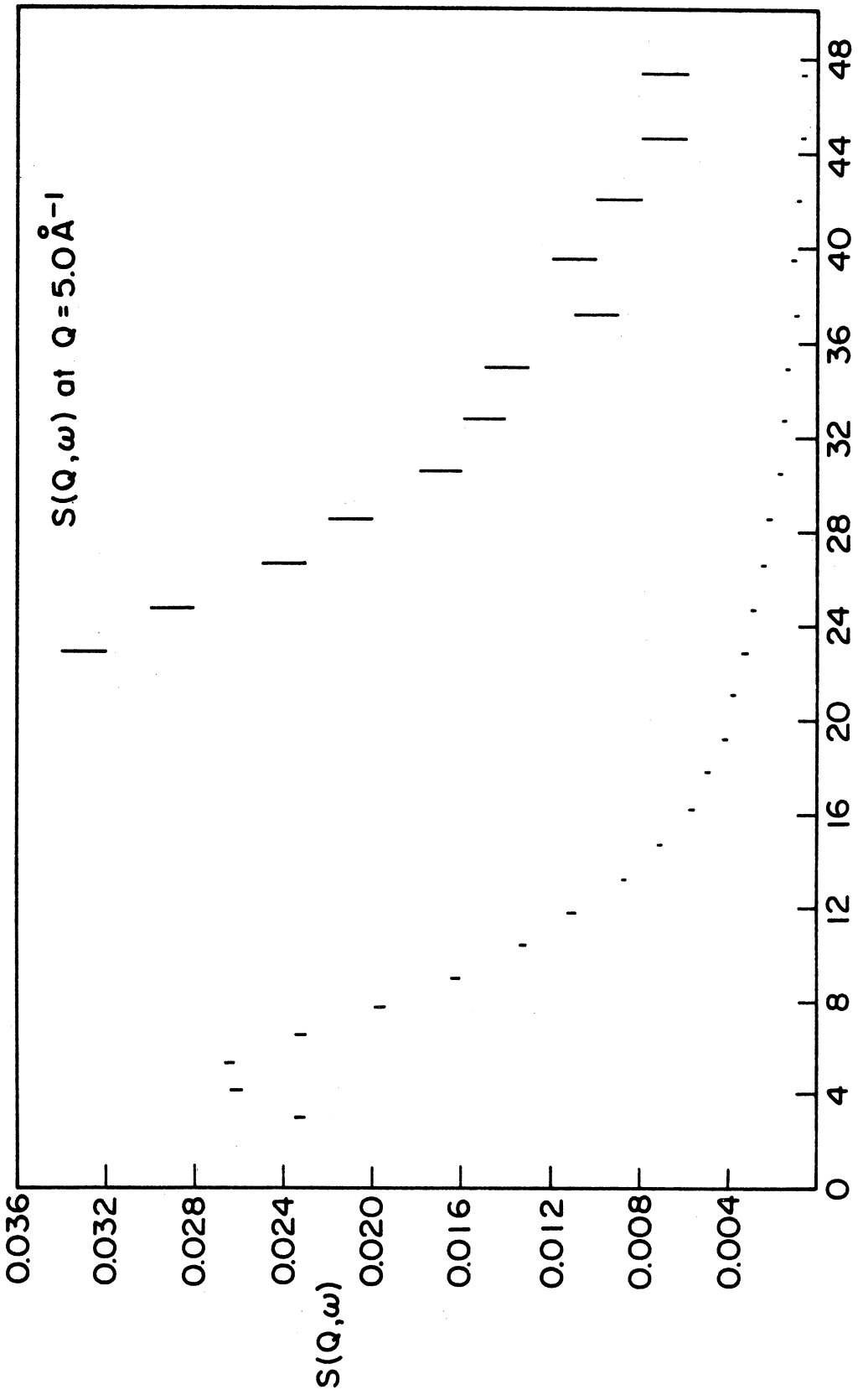

Figure A4. $S(Q,\omega)$ interpolated at Q= 5.0Å^{-1}

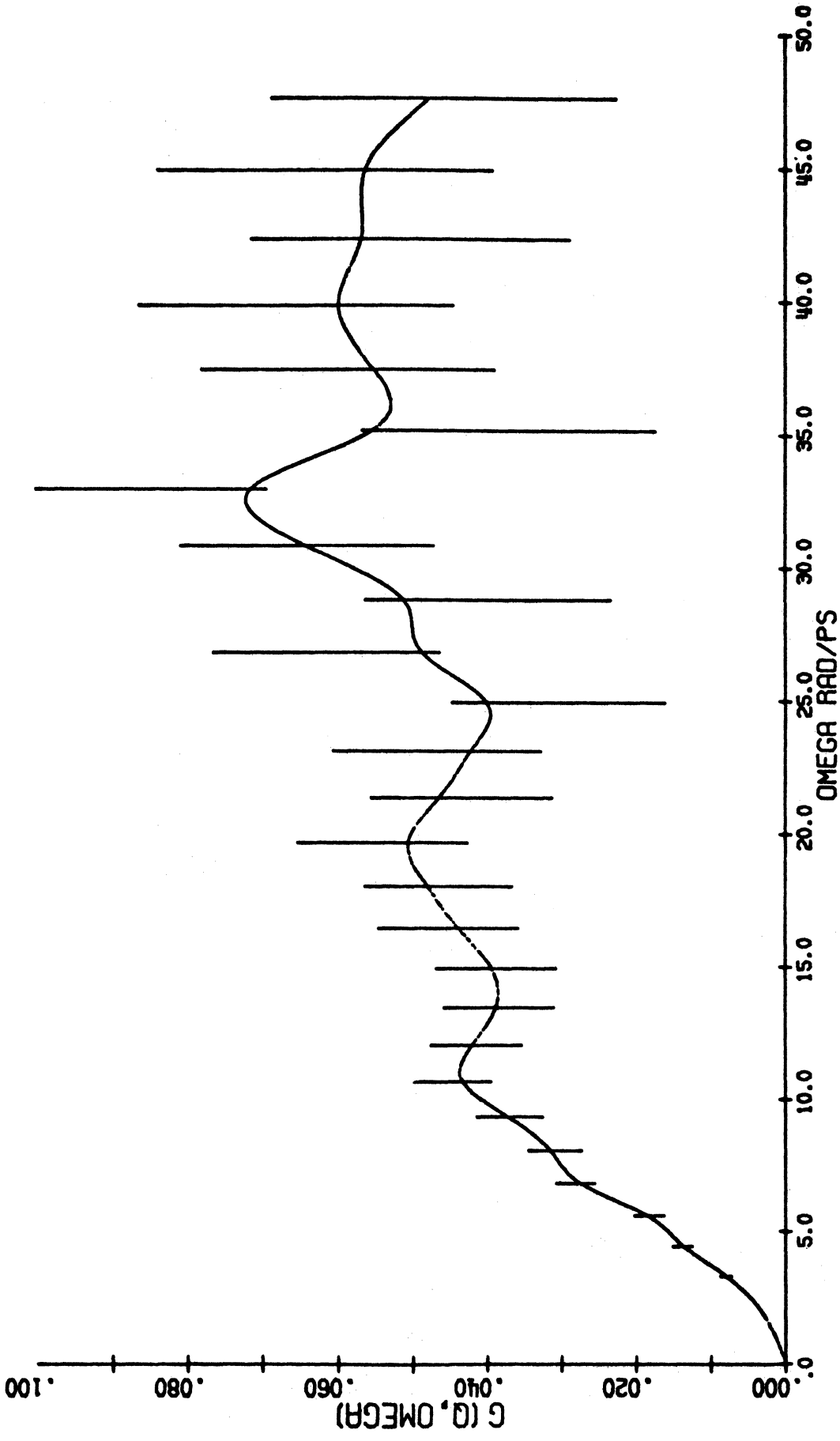

Figure A5. $G(Q, \omega)$ at 14.4° scattering angle.

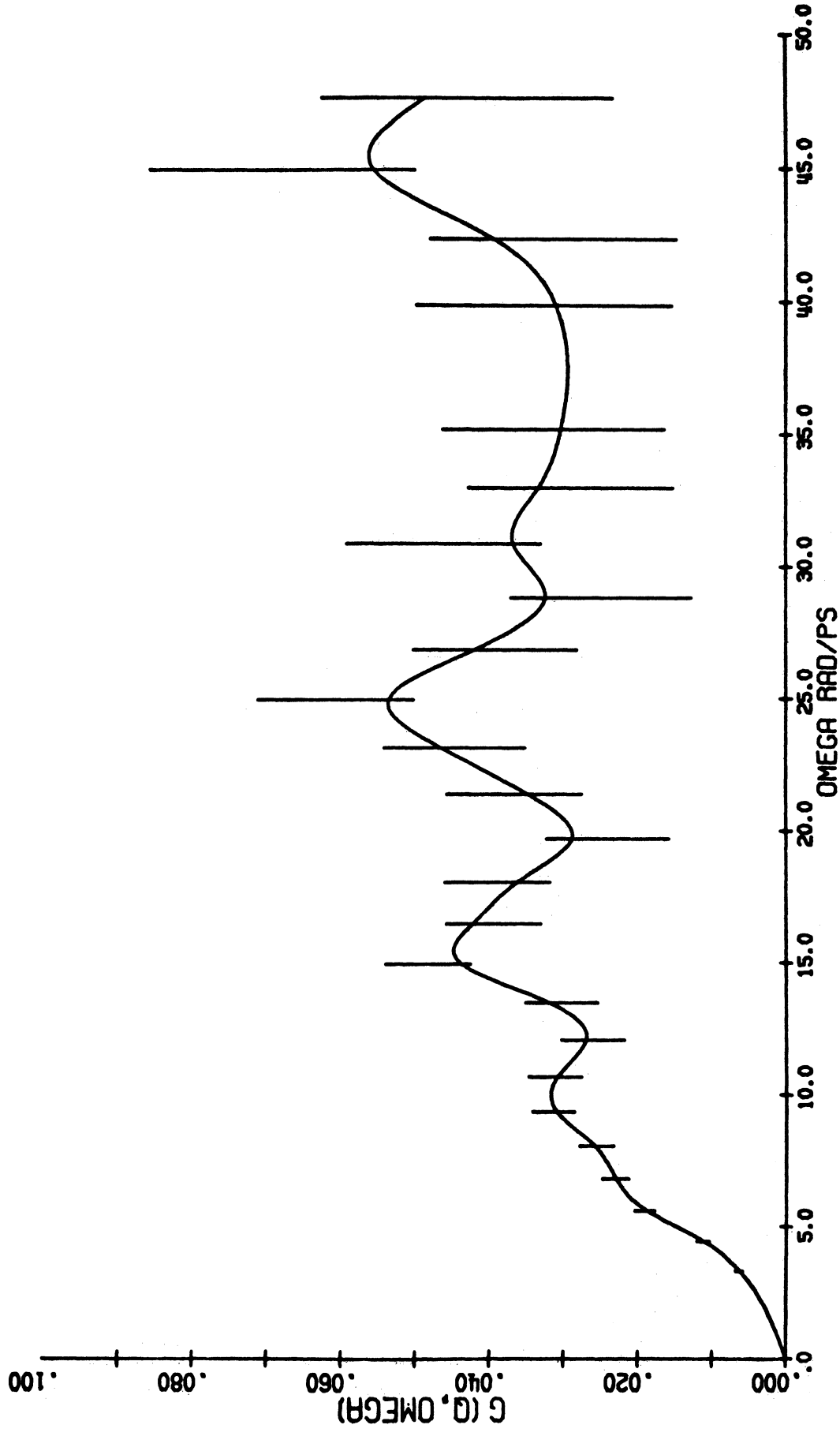

Figure A6. $G(Q, \omega)$ at 18.0° scattering angle.

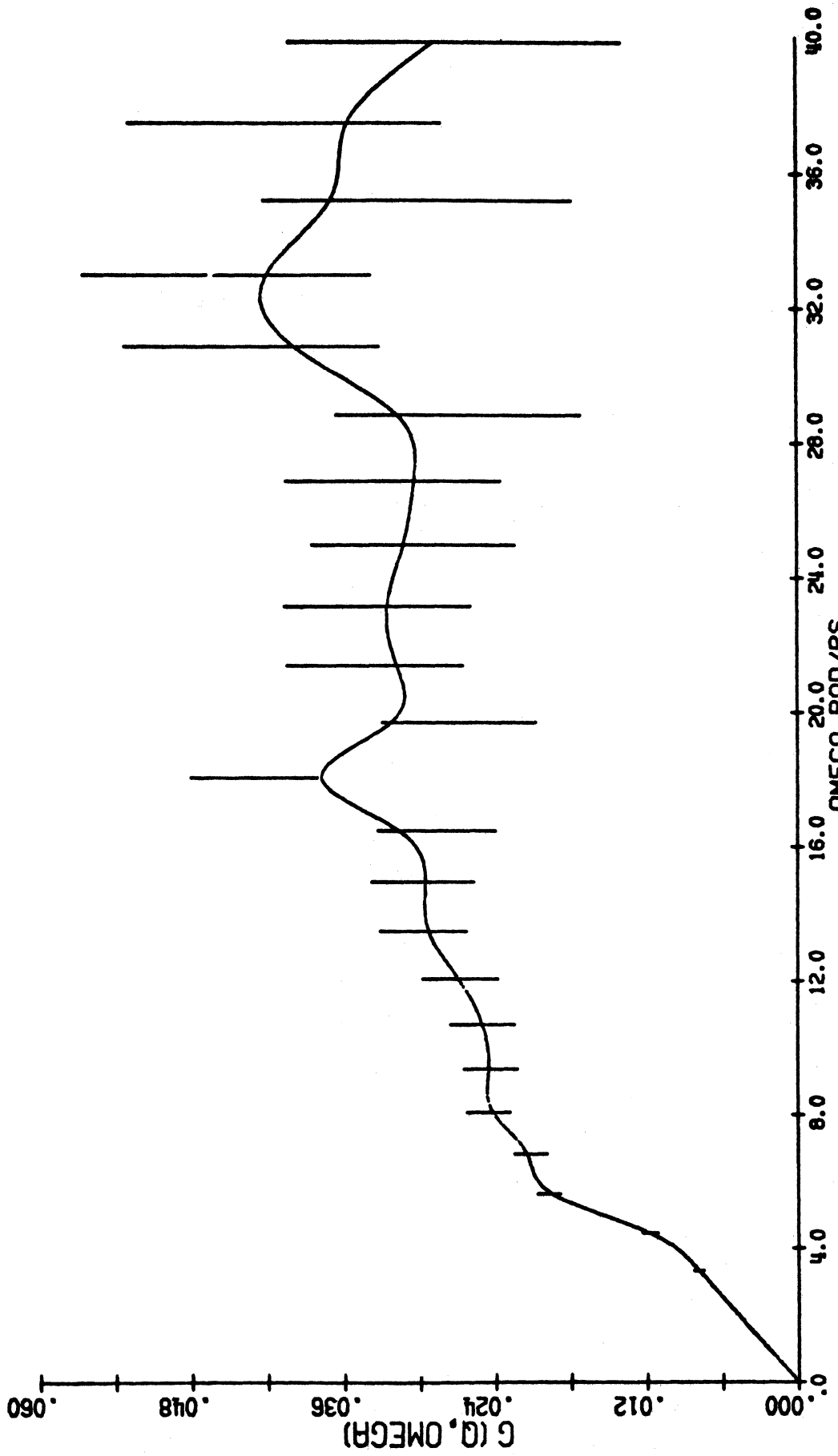

Figure A7. G(Q, ω) at 21.6° scattering angle.

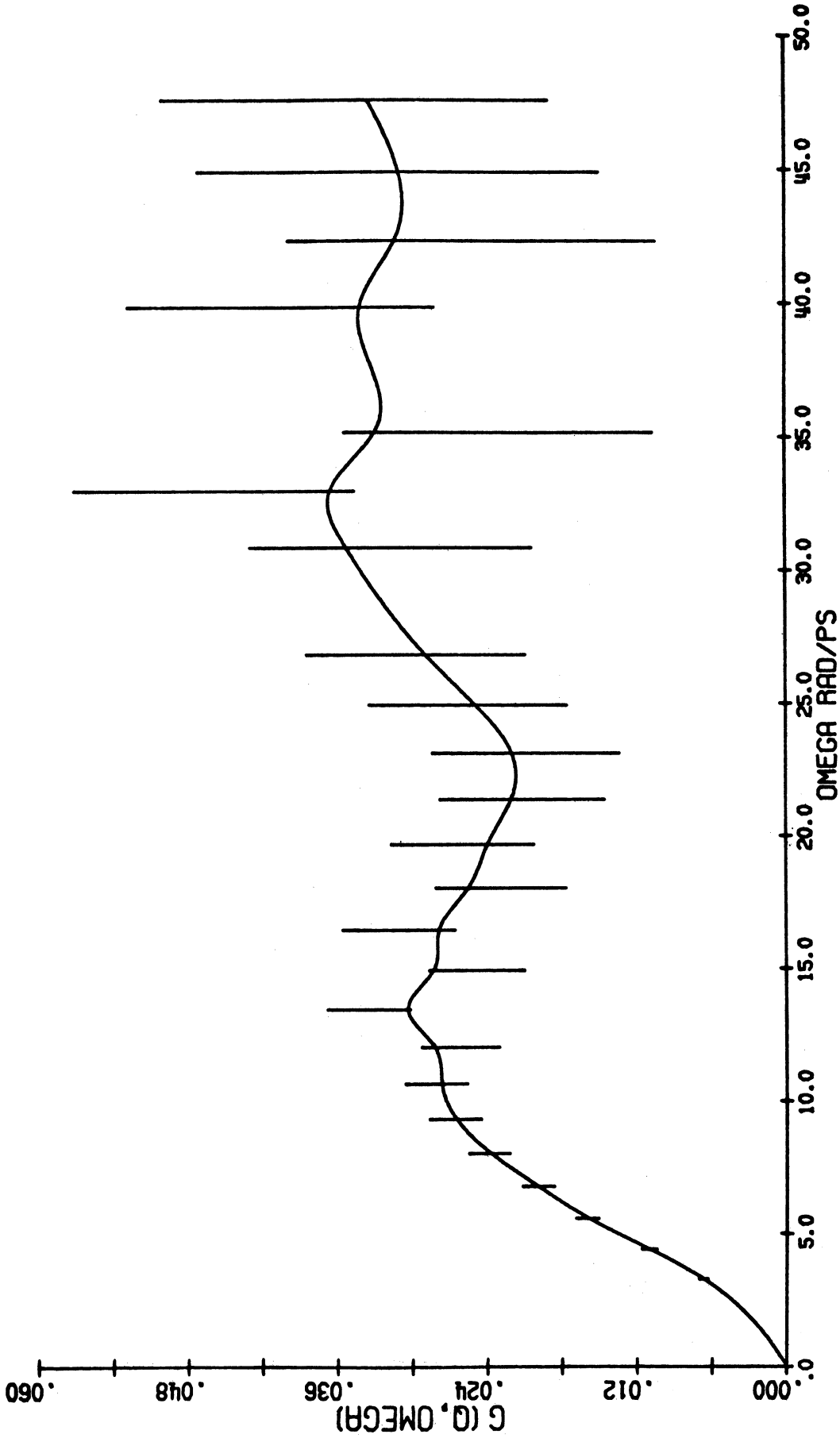

Figure A8. $S(Q, \omega)$ at 24.6 scattering angle.

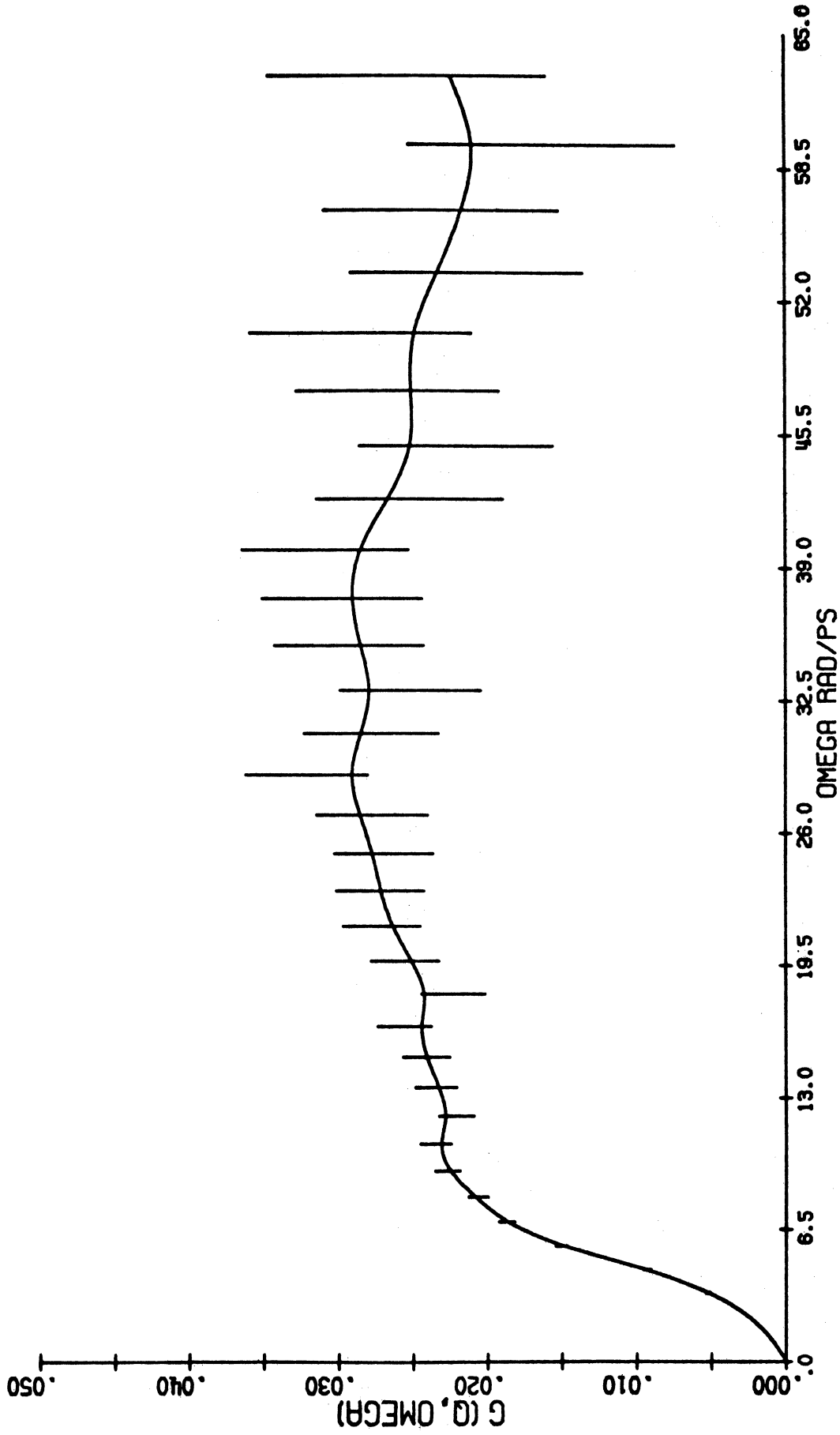

Figure A9. $G(Q,\omega)$ at 28.2° scattering angle.

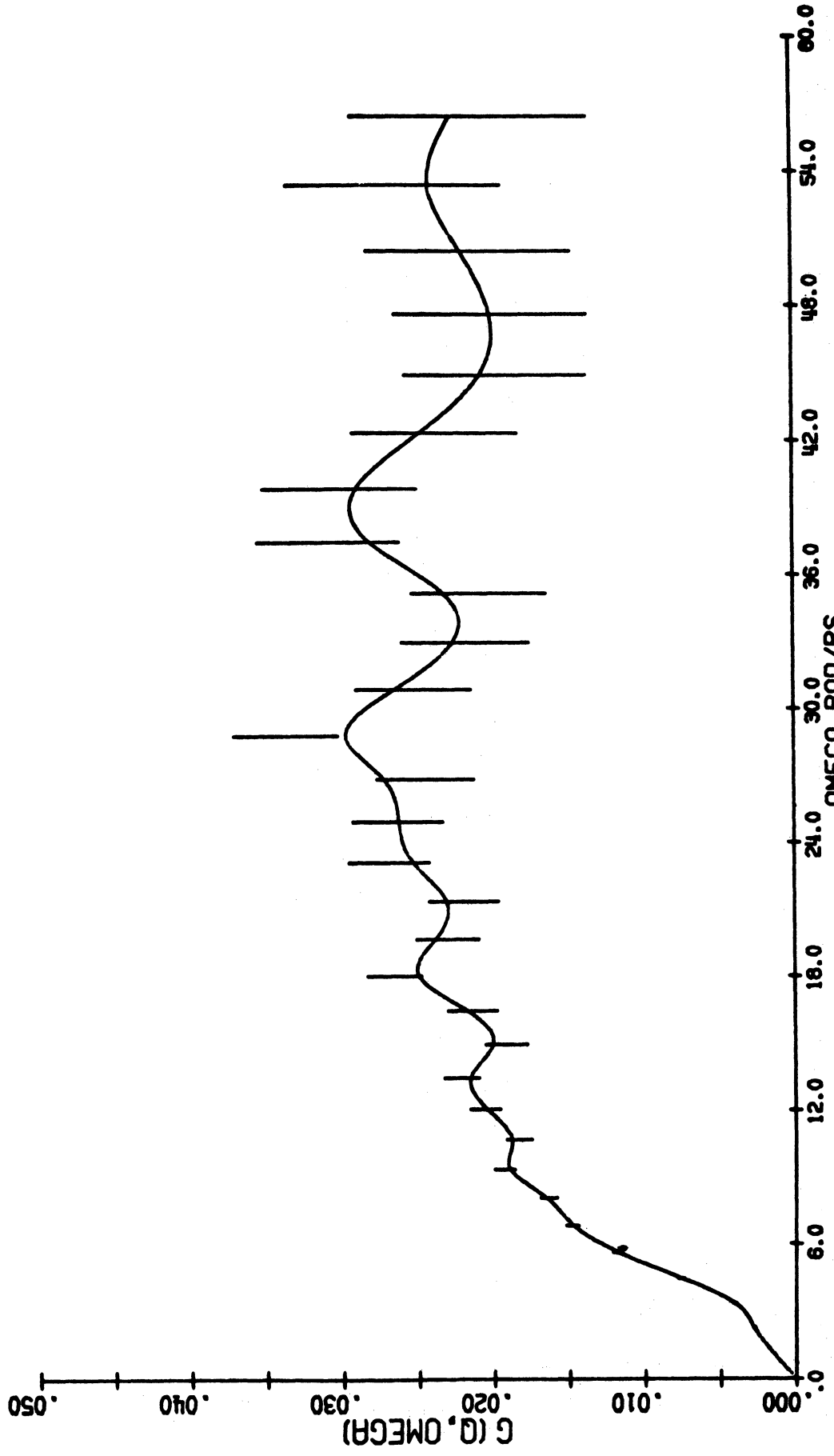

Figure A10. $G(Q,\omega)$ at 33.0° scattering angle.

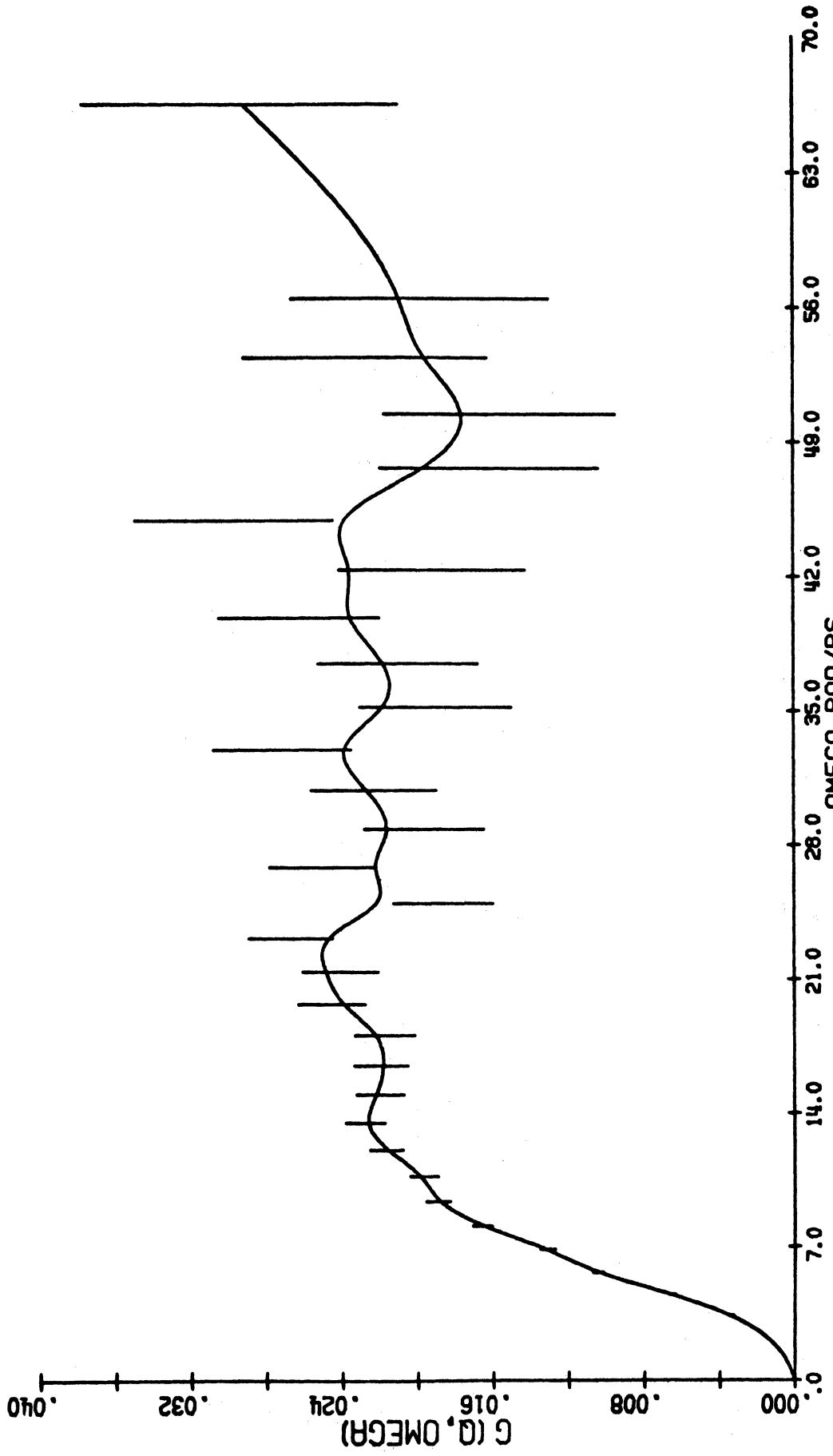

Figure A11. $G(Q, \omega)$ at 37.2° scattering angle.

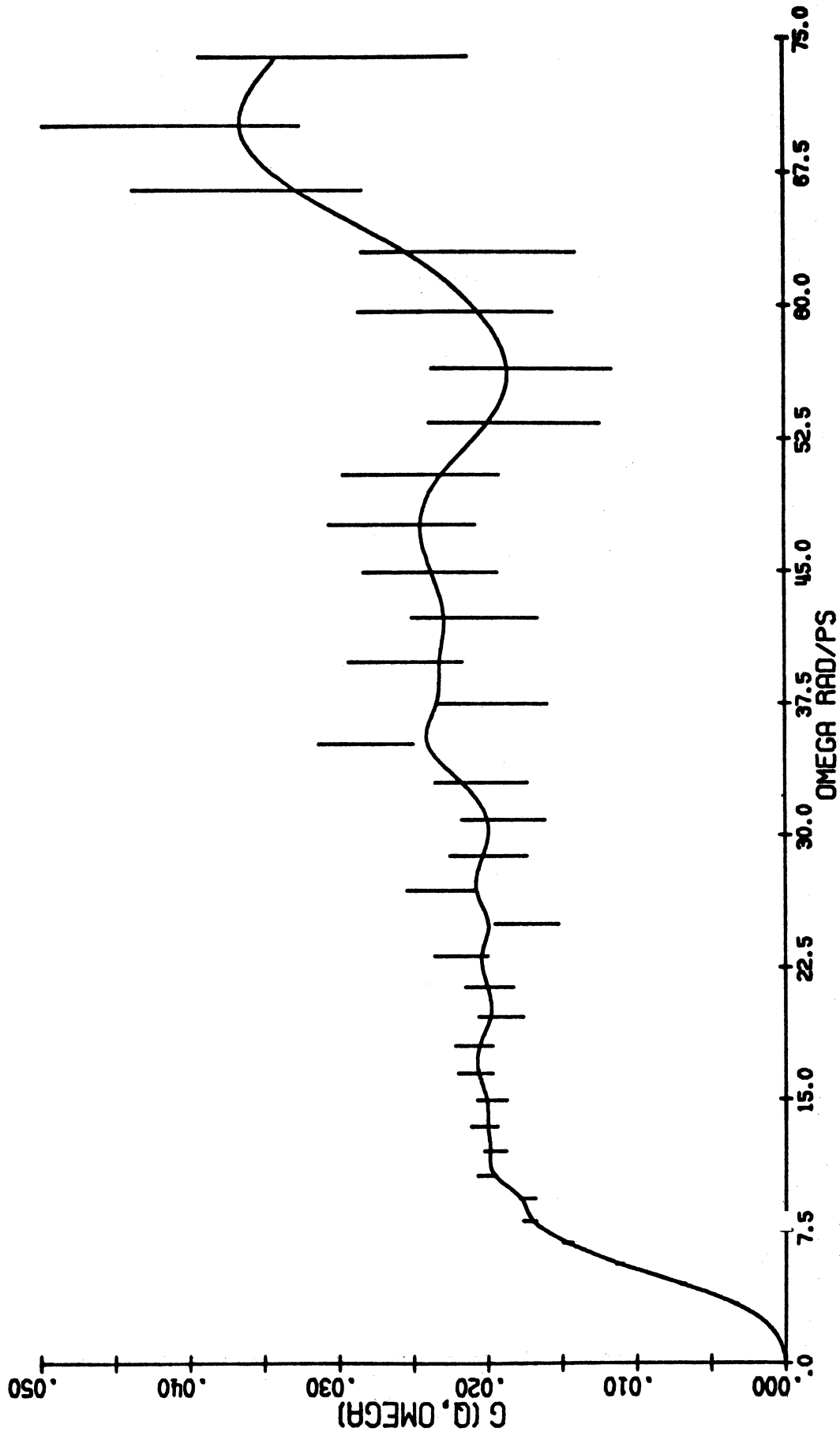

Figure A12. $G(Q,\omega)$ at 42.2° scattering angle.

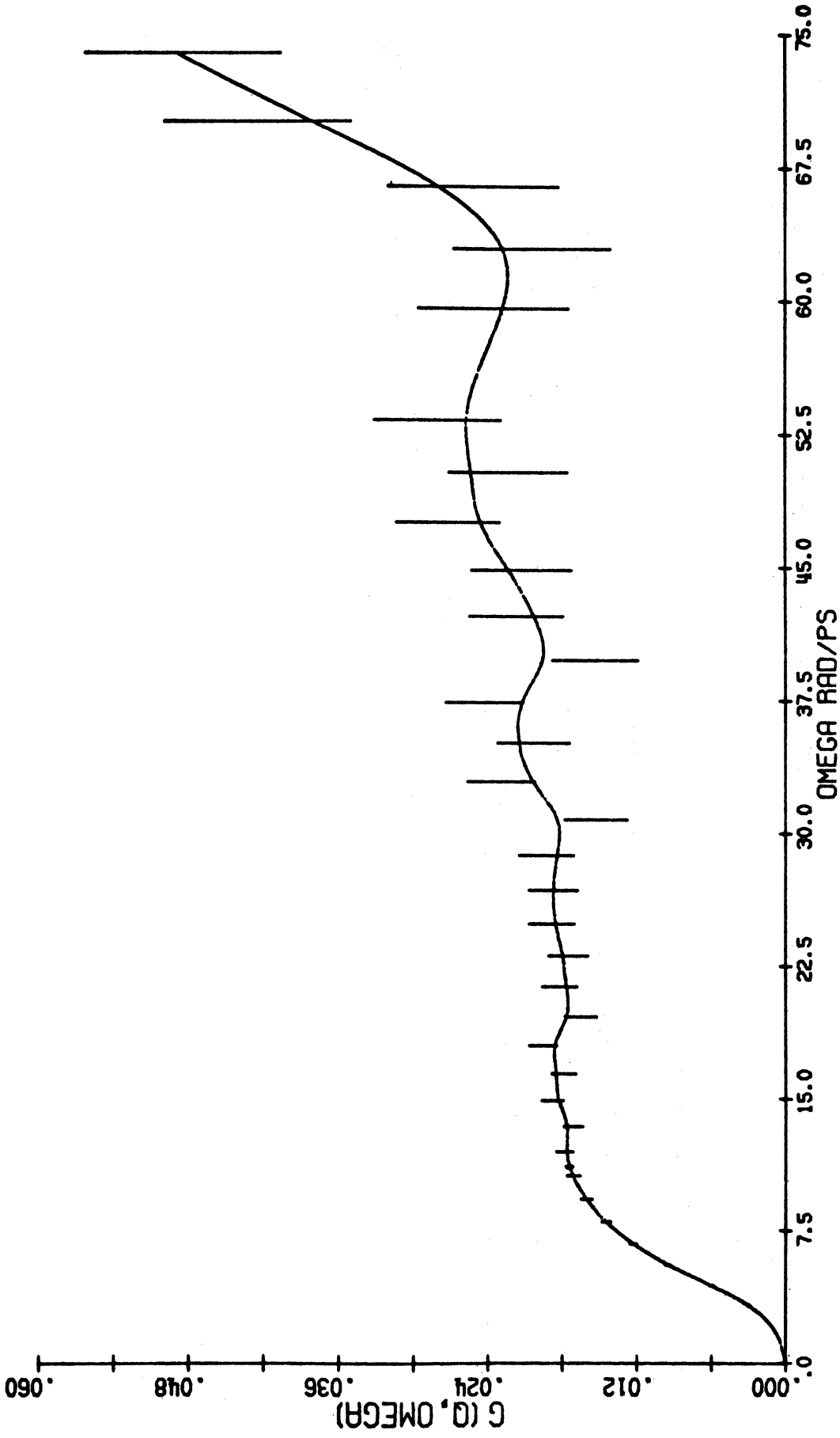

Figure A13. G(Q, ω) at 45.6° scattering angle.

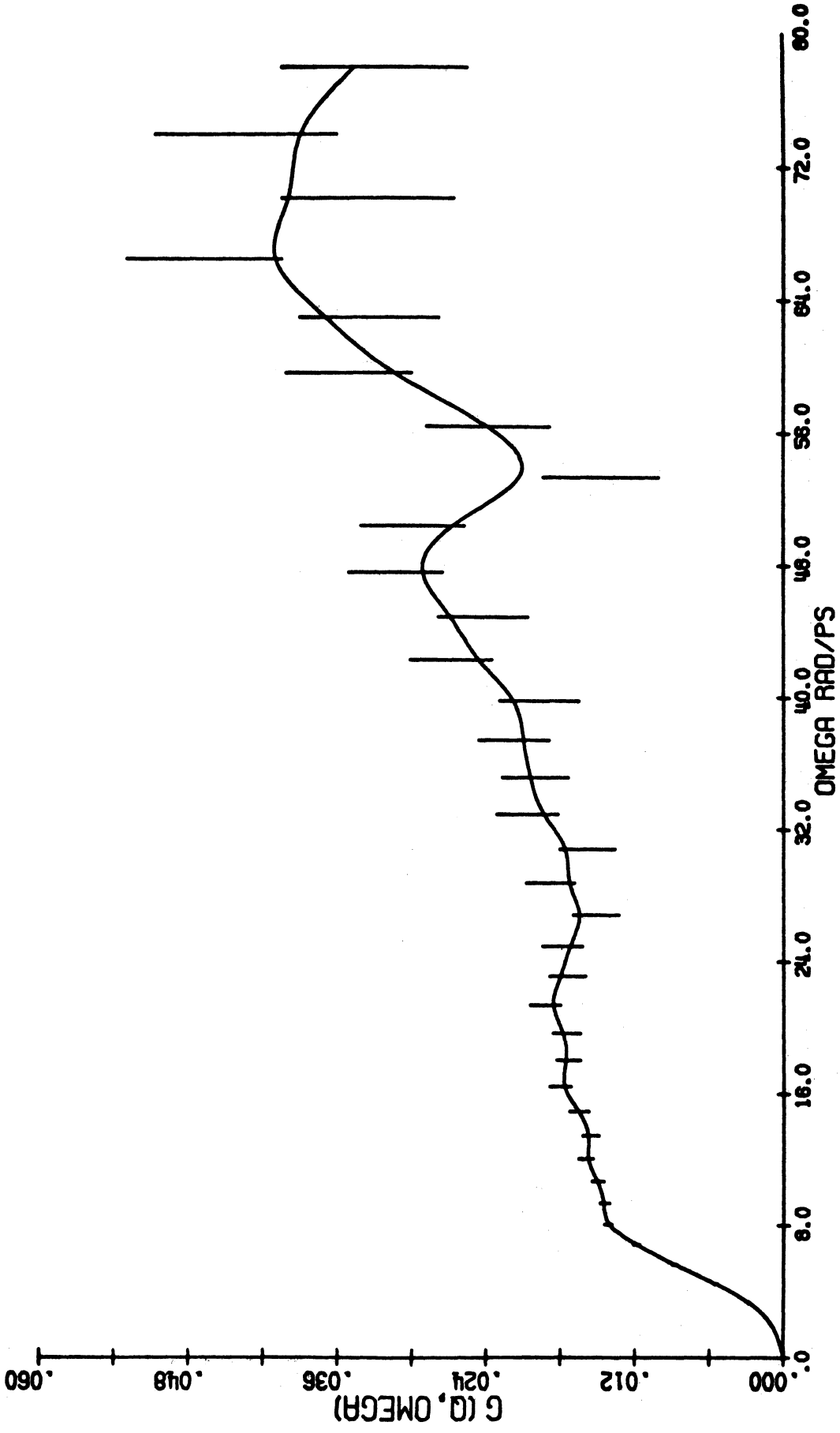

Figure A14. $S(Q,\omega)$ at 49.2° scattering angle.

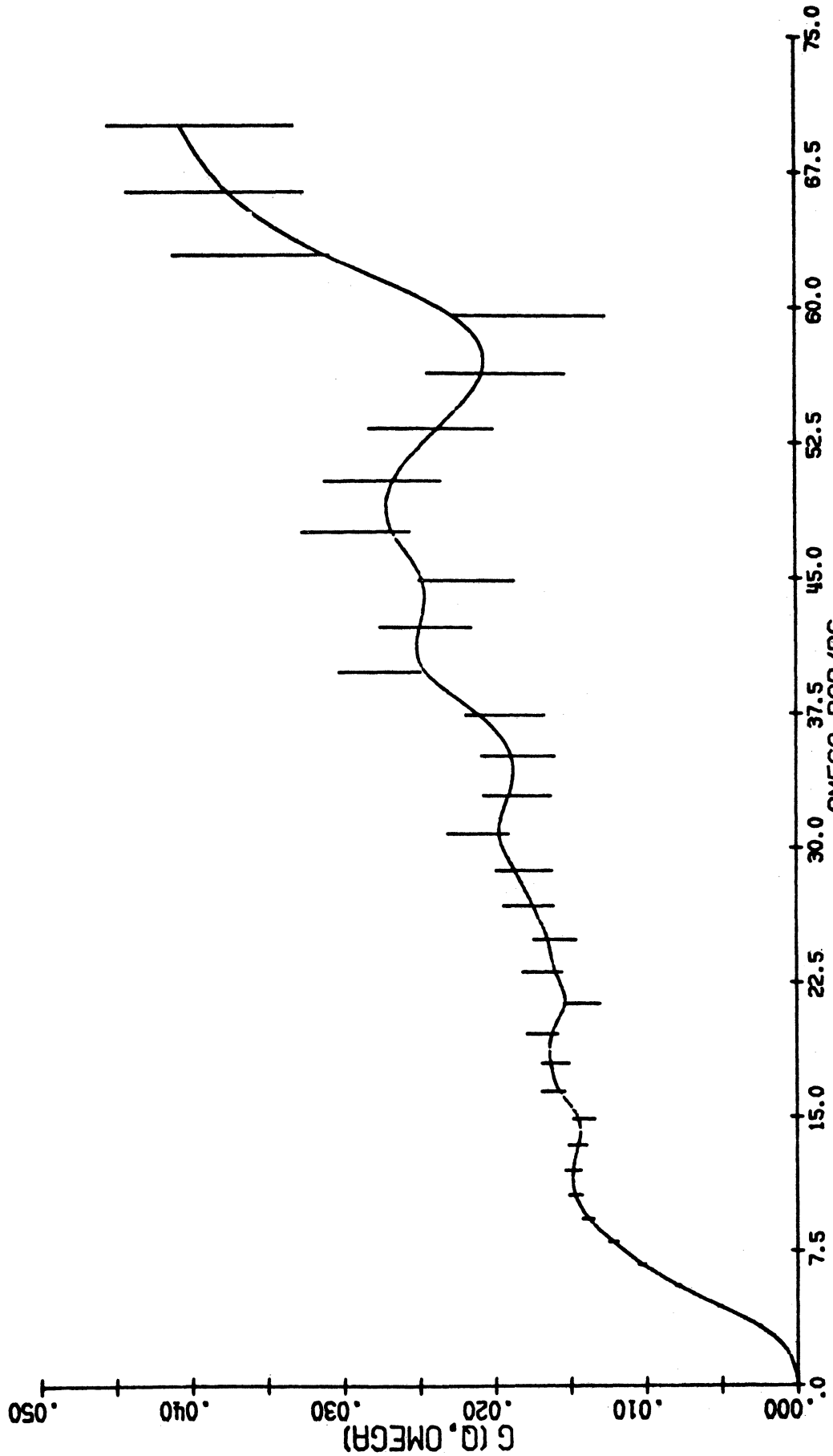

Figure A15. $G(Q,\omega)$ at 52.8° scattering angle.

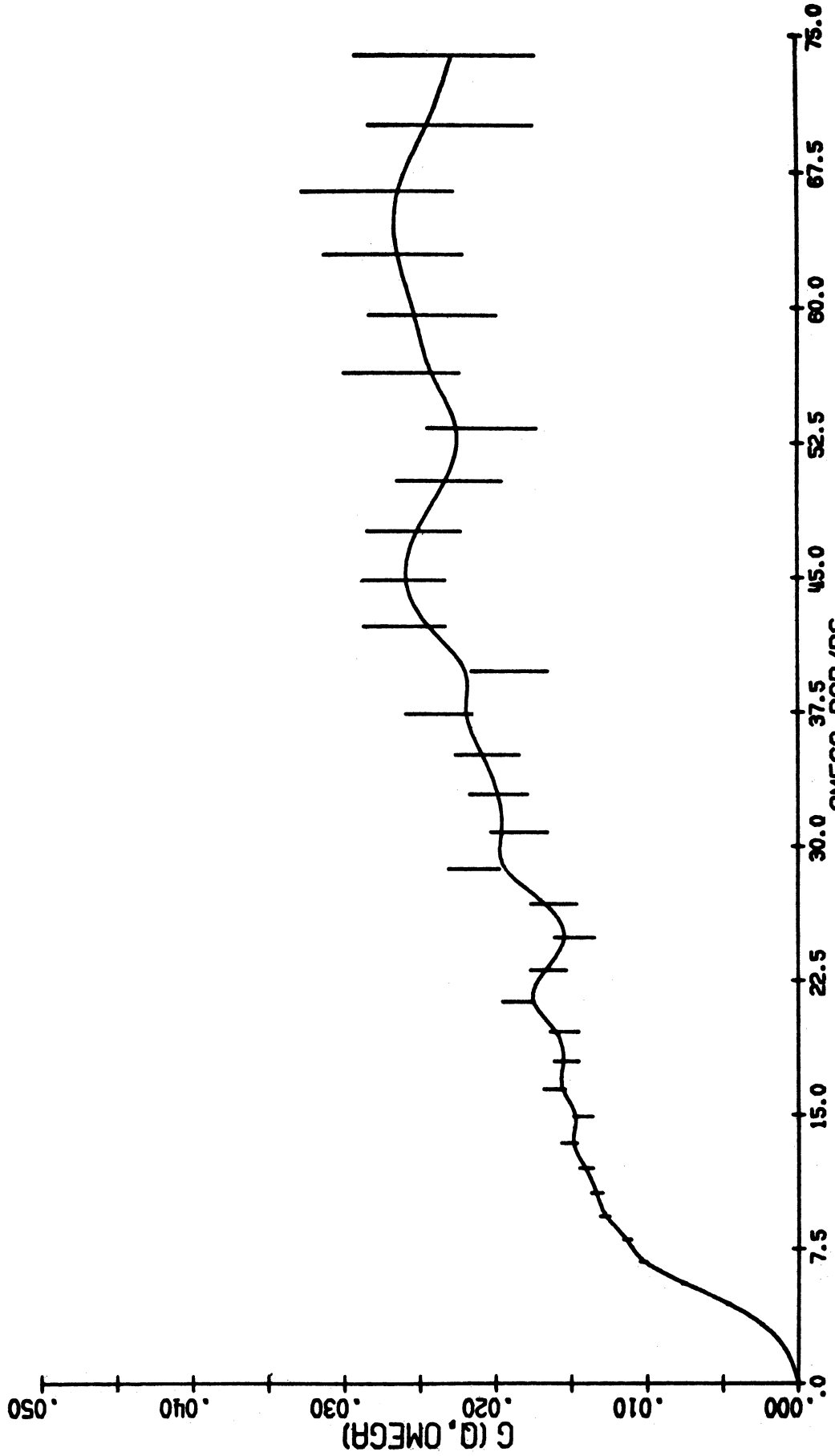

Figure A15. $G(Q,\omega)$ at 56.4° scattering angle.

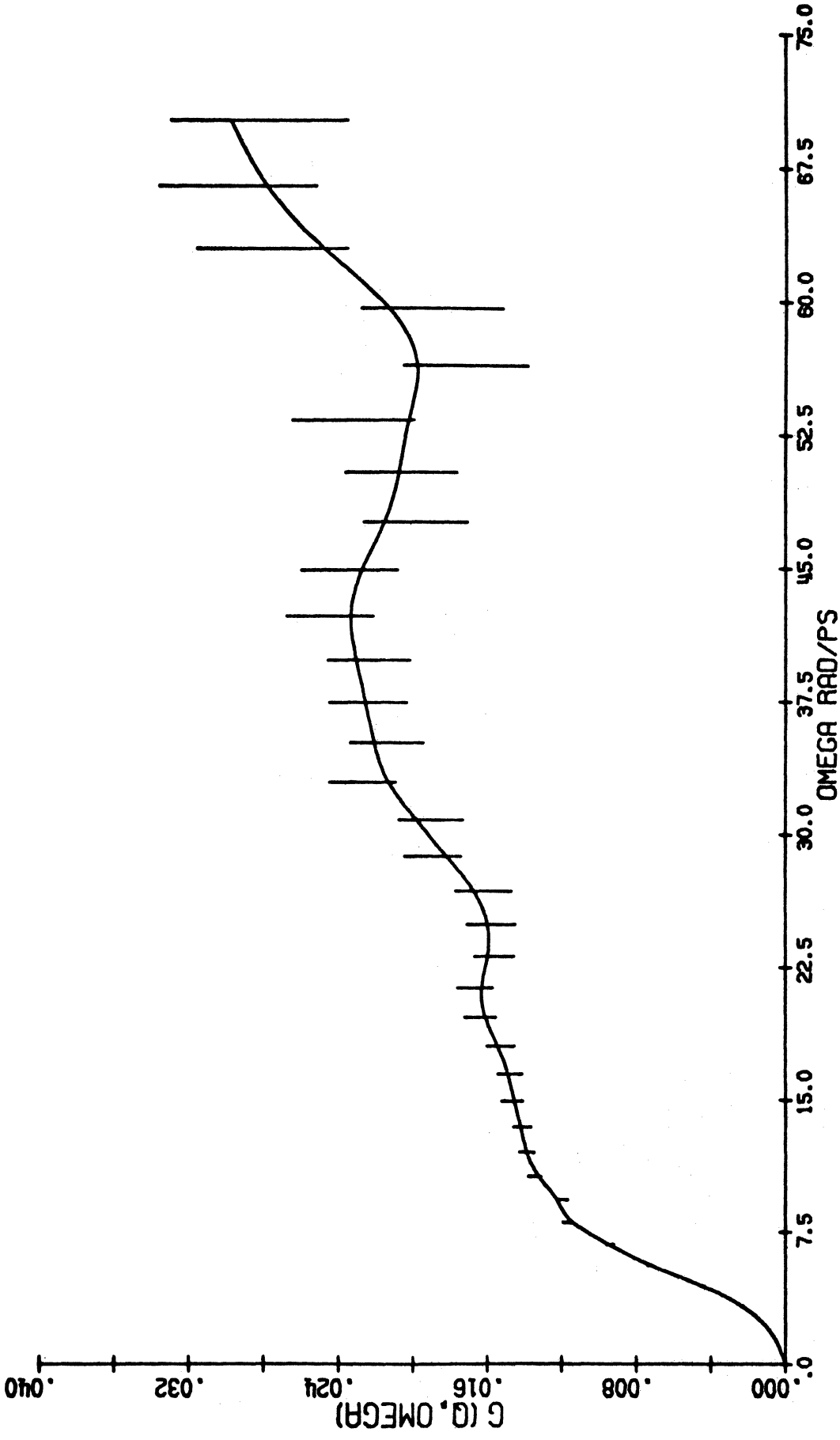

Figure A17. $G(Q,\omega)$ at 60.0° scattering angle.

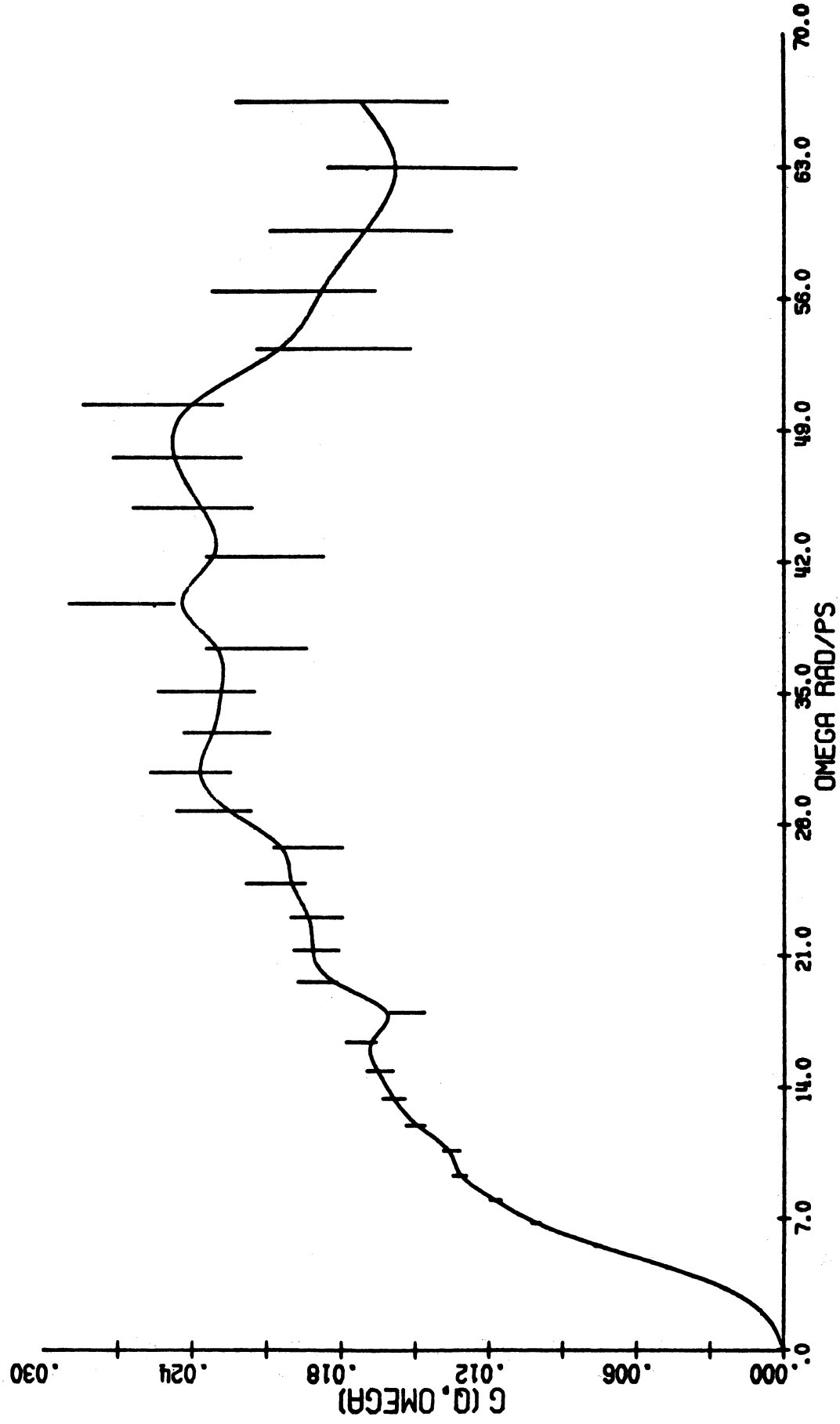

Figure A18. $G(Q,\omega)$ at 63.6° scattering angle.

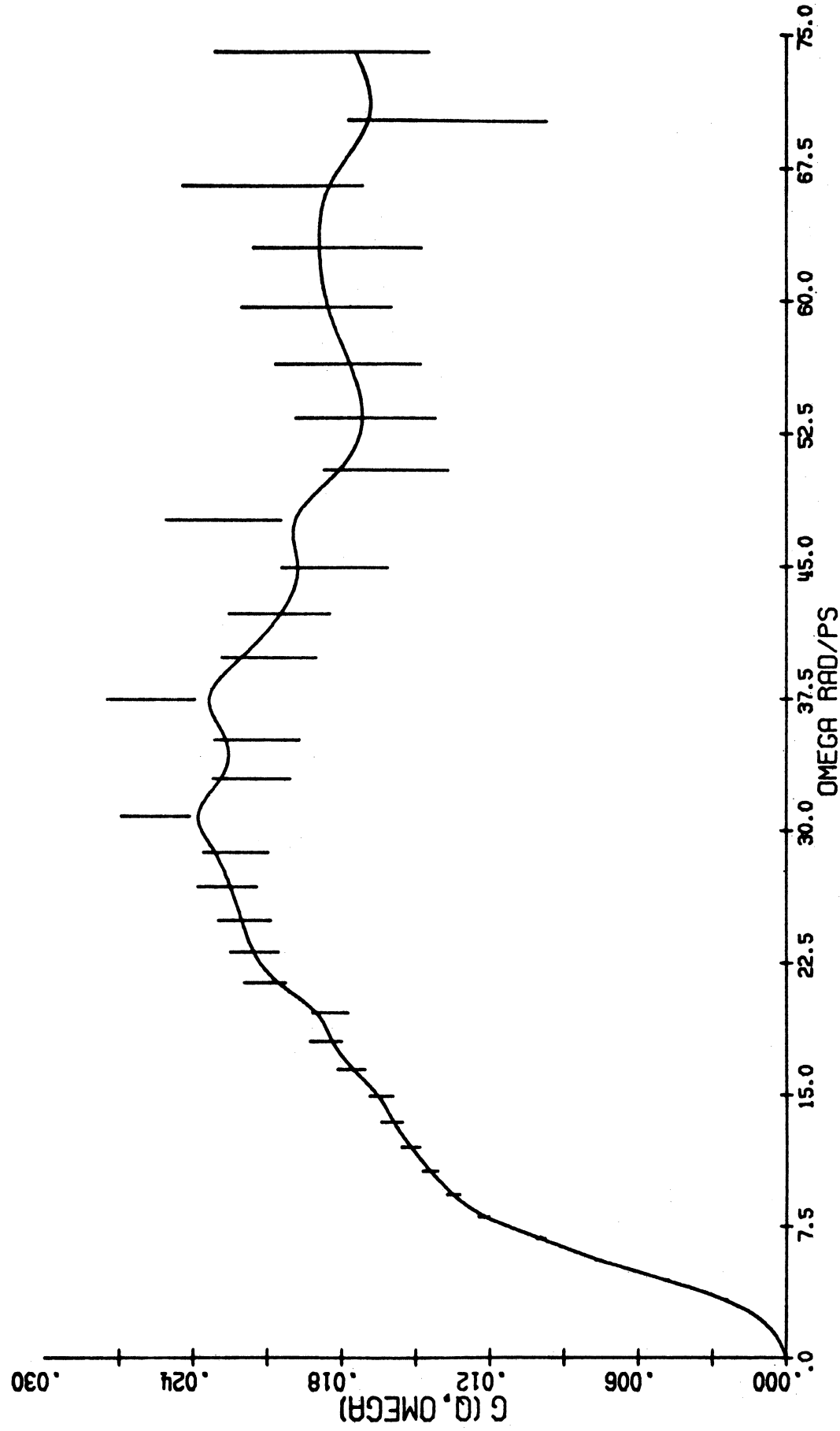

Figure A19. $S(Q,\omega)$ at 67.2° scattering angle.

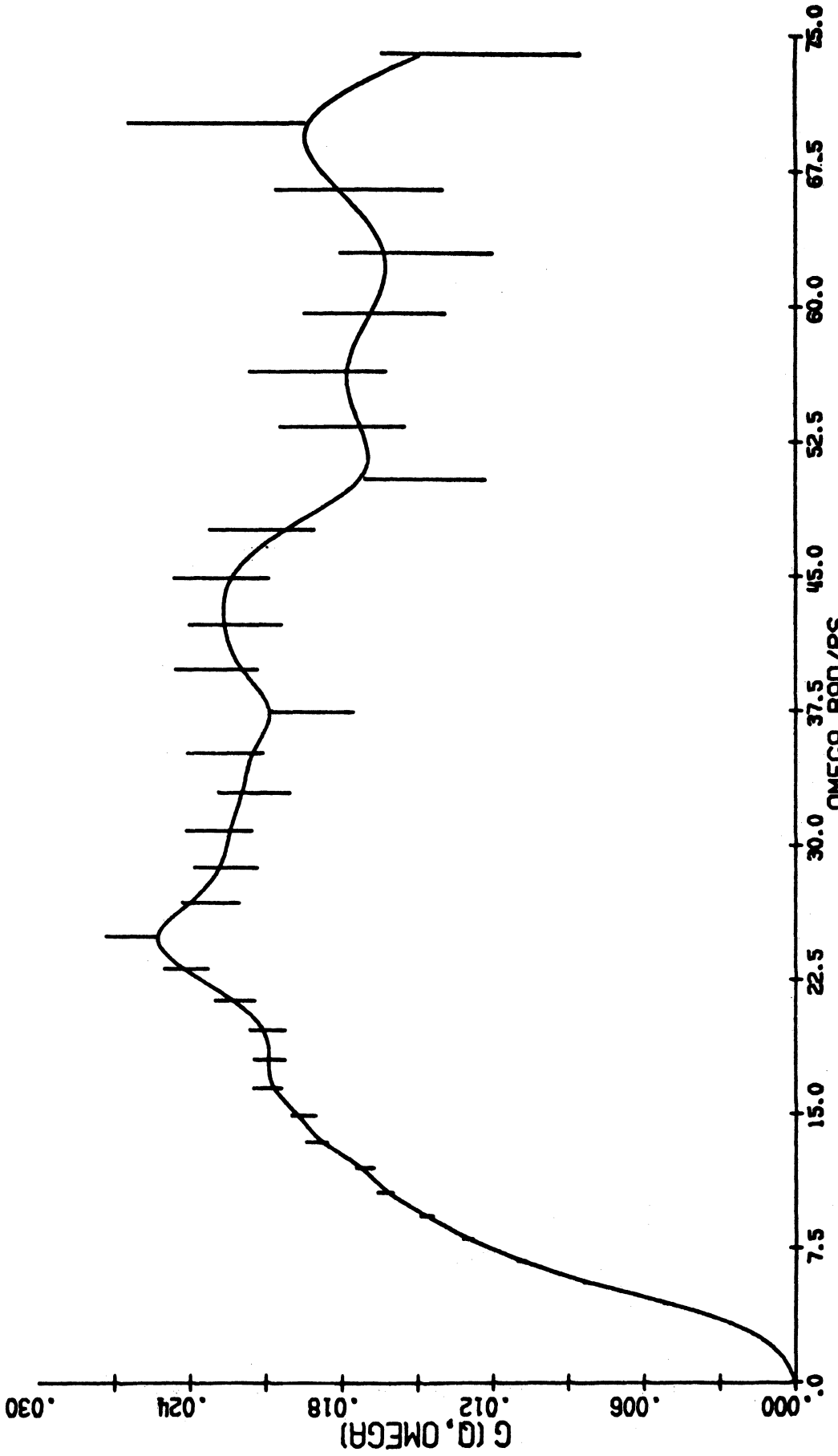

Figure A20. $G(Q,\omega)$ at 70.8° scattering angle.

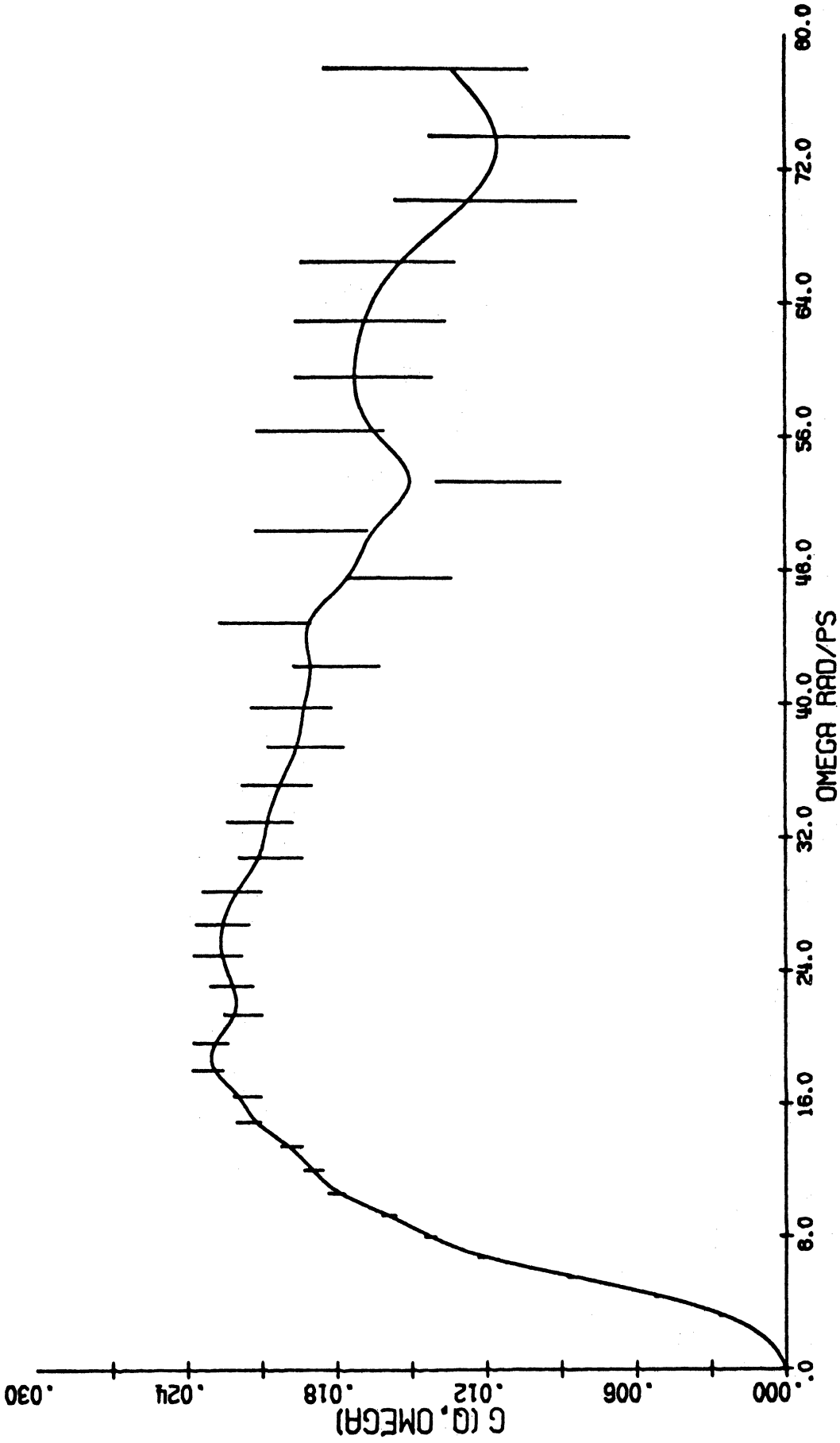

Figure A21. $G(Q,\omega)$ at 74.4° scattering angle.

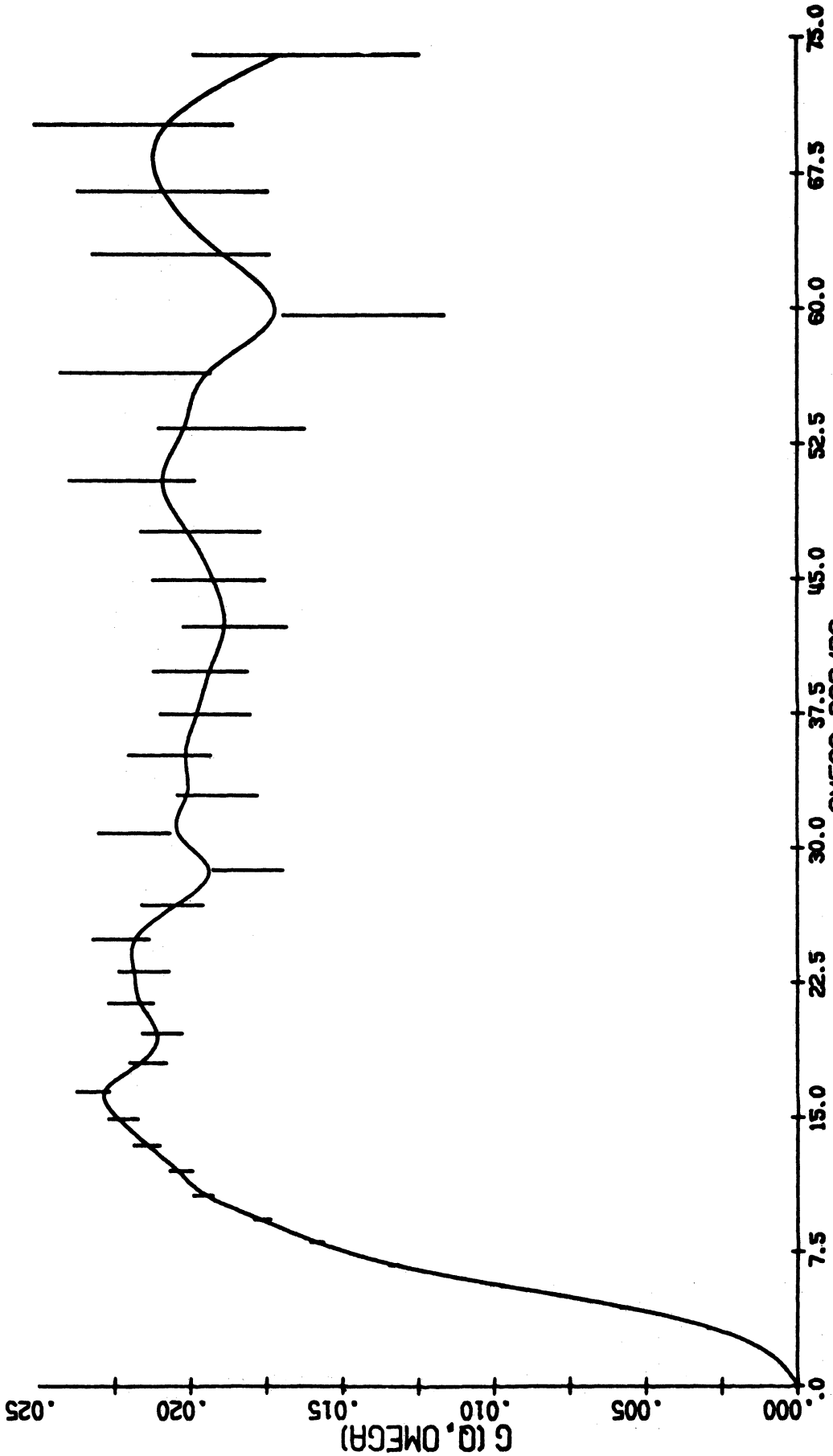

Figure A22. $G(Q, \omega)$ at 77.4° scattering angle.

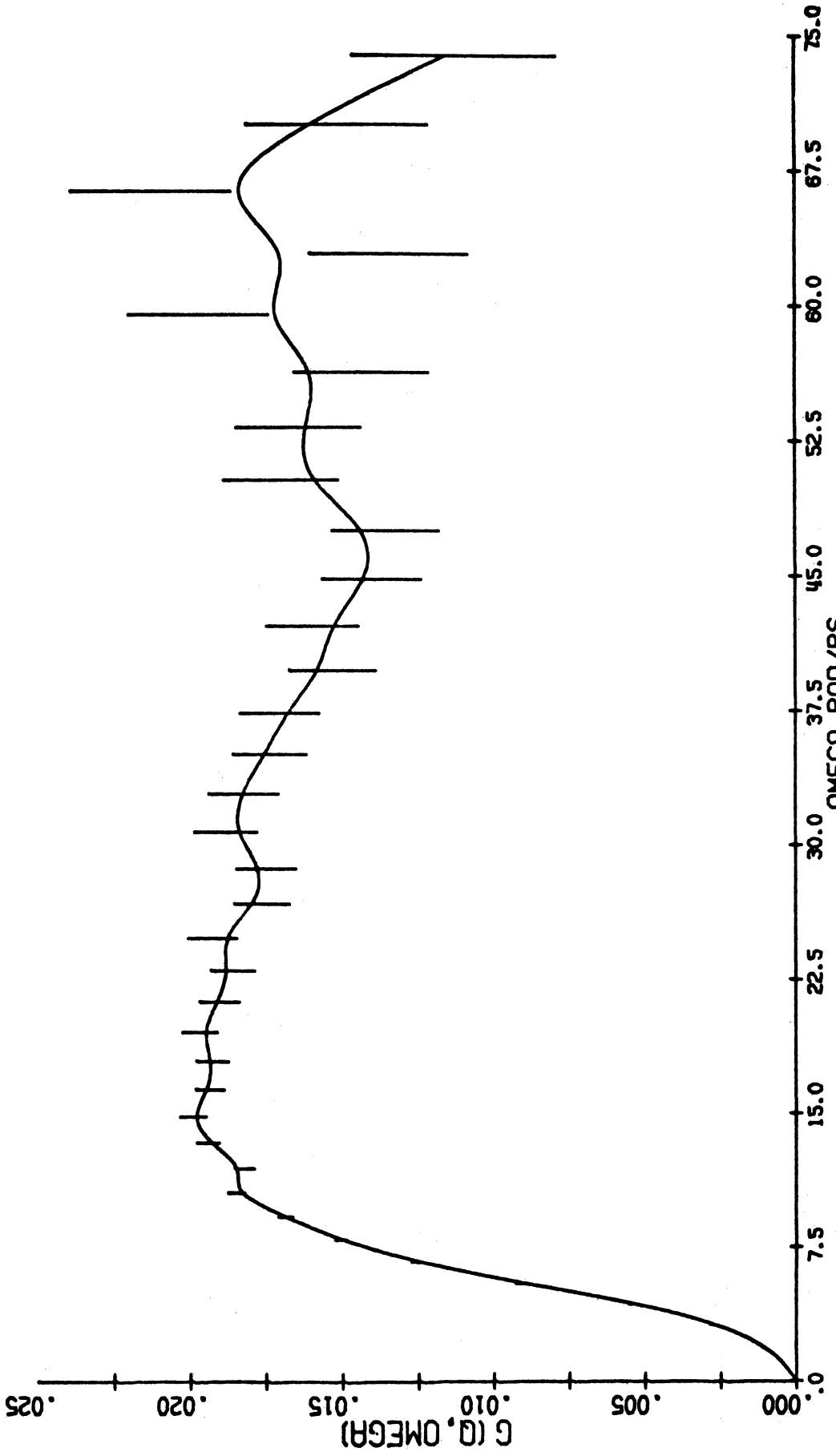

Figure A23. $G(Q,\omega)$ at 79.2° scattering angle.

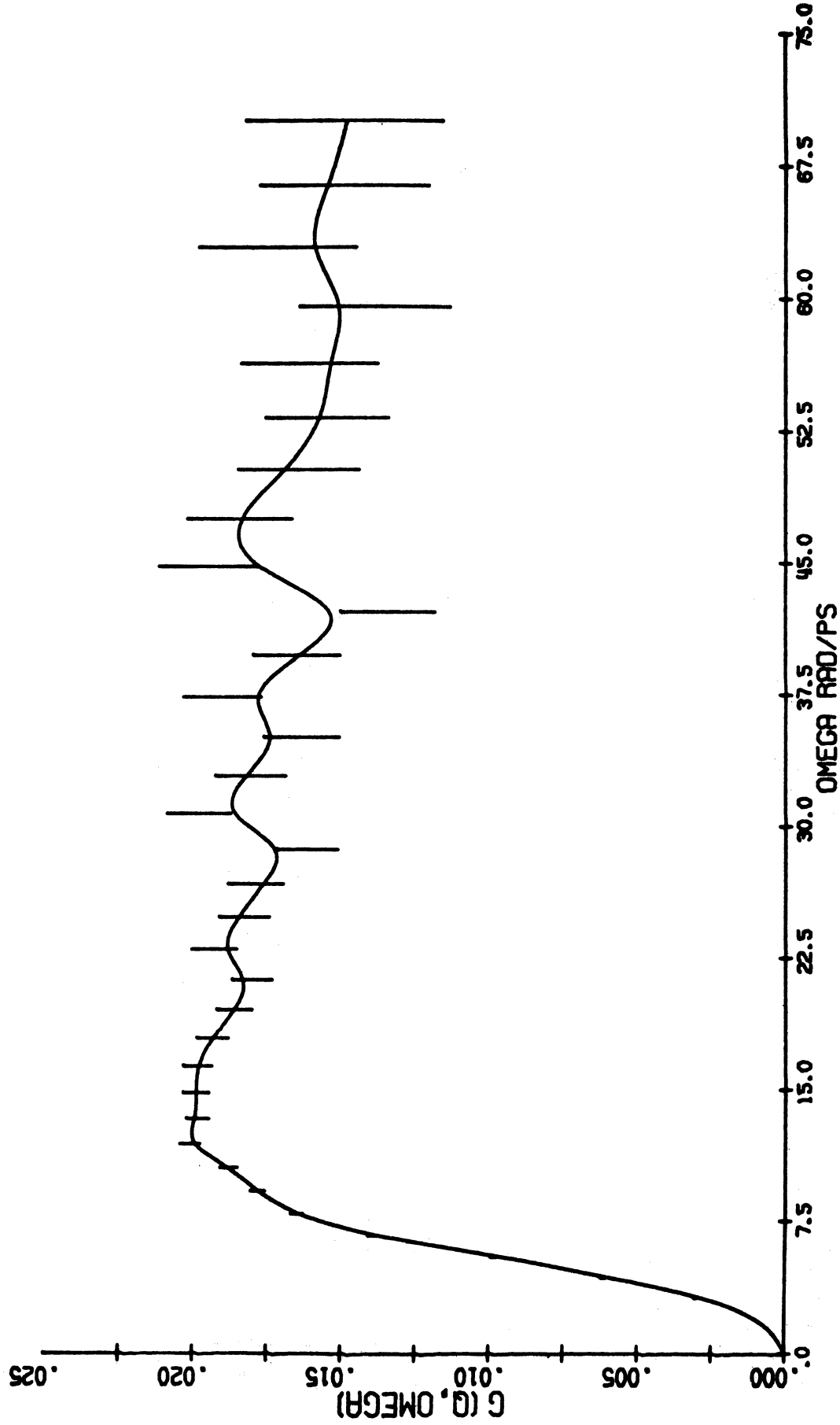

Figure A24. $G(Q,\omega)$ at 81.0° scattering angle.

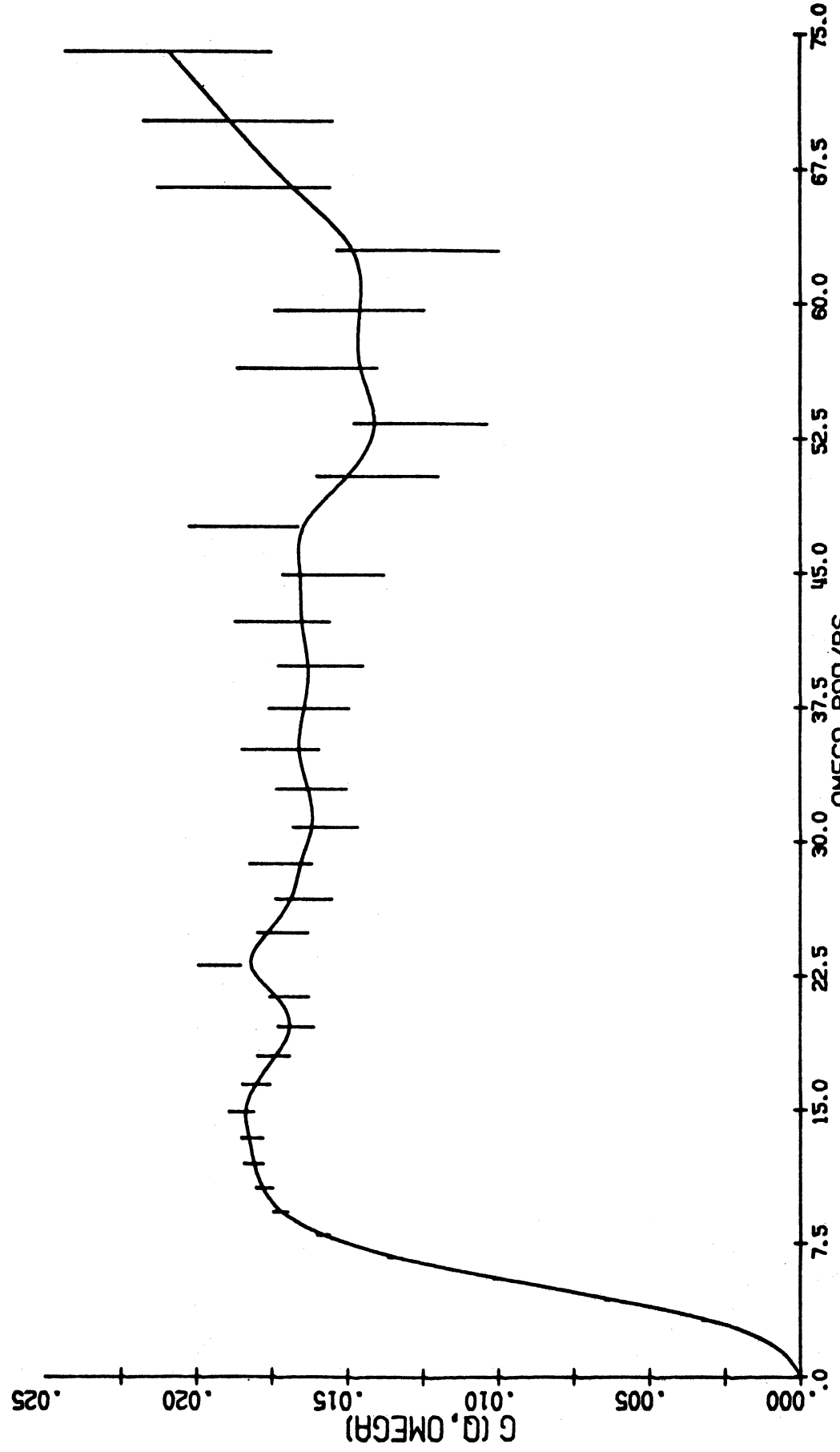

Figure A25. G(Q, ω) at 22.8° scattering angle.

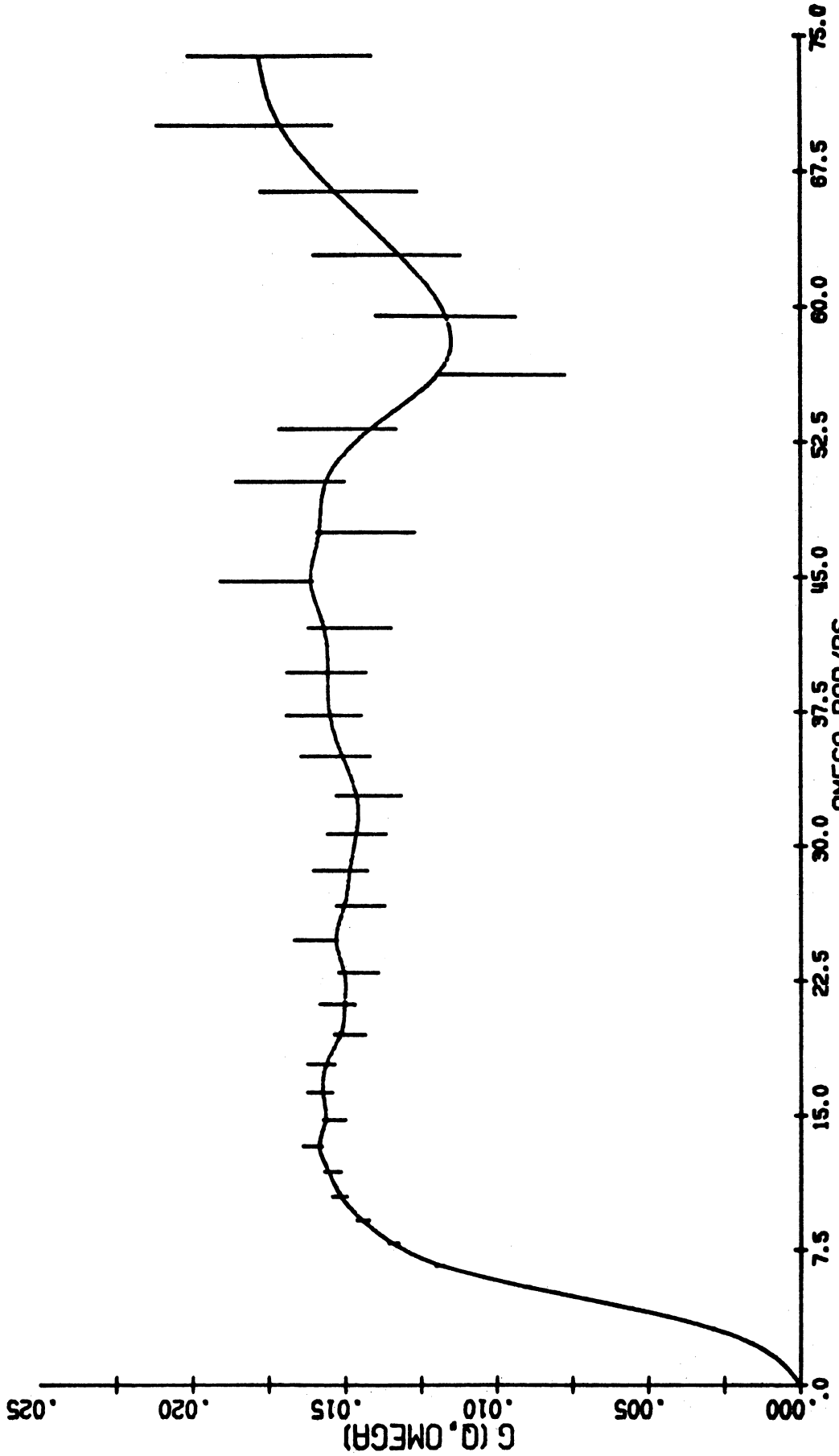

Figure A26. $G(Q,\omega)$ at 85.2° scattering angle.

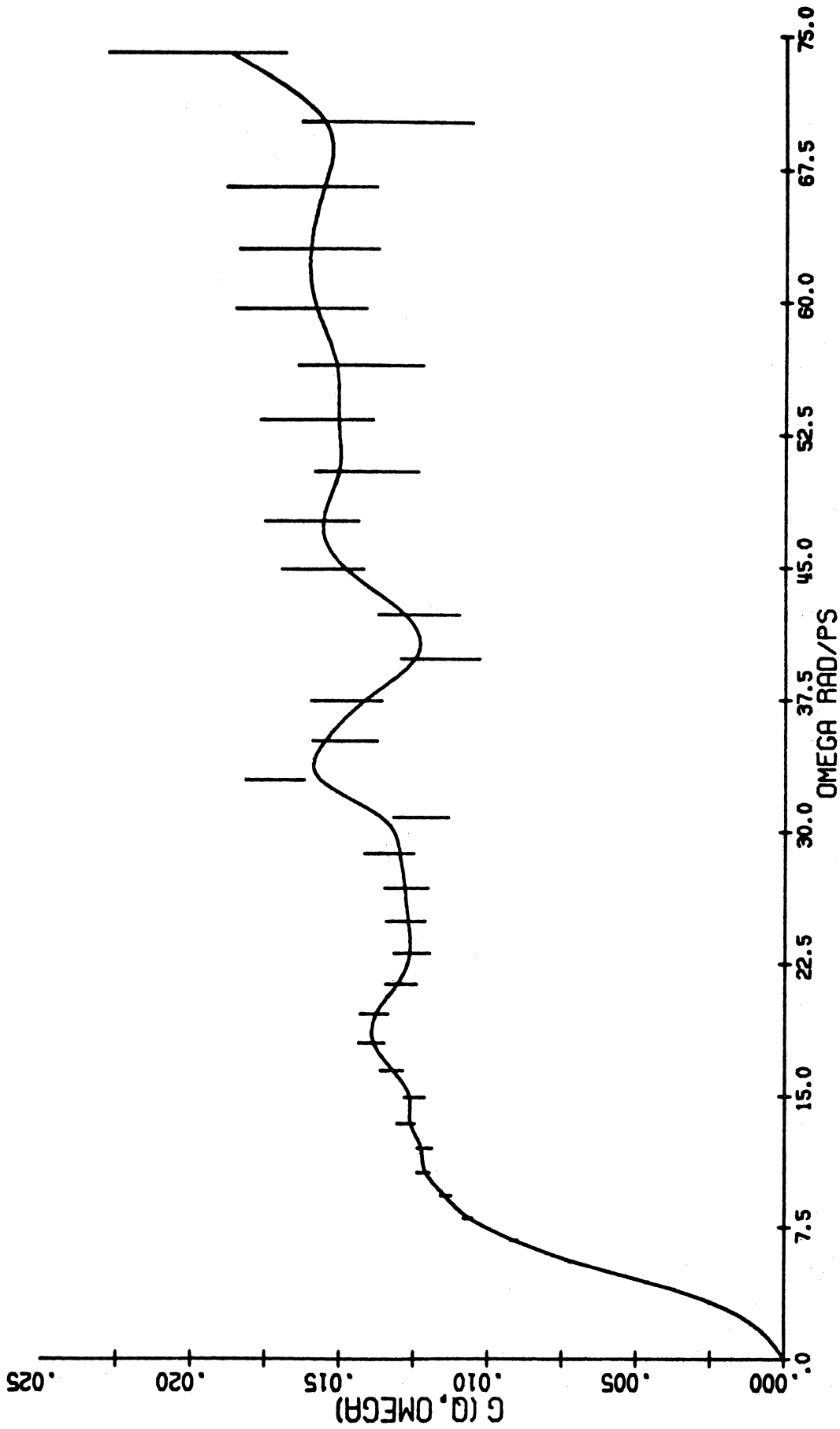

Figure A27. $G(Q,\omega)$ at 89.3 scattering angle.

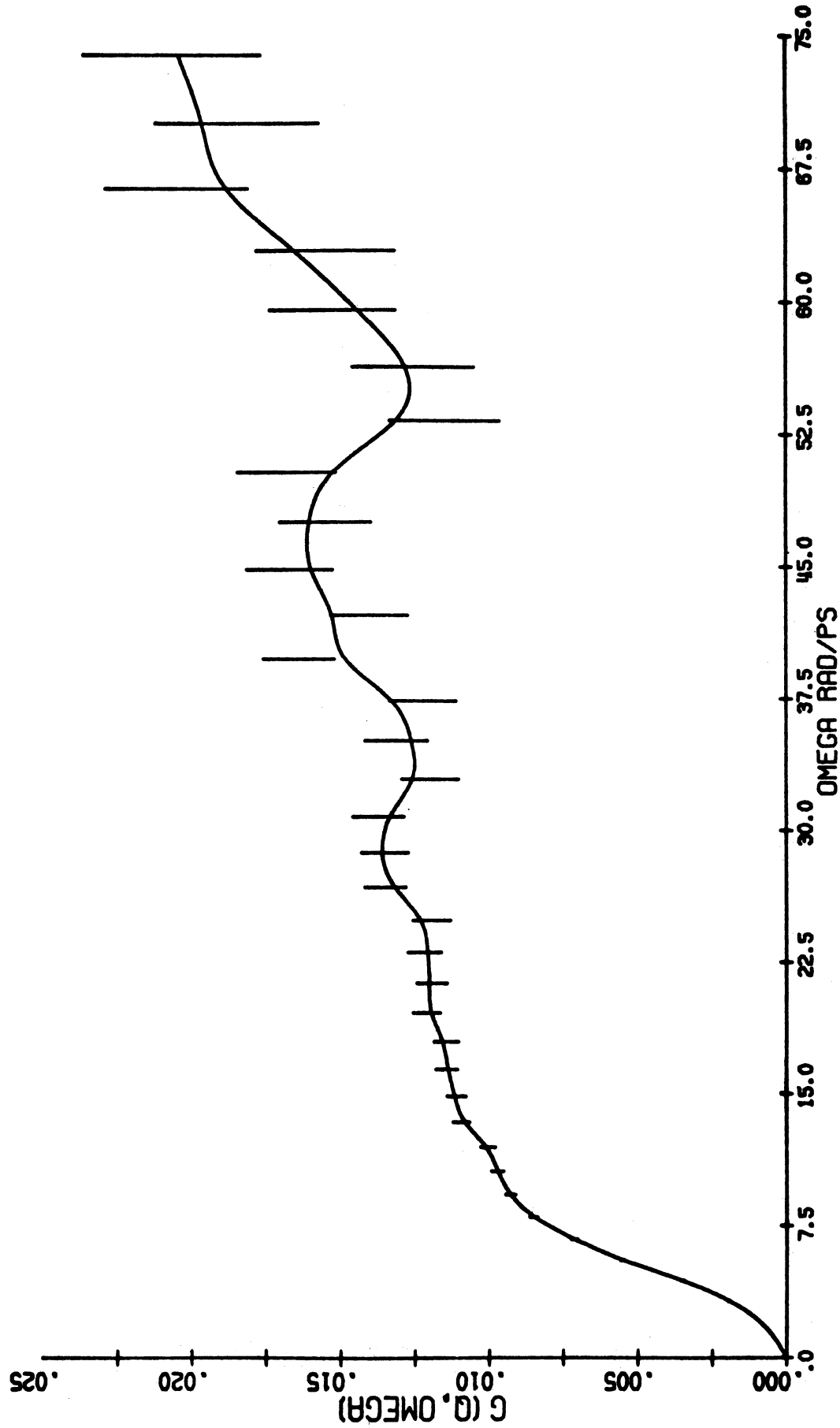

Figure A28. $G(Q,\omega)$ at 92.4° scattering angle.

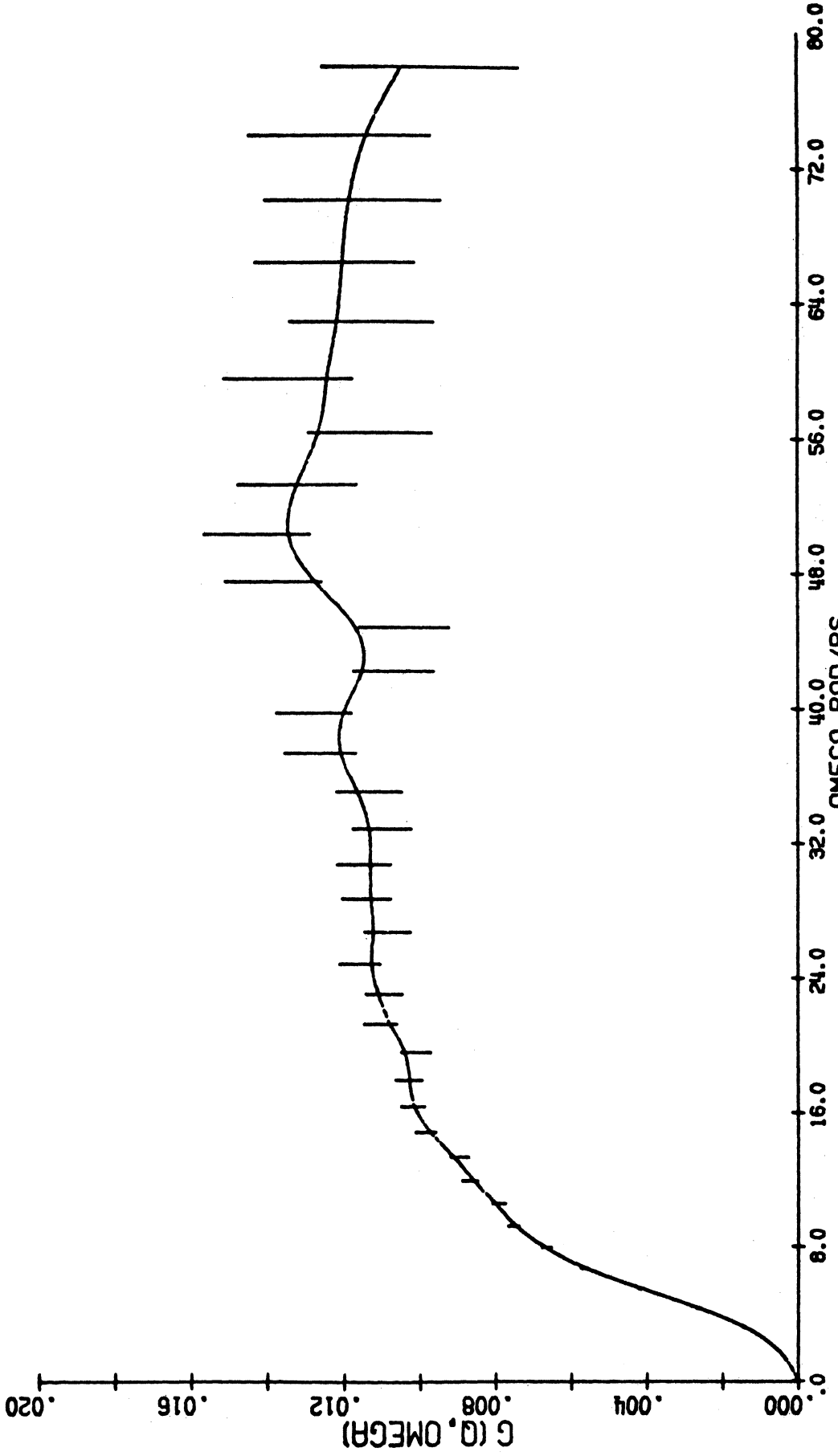

Figure A29. $G(Q,\omega)$ at 96.0° scattering angle.

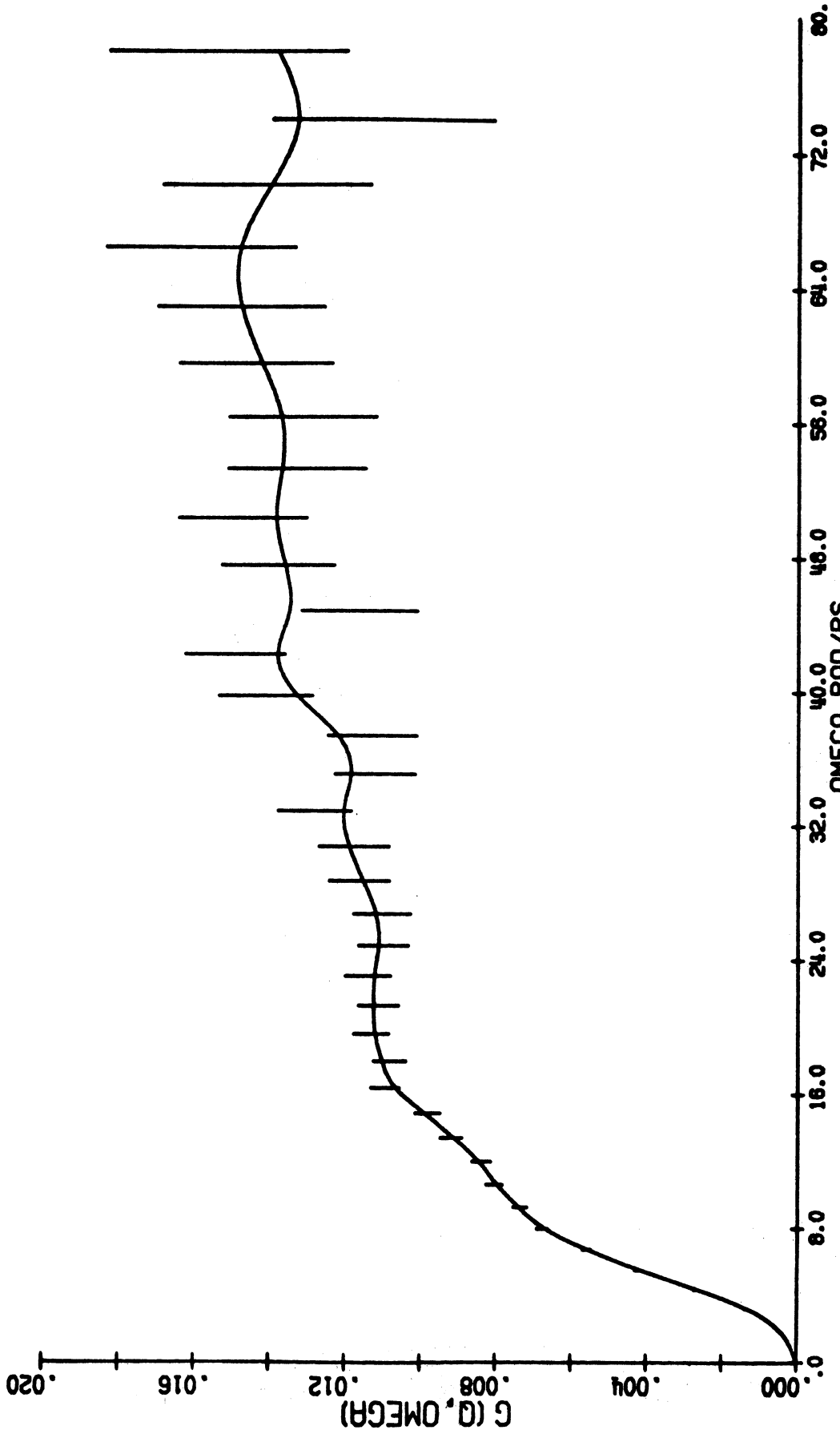

Figure A30. $G(Q,\omega)$ at 98.7° scattering angle.

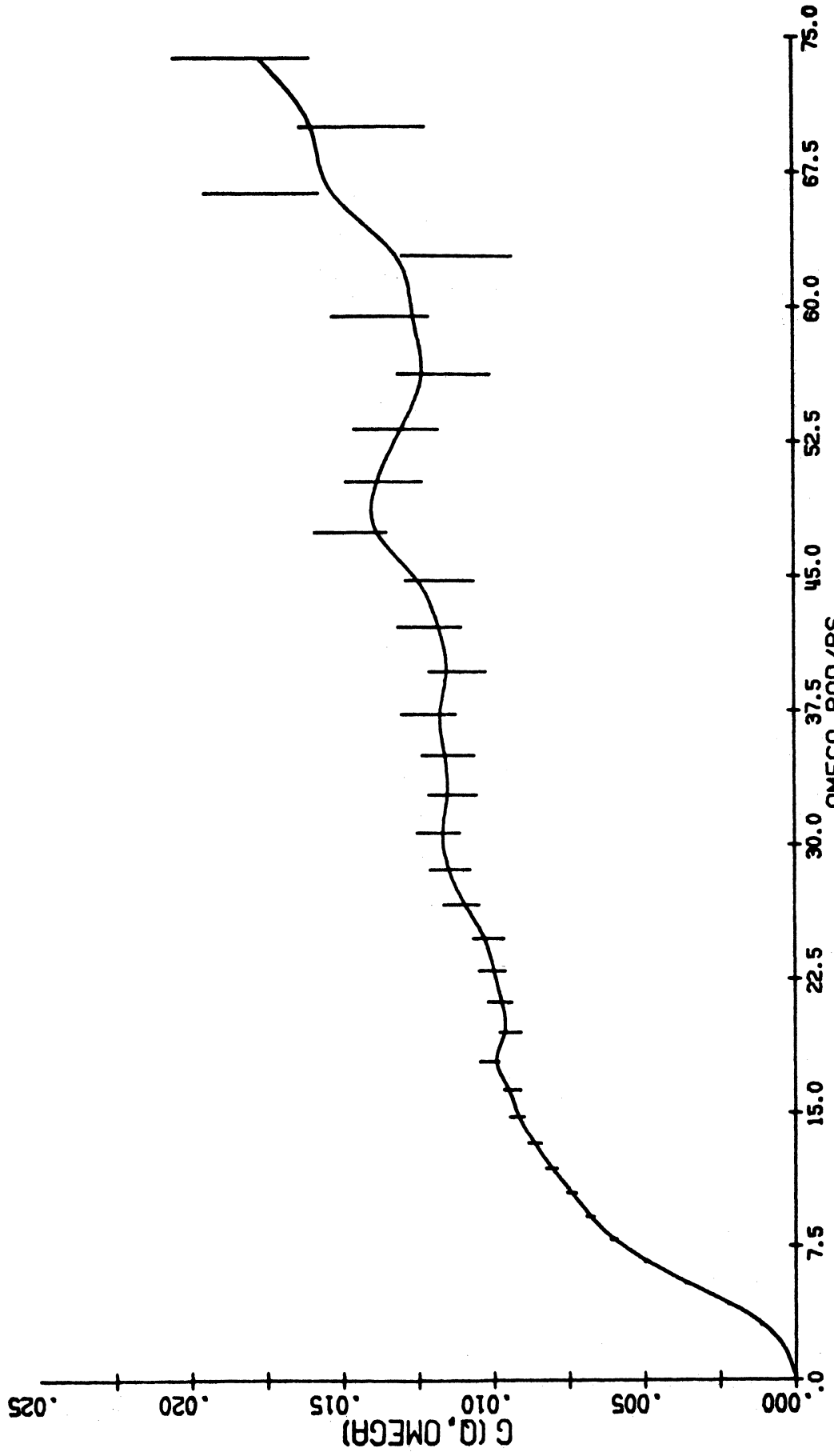

Figure A31. G(Q, ω) at 103.2° scattering angle.

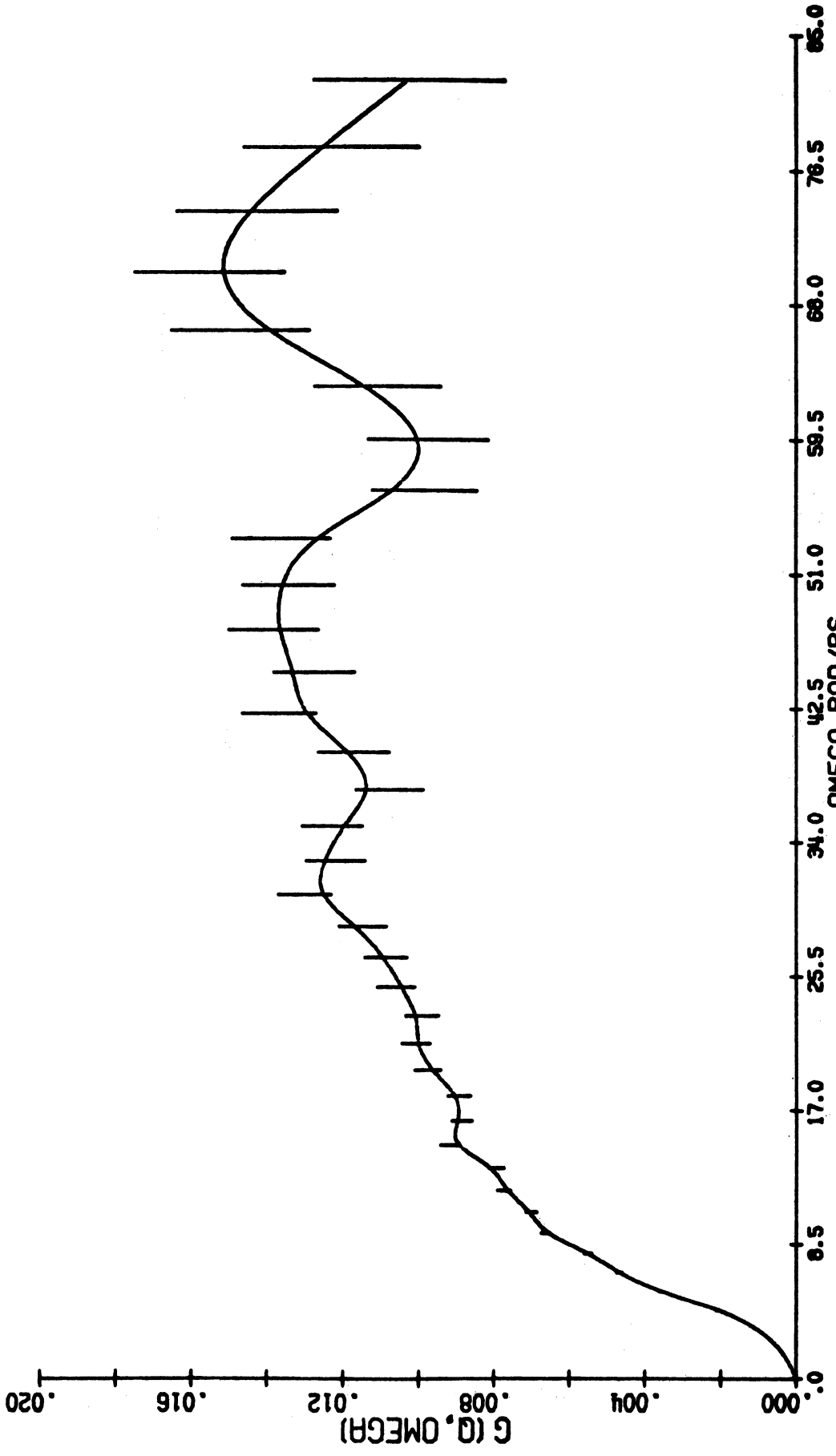

Figure A32. $G(Q,\omega)$ at 106.8° scattering angle.

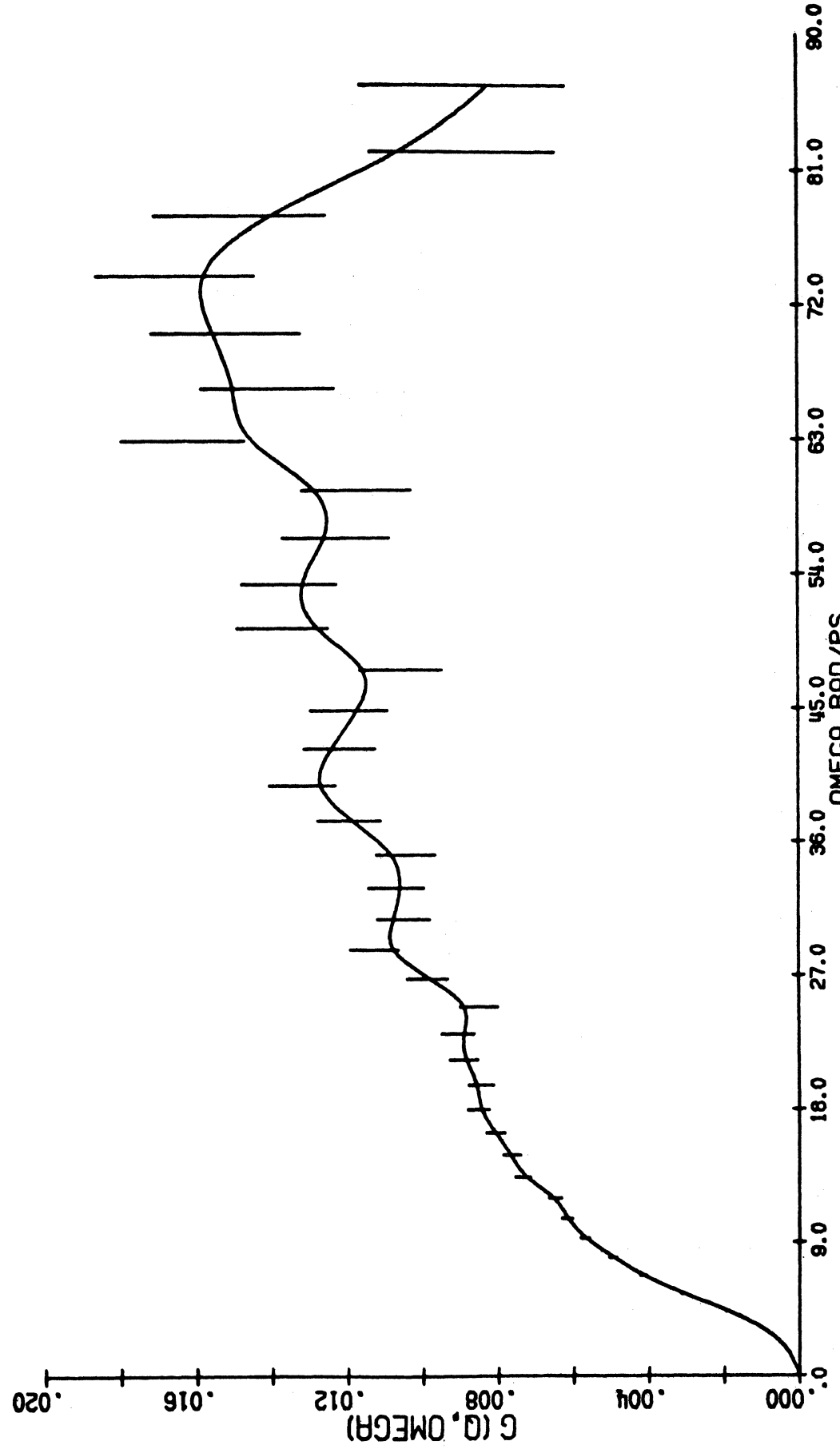

Figure A33. $C(Q,\omega)$ at 110.4° scattering angle.

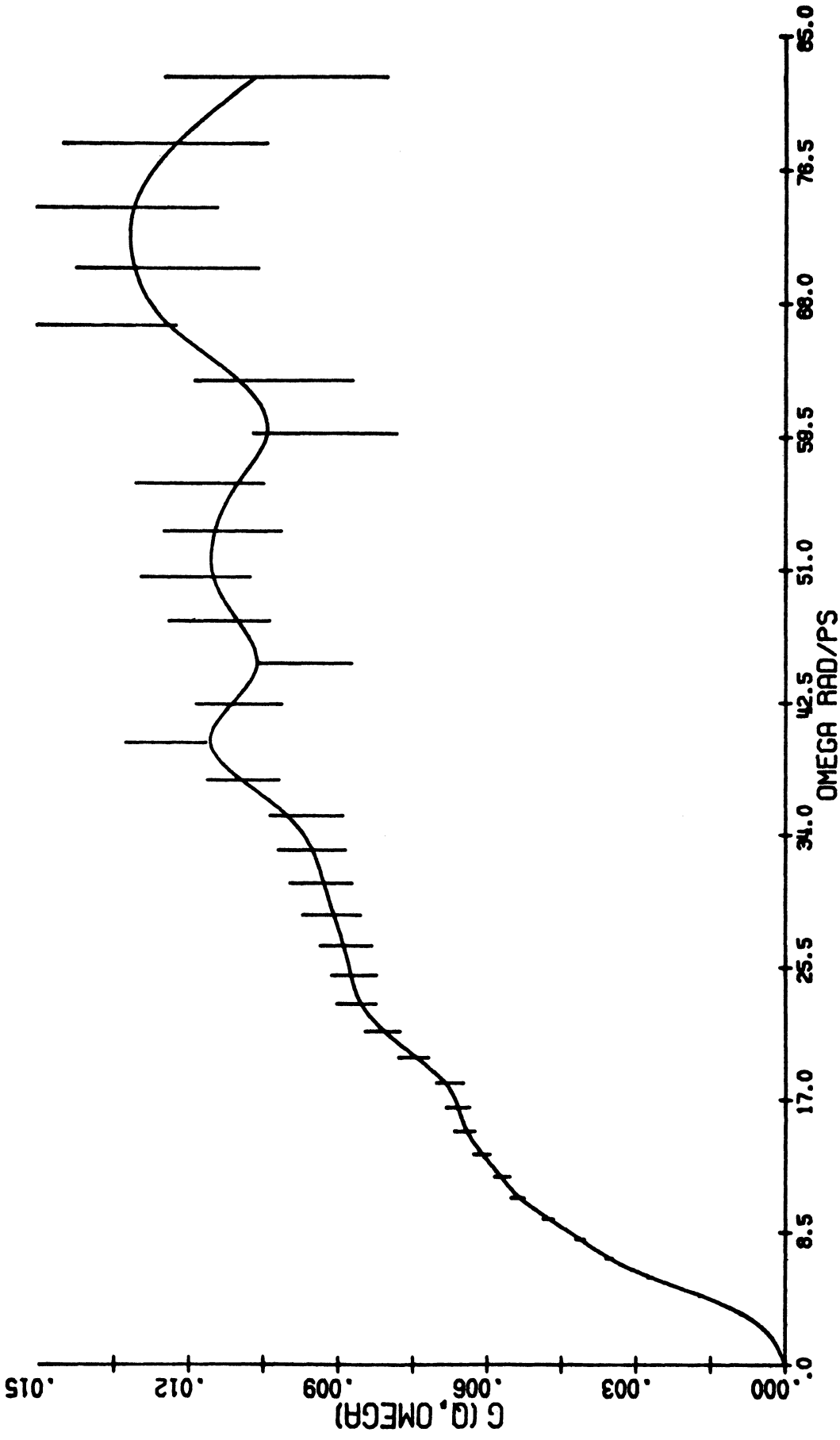

Figure A34. $G(Q,\omega)$ at 114.0° scattering angle.

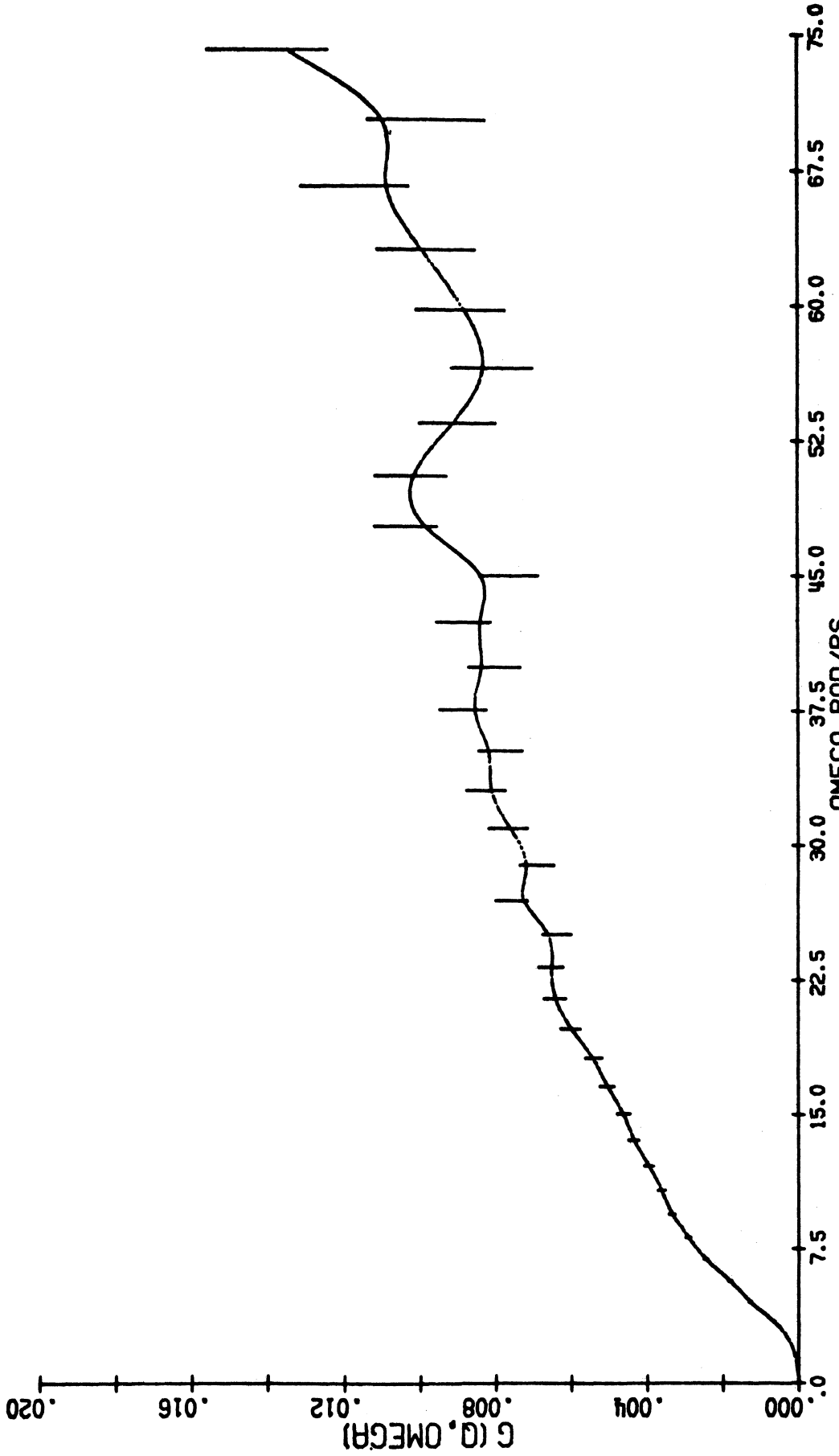

Figure A35. $G(Q,\omega)$ at 113.2° scattering angle.

APPENDIX TWO

MULTIPLE SCATTERING IN AN INCOHERENTLY SCATTERING PLATE

Consider a plate of thickness t and of infinite lateral extent. The incident beam (figure A36) makes angle θ_0 with

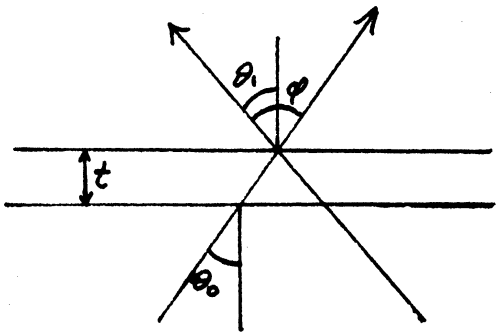

Figure A36.

the plate normal. The scattered beam makes angle θ_1 with the normal, and the scattering angle $\varphi = |\theta_0 - \theta_1|$. $(\theta_1 < 0)$

The first scattering is simply

$$V_1(Q) = R_1(\theta_1)\, e^{-2W(Q)}\, \frac{1 - e^{-\xi(\theta_0,\theta_1)}}{\xi(\theta_0,\theta_1)}$$

where

$$\xi(\theta_0,\theta_1) = \Sigma_T t (\sec\theta_0 - \sec\theta_1)$$

and

$$R_1(\theta_1) = \begin{cases} e^{-\Sigma_T t \sec\theta_1}, & \theta_1 < \pi/2 \quad \text{(transmission case)} \\ 1, & \theta_1 > \pi/2 \quad \text{(reflection case)} \end{cases}$$

Considering only elastic scattering, we have for the second scattering

$$V_2(Q) = \frac{\sigma_s}{\sigma_T} \frac{R_1(\theta_1)}{\Sigma_T t \sec\theta_0} \int_{-1}^{1}\int_{0}^{2\pi} \frac{e^{-2W(Q_1)}\, e^{-2W(Q_2)}}{(1 - \sec\theta_1/\sec\theta)}$$

$$\times \left\{ \frac{1 - e^{-\xi(\theta_0,\theta_1)}}{(1 - \sec\theta_1/\sec\theta_0)} - \frac{1 - e^{-\xi(\theta_0,\theta)}}{(1 - \sec\theta/\sec\theta_0)}\, e^{\xi(\theta_0,\theta)} \right\} \frac{d\alpha\, d\mu}{4\pi}$$

where

$$Q_1 = 2k \sin \varphi_1/2$$

$$Q_2 = 2k \sin \varphi_2/2$$

are the wave vector transfers for the intermediate scattering events, and the intermediate scattering angles are

$$\varphi_1 = \cos^{-1}[\sin\theta_0 \sin\theta \cos\alpha + \cos\theta_0 \cos\theta]$$

$$\varphi_2 = \cos^{-1}[\sin\theta \sin\theta_1 \cos\alpha + \cos\theta \cos\theta_1]$$

The indicated integrations are necessarily done numerically. The total scattering in Vineyard's approximation is expressed in terms of the first and second scattering as

$$V(Q) = V_1(Q) + V_2(Q)\left[1 - V_2(Q)/V_1(Q)\right]^{-1}$$

It is not obvious that this is a valid approximation for thin plates. The results of a calculation of P_T/P_I using this approximation, however, agree with results of Monte Carlo simulations for incoherently scattering plates. The Monte Carlo results are expected to be valid for a slowly varying cross section such as that of vanadium, so we can reasonably conclude that Vineyard's approximation is adequate for our reference scatterer.

APPENDIX THREE

SAMPLE ATTENUATION FACTOR

For a sample with macroscopic total cross section Σ_T^s contained in a holder of macroscopic total cross section Σ_T^c, we define the following distances:

d_o^c = distance traveled through container before scattering

d_o^s = distance traveled through sample before scattering

d_1^c = distance traveled through container after scattering

d_1^s = distance traveled through sample after scattering.

All these distances depend on the scattering point within the container, and the exit distances also depend on the scattering angle. The sample attenuation factor is the ratio of tube scattering with and without the sample, namely

$$SAF = \int_c \exp\left[-\Sigma_T^c(d_o^c + d_1^c) - \Sigma_T^s(d_o^s + d_1^s)\right] dV \div \int_c \exp\left[-\Sigma_T^c(d_o^c + d_1^c)\right] dV$$

with the integration taken over the container volume. In the case of a multiple tube sample container, one need only generalize the entry and exit distances as the total distance traveled through sample or container in all the tubes traversed, and extend the integration over the volume of all the tubes.

APPENDIX FOUR

ESTIMATION OF ERRORS IN RDF PEAK PARAMETERS

In order to arrive at an estimate of the uncertainity in our determination of the area, centroid and variance of the Be-F, F-F and Be-Be peaks in the refined experimental rdf, we have utilized the familiar error-propagation formula

$$\sigma^2[f(x,y,z,\cdots)] = \sigma^2(x)\left(\frac{\partial f}{\partial x}\right)^2 + \sigma^2(y)\left(\frac{\partial f}{\partial y}\right)^2 + \sigma^2(z)\left(\frac{\partial f}{\partial z}\right)^2 + \cdots$$

which is valid provided the variances of x,y,z...are independent. For our determination of coordination numbers, we used the relation

$$\bar{n} = K^{-1} \sum 4\pi r^2 \bar{g}(r) \Delta r$$

where K accounts for the scattering length weighting in the rdf, and Δr is the mesh spacing. For the variance in $\bar{n}$ due to errors in $4\pi r^2 \bar{g}(r)$ then, we have

$$\sigma^2(\bar{n}) = K^{-2} \sum \sigma^2(4\pi r^2 \bar{g}(r))(\Delta r)^2$$

Our determination of $\bar{r}$ used the relation

$$\bar{r} = \sum 4\pi r^3 \bar{g}(r) \Delta r / K\bar{n}$$

so that

$$\sigma^2(\bar{r}) = (K\bar{n})^2 \left\{ \sum \sigma^2(4\pi r^2 \bar{g}(r))(r\Delta r)^2 + \sigma^2(K\bar{n})\, \bar{r}^2 \right\}$$

And finally we calculated the variances using

$$\langle \Delta r^2 \rangle = \sum 4\pi r^2 \bar{g}(r)(r-\bar{r})^2 \Delta r / K\bar{n}$$

from which

$$\sigma^2(\langle \Delta r^2 \rangle) = (K\bar{n})^{-2} \left\{ \sum \sigma^2(4\pi r^2 \bar{g}(r))(r-\bar{r})^4 (\Delta r)^2 + \sigma^2(\bar{r}) \sum 4(r-\bar{r})^2 (4\pi r^2 \bar{g}(r))^2 (\Delta r)^2 + \sigma^2(K\bar{n})\, \bar{r}^2 \right\}$$

and

$$\sigma\left(\langle \Delta r^2 \rangle^{1/2}\right) = \frac{\sigma\left(\langle \Delta r^2 \rangle\right)}{2\langle \Delta r^2 \rangle^{1/2}}$$

We calculated the bond angles from the distances by

$$\measuredangle(X\text{-}Y\text{-}X) = 2\sin^{-1}\left(\frac{\bar{r}_{XX}}{2\bar{r}_{XY}}\right)$$

This gives for the variances

$$\sigma^2\left(\sin\tfrac{1}{2}\measuredangle(X\text{-}Y\text{-}X)\right) = \sigma^2(\bar{r}_{XX})(4\bar{r}_{XY})^{-2} + \sigma^2(\bar{r}_{XY})(-\bar{r}_{XX}/2\bar{r}_{XY}^2)^2$$

$$\sigma\left(\measuredangle(X\text{-}Y\text{-}X)\right) = 2\sigma\left(\sin\tfrac{1}{2}\measuredangle(X\text{-}Y\text{-}X)\right) / \cos\tfrac{1}{2}\measuredangle(X\text{-}Y\text{-}X)$$

We have calculated variances in our determinations of the various parameters by first assuming that there are independent errors in the values of $4\pi r^2\bar{g}(r)$ in the refined rdf. As an estimate of these errors, we used the mean squared deviation of the refined rdf with termination errors folded in, from the experimental rdf, in the peak regions (ie., the mean squared deviation of the crosses in figure 29 from the solid curve). This is probably an overestimate of the fitting errors in the refined rdf, but ignores the statistical imprecision of the diffraction data.

In this way we can associate an estimated uncertainity with each of the peak parameters derived from the refined rdf. These have been included in table 6.

LIST OF REFERENCES

1. Knipping, F.P. and M. von Laue, S.B. bayerishche Akad. Wiss. 315, (1912)

2. Debye, P. Ann. Phys. 461, 809 (1915)

3. Ehrenfest, P., Proc. Acad Sci. Amst. 23, 1138 (1915)

4. Randall, J.T., H.P. Rooksby and B.S. Cooper, Z. Krist. 75, 196 (1930)

5. Lebedev, A.A., Trans. State Optical Institute 2, #10 (1921)

6. Zachariasen, W.H., J. Am. Chem. Soc. 54, 3841 (1932)

7. Warren, B.E., J. Am. Ceram. Soc. 17, 249 (1934)

8. Warren, B.E. and C.F. Hill, Z. Krist. 89A, 481 (1934)

9. Valenkov, N.N., and E.A. Porai-Koshits, Nature 137, 273 (1936); Z. Krist. 95, 195 (1936)

10. Lebedev, A.A., Bull. Acad. Sci. USSR, phys. ser. 4, #4 (1940)

11. Evstropyev, K.S. and E.A. Porai-Koshits, J. Non-Crystalline Solids 11, 170 (1972)

12. Batsonova, L.R., G.S. Yur'ev and V.P. Dornina, Zh. Strukt. Khimii.9, 79 (1968)

13. Zarzycki, J. Phys. Chem. Glasses 12, 97 (1971)

14. Narten, A.H., J. Chem Phys. 56, 1905 (1972)

15. Zernike, F. and J.A. Prins, Z. Phys. 41, 184 (1927)

16. Debye, P. and H. Menke, Phys. Z. 31, 797 (1930)

17. Warren, B.E., H. Krutter and Morningstar, J. Am. Ceram. Soc. 19, 202 (1936)

18. Summerfield, G.C., J.M. Carpenter and N.A. Lurie, Introduction to the Theory of Slow Neutron Scattering (unpublished)

19. Turchin, V.F., Slow Neutrons (Jerusalem: Israel Program for Scientific Translations, 1965); W. Marshall and S.W. Lovesey, Theory of Thermal Neutron Scattering (Oxford: Clarendon Press, 1971)

20. Merzbacher, E., Quantum Mechanics, (Wiley, New York; 1961) chapter 15

21. Van Hove, L., Phys. Rev. 95, 249 (1954)

22. Ascarelli, P. and G. Caglioti, Nuovo Cimento 43, 375 (1966)

23. Zemach, A.C. and R. J. Glauber, Phys. Rev. 101, 118 (1956); ibid, p. 129 (1956)

24. Carpenter, J.M. and J.D. Sutton, Nucl. Inst. and Meth. 99, 453 (1972)

25. Powles, J.G., submitted to Molecular Physics

26. Sinclair, R.N. and A.C. Wright, in preparation

27. Placzek, G., Phys. Rev. 86, 377 (1952)

28. Wick, G.C., Phys. Rev. 94, 1228 (1954)

29. Carpenter, J.M., D.F.R. Mildner, C.A. Pelizzari, J.D. Sutton and J.E. Gunning, to be published in Nucl. Inst. and Meth.

30. Bullock, J.B., E.A. Daniels and J.S. King, Trans. Am. Nuc. Soc. 8, 302 (1965)

31. Carpenter, J.M., Nucl. Inst. and Meth. 47, 179 (1967); A. Holas, report INR-742 (Warsaw, 1966)

32. Lurie, N.A., unpublished (1966)

33. Wraight, L.A., D.H.C. Harris, and P.A. Egelstaff, Nucl. Inst. and Meth. 33, 181 (1965); K.F Graham, University of Michigan thesis, 1971 (available from University Microfilms, Ann Arbor)

34. Hughes, D.J., and R.L. Schwartz, USAEC document BNL-325, Second edition (1958)

35. Beyster, J.R., private communication to J.D. Sutton (1967)

36. Kleb, R., G.E. Ostrowski, D.L. Pine, and J.M. Rowe, Nucl. Inst. and Meth. 106, 221 (1973)

37. Garbow, B.S., Argonne Applied Mathematics Division Library Subroutine E350S (1968)

38. Krogh-Moe, J., Acta Cryst., 9, 951 (1956)

39. Rahman, A., J. Chem. Phys. 42, 3540 (1965)

40. Copley, J.R.D., Nucl. Inst. Meth. 107, 501 (1973)

41. Vineyard, G.H., Phys. Rev. 96, 93 (1954)

42. Bischoff, F.G., R.P.I. thesis 1970 (available from University Microfilms, Ann Arbor)

43. Bischoff, F.G., M.L. Yeater and W.E. Moore, Nucl. Sci. Eng. 48, 266 (1972)

44. Gaerttner, E.R., M.L. Yeater and R.R. Fullwood, in Neutron Physics (New York: Academic Press, 1962), p. 263

45. Copley, J.R.D., submitted to Comp. Phys. Commun.

46. Mildner, D.F.R., unpublished

47. Cooley, J.W. and J.W. Tukey, Math. of Comp. 19, 297 (1965)

48. Waser, J. and V. Schomaker, Revs. Mod. Phys. 25, 671 (1953)

49. Kaplow, R., S.L. Strong and B.L. Averbach, Phys. Rev 138A, 1336 (1965)

50. Yarnell, J.L., M.J. Katz, R.G. Wenzel and S.H. Koenig, Phys. Rev. A7, 2130 (1973)

51. Konnert, J.H. and J. Karle, submitted to Acta Cryst.; Nature Phys. Sci. 236, 92 (1972); ___, ___ and G.A. Ferguson, Science 179, 177 (1973)

52. Narten, A.H. and H.A. Levy, Science 165, 447 (1969)

53. Sutton, J.D., University of Michigan thesis, 1971, (available from University Microfilms, Ann Arbor)

54. Bates, J.B., J. Chem. Phys. 56, 1910 (1972)

56. Bell, R.J., private communication to J.M. Carpenter, 1971

57. Rahman, A., private communication, 1973.

58. Zarzycki, J. and F. Naudin, Verres et Refractaires 14, 113 (1960)

59. Quist, A.S., J.B. Bates and G.E. Boyd, USAEC document ORNL-4581, p. 166

60. Bell, R.J., N.F. Bird and P. Dean, J. Phys. C 1, 299 (1968)

61. Leadbetter, A.J. and A.C. Wright, J. Non-Crystalline Solids 3, 239 (1970)

62. Kroo, N., G. Borgonovi, K. Sköld and K.E. Larsson, Swedish AEC report RFX-326, (1964)

63. deWette, F.W. and A. Rahman, Phys. Rev. 176, 784 (1968)

64. Leadbetter, A.J. and K.E. Wycherley, Phys. Chem Glasses 12, 41 (1971)

65. Lingus, C., private communication (1969)